UNIVERSITY OF CASSINO AND SOUTHERN LAZIO

Department of Electrical and Information Engineering

Radio Resource Allocation in RIS-based Wireless Networks

A thesis submitted in fulfillment of the requirements
for the degree of *Doctor of Philosophy* in
Electrical and Information Engineering

PhD Cycle XXXVIII

January 2026

Cassino, Italy

SUPERVISOR:
Prof. Alessio Zappone

AUTHOR:
Robert Kuku Fotock

COORDINATOR:
Prof. Fabrizio MARIGNETTI

E-mail:
robertkuku.fotock@unicas.it

UNIVERSITY OF CASSINO AND SOUTHERN LAZIO

DEPARTMENT OF ELECTRICAL AND INFORMATION ENGINEERING

Date: **January 11, 2026**

Author: **Robert Kuku Fotock**

Title: **Radio Resource Allocation in RIS-based Wireless Networks**

Department: **Department of Electrical and Information Engineering**

Degree: **PHILOSOPHIAE DOCTOR**

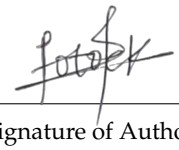

Signature of Author

"The present is theirs; the future, for which I really worked, is mine."
– Nikola Tesla

*To **Almighty God**, who blessed me with knowledge, wisdom, and understanding, and whose grace, love, and mercy sustained me through every stage of this journey. All strength, inspiration, and good health are gifts of His boundless faithfulness.*

*To my beloved **family**—my parents, brothers, and sisters— for your endless prayers, encouragement, and love. To my **wife and children**, whose patience and unwavering support gave meaning to each day and made this accomplishment possible.*

This milestone is not an end, but the beginning of an exciting journey toward greater discoveries and understanding.

Acknowledgements

Completing this doctorate has been a long and formative chapter of my life, marked by hard work, reflection, and continual learning. The path has had its challenges and its rewards, and I owe its success to the patience, generosity, and encouragement of many people and institutions.

My deepest gratitude goes to my supervisor, **Professor Alessio Zappone**. His steady guidance and clear way of thinking shaped the direction of this research from the very beginning. I have learned a great deal from his precision, integrity, and high standards, which have influenced not only this thesis but also the way I approach scientific work.

I am sincerely thankful to **Professor Stefano Buzzi**, **Dr. Carmen D'Andrea**, and **Dr. Giovanni Interdonato** for their constant help and encouragement. Their advice and readiness to assist made the more demanding periods of my Ph.D. easier to navigate, and their example created a friendly and collaborative atmosphere that allowed me to grow both personally and professionally.

I am also grateful to **Professor Marco Di Renzo** for the time, ideas, and guidance he shared during our collaborations. Working with him was a privilege, and his insight into wireless communications has been a lasting source of motivation and learning.

My thanks go as well to **Dr. Risto Valkonen** and to my colleague **Sravan Kumar Reddy Vuyyuru** for hosting me during my secondment at **Nokia, Oulu, Finland**. The period spent there discussing ideas, testing approaches, and experiencing an industrial research setting was invaluable for my development as an engineer and researcher.

This work has been carried out within the **MetaWireless Project**, funded by the European Union's Horizon 2020 Research and Innovation Programme under the **Marie Skłodowska-Curie Grant Agreement No. 956256**, which supported my research activities until November 30th, 2024. Being part of

this project provided me with the resources, structure, and international research environment that made the early stages of this thesis possible. Subsequently, this work was supported by the **GARDEN Project**, funded by the European Union under the **NextGenerationEU** plan, **Mission 4, Component 1**, through the Italian Ministry of University and Research (MUR) within the **PRIN 2022 programme** (D.D. 104 del 02-02-2022), CUP **H53D23000480001**. This support was instrumental in enabling the continuation and completion of the research presented in this thesis. I warmly thank all professors, supervisors, administrative staff, and fellow early-stage researchers involved in the MetaWireless project for their commitment, collaboration, and valuable scientific exchanges throughout my doctoral journey.

Beyond the academic setting, I owe more than words can express to my **family**. To my parents, **Fonsah James Fotock** and **Fossung Christina Cella**, whose sacrifices and faith have guided every step of my education. To my wife, **Tata Blessing Ngwashang**, your patience, prayers, and strength have held everything together and made this achievement possible. And to my children—**Kuku Koutney**, **Kuku Seth**, **Kuku Sheryl**, **Kuku Jeraiah**, and **Kuku Jenaiah**—thank you for your love and laughter, which gave every day of this journey its meaning.

Finally, I thank all friends, colleagues, and mentors whose advice or simple words of encouragement helped me along the way. Each of you has, in one way or another, shaped the person and the researcher I have become.

To all who made this possible—thank you.

Abstract

Future wireless systems must deliver higher data rates and reliability while meeting strict power consumption limits and hardware costs. In recent years, researchers have begun using **Reconfigurable Intelligent Surfaces (RIS)** and **Reconfigurable Holographic Surfaces (RHS)** to control the way signals move through space, relying on dense panels made of simple reflective units that require little power. This thesis investigates the design, modelling, and optimization of such metasurface-aided communication systems with a focus on **energy efficiency**, **spectral performance**, and **physical-layer security**.

The first part of the work analyses the role of active and nearly-passive RIS architectures under a global reflection constraint. Closed-form models for power consumption and achievable rate are derived, and new optimization frameworks are proposed for joint beamforming and reflection control. Results show that nearly-passive designs can approach, and in specific regimes surpass, the performance of active RISs when hardware losses are accurately accounted for. The analysis also clarifies how the power budget, amplifier efficiency, and the number of reflecting elements determine the optimal architecture.

The second part addresses the **Global Energy Efficiency (GEE)** and **Secrecy Energy Efficiency (SEE)** of metasurface-assisted multi-user MIMO systems. Novel algorithms are developed by combining fractional programming, sequential convex approximation, and the Dinkelbach-type method. Both the transmitter and the RIS/RHS coefficients are jointly optimized under realistic power and hardware constraints. The proposed schemes guarantee convergence to stationary points and significantly improve energy-per-bit and secrecy performance compared with conventional designs. The study also highlights the importance of explicitly optimizing for SEE rather than only maximizing the secrecy rate, as efficiency-driven formulations yield stable operation at moderate power levels without sacrificing security.

The final part explores **dual-metasurface configurations**, in which a transmit-side RHS is combined with an environmental RIS. This setting enables fine control of both the transmitted and reflected wavefronts. A dedicated optimization framework is introduced to coordinate the two surfaces under the unit-modulus constraint, enabling joint adaptation of the transmit and reflecting metasurfaces. Simulation results confirm that a base station with a few radio-frequency chains, assisted by a dual-metasurface arrangement, can outperform a much larger fully-digital array in overall

system efficiency. These findings establish dual-metasurface architectures as a viable path toward secure and sustainable sixth-generation (6G) wireless networks.

All optimization algorithms were implemented in PYTHON and MATLAB using MOSEK and `CVX`/`CVXPY` toolboxes. Extensive numerical experiments validate the analytical developments and provide design guidelines for future metasurface-assisted systems. In summary, the thesis contributes new theoretical insight and practical tools for realizing energy-efficient, secure, and programmable wireless environments.

Contents

List of Figures

List of Tables

List of Abbreviations

AN	**A**rtificial **N**oise
AO	**A**lternating **O**ptimization
AOA	**A**ngle of **A**rrival
AOD	**A**ngle of **D**eparture
BS	**B**ase **S**tation
BW	**B**and**w**idth
CPU	**C**entral **P**rocessing **U**nit
CSI	**C**hannel **S**tate **I**nformation
CSI-R	**C**hannel **S**tate **I**nformation at the **R**eceiver
CSI-T	**C**hannel **S**tate **I**nformation at the **T**ransmitter
CVX	**C**on**vex** Optimization Toolbox (MATLAB)
CVXPY	**C**on**vex** Programming for **P**ython
DFP	**D**inkelbach-type **F**ractional **P**rogramming
EE	**E**nergy **E**fficiency
EM	**E**lectro**m**agnetic
FP	**F**ractional **P**rogramming
GEE	**G**lobal **E**nergy **E**fficiency
GHz	**G**iga**h**ertz
HBF	**H**olographic **B**eam**f**orming
HMIMO	**H**olographic **MIMO**
KKT	**K**arush–**K**uhn–**T**ucker
LoS	**L**ine of **S**ight
MATLAB	**M**atrix **Lab**oratory (Numerical Computing Environment)
MB	**M**ega**b**yte
MIMO	**M**ultiple-**I**nput **M**ultiple-**O**utput
MM	**M**ajorization–**M**inimization
MMSE	**M**inimum **M**ean **S**quare **E**rror
MOSEK	**MOSEK** Optimization Solver
MRC	**M**aximal **R**atio **C**ombining
MRT	**M**aximum **R**atio **T**ransmission
NF	**N**ear-**F**ield

NLoS	**N**on-**L**ine-of-**S**ight
NOMA	**N**on-**O**rthogonal **M**ultiple **A**ccess
NR	**N**ew **R**adio (5G Standard)
OFDM	**O**rthogonal **F**requency **D**ivision **M**ultiplexing
PA	**P**ower **A**mplifier
PLS	**P**hysical **L**ayer **S**ecurity
PYTHON	**P**ython Programming Language
QoS	**Q**uality of **S**ervice
RAM	**R**andom **A**ccess **M**emory
RB	**R**esource **B**lock
RF	**R**adio **F**requency
RIS	**R**econfigurable **I**ntelligent **S**urface
RHS	**R**econfigurable **H**olographic **S**urface
Rx	**R**eceiver
SCA	**S**equential (**S**uccessive) **C**onvex **A**pproximation
SDP	**S**emi-**D**efinite **P**rogramming
SDR	**S**emi-**D**efinite **R**elaxation
SE	**S**pectral **E**fficiency
SEE	**S**ecrecy **E**nergy **E**fficiency
SFP	**S**equential **F**ractional **P**rogramming
SIM	**S**tacked **I**ntelligent **M**etasurfaces
SINR	**S**ignal-to-**I**nterference-plus-**N**oise **R**atio
SISO	**S**ingle-**I**nput **S**ingle-**O**utput
SNR	**S**ignal-to-**N**oise **R**atio
SOCP	**S**econd-**O**rder **C**one **P**rogramming
SR	**S**ecrecy **R**ate
SSR	**S**ecrecy **S**um **R**ate
SVD	**S**ingular **V**alue **D**ecomposition
SWIPT	**S**imultaneous **W**ireless **I**nformation and **P**ower **T**ransfer
Tx	**T**ransmitter
UAV	**U**nmanned **A**erial **V**ehicle
UE	**U**ser **E**quipment
UT	**U**ser **T**erminal
WsRHS	**W**ireless **R**econfigurable **H**olographic **S**urface

List of Symbols

Category	Description
Scalars, Vectors, Matrices	Scalars in italics (a, b); vectors in bold lowercase ($\mathbf{a}$); matrices in bold uppercase ($\mathbf{A}$).
System and Channel Parameters	Quantities defining antennas, users, channels, reflecting elements, and noise (e.g., N_T, N_R, N, $\mathbf{H}$, $\mathbf{G}$, σ^2).
RIS/RHS Variables	Reflection matrices and coefficients ($\mathbf{\Gamma}$, γ_n, ρ_n, φ_n), and phase profiles ($\mathbf{\Phi}_{\text{RIS}}$, $\mathbf{\Phi}_{\text{RHS}}$).
Power and Hardware Terms	Transmit, circuit, and amplifier powers (p_k, P_t, P_c, μ, $P_{R,\max}$).
Propagation Parameters	Path-loss, distance, Rician factor, and wavelength terms (d, ν, PL_0, K_{Rice}, λ, f_c).
Optimization Variables	Variables used in optimization and algorithm iterations (α, β, τ, ξ, ζ, ψ, $\mathbf{x}^{(t)}$, $\mathbf{x}^\star$).
Performance Metrics	Evaluation metrics such as EE, GEE, SEE, SE, SR, SSR, SNR, SINR.
Operators and Functions	Mathematical operators and functions ($\text{tr}(\cdot)$, $\|\cdot\|$, $\mathbb{E}[\cdot]$, $\Re\{\cdot\}$, $\Im\{\cdot\}$, $\log(\cdot)$).
Constants	Fundamental constants (e, j, c_0).

Summary of symbol categories used throughout the thesis.

Notation

a, b	Scalar quantities.
$\mathbf{a}, \mathbf{b}$	Column vectors.
$\mathbf{A}, \mathbf{B}$	Matrices.
$[\mathbf{A}]_{m,n}$	(m, n)-th entry of $\mathbf{A}$.
$(\cdot)^T, (\cdot)^H, (\cdot)^*$	Transpose, Hermitian transpose, and complex conjugate.
$\mathrm{tr}(\mathbf{A})$	Trace of $\mathbf{A}$.
$\|\mathbf{A}\|_F, \|\mathbf{a}\|_2$	Frobenius and Euclidean norms.
$\mathrm{vec}(\mathbf{A})$	Vectorization of $\mathbf{A}$.
$\otimes$	Kronecker product.
$\Re\{\cdot\}, \Im\{\cdot\}$	Real and imaginary parts.
$\mathbb{R}, \mathbb{C}$	Sets of real and complex numbers.
$\mathbb{E}[\cdot]$	Expectation operator.
N_T, N_R, N	Number of transmit/receive antennas and reflecting elements.
K	Number of users.
B	System bandwidth (Hz).
f_c	Carrier frequency.
λ	Wavelength.
c_0	Speed of light (3×10^8 m/s).
$\mathbf{H}, \mathbf{G}$	Channel matrices for BS–RIS/RHS and RIS/RHS–Rx links.
$\mathbf{h}_k, \mathbf{g}_k$	Channel vectors of user k.
$\mathbf{R}$	Positive-definite matrix in RIS/RHS power constraint.
$\boldsymbol{\Gamma}$	Diagonal reflection matrix $\mathrm{diag}(\gamma_1, \ldots, \gamma_N)$.
γ_n	Complex reflection coefficient of element n.
ρ_n, φ_n	Amplitude and phase of element n.
$\mathbf{y}$	Received signal vector.
$\mathbf{s}$	Transmitted symbol vector.
$\boldsymbol{\omega}$	Receiver thermal-noise vector.
$\mathbf{n}$	RIS internal noise vector (active RIS case).
$\mathbf{W}$	Noise covariance matrix.
p_k	Transmit power of user k.

$P_t, P_{\max}$	Total transmit power and its maximum.
P_c	Static circuit power consumption.
μ	Inverse of amplifier efficiency.
$P_{R,\max}$	Maximum amplification power at active RIS/RHS.
$K_{\mathbf{Rice}}$	Rician factor.
d	Propagation distance.
ν	Path-loss exponent.
PL_0	Reference path-loss.
σ^2	Noise variance.
η	SNR gain or efficiency factor.
α, β	Auxiliary parameters in fractional programming.
τ, δ, ϵ	Iteration or convergence tolerance parameters.
ξ, ψ, ζ	Auxiliary or penalty variables.
$\mathbf{x}^{(t)}$	Optimization variable at iteration t.
$\mathbf{x}^\star$	Optimal solution.
$\mathcal{L}$	Lagrangian function.
$\mathcal{S}$	Feasible set.
$\nabla_{\mathbf{x}} f$	Gradient operator.
$\mathcal{O}(\cdot)$	Computational complexity order.
$\mathbf{\Phi_{RIS}}, \mathbf{\Phi_{RHS}}$	Optimized RIS/RHS phase profiles.
$\mathbf{U}, \mathbf{V}$	Unitary matrices from SVD.
$\mathbf{I}_N, \mathbf{0}_{N\times M}$	Identity and zero matrices.
e	Euler's number.
j	Imaginary unit ($j^2 = -1$).
$\log(\cdot)$	Natural logarithm.
$\log_2(\cdot)$	Base-2 logarithm.
$\min(\cdot), \max(\cdot)$	Minimum and maximum operators.

Chapter 1

General Introduction

1.1 Motivation and Vision: Why RISs? Why EE and SEE matter for 6G?

The evolution of wireless connectivity has transitioned from a best-effort broadband model to a *critical infrastructure* essential for industries, transportation, healthcare, and public services. Traditionally, the advancement of new generations has relied on three main pillars: spectral efficiency, reliability, and latency. As the focus shifts towards sixth-generation (6G) systems, a necessary fourth pillar emerges: *sustainability* [70]. 6G must simultaneously cater to ultra-dense machine-type communications, immersive XR experiences, and safety-critical automation, all while adhering to strict *energy* and *security* requirements. This thesis acknowledges the dual requirement and prioritizes *energy efficiency (EE)* and *secrecy energy efficiency (SEE)* as primary design metrics.

Technological advancements such as massive MIMO and mmWave access have achieved significant gains in spectral efficiency; however, the improvements in *energy efficiency* observed in 5G have not met initial expectations. Projections anticipated substantial gains (e.g.,$\sim$2000$\times$ over LTE) [36]. Progress has been far more limited, constrained mainly by a significant *static power floor* resulting from numerous RF chains, high-speed data converters, baseband processing, and cooling needs. Evaluations from the industry suggest that while 5G enhances peak rates, its infrastructure may consume more power than 4G due to extensive digital arrays [45], [54]. In lightly loaded scenarios, the transmit power becomes insignificant compared to static consumption, leading to a *nearly linear* association between traffic growth and energy usage, an unsustainable path for 6G [34].

Equally vital is the issue of *intrinsic confidentiality*. 5G primarily depends on higher-layer cryptography; despite being robust, this cryptography increases processing and latency while not altering the broadcast nature of radio transmission. Emerging applications like vehicular coordination, remote actuation, and financial transactions require *physical-layer* protection to complement cryptographic measures. *Secrecy energy efficiency (SEE)* measures the securely transmitted information bits per Joule [14], [92], thereby integrating sustainability with confidentiality into a single, deployment-relevant metric. Based on this perspective, our research approaches energy and secrecy as *joint* physical-layer goals rather than isolated targets [31].

Reconfigurable intelligent surfaces (RISs) address both challenges by transforming the radio environment into a *programmable resource*. By electronically adjusting sub-wavelength elements, an RIS can control the phase and in some cases, the amplitude of incoming waves, enabling reflection shaping, interference suppression, and spatial energy steering [22], [23], [84]. Since the control mechanism is mainly analog, and per-element static power consumption is minimal, RISs enable extensive wave manipulation at a significantly reduced energy cost compared to fully digital arrays. When paired with physical-layer security (PLS) designs, RISs can reshape propagation in favor of legitimate users while hindering eavesdroppers, providing inherent secrecy benefits *by construction* [22].

This thesis examines three complementary architectures within a cohesive modeling framework:

- **Nearly-passive RISs** operate in a phase-only (or near unit-modulus) mode with extremely low circuit power. Their primary drawback is the well-established issue of *double (multiplicative) fading*: the total gain is the product of Tx→RIS and RIS→Rx path losses, which can significantly weaken cascaded links unless the geometry and placement are optimized [23]. This drives the need for careful design and large-aperture solutions.

- **Active RISs** incorporate reflection-type amplification to alleviate double fading. Amplification occurs in the electromagnetic domain (as opposed to relays) and does not require RF chains; however, it introduces internal noise and non-negligible static power, making overall gains *regime-dependent* [32], [53], [99]. Determining the conditions under which active RISs surpass nearly-passive ones in terms of *SEE/EE* is a key focus of this thesis.

- **Dual-metasurface systems** combine a reconfigurable holographic surface (RHS) in the base station near field (for analog-domain beamforming) with an external RIS that modifies the environment. This combination reduces dependence on energy-intensive digital RF chains while maintaining strong spatial control, resulting in significant EE improvements and, under secrecy constraints, SEE advantages compared to traditional designs [33].

Traditional abstractions enforce constraints of unit-modulus (or limited amplitude) on each element. Instead, we take a *global-reflection* approach that views the surface as a macro-reflector bound by an *aggregate* power-balance constraint: energy is conserved during nearly-passive operation and *budgeted* for active operation. This physics-informed relaxation facilitates the redistribution of reflection power among elements, expands the feasible set compared to unit-modulus designs, and offers a *common ground* for evaluating both nearly-passive and active scenarios. The resulting design space provides significant enhancements in both energy efficiency (EE) and secrecy energy efficiency (SEE) and is better aligned with realistic wave interactions [34], [79].

Our primary vision is that *programmable propagation* achieved through nearly-passive RISs, active RISs, and dual-metasurface designs is a fundamental element of sustainable and secure 6G networks. By prioritizing EE and SEE as key goals and integrating all three architectures within a global-reflection model that accounts for realistic circuit/noise considerations, this thesis provides a cohesive framework and implementable design guidelines for 6G implementations. Conceptual comparisons are illustrated in Fig. 1.1.1 and discussed in detail throughout; the optimization strategies (fractional programming, alternating optimization, SCA, and SDP-based rank-1 enforcement) are outlined in Section 1.4 and thoroughly derived in the Appendices.

1.2 Research Context: Limitations of 5G and the "gaps"

The fifth generation of mobile systems has introduced transformative technologies, including massive MIMO, millimeter-wave access, and network slicing; however, it has not adequately resolved two critical structural deficiencies on the trajectory to 6G: the energy-efficiency gap and the security

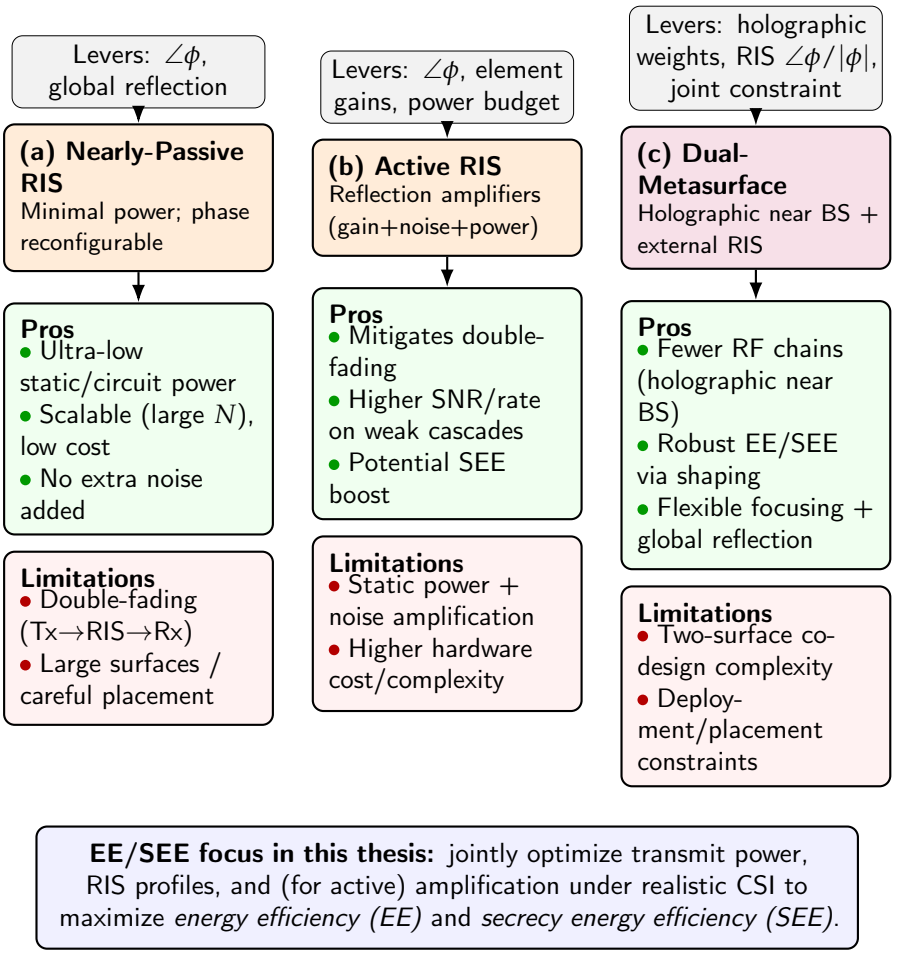

FIGURE 1.1.1: Summary of RIS architectures with advantages/limitations and design levers.

gap. Both are grounded in essential elements of 5G's physical-layer architecture and implementation strategies, necessitating a paradigm shift to achieve the lofty performance and sustainability objectives of 6G.

The energy-efficiency gap

Massive MIMO utilizing completely digital beamforming has emerged as the technological hallmark of 5G. The system may spatially multiplex multiple users by outfitting base stations with numerous active antenna elements and specialized RF chains, and achieve significant capacity enhancements. This architectural decision incurs a considerable energy expenditure. Each

RF chain requires power-intensive components—such as data converters, mixers, filters, and cooling systems—that create a *static power floor* regardless of the traffic load [9]. Consequently, the energy efficiency (EE), quantified in bits per Joule, demonstrates only marginal enhancements relative to LTE, far behind the thousand-fold advancement anticipated in initial 5G roadmaps [36]. In weakly loaded or idle conditions, where transmission power is minimal, static circuit consumption predominates the overall energy expenditure, resulting in suboptimal energy efficiency. This scaling limitation indicates that increasing network density with larger arrays and higher carrier frequencies would not yield lasting improvements. Without innovative physical-layer approaches, the demand for 6G traffic may lead to a nearly proportional increase in network power consumption.

The security gap

Alongside its efficiency, 5G also raises ongoing concerns related to confidentiality and reliability. The security framework predominantly depends on advanced cryptographic algorithms at higher layers for authentication, key management, and data protection. Although established and stable, these systems introduce latency, elevate computing demands, and are susceptible to scaling and backward compatibility challenges. Crucially, they do not modify the *broadcast nature of the wireless medium*: adversaries within the vicinity of a transmitter may invariably intercept radio signals, irrespective of the encryption employed [11]. Physical-layer security (PLS) provides an auxiliary method by utilizing the intrinsic randomness of channels to ensure confidentiality at the waveform level. Methods such as artificial noise production, cooperative jamming, or beamforming nulls can enhance secrecy capacity. Nonetheless, these methods generally incur significant transmit power, diminished data speeds, or considerable energy consumption. Although standard PLS approaches are theoretically promising, they have yet to exhibit the scalability or efficiency required to meet the demands of ubiquitous 6G services.

Implications for 6G

The simultaneous presence of these two gaps carries substantial ramifications. Energy sustainability and inherent confidentiality are not distinct design goals but interdependent constraints: secure transmission must be accomplished without incurring excessive energy expenditure, and efficient communication must be resilient against eavesdropping. Addressing these

gaps necessitates a novel paradigm wherein energy and secrecy are regarded as *joint optimization objectives* at the physical layer, rather than as separate aims across various stack tiers. When created with stringent energy-efficient and secrecy-conscious standards, reconfigurable intelligent surfaces (RISs) present a compelling solution to address this gap. By enabling low-power, programmable wave management, RISs provide additional spatial degrees of freedom that can simultaneously enhance energy efficiency and guarantee physical-layer security, thereby addressing the limitations that 5G has not resolved.

1.3 RIS as an Enabler: Architectures, Double Fading, and Global Reflection

Reconfigurable intelligent surfaces (RISs) are planar metasurfaces populated by many sub-wavelength scattering elements whose boundary impedances can be electronically tuned to control the phase (and, in some implementations, the amplitude) of impinging electromagnetic waves. By programming the reflection profile across the surface, the wireless medium itself becomes a design parameter, enabling environment-aware beamforming with vanishingly small radio-frequency (RF) footprint compared to fully-digital arrays [10], [84]. In this thesis, we consider three architectural families: nearly-passive RISs, active RISs, and dual-metasurface systems, and adopt a unified modeling viewpoint based on *global reflection constraints* suited for energy/secrecy analyses. [34].

1.3.1 Nearly-Passive RISs and the Double-Fading Bottleneck

A nearly-passive RIS comprises N reconfigurable elements with reflection coefficients $\phi_n = \rho_n e^{j\theta_n}$, typically operated in phase-only mode ($\rho_n \approx 1$) to minimize circuit power. Let $\mathbf{H} \in \mathbb{C}^{N\times N_t}$ denote the Tx→RIS channel, $\mathbf{G} \in \mathbb{C}^{N_r\times N}$ the RIS→Rx channel, and $\mathbf{\Phi} = \mathrm{diag}(\phi_1, \ldots, \phi_N)$ the RIS response. The end-to-end (cascaded) MIMO channel is

$$\mathbf{H}_{\text{eff}} \;=\; \mathbf{G}\,\mathbf{\Phi}\,\mathbf{H}, \qquad (\text{SISO: } h_{\text{e2e}} = \mathbf{g}^H \mathbf{\Phi} \mathbf{h}). \tag{1.3.1}$$

For clarity of exposition, the direct transmitter–receiver (Tx→Rx) path is not included in (1.3.1). This modeling choice is motivated by practical deployment scenarios in which the direct link is severely attenuated or blocked, such as dense urban environments, indoor layouts with obstructions, or

unfavorable propagation geometries. In these cases, the RIS-assisted link becomes the dominant or most reliable communication path, and isolating its contribution allows the impact of the reconfigurable surface to be more clearly analyzed. The inclusion of a direct link would result in an additional additive channel term and does not alter the structure of the optimization frameworks developed in this thesis.

While coherent phase alignment across elements can yield an $O(N^2)$ *array-product* gain in the best case, the effective large-scale attenuation is the *product* of the Tx→RIS and RIS→Rx path losses. This *double-fading effect* is the fundamental bottleneck of nearly-passive RISs [22], [85], [99]. Unless the surface is large and optimally placed (favorable distances/angles), the cascaded link can be substantially weaker than a direct link, limiting achievable rates and coverage [10], [44].

From an energy perspective, nearly-passive RISs are attractive because they require only quasi-static control power (for biasing and switching) and introduce no additional RF noise [85]. In practice, discrete phase quantization and element losses slightly reduce ideal gains, but the overall *static power floor* remains orders of magnitude below that of fully-digital arrays. Consequently, nearly-passive RISs can deliver significant energy-efficiency (EE) benefits whenever geometry permits strong cascaded channels [22], [34], [44].

1.3.2 Active RISs: Gain Versus Power/Noise Trade-Off

To alleviate double fading, *active RISs* embed low-power reflection-type amplifiers at the elements, enabling $\rho_n > 1$ and direct compensation of the cascaded attenuation at the electromagnetic wavefront. Modeling-wise, the received signal at the BS (uplink) or at the UE (downlink) acquires an additional term due to the RIS internal noise: if $\mathbf{n}_R \sim \mathcal{CN}(\mathbf{0}, \sigma_R^2\mathbf{I})$ is the amplified thermal noise introduced at the surface, the receiver collects both the desired $\mathbf{G\Phi Hx}$ and the colored noise $\mathbf{G\Phi n}_R$, on top of receiver noise. At the same time, amplification incurs non-negligible *static* power in the RIS circuits.

Therefore, active RISs offer a *conditional* advantage: they can deliver higher SNR (and, under secrecy constraints, a stronger legitimate channel with better spatial selectivity), but only when the *net* gain outweighs the penalties due to (i) amplified noise and (ii) added circuit power. In short, their merit depends on three coupled factors: the strength of the cascaded channels, the amplification profile $\{\rho_n\}$, and realistic static power budgets. This thesis quantifies trade-offs under secrecy-energy efficiency (SEE) and

EE metrics. It shows that active RISs can outperform nearly-passive ones in weak-link regimes or unfavorable placements provided circuit budgets are judiciously managed.

1.3.3 Global Reflection Constraints: A Unified, Physics-Aware Model

Classical communication-centric formulations impose *local* constraints on each element (e.g., unit-modulus $|\phi_n| = 1$ for passive RISs, or per-element amplitude ceilings). However, from an electromagnetic standpoint, the surface behaves as a coupled structure wherein power can be redistributed across elements while respecting an *aggregate* conservation law (passive) or an *aggregate* amplification budget (active). This motivates the *global reflection* model adopted in this thesis.

Let $\mathbf{R} \succeq \mathbf{0}$ denotes the covariance of the impinging field at the RIS (including multiuser contributions and, for active RISs, the internal noise term). With $\boldsymbol{\gamma} = [\phi_1, \ldots, \phi_N]^T$ the vector of reflection coefficients, a compact expression of the surface power balance is [32], [34]:

$$\underbrace{\mathrm{tr}\big(\mathbf{R}\,\boldsymbol{\gamma}\boldsymbol{\gamma}^H\big)}_{\text{reflected RF power}} - \underbrace{\mathrm{tr}(\mathbf{R})}_{\text{impinging RF power}} \leq P_{R,\max}, \tag{1.3.2}$$

where $P_{R,\max} = 0$ yields the *nearly-passive* case (no RF power injection), and $P_{R,\max} > 0$ models an *active* RIS with a total amplification headroom. Constraint (1.3.2) treats the RIS as a *macro-reflector*: some elements may use $|\phi_n| > 1$ if compensated by others with $|\phi_m| < 1$ (or vice-versa), as long as the net power balance is respected.

This physics-aware abstraction has two key consequences:

1. It *strictly generalizes* the unit-modulus model and enlarges the feasible set of $\boldsymbol{\gamma}$, enabling better alignment with composite channels $\mathbf{G}$ and $\mathbf{H}$. Analytical and numerical results show tangible SNR/EE gains over local constraints, even in single-user settings [34].

2. It provides a *unified* framework to compare nearly-passive and active RISs on common ground by simply varying $P_{R,\max}$ and the noise term σ_R^2 (present only in the active case). This unification is pivotal for fair EE/SEE comparisons and algorithmic designs that seamlessly specialize to either regime [32], [34].

In the remainder of the thesis, we leverage (1.3.2) to develop provably convergent EE/SEE optimization algorithms and to derive closed-form structures in exceptional cases (e.g., single-stream or single-antenna), thereby quantifying when and why global-reflection-aware RIS designs yield decisive performance advantages over classical unit-modulus formulations.

1.4 Scope and Assumptions

This thesis adopts a set of modeling choices that strike a balance between physical fidelity and analytical tractability and that remain consistent across all chapters unless explicitly stated otherwise.

Network Topology and Roles

We consider a single-cell uplink/downlink system in which a multi-antenna base station (BS) communicates with K single-antenna or few-antenna user terminals (UTs). One or two reconfigurable metasurfaces are deployed as part of the environment: (i) a reconfigurable intelligent surface (RIS) placed at a favorable, fixed location to assist the cascaded Tx$\rightarrow$RIS$\rightarrow$Rx path; and, in some chapters, (ii) a reconfigurable holographic surface (RHS) located in the near field of the BS to provide analog-domain beamforming (dual-metasurface architecture). Unless otherwise stated, the eavesdropper (Eve) is modeled as a passive single-antenna device positioned in less favorable propagation conditions than the legitimate receiver, which reflects practical cases where the BS and RIS are placed deliberately to enjoy line-of-sight (LoS) or strong components while Eve is mobile and unsynchronized.

Propagation and Channel Models

- *Far-field RIS links:*The UT$\rightarrow$RIS and RIS$\rightarrow$BS/UE channels are modeled as frequency-flat Rician block-fading with path-loss and shadowing. The Rician K-factors differ across links to reflect deployment asymmetry (e.g., stronger LoS for RIS$\rightarrow$BS than for UTs/Eve$\rightarrow$RIS). Path-loss exponents are set in line with urban macro/micro deployments (e.g., $n \approx 4$ for UT/Eve$\rightarrow$RIS, $n \approx 2$ for RIS$\rightarrow$BS), unless specified in each experiment.
- *Near-field RHS links (dual metasurface):* When an RHS is deployed in the BS near field, Tx$\leftrightarrow$RHS (and RHS$\leftrightarrow$Rx if applicable) are modeled using a spherical-wave propagation model; the RIS in the environment still

uses far-field modeling. This preserves the distinct physics of near-field focusing at the RHS and environment shaping at the RIS.

- *Block fading & independence:* Channels remain constant over a coherence block and change independently between blocks. Spatial correlation at the RIS is implicitly captured via the global-reflection formulation (see below) through the impinging-field covariance.

Channel State Information (CSI)

- *Legitimate links:* The BS has perfect or estimated CSI for UT↔BS and RIS-assisted cascaded channels, depending on the scenario. In robust designs, the quality of a statistically known channel (e.g., RIS→Eve) is parameterized via a normalized error variance (NEV) and tested over Monte Carlo realizations to emulate partial/uncertain knowledge.
- *Eavesdropper links:* Two regimes are considered: (i) *perfect Eve CSI* for benchmark upper bounds; and (ii) *statistical Eve CSI* (or even absent Eve CSI), where only distributional information is used in design while performance is evaluated on true channel draws. This reflects practical cases where Eve is hidden or only roughly localized.
- *RIS coefficients:* The reflection vector $\boldsymbol{\gamma} = [\gamma_1, \ldots, \gamma_N]^T$ is optimized centrally at the BS and treated as quasi-static over the coherence block for which it is configured.

RIS Modeling: Global Reflection, Active vs. Nearly-Passive

- *Global reflection constraint:* The RIS is modeled as a *macro-reflector* that enforces a single power-balance constraint on the total reflected RF power, rather than independent per-element amplitude constraints. Let $\mathbf{R}$ be the covariance of the impinging field on the RIS (accounting for multiuser signals and, for active RISs, internal noise). With $\Gamma = \mathrm{diag}(\boldsymbol{\gamma})$,

$$\text{(Passive)}\ \ \mathrm{tr}(\mathbf{R}\Gamma\Gamma^H) \le \mathrm{tr}(\mathbf{R}), \qquad \text{(Active)}\ \ \mathrm{tr}(\mathbf{R}\Gamma\Gamma^H) \le \mathrm{tr}(\mathbf{R}) + P_{R,\max}.$$

  This permits local $|\gamma_n| > 1$ as long as the *aggregate* power balance holds, consistent with physically plausible power exchange along the surface. The nearly-passive case is recovered by setting $P_{R,\max} = 0$ and the RIS internal noise to zero.

- *Noise model (active RIS):* Reflection-type amplifiers introduce an additive Gaussian noise at the RIS with variance σ_{RIS}^2; after reflection, this noise is

filtered by the RIS→Rx channel and contributes to the receiver covariance. Nearly-passive RISs do not inject RF noise.

- *Local-constraint baseline:* Unit-modulus ($|\gamma_n| = 1$) designs are used as a baseline. The global-reflection feasible set strictly contains the local set, enabling performance gains and a fair comparison across passive/active regimes by continuity in $P_{R,\max}$.

Power Accounting and Static Budgets

- *Amplification power at the RIS:* The RIS RF amplification power is modeled as the *net* difference $P_{\text{out}} - P_{\text{in}} = \text{tr}\big((\Gamma\Gamma^H - \mathbf{I})\mathbf{R}\big)$; this correctly discounts the impinging RF power, which the RIS does not consume.
- *Static power:* total consumed power includes BS/UT RF power with amplifier inefficiencies, plus static circuit terms. For the RIS, static power has a per-element bias/control term and a surface-level term; active RISs use larger static budgets than nearly-passive ones due to amplifier biasing and control.
- *Bandwidth/noise:* The system bandwidth B and receiver noise figure define the thermal-noise floor; where needed, we adopt $N_0 = -174\,\text{dBm/Hz}$ with a 5 dB noise figure as a reference and scale with B.

User and Array Configurations

- *Users:* Unless otherwise noted, UTs and Eve use single antennas; extensions to few-antenna UTs are stated in the relevant chapters.
- *BS arrays:* The BS employs a moderate number of RF chains (far fewer than fully digital massive MIMO) in dual-metasurface chapters, leveraging the RHS for analog-domain beam shaping; in single-RIS chapters, the BS/UE arrays follow conventional MIMO assumptions.
- *RIS/RHS sizes:* The number of RIS elements N and RHS elements is scenario-specific and stated in each study; placement is chosen to ensure favorable geometry for legitimate links while keeping Eve in a less favorable region.

Performance Metrics

- *Global Energy Efficiency (GEE/EE):*

$$\mathrm{EE} \;=\; \frac{B\sum_{k=1}^{K}\log_2\!\left(1+\mathrm{SINR}_k\right)}{\underbrace{\mathrm{tr}\!\left((\Gamma\Gamma^H-\mathbf{I})\mathbf{R}\right)}_{\text{RIS RF amp. (active only)}} \;+\; \sum_{k=1}^{K}\mu_k p_k \;+\; P_c},$$

  where μ_k are PA inefficiency factors and P_c collects static terms (BS/UT/RIS). For nearly-passive RISs, the RIS RF amplification term is zero, and only static RIS power remains.

- *Secrecy Energy Efficiency (SEE):* We adopt $\mathrm{SEE} = \frac{\mathrm{SSR}}{P_{\mathrm{tot}}}$, where $\mathrm{SSR} = \sum_k \left[\log_2(1+\mathrm{SINR}_{k,B}) - \log_2(1+\mathrm{SINR}_{k,E})\right]_+$ is the (sum) secrecy rate and P_{tot} is total consumed power as above. For dual-metasurface chapters, we also consider min-SEE formulations across users, as specified later.

Optimization and Algorithmic Assumptions

EE/SEE maximization under global-reflection constraints with (nearly-)passive or active metasurfaces, linear receivers/precoders, artificial noise (AN), and power budgets are the optimization challenges in this thesis. These tasks are intrinsically *non-convex* and *block-coupled*. We summarize the algorithmic foundation and guiding assumptions here to maintain rigor without overcrowding the Introduction with technicalities; complete derivations, proofs, and per-problem specializations are left to the Appendices (see the guidelines below).

Alternating optimization (AO) and block structure. The variables

$$\{\,\boldsymbol{\gamma}\ (\text{RIS/RHS}),\ \mathbf{Q}\ (\text{Tx cov./powers}),\ \mathbf{C}\ (\text{lin. Rx/Tx}),\ \mathbf{C}_z\ (\text{AN})\,\}.$$

represent all designs as block-structured programs.

We implement a strategy known as *Alternating Optimization (AO)*, which utilizes a block-coordinate descent/ascent method, optimizing one block at a time while keeping the others constant. Each block subproblem is chosen in a manner that it either allows for a *tight convex surrogate* (solved effectively and updated in a monotonic manner) or is *convex* (solved to achieve optimality). AO converges to *first-order stationary* points and produces a *monotone*

sequence of objective values, provided that standard regularity conditions (continuity, a bounded feasible set, exact/majorizing surrogates) are met.

Dinkelbach transforms and fractional programming (FP) The standard *single-ratio* form for EE and SEE is $\max_{\mathbf{x}} \frac{f(\mathbf{x})}{g(\mathbf{x})}$. with $g(\cdot) > 0$ an affine/convex total-power model that incorporates transmit, circuit, and (for active surfaces) *net* RIS/RHS amplification power, and $f(\cdot)$ a (surrogate) concave utility (e.g., $\sum_k \log(1 + \mathrm{SINR}_k)$ or its tight lower bound). We use a parametric transform of the *Dinkelbach-type*:

$$\max_{\mathbf{x}} \frac{f(\mathbf{x})}{g(\mathbf{x})} \quad \Longleftrightarrow \quad \exists\, \eta^\star : \max_{\mathbf{x}} f(\mathbf{x}) - \eta^\star g(\mathbf{x}) = 0, \quad \eta_{t+1} = \frac{f(\mathbf{x}_t)}{g(\mathbf{x}_t)}.$$

The inner problem becomes *subtractive* at each outer iteration (η_t fixed), and it is resolved via AO/SCA (see below). Under the surrogate qualities used here, classic FP theory predicts a monotone ascent of the objective and global convergence of (η_t) to the optimal ratio. Appendix A.3 contains the derivations and halting rules for the Dinkelbach updates, including imprecise inner solves.

Majorization–minimization (MM) / successive convex approximation (SCA). Nonconvexities in our inner problems (at fixed Dinkelbach parameter) arise from three sources: (i) secrecy/AN terms under Eve's statistical CSI, (ii) quadratic couplings in the metasurface coefficients γ induced by the global-reflection model, and (iii) the $\log(1 + \mathrm{SINR})$ rate utilities. We handle them via a blockwise MM/SCA scheme that constructs, at iteration t, a *concave lower surrogate* $\tilde{f}(\cdot \mid \mathbf{x}^{(t)})$ satisfying tangency and global lower-bounding, and then maximizes this surrogate over the current block. In keeping with the surrogate templates formalized in Appendix A.4, we only use:

- *First-order minorizers of concave utilities:* $\log(1+z) \geq \log(1+z^{(t)}) + \frac{1}{1+z^{(t)}}(z - z^{(t)})$ applied to per-block SINR arguments;
- *DC (difference-of-convex) quadratic linearization:* for terms of the form $\mathbf{x}^H\mathbf{A}\mathbf{x} - \mathbf{x}^H\mathbf{B}\mathbf{x}$, we linearize $-\mathbf{x}^H\mathbf{B}\mathbf{x}$ at $\mathbf{x}^{(t)}$ to obtain an affine (concave) lower bound used in the γ-update under global reflection;
- *Log-det affine lower bound:* $\log\det\mathbf{Y} \geq \log\det\mathbf{Y}^{(t)} + \mathrm{tr}\big[(\mathbf{Y}^{(t)})^{-1}(\mathbf{Y} - \mathbf{Y}^{(t)})\big]$ when rates are expressed in covariance form.

Each SCA step yields a *concave* subproblem in the active block over a convex feasible set and is solved optimally; by MM theory, it ensures a monotone

ascent of the inner objective. When these block updates are cycled (sequential optimization), the resulting sequence converges to a block-stationary point under standard assumptions (Proposition A.4.1, Appendix A.4). Coupled with the outer Dinkelbach loop (Appendix A.3), the algorithm converges to a first-order stationary solution of the original EE/SEE fractional program.

Global Reflection Model and Projection Updates. Throughout this thesis, the metasurface is modeled as a *macro-reflector* subject to an *aggregate* power-balance constraint. Let $\mathbf{R} \succeq \mathbf{0}$ denote the impinging-field covariance at the surface, and let $\Gamma \triangleq \mathrm{diag}(\boldsymbol{\gamma})$ collect the complex reflection coefficients. The net reflected RF power is given by

$$P_{\mathrm{ref}} = \mathrm{tr}(\mathbf{R}\,\Gamma\Gamma^H) = \sum_{n=1}^{N} |\gamma_n|^2 R_{nn} = \boldsymbol{\gamma}^H \mathbf{D}\,\boldsymbol{\gamma},$$

where $\mathbf{D} \triangleq \mathrm{diag}(\mathrm{diag}(\mathbf{R}))$. Energy conservation (nearly passive) and budgeted amplification (active) are ensured by the *global-reflection* sets:

$$\mathcal{G}_{\mathrm{pass}} = \left\{ \boldsymbol{\gamma} : \boldsymbol{\gamma}^H \mathbf{D}\,\boldsymbol{\gamma} \le \mathrm{tr}(\mathbf{R}) \right\},$$

$$\mathcal{G}_{\mathrm{act}} = \left\{ \boldsymbol{\gamma} : \boldsymbol{\gamma}^H \mathbf{D}\,\boldsymbol{\gamma} \le \mathrm{tr}(\mathbf{R}) + P_{R,\max} \right\}.$$

Within the AO/SCA pipeline, the $\boldsymbol{\gamma}$ block is updated either by (i) a *closed-form* step in single-stream cases (phase alignment plus amplitude redistribution) or (ii) a *projection* onto $\mathcal{G}_{\mathrm{pass}}$ or $\mathcal{G}_{\mathrm{act}}$ when a gradient-like step yields an infeasible tentative iterate $\tilde{\boldsymbol{\gamma}}$.

Projection as Weighted Radial Rescaling. The projection problem can be formulated as

$$\min_{\boldsymbol{\gamma} \in \mathbb{C}^N} \|\boldsymbol{\gamma} - \tilde{\boldsymbol{\gamma}}\|_2^2 \quad \text{s.t.} \quad \boldsymbol{\gamma}^H \mathbf{D}\,\boldsymbol{\gamma} \le B, \quad B \in \{\mathrm{tr}(\mathbf{R}),\, \mathrm{tr}(\mathbf{R}) + P_{R,\max}\},$$

which reduces to a *scalar rescaling* along the current search direction, as the constraint set forms an origin-centered ellipsoid with a diagonal metric $\mathbf{D} \succeq 0$. The KKT conditions yield

$$\boldsymbol{\gamma}^\star = \alpha^\star\, \tilde{\boldsymbol{\gamma}}, \qquad \alpha^\star = \min\left\{ 1, \sqrt{\frac{B}{\tilde{\boldsymbol{\gamma}}^H \mathbf{D}\,\tilde{\boldsymbol{\gamma}}}} \right\}.$$

Therefore, feasibility is enforced through a *weighted radial* shrinkage in the metric induced by $\mathbf{D}$; no element-wise clipping is necessary under the global model.

All derivations concerning the global-reflection sets, including the impact of aggregate versus element-wise coupling, the Hadamard/diagonal structure $\mathbf{D} = \mathrm{diag}(\mathrm{diag}(\mathbf{R}))$, and the ellipsoidal projection described above, are provided in Appendix A.1.3. The single-stream closed forms (phase alignment and amplitude redistribution under the global constraint) are detailed in Appendix A.1.4.

Rank-1 enforcement and SDP relaxations (selected cases) We apply semidefinite programming (SDP) through standard lifting and rank-1 relaxation methods when dealing with coupled quadratic terms that occur in problems (e.g., bilinear interactions between transmit covariance/beamformer and metasurface coefficients and QoS-type constraints on SINR/secrecy). In particular, under convex side constraints (power budgets, global-reflection bounds, etc.), vector variables are lifted to Hermitian PSD matrices (e.g., $\mathbf{x}\mathbf{x}^H \mapsto \mathbf{X} \succeq \mathbf{0}$), converting non-convex quadratic forms and products into linear functions of $\mathbf{X}$. However, this introduce a constraint $\mathrm{rank}(\mathbf{X}) = 1$, which is an intractable condition that needs to be loosened to produce a convex SDP, which we solve effectively and utilize as a high-quality *initializer* for the first-order AO/SCA pipelines and (i) as a fair-performance *baseline*. We emphasize rank-1 by using a spectral projection when a workable, high-quality solution in vector form is required: The relaxed solution's primary eigenpair $(\lambda_{\max}, \mathbf{u}_{\max})$ is extracted, and $\hat{\mathbf{x}} = \sqrt{\lambda_{\max}}\mathbf{u}_{\max}$ is set. A feasibility projection (such as power normalization and projection onto the global-reflection set) is then performed. The algorithm provides two optional features, which include (a) eigenvector randomization of $\mathbf{X}$ to find the best candidate or (b) a proximal refinement step that adds a penalty term for high-rank structure before the final projection for multiuser applications or vigorous enforcement. The thesis depends on AO/SCA with Dinkelbach for its main computations. However, the SDP relaxations are essential for measuring solution tightness, generating initial points, and confirming the quality of first-order solutions. The following information about lifting formulations, solver parameters, and spectral-projection/penalization stages is located in Appendix A.1.7.

Linear receivers/precoders and AN. Given transmit covariances and metasurface variables, *LMMSE* linear receivers (uplink) and linear precoders

(downlink) admit closed-form updates; their expressions (including colored-noise covariances induced by active metasurfaces) are provided in Appendix A.1.1. The system implements AN for secrecy through its operation within authorized data rate subspaces, which enables $\mathbf{C}_z$ initializations in AO using convex surrogates (Appendix A.2.2).

Statistical CSI and robustness. For the eavesdropper links, we consider two regimes: (i) *perfect CSI* (used as an optimistic upper bound), and (ii) *statistical CSI*, where only channel statistics are known. In the statistical case we adopt a *Jensen-based* surrogate: by concavity of $\log(\cdot)$,

$$\mathbb{E}\big[\log\big(1+\mathrm{SINR}(x,\xi)\big)\big] \;\le\; \log\big(1+\mathbb{E}[\mathrm{SINR}(x,\xi)]\big),$$

Moreover, we design against the deterministic right-hand side, computed from the available moments (e.g., $\mathbb{E}[|\mathbf{h}^H\mathbf{f}|^2] = \mathbf{f}^H\mathbf{R}\mathbf{f}$). The replacement inside the AO/SCA loop becomes straightforward to handle.

Initialization, complexity, and stopping. The system operates according to physical principles during initialization through MRT/MRC for $\mathbf{C}$ and phase-aligned metasurface coefficients for γ in passive or small-gain active systems and water-filling or equal-power for $\mathbf{Q}$. The stopping criteria depend on how much better the Dinkelbach-subproblem objective (inner loop) and the ratio (outer loop) get; tolerances are given for each experiment. Inversions of matrices about the same size as the number of antennas or elements are the most complicated part of each iteration. This leads to a *polynomial* overall cost.

1.5 Thesis Objectives

This thesis aims to create a unified and physics-aware framework for designing and optimizing RIS-aided wireless networks, prioritizing energy efficiency (EE) and secrecy energy efficiency (SEE) as primary objectives. This approach addresses the two structural gaps left by 5G: energy sustainability and intrinsic confidentiality. It leverages programmable propagation through nearly-passive, active, and dual-metasurface (holographic+RIS) architectures within a unified global reflection modeling paradigm [22], [23], [32], [34], [35], [84].

Primary Objective

PO. Develop a unified optimization framework for RIS-aided networks that (i) incorporates both nearly-passive and active surfaces through a global reflection power-balance constraint, (ii) considers realistic circuit and noise power models, and (iii) facilitates the systematic maximization of energy efficiency (EE) and secrecy energy efficiency (SEE) in single-RIS and dual-metasurface architectures.

Specific Objectives

O1. Unified modeling through global reflection. Develop a global-reflection-based RIS model that conceptualizes the surface as a macro-reflector, ensuring either passive aggregate RF power conservation or an active aggregate amplification budget. Demonstrate that the model strictly generalizes local unit-modulus constraints and derive the corresponding power accounting. This includes the net RIS RF amplification power for active RIS and the effects of amplified internal noise [34]. This results in a unified set of constraints that provides a continuous interpolation between nearly-passive and active regimes, facilitating equitable comparisons of EE and SEE.

O2. Energy-efficiency maximization (single-RIS). Formulate and address the RIS-assisted links' global energy efficiency maximization problem, considering multiuser interference, transmit power limitations, and overall reflection constraints. Design low-complexity alternating and fractional programming algorithms that exhibit: *(i)* monotonic improvement and convergence to first-order stationary points, *(ii)* closed-form updates or tight convex surrogates when feasible, and *(iii)* rigorous baselines (unit-modulus RIS, no-RIS, relay-like) for benchmarking purposes. Analyze specific scenarios, such as single-user or streaming contexts, and quantify the conditions under which nearly-passive RISs yield significant energy efficiency advantages compared to fully-digital arrays [34].

O3. Secrecy energy-efficiency maximization (single-RIS). Formulate the maximization of the secrecy capacity under the assumptions of perfect and statistical channel state information for the eavesdropper. Examine the distinctions between nearly-passive and active RISs within the unified model and develop algorithms that effectively preserve secrecy benefits in the presence of channel state information uncertainty, while

clearly delineating the trade-offs among reflection gain, amplified noise, and fixed budgets [32]. Determine the operating regions (Rician factors, placements, budgets) where active RISs significantly outperform SEE, as opposed to regions where nearly-passive RISs are more advantageous.

O4. Dual-metasurface (holographic+RIS) architectures for SSR/SEE. Introduce and analyze a dual-metasurface system comprising a reconfigurable holographic surface (RHS) that facilitates analog-domain beamforming in the BS near field, alongside an external reconfigurable intelligent surface (RIS) that modifies the surrounding environment. (i) Implement a joint optimization approach for RHS weights, RIS coefficients (*both* under local unit-modulus constraints), and transmit covariance/powers plus artificial-noise (AN) structures to achieve secrecy rate and energy efficiency objectives; and (ii) Quantify the conditions under which the dual approach can reduce the required number of digital RF chains while preserving or improving secrecy rate/SEE, in comparison to large fully-digital arrays [33]. Present max-min SEE fairness formulations as applicable.

O5. Complexity, scalability, and convergence assurances. For each algorithm, determine the complexity per iteration, assess the memory requirements, and define the stopping criteria. Additionally, demonstrate the monotonicity and convergence to stationary points under typical regular conditions. Analyze scalability in relation to the number of RIS elements, antennas, and users. Identify implementation-friendly variants, such as block-coordinate or two-stage updates, that preserve most benefits while minimizing computational costs.

O6. Comprehensive benchmarking and design guidelines. Conduct comprehensive Monte Carlo simulations, usually using 10^3 realizations, focusing on critical parameters such as Rician K-factors, path-loss exponents, RIS size and placement, static and amplification budgets, quantization losses, and the quality of channel state information (CSI). Conduct a benchmark comparison with local unit-modulus RIS designs and fully-digital baselines. Develop actionable guidelines for 6G designers regarding: (i) the deployment of nearly-passive versus active RISs; (ii) optimal placement of surfaces to reduce double fading; (iii) sizing of static/amplification budgets to enhance EE/SEE; and (iv) the conditions under which a dual-metasurface architecture is favored over scaling digital arrays [32], [35].

Intended Outcomes

The proposed scientific outcomes include: *(i)* a principled and reusable modeling layer for RISs that accurately represents power flows through global reflection; *(ii)* a set of provably convergent algorithms for maximizing EE/SEE in passive, active, and dual-metasurface systems; and *(iii)* validated deployment rules that provide specific recommendations for 6G design. These outcomes collectively address the energy and security gaps of 5G by prioritizing energy efficiency (EE) and security efficiency (SEE) as primary design targets in programmable wireless environments.

1.6 Research Questions

This thesis is organized around six specific questions, examined within the cohesive framework of global-reflection modeling, EE/SEE metrics, and AO/SCA utilizing fractional programming (Secs. 1.1–1.4).

RQ1. What operating regimes allow active RISs to provide a net energy efficiency or spectral efficiency advantage compared to nearly-passive RISs? Scope: geometry and path loss of the cascaded links, K-factors, aperture size, amplification, and circuit budgets.

RQ2. What is the extent of improvement in EE/SEE provided by *global-reflection* constraints compared to unit-modulus RIS designs? Scope: quantitative gains compared to unit-modulus RIS, no-RIS, and relay baselines under the same power budgets; limits for single-user/stream scenarios.

RQ3. What is the robustness of SEE-optimal designs in the presence of imperfect or statistical eavesdropper channel state information (CSI)? Scope: gaps in the secrecy rate and secrecy energy efficiency between perfect CSI and statistical CSI treatments across varying levels of uncertainty.

RQ4. Can dual-metasurface systems (RHS and RIS) decrease the number of digital RF chains while maintaining or enhancing energy efficiency and spectral efficiency? Scope: Co-design of RHS/RIS apertures, placement, and power budgets to achieve target EE/SEE with fewer RF chains.

RQ5. What are the scalable algorithms with provable convergence that effectively address large-scale RIS co-design? Scope: AO/SCA utilizes

fractional programming and SDP relaxation with rank-1 enforcement as necessary, resulting in monotone ascent and first-order stationarity, characterized by polynomial complexity per iteration.

RQ6. What are the deployment and budgeting guidelines that facilitate sustainable and secure 6G? Scope: Develop charts and heuristics for architecture selection (passive, active, dual), placement strategies to reduce double fading, and static/amplification budgeting for net energy and spectral efficiency gains.

All questions are addressed uniformly, utilizing identical channel abstractions, power accounting, and global-reflection feasibility, allowing for direct conclusions comparability across architectures and CSI regimes.

1.7 Thesis Contributions and Structure

The thesis is structured in **five chapters**. Chapter 1 (this chapter) motivates the problem, positions the work within 6G, and states the scope, assumptions, objectives, and research questions. The three *technical* chapters, Chapters 2–4, develop our unified framework and results; Chapter 5 concludes with design guidelines. Below, we summarize the main contributions of each chapter and relate them to the associated publications.

To improve coherence and avoid repetition, Chapter 1 provides the unified background used throughout the thesis, including the key architectures (nearly-passive RIS, active RIS, and RHS/RIS dual-metasurface systems), the adopted power-consumption modeling principles, and the global-reflection paradigm that enables a common comparison framework. The subsequent technical chapters therefore keep their introductory parts concise and focus only on the chapter-specific problem formulations and contributions, each including an explicit chapter roadmap to guide the reader.

- **Chapter 2: Energy Efficiency with Global-Reflection RIS (Active vs. Nearly-Passive).** This chapter formulates and solves the *global energy-efficiency (EE)* maximization problem for RIS-aided links under a *global reflection* model that treats the surface as a macro-reflector. The key contributions are:

  1. *Unified, physics-aware RIS modeling.* We formalize a single power-balance constraint that enforces aggregate RF conservation (passive) or an aggregate amplification headroom (active). We derive a correct RIS power accounting based on the *net* RF amplification $P_{\text{out}} - P_{\text{in}} = \text{tr}((\Gamma\Gamma^H - \mathbf{I})\mathbf{R})$,

in contrast to models that equate RIS power to P_{out} alone. The nearly-passive case is recovered by $P_{R,\max} = 0$ and zero RIS noise; the active case by $P_{R,\max} > 0$ and nonzero RIS internal noise variance. This modeling strictly *generalizes* unit-modulus designs and enables fair active/passive comparisons.

2. *Optimization and algorithms.* We pose the GEE problem over user powers, linear combiners/precoders, and RIS coefficients. We devise a low-complexity alternating (sequential fractional) procedure with monotonic ascent and convergence to first-order stationary points. In the single-user scenario, a closed-form solution for the optimal RIS allocations is presented, which considers global reflection, including phase alignment and amplitude redistribution. This approach reveals the structure of the SNR gain in relation to unit-modulus baselines.
3. *Design insights and placement rules.* Through extensive Monte Carlo averaging (typically 10^3 realizations), we quantify the GEE gains of global reflection over local constraints, characterize sensitivity to Rician K-factors and path-loss exponents, and extract RIS placement guidelines that mitigate double fading while maximizing EE. We also benchmark against no-RIS and relay-like baselines to isolate the benefits due to programmable reflection.

Related Publications.

– R. K. Fotock, A. Zappone and M. D. Renzo, *Energy Efficiency Optimization in RIS-Aided Wireless Networks: Active Versus Nearly-Passive RIS With Global Reflection Constraints,* in IEEE Transactions on Communications, vol. 72, no. 1, pp. 257-272, Jan. 2024, doi: 10.1109/TCOMM.2023.3320700. (full paper; integrated and extended in this thesis). [35]

– R. K. Fotock, A. Zappone and M. D. Renzo, *Energy Efficiency Maximization in RIS-aided Networks with Global Reflection Constraints,* ICASSP 2023 - 2023 IEEE International Conference on Acoustics, Speech and Signal Processing (ICASSP), Rhodes Island, Greece, 2023, pp. 1-5, doi: 10.1109/ICASSP49357.2023.10096617 (conference paper) [29]

– R. K. Fotock, A. Zappone and M. Di Renzo, *Energy Efficiency in RIS-Aided Wireless Networks: Active or Passive RIS?,* ICC 2023 - IEEE International Conference on Communications, Rome, Italy, 2023, pp. 2704-2709, doi: 10.1109/ICC45041.2023.10279284 (conference paper) [28]

– Fotock, Robert Kuku, Alessio Zappone, and Marco Di Renzo. *Energy Efficiency Maximization in RIS-Assisted Networks: Exploring the Benefits of Global Reflection Constraints*, 1st INTERNATIONAL PhD SYMPOSIUM ON ENGINEERING AND SPORT SCIENCE. (extended in this thesis). [34]

- **Chapter 3: Secrecy Energy Efficiency (SEE) in RIS-Aided Networks (Active vs. Nearly-Passive).** Here we elevate privacy to a first-class objective and develop a *unified* SEE framework under perfect and statistical eavesdropper CSI. The main contributions are:

  1. *Unified SEE formulation with global reflection.* We cast the problem as a single *network SEE maximization*—the ratio between the *sum secrecy rate* and the *total consumed power* (transmit power + circuit power + RIS static power and, when applicable, RF amplification). The same macro-reflector (global-reflection) constraint used in Chapter 2 is adopted, so that nearly-passive and active RIS are obtained by tuning $(P_{R,\max}, \sigma^2_{RIS})$ (with active RIS including amplification noise and static overhead). The formulation accommodates perfect and statistical Eve-CSI and is solved via AO/SCA coupled with a Dinkelbach-type outer loop.
  2. *Robust design under imperfect/statistical Eve CSI.* We develop effective alternating optimization schemes even when Eve's channel is known only statistically. We handle the expectations within secrecy-rate expressions using the Jensen inequality-based approach, which allows us to derive closed-form moments of random quadratic forms. This results in deterministic, concave subproblems for each block. The design leverages spatial selectivity (beamforming and RIS phasing under the global-reflection model) to limit leakage while preserving legitimate-rate efficiency, and it maintains monotone ascent with convergence to a block-stationary point across uncertainty levels.
  3. *Active vs. nearly-passive regimes for SEE and operating frontiers.* We identify operating regions where active RISs *truly* dominate SEE (weak cascaded links, moderate amplification budgets) versus regions where nearly-passive RISs remain preferable (strong cascades, tight static budgets). We also plot the working frontiers for GEE-SR and SEE-SSR to quantify the trade-off between energy-oriented and rate-oriented designs.

Related Publications.

  - R. K. Fotock, A. Lucky Imoize, A. Zappone, M. Di Renzo and R. Garello, *Secrecy Energy Efficiency in RIS-Aided Networks: Active or Nearly-Passive RIS?* (journal manuscript/extended preprint; integrated and expanded here). [32]
  - R. K. Fotock, A. Zappone and M. Di Renzo, *Secrecy Energy Efficiency Maximization in RIS-Aided Wireless Networks,* ICC 2024 - IEEE International Conference on Communications, Denver, CO, USA, 2024, pp. 3065-3070, doi: 10.1109/ICC51166.2024.10623096 (conference manuscript). [26]
  - R. K. Fotock, A. Lucky Imoize, A. Zappone, M. Di Renzo and R. Garello, *Secrecy Energy Efficiency Maximization in RIS-Aided Wireless Networks with Statistical CSI,* 2024 IEEE 25th International Workshop on Signal Processing Advances in Wireless Communications (SPAWC), Lucca, Italy, 2024, pp. 696-700, doi: 10.1109/SPAWC60668.2024.10694589 (conference manuscript). [27]

- **Chapter 4: Dual-Metasurface Architectures (Holographic Surface + RIS) for EE/SEE.** We introduce a dual-surface architecture that pairs a reconfigurable holographic surface (RHS) in the BS near field with an external RIS that shapes the environment. The contributions are:

  1. *System modeling and near-/far-field coupling.* We adopt a tractable, EM-aware channel model with spherical-wave (near-field) propagation for Tx↔RHS (and RHS↔Rx when applicable) and Rician far-field links for the environmental paths. **In this chapter, both the RHS weights and the external RIS coefficients obey *local unit-modulus* constraints** ($|\beta_m| = 1$, $|\gamma_n| = 1$), i.e., phase-only control per element; *no* global-reflection relaxation is used. This modeling choice isolates the impact of holographic analog beamforming at the transmitter and clarifies the incremental role of the environmental RIS within the dual-surface architecture.
  2. *Max–min SEE optimization with artificial noise.* We formulate a fairness-oriented *max–min* SEE problem that *jointly* optimizes the RHS phases $\boldsymbol{\beta}$, RIS phases $\boldsymbol{\gamma}$ (both with *local unit-modulus* constraints), the transmit beamforming/covariance $\mathbf{Q}$, and an artificial-noise (AN) covariance $\mathbf{C}_z$ (including power splitting between data and AN). The problem is tackled via a generalized Dinkelbach framework for fractional max–min objectives, combined with blockwise MM/SCA updates: phase variables are updated through phase-only projections. At the same time, covariance blocks use SDP relaxation with *rank-1 enforcement* by spectral projection where applicable. The algorithm exhibits monotone ascent

of the inner surrogate and converges to a block-stationary point with polynomial per-iteration complexity.

3. *Digital RF-chain reduction.* We show that a dual-metasurface design, RHS at the transmitter and an external RIS, can achieve *equal or higher* EE/SEE with *fewer* digital RF chains than large fully-digital arrays. Under identical power accounting and local unit-modulus constraints on both surfaces, the RHS's analog holographic beamforming plus environmental shaping by the RIS offsets the circuit-power floor of large digital arrays; gains are most pronounced in weak-cascade geometries and moderate K-factors where scaling digital chains yields diminishing returns.

Related Publications.

– Fotock, R.K., Imoize, A.L., Zappone, A. et al. *Secrecy energy efficiency maximization in dual-metasurface-aided wireless networks.* EURASIP J. Adv. Signal Process. 2025, 24 (2025). https://doi.org/10.1186/s13634-025-01231-w (journal manuscript; integrated here). [31]

- **Chapter 5 : Conclusions and Design Guidelines for RIS-Aided Sustainable and Secure 6G.** This chapter merges the analytical and numerical findings from Chapters 2 to 4 into actionable design recommendations. It includes four key contributions:

1. *Architecture selection.* It consolidates the tradeoffs between nearly-passive, active, and dual-metasurface (RHS + RIS) solutions into decision charts indexed by cascaded geometry, K-factors, circuit/amplification budgets, and secrecy targets, thereby indicating when reflection gain offsets amplified noise/static power and when passive operation (or dual-surface cooperation) is preferable.
2. *Placement and sizing.* It translates the global-reflection perspective into practical rules for mitigating double fading (favorable RIS placement, aperture orientation), and for right-sizing surfaces and amplification headroom so that net EE/SEE gains are realized under realistic power accounting.
3. *Algorithmic guidance.* It distills complexity-aware prescriptions for AO/SCA + fractional programming with spectral rank enforcement, including block-coordinate variants that recover most of the performance with controlled runtime, and robustness notes for statistical-CSI operation and coefficient quantization.

4. *Outlook.* It identifies open directions prompted by the global-reflection and dual-surface paradigms—hardware-aware constraints (coupling, quantization, amplifier dynamics), near-field holography, learning-assisted control under partial/delayed CSI, integrated sensing and communication (ISAC) co-design (secure and energy-efficient joint beampatterning and sensing-aware global reflection), and cross-layer integration toward standards-ready deployments.

In short, Chapter 5 converts the thesis' unified modeling and optimization framework into practitioner-ready guidelines linking architecture choice, deployment geometry, and budget allocation to provable EE/SEE benefits for 6G.

Throughout the thesis, appendices collect detailed mathematical derivations (including initialization strategies and convergence proofs), extended figures/tables, and parameter settings to ensure full reproducibility of the reported results.

1.8 Other contributions

Beyond the core articles integrated in this dissertation, the author has produced additional publications and submissions during the Ph.D. studies. Brief abstracts and the author's role for each paper are provided below.

1.8.1 Journal Articles

- R. K. Fotock, A. Zappone, A. L. Imoize and M. Di Renzo, "Energy Efficiency Maximization of MIMO Systems through Reconfigurable Holographic Beamforming," *IEEE Transactions on Communications*, under review, 2025 [33].
  Abstract. The paper studies a point-to-point MIMO architecture endowed with two reconfigurable holographic surfaces (RHSs) operating near the transceiver arrays' near field, thereby realizing fully analog holographic beamforming. The global energy efficiency is optimized with the transmit covariance and RHS reflection matrices, following a physics-aware global reflection power-balance model. A sequential fractional programming algorithm is developed, which features monotonic ascent and converges to first-order stationary points. Closed-form solutions for single-stream RHS have also been derived to provide structural insights. Simulation results demonstrate significant energy efficiency gains compared to fully digital arrays, even when the latter preserve advantages in multiplexing. This highlights analog-domain spatial processing as an energy-efficient alternative.
  Author's role. Led modeling (near-/far-field coupling, global-reflection power

accounting), algorithm design and proofs, closed-form derivations, codebase and experiments, and co-wrote the manuscript.

- A. I. Tunalı, R. K. Fotock, A. Zappone, G. Taricco, G. Alfano and H. A. Çırpan, "Energy efficiency maximization in MIMO links aided by metasurfaces with global reflection constraints," *EURASIP Journal on Advances in Signal Processing*, 2025:29, 2025 [79].
  Abstract. This study investigates a MIMO link assisted by a single RHS placed close to the transmitter and addresses EE maximization under *global reflection* constraints, which combine nearly-passive and active metasurface regimes. The RHS is optimized through the use of sequential fractional programming. At the same time, the transmit covariance is obtained either by fractional programming or by a standard-compliant CSI codebook, enabling a practical complexity–performance trade-off. The research incorporates an active RHS extension, considering amplifier noise and overall RF amplification, along with detailed simulations that measure the energy efficiency improvements resulting from power redistribution across surface elements. *Author's role.* Co-developed the global-reflection model and sequential optimizer, implemented part of the numerical pipeline (including the codebook branch), contributed to the active-RHS extension, and co-wrote methods/results.

1.8.2 Magazine Articles

- A. Zappone, M. Di Renzo and R. K. Fotock, "Surface-Based Techniques for IoT Networks: Opportunities and Challenges," *IEEE Internet of Things Magazine*, vol. 5, no. 4, pp. 72–77, Dec. 2022 [93].
  Abstract. A perspective on surface-based wireless environments (RIS, holographic, active/plug-and-play metasurfaces) tailored to IoT. The article delineates architectural options, energy-efficiency implications, and self-organization prospects; it provides illustrative results and a roadmap toward energy-neutral, programmable IoT infrastructures. *Author's role.* Co-authored the EE motivation, taxonomy (passive/active/holographic), numerical examples, and future directions that informed parts of the thesis modeling.

1.8.3 Conferences

- R. K. Fotock, A. L. Imoize, A. Zappone, M. Di Renzo and Y. Zhang, "Energy Efficiency Maximization of Holographic Beamforming Empowered by Nearly-Passive RHS," in *Proc. IEEE SPAWC 2025*, Surrey, UK, 2025, pp. 1–5 [30].
  Abstract. This research investigates nearly-passive holographic beamforming with reconfigurable holographic surfaces (RHSs) under a single-stream assumption, yielding closed-form surface weight solutions and an EE-oriented transmit strategy. Numerical results show notable improvements in energy efficiency compared to

traditional massive digital arrays while maintaining competitive data rates. This research establishes modeling and design benchmarks for near-field and far-field applications, which are later generalized at the journal level.*Author's role.* Lead technical contributor: derived closed-form RHS allocations, built the end-to-end evaluation framework, and co-wrote the paper.

- A. I. Tunalı and R. K. Fotock (co-first), "Energy-Efficient MIMO Communication Assisted by Metasurfaces with Global Reflection Constraints," *IEEE ICEAA 2025*, Palermo, Italy, Sept. 8–12, 2025 [80].
  Abstract. A joint design for an RHS-assisted MIMO link is presented: the RHS is optimized by sequential programming. At the same time, the transmit covariance is computed either via fractional programming or by a standard-compliant codebook search. Results show that the codebook approach closely tracks the performance of full optimization at markedly lower complexity, validating the *global reflection* paradigm as a physical power-balance model for practical implementations. *Author's role.* Co-first Author: co-designed algorithms, implemented the sequential optimizer and simulation stack (including CSI codebooks), performed the complexity–performance study.

Chapter 2

Energy Efficiency Optimization in RIS-Aided Wireless Networks

This chapter refers to articles published in the *2023 IEEE International Conference on Acoustics, Speech and Signal Processing (ICASSP)*, in the *2023 IEEE International Conference on Communication (ICC)*, and in the *IEEE Transactions on Communications (TCOM), doi: 10.1109/TCOMM.2023.3320700*, 2023.

2.1 Introduction and Related Works

2.1.1 Introduction

This chapter investigates the maximization of the *global energy efficiency* (GEE) in uplink multi-user wireless networks assisted by reconfigurable intelligent surfaces (RISs). The focus is on understanding the fundamental trade-offs between *nearly-passive* and *active* RIS architectures when realistic power-consumption models are accounted for.

Nearly-passive RISs are attractive due to their extremely low circuit power consumption, since they require only quasi-static control energy and introduce no additional RF noise. However, their performance is fundamentally limited by the well-known *double (multiplicative) fading* effect, whereby the end-to-end channel gain scales with the product of the transmitter–RIS and RIS–receiver path losses. As a result, achieving strong cascaded links often requires very large surfaces or favorable deployment geometries. Active RISs have been proposed to alleviate this bottleneck by incorporating

reflection-type analog amplification at the surface elements. While amplification can significantly enhance the received signal power, it also introduces additional RF power consumption, static circuit costs, and amplified noise, making the net energy-efficiency gain strongly dependent on the operating regime.

Beyond the conventional passive–active dichotomy, this chapter adopts a *global reflection* modeling paradigm, in which the RIS is treated as a macro-reflector governed by an aggregate power-balance constraint rather than element-wise local constraints. This physics-aware abstraction generalizes traditional unit-modulus formulations, enlarges the feasible set of reflection coefficients, and enables a unified treatment of nearly-passive and active RIS architectures within a single optimization framework. Building on this model, the chapter develops energy-efficiency optimization methods that explicitly account for RIS power consumption, noise effects, and multi-user interference, thereby providing new analytical insights and practical design guidelines.

2.1.2 Related Works

This section reviews prior contributions on RIS-assisted communications with an emphasis on energy efficiency and active versus nearly-passive surface architectures. The discussion is intentionally focused on works most closely related to the modeling and optimization aspects addressed in this chapter, while broader background on RIS technology and 6G motivations is provided in Chapter 1.

Research into RIS technology during its early stages concentrated on spectral efficiency (SE) and rate optimization through deployment methods and beamforming and hybrid system designs, which demonstrated that large aperture RIS systems can achieve significant rate gains at minimal energy expenditure [23], [24], [42], [83], [84]. Various *active* RIS architectures aim to mitigate the double fading bottleneck. The research in [90], [102] shows that active RISs achieve better performance than nearly-passive RISs in uplink/downlink positioning and single-user scenarios except when power constraints reach their limits or surface sizes remain small. The hybrid design simplifies channel estimation through passive elements and restricted RF sensing or amplification according to [1], [71], [76], [89]. The research field of application-oriented studies includes device-to-device communications [67] and secure satellite-terrestrial data transfer [62] as well as physical-layer security for wiretap channels [47] and STAR/dual-side operation [52] and mobile edge computing [68].

Most EE research with active RIS systems concentrates on power reduction at the transmitter instead of actual EE optimization, making the problem easier to solve but hiding the total power consumption of RIS circuits. The research includes active RISs for omnidirectional vehicular communication [16] and power minimization for secrecy-rate-constrained systems [56], as well as SWIPT and WPT applications [96] and studies on active RIS architectures that compare fully-connected and sub-connected systems [51], [103]. The optimization of network-level EE with active RISs has been studied through fractional programming and its associated transforms in [51], [58], [73]. However, the convergence and optimality of the solution may be affected when the subproblems are not solved exactly. Researchers have investigated hybrid surfaces that combine passive elements with active components under single-antenna base station configurations to analyze worst-case (ergodic) EE performance and multi-user interference-limited scenarios as reported in [66].

A common modeling assumption across most of the above works is the use of *local*, element-wise reflection constraints. In contrast, the *global reflection* framework adopted in this chapter models the RIS as a macro-reflector governed by a single power-balance constraint. Its implications for communication-theoretic performance and energy efficiency are introduced in [20] and are further developed and extended in this work.

2.1.3 Contributions

This chapter focuses on the maximization of the *global energy efficiency* (GEE) in the uplink of an interference-limited, multi-user RIS-assisted network operating under *global reflection constraints*. The discussion encompasses both *active* and *nearly-passive* RIS architectures to clarify how their different reflection mechanisms impact the energy and spectral performance of the system. The main contributions are summarized as follows.

- **Formulation of a system-level GEE model under global reflection.** A unified framework is developed that jointly optimizes the users' transmit powers, the RIS reflection coefficients, and the base station's linear receive filters. The model accounts for the colored noise induced by active amplification and treats the global reflection constraint as a unifying condition, of which the classical local model is a limiting case.
- **Sequential fractional programming framework.** Two optimization strategies are developed based on a sequential fractional programming (SFP) approach to address the non-convex GEE maximization problem.

The proposed algorithms monotonically improve the objective and converge to first-order stationary points with reasonable computational complexity, while explicitly incorporating the global reflection constraint.

- **Analytical characterization under global reflection.** For the single-user, nearly-passive case, closed-form expressions are derived for the optimal reflection pattern. This analysis quantifies the gains enabled by global reflection compared with conventional local (unit-modulus) designs and provides intuition on the operating regimes in which these gains are most significant.
- **Numerical comparison of active vs. nearly-passive RISs.** A detailed numerical study evaluates the proposed algorithms for both active and nearly-passive RIS architectures. The results identify the regimes in which active RISs provide net GEE gains despite their additional circuit and RF power consumption, and confirm that global reflection consistently improves energy efficiency compared with element-wise local constraints.

Chapter Roadmap

The remainder of this chapter is organized as follows. Section 2.2 presents the uplink multi-user system model and formulates the GEE maximization problem under global reflection constraints for both active and nearly-passive RIS architectures. Section 2.3 discusses the relationship between global and local reflection models, focusing on the single-user configuration for which closed-form analytical results are obtained. Section 2.4 develops the proposed sequential fractional programming algorithms and analyzes their convergence behavior and computational complexity. Finally, Section 2.5 reports numerical results and highlights the main design insights derived from the analysis.

2.2 System Model and Problem Formulation

We consider the uplink of an RIS-aided multi-user system in which K single-antenna user terminals (UTs) communicate over the same resource block with a base station (BS) equipped with N_R antennas. The propagation is assisted by a reconfigurable intelligent surface (RIS) comprising N reflecting elements as shown in Fig. 2.2.1. Let

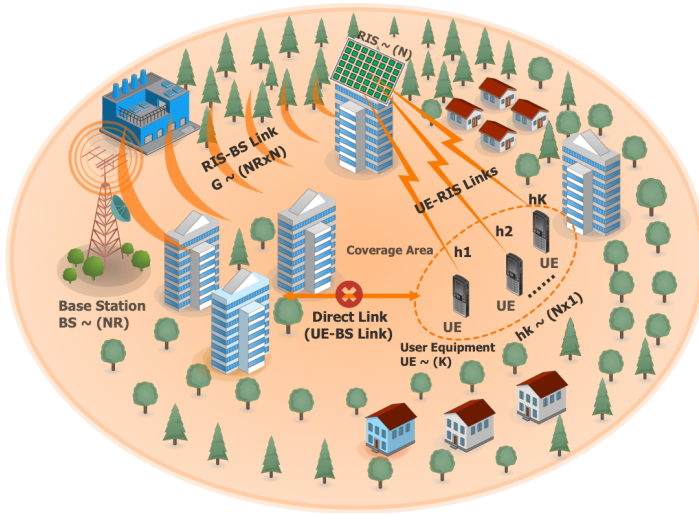

FIGURE 2.2.1: Considered RIS-aided wireless network.

- $\mathbf{h}_k \in \mathbb{C}^{N\times 1}$ denote the channel from user k to the RIS,
- $\mathbf{G} \in \mathbb{C}^{N_R\times N}$ denote the channel from the RIS to the BS,
- $\mathbf{\Gamma} = \text{diag}(\gamma_1, \ldots, \gamma_N)$ be the RIS reflection matrix, with $\boldsymbol{\gamma} = [\gamma_1, \ldots, \gamma_N]^\top$.

Each user transmits a unit-variance symbol s_k with power p_k ($\mathbb{E}[|s_k|^2] = 1$). For notational convenience, we define $\mathbf{H}_k = \text{diag}(h_k(1), \ldots, h_k(N))$, so that $\mathbf{\Gamma}\mathbf{h}_k = \mathbf{H}_k\boldsymbol{\gamma}$, and $\mathbf{A}_k \triangleq \mathbf{G}\mathbf{H}_k$.

Here, the RIS is modeled using a *global reflection constraint*, in contrast to the conventional *local* formulation that enforces $|\gamma_n|^2 \leq 1$ for each individual reflecting element. In the local formulation, the RIS is treated as a set of N independent meta-atoms, each behaving like an isolated mirror that cannot radiate more power than it receives. This leads to N scalar inequalities, one per element, and has been widely used in early RIS studies for its analytical simplicity and intuitive appeal. However, such a model overlooks two important physical realities. First, it disregards the possibility of near-field or surface-wave coupling between adjacent elements, which allows local power redistribution across the surface. Second, enforcing identical per-element bounds underestimates the design freedom of practical metasurfaces, especially when electromagnetic interactions are strong. The *global reflection* model views the RIS not as a set of independent elements but as a unified electromagnetic aperture governed by an overall power balance. In this setting, the amount of power re-emitted by the RIS is physically limited by the energy arriving at its surface. Only when the RIS is equipped with active

components can additional energy be introduced to the reflected signal. This physical constraint can therefore be stated as

$$P_{\text{out}} - P_{\text{in}} \leq 0 \quad \text{(nearly-passive RIS)}, \qquad P_{\text{out}} - P_{\text{in}} \leq P_{R,\max} \qquad \text{(active RIS)}, \tag{2.2.1}$$

wherein P_{in} and P_{out} both represent the incident and reflected powers, respectively, where as $P_{R,\max}$ denotes the maximum additional RF power that the RIS amplifiers can supply.

Remark 2.2.1 (Generalization of Local Constraints). The global model provides a strict generalization of the local model, which states: $|\gamma_n| \leq 1$ for all n, then it follows that $P_{\text{out}} \leq P_{\text{in}}$. This means that the set of feasible solutions defined by the local model is a subset of the feasible solutions in the global model. Moreover, the global model permits certain elements to have $|\gamma_n| > 1$, while other elements can have lower values, as long as the overall surface balance remains unchanged.

The difference between local and global reflection constraints is physical and analytical in importance. In the local case, every RIS element acts independently, each reflecting no more power than it receives. Therefore, the total reflection pattern is the sum of many independent, power-limited responses. However, when a global constraint is applied, the surface behaves as a cooperative structure: energy can flow across elements, allowing some to radiate more strongly while others compensate by radiating less. Recent work in electromagnetics indicates that elements placed close to each other on a metasurface do not behave independently. They exchange energy through near-field effects, such as evanescent and surface-wave coupling. Because of this interaction, slight variations in the reflected amplitude at one element can occur without breaking the overall energy balance of the surface. From an optimization point of view, the global formulation widens the feasible region for the reflection vector γ, meaning it can achieve equal or better performance than the local model. As shown later in Section 2.3, this added flexibility becomes especially useful when the composite user–RIS–BS channel exhibits uneven magnitudes, since the surface can redirect more power along stronger paths and scale down weaker ones. In an *active* configuration, reflection-type amplifiers introduce additional RF energy through active circuits or current inverters. Here, the power balance allows the surface to emit more energy than it receives, within the limit of the

amplifier budget $P_{R,\max}$:

$$\operatorname{tr}(\mathbf{R}\boldsymbol{\gamma}\boldsymbol{\gamma}^H) \leq \operatorname{tr}(\mathbf{R}) + P_{R,\max}, \tag{2.2.2}$$

where $\mathbf{R}$ denotes the covariance of the incoming signal. To guarantee that the RIS enhances rather than attenuates the signal, it must also satisfy $\operatorname{tr}(\mathbf{R}\boldsymbol{\gamma}\boldsymbol{\gamma}^H) \geq \operatorname{tr}(\mathbf{R})$. This global formulation reflects more accurately how practical metasurfaces behave and, at the same time, offers a richer mathematical foundation for system-level design. It bridges electromagnetic modeling and performance metrics such as spectral and energy efficiency.

2.2.1 Channel model and assumptions

In this work, the channel is assumed to follow a block-fading behavior. That is, it stays roughly constant over a single coherence interval but changes from one interval to the next independently. Both user–RIS and RIS–BS links follow *Rician fading*, which captures the presence of a deterministic line-of-sight (LoS) component together with a scattered non-line-of-sight (NLoS) component. The small-scale fading terms are assumed to be independent across users and links.

For notational simplicity, a direct transmitter–receiver channel is omitted; its inclusion would result in an additional additive channel term and does not affect the structure of the proposed optimization framework.

Path-loss model. We model the large-scale path-loss as

$$L(d) = C_0 \left(\frac{d}{d_0}\right)^{-\alpha}, \tag{2.2.3}$$

where d is the link distance, α is the path-loss exponent, d_0 is a reference distance (typically 1 m), and C_0 is the path-loss at d_0. To make the model more realistic, a random log-normal term can be added to represent the slow variations in power caused by shadowing from surrounding objects. Accordingly, we denote by $L_{\mathrm{UR},k}$ the large-scale gain of the user k–RIS link and by L_{RB} that of the RIS–BS link.

Rician fading model. We model the small-scale fading as Rician:

$$\mathbf{h}_k = \sqrt{L_{\mathrm{UR},k}}\left(\sqrt{\tfrac{K_\mathrm{T}}{1+K_\mathrm{T}}}\,\mathbf{h}_k^{\mathrm{LoS}} + \sqrt{\tfrac{1}{1+K_\mathrm{T}}}\,\tilde{\mathbf{h}}_k\right), \tag{2.2.4}$$

$$\mathbf{G} = \sqrt{L_{\mathrm{RB}}}\left(\sqrt{\tfrac{K_\mathrm{R}}{1+K_\mathrm{R}}}\,\mathbf{G}^{\mathrm{LoS}} + \sqrt{\tfrac{1}{1+K_\mathrm{R}}}\,\tilde{\mathbf{G}}\right), \tag{2.2.5}$$

where K_T and K_R denote the Rician factors corresponding to the transmitter–RIS and RIS–receiver links, respectively. The deterministic line-of-sight portions of the channels are represented by $\mathbf{h}_k^{\mathrm{LoS}}$ and $\mathbf{G}^{\mathrm{LoS}}$, whereas $\tilde{\mathbf{h}}_k$ and $\tilde{\mathbf{G}}$ describe the scattered non-LoS components that arise from multipath propagation. Each latter entry is independently drawn from a complex Gaussian distribution $\mathcal{CN}(0,1)$.

Remark 2.2.2 (Cascaded path-loss and double fading). The end-to-end user–RIS–BS attenuation scales with the *product* $L_{\mathrm{UR},k} \cdot L_{\mathrm{RB}}$. This multiplicative loss is commonly referred to as the *double fading effect* and constitutes a major limitation of nearly-passive RISs. It motivates practical RIS deployment close to the BS or user clusters, or the adoption of active RISs that can partly compensate for this effect through amplification.

CSI assumption. Unless otherwise stated, we assume the BS has perfect instantaneous CSI knowledge of the channels $\{\mathbf{h}_k\}$ and $\mathbf{G}$ at the timescale of resource allocation. A dedicated low-rate control channel links the RIS controller with the base station, through which the optimized reflection vector $\boldsymbol{\gamma}$ is communicated. Throughout the analysis, all logarithms are expressed in base 2 (so that rates are measured in bps/Hz). The total system bandwidth is denoted by B Hz, while the noise variances σ^2 and σ_{RIS}^2 are defined per complex dimension.

2.2.2 Active RIS

In the active configuration, each RIS element is equipped with a low-power reflection-type amplifier capable of boosting the magnitude of the impinging electromagnetic field. This design mitigates the so-called "double fading" effect of cascaded RIS channels but introduces additional hardware power consumption and amplifier noise. We now derive the complete signal model, the associated SINR expression, and the power balance equations governing active RIS operation under global reflection constraints.

Signal model. The baseband signal impinging on the RIS can be written as

$$\mathbf{y}_{\text{in}}^{\text{RIS}} = \sum_{k=1}^{K} \sqrt{p_k}\, \mathbf{h}_k s_k + \mathbf{n}, \tag{2.2.6}$$

where s_k is the normalized transmit symbol of user k ($\mathbb{E}[|s_k|^2] = 1$), p_k its transmit power, $\mathbf{h}_k \in \mathbb{C}^N$ the user–RIS channel, and $\mathbf{n} \sim \mathcal{CN}(\mathbf{0}, \sigma_{\text{RIS}}^2 \mathbf{I}_N)$ denotes the thermal/amplifier noise at the RIS elements.[1]

After applying the reflection matrix $\mathbf{\Gamma} = \text{diag}(\gamma_1, \ldots, \gamma_N)$, the radiated signal is

$$\mathbf{y}_{\text{out}}^{\text{RIS}} = \mathbf{\Gamma} \mathbf{y}_{\text{in}}^{\text{RIS}} = \sum_{k=1}^{K} \sqrt{p_k}\, \mathbf{\Gamma} \mathbf{h}_k s_k + \mathbf{\Gamma} \mathbf{n} = \sum_{k=1}^{K} \sqrt{p_k}\, \mathbf{H}_k \boldsymbol{\gamma} s_k + \mathbf{\Gamma} \mathbf{n}, \tag{2.2.7}$$

where $\mathbf{H}_k = \text{diag}(h_k(1), \ldots, h_k(N))$ and $\boldsymbol{\gamma} = [\gamma_1, \ldots, \gamma_N]^T$ collects the reflection coefficients. In principle, each element of $\boldsymbol{\gamma}$ can adjust its amplitude and phase.

The received signal at the BS is then:

$$\begin{aligned} \mathbf{r} &= \mathbf{G} \mathbf{y}_{\text{out}}^{\text{RIS}} + \boldsymbol{\omega} \\ &= \sum_{k=1}^{K} \sqrt{p_k}\, \mathbf{G} \mathbf{H}_k \boldsymbol{\gamma}\, s_k + \mathbf{G} \mathbf{\Gamma} \mathbf{n} + \boldsymbol{\omega}, \end{aligned} \tag{2.2.8}$$

with $\boldsymbol{\omega} \sim \mathcal{CN}(\mathbf{0}, \sigma^2 \mathbf{I}_{N_R})$ denoting the receiver thermal noise. Defining $\mathbf{A}_k = \mathbf{G} \mathbf{H}_k$, the effective cascaded channel of user k through the RIS is $\mathbf{A}_k \boldsymbol{\gamma}$.

Linear detection and SINR. Each user signal is detected at the BS through a linear receive filter. Let $\mathbf{c}_k \in \mathbb{C}^{N_R}$ denote the combining vector associated with user k. The BS forms the scalar decision statistic

$$r_k = \mathbf{c}_k^H \mathbf{r}, \tag{2.2.9}$$

where $\mathbf{r}$ is the received signal in (2.2.8). The performance of user k is quantified by the signal-to-interference-plus-noise ratio (SINR), which can be expressed as

$$\text{SINR}_k = \frac{p_k \left| \mathbf{c}_k^H \mathbf{A}_k \boldsymbol{\gamma} \right|^2}{\mathbf{c}_k^H \mathbf{W} \mathbf{c}_k + \sum_{m \neq k} p_m \left| \mathbf{c}_k^H \mathbf{A}_m \boldsymbol{\gamma} \right|^2}, \tag{2.2.10}$$

[1] Unlike a nearly-passive RIS, an active RIS necessarily injects noise because amplification takes place in the analog RF domain.

with $\mathbf{A}_k = \mathbf{G}\mathbf{H}_k$ and where the colored noise covariance matrix is given by

$$\mathbf{W} = \sigma^2 \mathbf{I}_{N_R} + \sigma_{\text{RIS}}^2 \mathbf{G}\boldsymbol{\Gamma}\boldsymbol{\Gamma}^H \mathbf{G}^H. \tag{2.2.11}$$

The structure of (2.2.10) is intuitive: the numerator represents the valuable power of user k after combining, while the denominator accounts for both multi-user interference and the colored noise induced by the receiver and the active RIS.

Remark 2.2.3 (Optimal receive filters). For fixed transmit powers $\mathbf{p}$ and RIS coefficients $\boldsymbol{\gamma}$, the SINR in (2.2.10) is maximized by the well-known *minimum mean-square error* (MMSE) receive filter. Its closed-form expression is

$$\mathbf{c}_k^\star = \sqrt{p_k}\, \mathbf{M}_k^{-1} \mathbf{A}_k \boldsymbol{\gamma}, \tag{2.2.12}$$

where the matrix

$$\mathbf{M}_k = \sum_{m \neq k} p_m \mathbf{A}_m \boldsymbol{\gamma}\boldsymbol{\gamma}^H \mathbf{A}_m^H + \mathbf{W} \tag{2.2.13}$$

is the interference-plus-noise covariance matrix seen by user k at the BS. The first term in (2.2.13) accounts for the multi-user interference caused by all other transmitters $m \neq k$. In contrast, the second term $\mathbf{W}$ represents the contribution of both the BS receiver noise and the colored noise injected by the active RIS.

This MMSE filter (2.2.12) will be assumed throughout the performance analysis of this chapter, as it maximizes the achievable SINR for fixed $(\mathbf{p}, \boldsymbol{\gamma})$. For completeness, a step-by-step derivation of (2.2.12) is provided in Appendix A.1.1.

Incident and radiated powers. To analyze how energy flows through the RIS, we begin by quantifying the total RF power that reaches the surface and the portion that it re-radiates back into the environment. The overall incident power is given by

$$P_{\text{in}} = \sum_{k=1}^{K} p_k \|\mathbf{h}_k\|^2 + \sigma_{\text{RIS}}^2 N = \sum_{k=1}^{K} p_k \,\text{tr}(\mathbf{H}_k \mathbf{H}_k^H) + \sigma_{\text{RIS}}^2 N, \tag{2.2.14}$$

The initial term represents the aggregate signal power from all K users, whereas the subsequent term denotes the noise produced by the N reflecting units of the RIS. The overall RF power radiated back by the surface is then

given by:

$$P_{\text{out}} = \sum_{k=1}^{K} p_k \operatorname{tr}(\mathbf{H}_k \boldsymbol{\gamma}\boldsymbol{\gamma}^H \mathbf{H}_k^H) + \sigma_{\text{RIS}}^2 \operatorname{tr}(\boldsymbol{\gamma}\boldsymbol{\gamma}^H). \tag{2.2.15}$$

The first term reflects the useful re-emission of the incident user signals, whereas the second term captures the additional contribution of the amplified thermal noise after reflection. When no amplification is present ($|\gamma_n| = 1$ for all n), it follows that $P_{\text{out}} = P_{\text{in}}$, which is consistent with a passive, lossless surface.

Net amplification power. In the active configuration, reflection-type amplifiers embedded in the RIS can inject additional RF power into the re-radiated signal. The net amount of energy contributed by the surface can therefore be quantified as the difference between the total outgoing and incoming powers, yielding:

$$P_{\text{out}} - P_{\text{in}} = \operatorname{tr}\Big((\boldsymbol{\gamma}\boldsymbol{\gamma}^H - \mathbf{I}_N)\mathbf{R}\Big), \tag{2.2.16}$$

where

$$\mathbf{R} = \sum_{k=1}^{K} p_k \mathbf{H}_k^H \mathbf{H}_k + \sigma_{\text{RIS}}^2 \mathbf{I}_N \tag{2.2.17}$$

is a positive-definite diagonal matrix that captures the spatial distribution of power from the incoming user signals and the noise generated at the RIS. A detailed derivation of this expression, starting from the definitions of P_{in} and P_{out}, is given in Appendix A.1.2. This relationship, therefore, leads to the *global reflection constraint*, which defines the feasible operating region of an active RIS.

$$\operatorname{tr}(\mathbf{R}) \;\leq\; \operatorname{tr}(\mathbf{R}\boldsymbol{\gamma}\boldsymbol{\gamma}^H) \;\leq\; \operatorname{tr}(\mathbf{R}) + P_{R,\max}, \tag{2.2.18}$$

where $P_{R,\max}$ represents the maximum RF power that the RIS hardware can supply through its amplification circuitry.

Remark 2.2.4 (Feasibility in the active regime). The lower bound $\operatorname{tr}(\mathbf{R}\boldsymbol{\gamma}\boldsymbol{\gamma}^H) \geq \operatorname{tr}(\mathbf{R})$ guarantees that the RIS operates in the active regime, indicating that the surface re-radiates no less power than it receives. This condition is always met; for instance, choosing $|\gamma_n| = 1$ for every element results in equality, corresponding to the nearly-passive boundary case.

Power consumption model. To evaluate the system's global energy efficiency (GEE), we must carefully account for all relevant power expenditures, distinguishing between dynamic amplification costs and static circuit consumptions. The power consumed by the RIS consists of three parts: the net RF amplification power, the static per-element cost, and other fixed RIS hardware costs. Consequently, the overall power requirement of the RIS is given by

$$\begin{aligned} P_{\text{RIS}} &= (P_{\text{out}} - P_{\text{in}}) + NP_{c,n}^{(a)} + P_{0,\text{RIS}}^{(a)} \\ &= \text{tr}\Big((\boldsymbol{\gamma}\boldsymbol{\gamma}^H - \mathbf{I}_N)\mathbf{R}\Big) + NP_{c,n}^{(a)} + P_{0,\text{RIS}}^{(a)}. \end{aligned} \tag{2.2.19}$$

where $(P_{\text{out}} - P_{\text{in}})$ is the net RF power injected by the active RIS amplifiers, $P_{c,n}^{(a)}$ is the static power consumption per active element (to enable phase and amplitude tuning), and $P_{0,\text{RIS}}^{(a)}$ captures all other fixed overheads of the RIS hardware (e.g., control circuitry, biasing networks). Other components also influence the overall energy use of the system in the network. In particular, the transmit amplifiers at the user terminals contribute:

$$P_t = \sum_{k=1}^{K} \mu_k p_k + P_0, \tag{2.2.20}$$

where $\mu_k \geq 1$ is the reciprocal of the power amplifier efficiency of user k (with $\mu_k = 1$ corresponding to an ideal amplifier), and P_0 denotes static circuit power associated with the BS and user terminals, excluding the RIS. The total system power consumption is then obtained by summing the RIS and non-RIS contributions:

$$P_{\text{tot}} = \text{tr}\Big((\boldsymbol{\gamma}\boldsymbol{\gamma}^H - \mathbf{I}_N)\mathbf{R}\Big) + \sum_{k=1}^{K} \mu_k p_k + P_c, \tag{2.2.21}$$

where

$$P_c = P_0 + NP_{c,n}^{(a)} + P_{0,\text{RIS}}^{(a)} \tag{2.2.22}$$

denotes the overall static power drawn by the system, including the base station's fixed consumption P_0, the per-element static cost of the active RIS $NP_{c,n}^{(a)}$, and additional hardware overheads $P_{0,\text{RIS}}^{(a)}$.

Remark 2.2.5 (Conventional vs. proposed power model). Much of the existing literature [41], [84], [98] tends to overstate the power usage of active RISs by assuming it equals the total radiated power P_{out}. In practice, however,

the surface only draws the additional RF energy needed for amplification, that is, $P_{\text{out}} - P_{\text{in}}$, because the incident RF signal is directly processed in the analog domain rather than being regenerated at baseband. Our model in (2.2.16) therefore provides a more accurate description of the physical power budget of active RISs.

Global energy efficiency. With the power consumption model established, we now introduce the main performance measure of interest—the *global energy efficiency* (GEE). This metric, expressed in bit/Joule, quantifies the number of reliable information bits transmitted per unit of consumed energy. Formally, it is defined as

$$\text{GEE}(\boldsymbol{\gamma}, \mathbf{p}, \mathbf{C}) = \frac{B \sum_{k=1}^{K} \log_2\left(1 + \text{SINR}_k\right)}{\text{tr}\left((\boldsymbol{\gamma}\boldsymbol{\gamma}^H - \mathbf{I}_N)\mathbf{R}\right) + \sum_{k=1}^{K} \mu_k p_k + P_c}, \tag{2.2.23}$$

where the numerator gives the total data throughput achieved by all K users within the system bandwidth B (bit/s), and the denominator represents the corresponding overall power consumption P_{tot}, as shown in (2.2.21). This definition directly evaluates how efficiently the network converts electrical energy into useful information transfer. Several factors influence the global energy efficiency: the users' transmit powers $\mathbf{p}$, the RIS reflection vector $\boldsymbol{\gamma}$, the receive filter matrix $\mathbf{C}$, and the static hardware power term P_c. These parameters determine how effectively the available energy is translated into useful data transmission.

Optimization problem. The maximization of the GEE for an active RIS can be formulated as follows:

$$\max_{\boldsymbol{\gamma}, \mathbf{p}, \mathbf{C}} \quad \text{GEE}(\boldsymbol{\gamma}, \mathbf{p}, \mathbf{C}) \tag{2.2.24a}$$

$$\text{s.t.} \quad \text{tr}(\mathbf{R}) \;\leq\; \text{tr}(\mathbf{R}\boldsymbol{\gamma}\boldsymbol{\gamma}^H) \;\leq\; \text{tr}(\mathbf{R}) + P_{R,\max}, \tag{2.2.24b}$$

$$0 \leq p_k \leq P_{\max,k}, \quad k = 1, \ldots, K, \tag{2.2.24c}$$

where (2.2.24b) enforces the overall power balance at the RIS and limits its amplification capability, while (2.2.24c) constrains the transmit power of each individual user to its maximum allowable level.

Remark 2.2.6. The expression in (2.2.23) makes clear that the RIS has a dual impact on the system. The reflection vector $\boldsymbol{\gamma}$ influences the system in two interconnected ways. It governs the achievable data rates through its effect on the SINR terms in the numerator, and at the same time determines the overall

energy expenditure through the amplification component $\mathrm{tr}((\boldsymbol{\gamma}\boldsymbol{\gamma}^H - \mathbf{I}_N)\mathbf{R})$ appearing in the denominator. Because these effects are interdependent, the optimization landscape becomes inherently non-convex, motivating the development of the dedicated algorithms discussed in the next sections.

2.2.3 Nearly-Passive RIS

We will now focus on the nearly-passive regime, which corresponds to the traditional RIS model widely studied in the literature. In this model, the reflecting elements do not use amplifiers and therefore do not actively add RF power to the system. This design features simpler hardware and reduced static power consumption, but it is affected by the well-known "double fading" effect caused by cascaded path-loss.

System assumptions. The nearly-passive model is obtained by setting

$$\sigma^2_{\mathrm{RIS}} = 0, \qquad P_{R,\max} = 0,$$

which removes both amplification and internally generated noise at the RIS. Consequently, the surface draws only the static power required for configuring and controlling its reflective elements, expressed as

$$NP^{(p)}_{c,n} + P^{(p)}_{0,\mathrm{RIS}},$$

where $P^{(p)}_{c,n}$ denotes the control power consumed by each reflecting element, and $P^{(p)}_{0,\mathrm{RIS}}$ represents the fixed hardware overhead, including biasing and control circuitry.

Global reflection constraint. With these parameters in place, the global reflection condition simplifies to

$$\mathrm{tr}\big(\mathbf{R}(\mathbf{p})\,\boldsymbol{\gamma}\boldsymbol{\gamma}^H\big) \le \mathrm{tr}\big(\mathbf{R}(\mathbf{p})\big), \qquad \mathbf{R}(\mathbf{p}) = \sum_{k=1}^{K} p_k \mathbf{H}_k^H \mathbf{H}_k, \tag{2.2.25}$$

which ensures that the RIS's total power reradiated does not exceed the total power received across its surface.

Energy efficiency expression. The global energy efficiency (GEE) of a nearly-passive RIS can therefore be written as

$$\mathrm{GEE}(\boldsymbol{\gamma}, \mathbf{p}, \mathbf{C}) = \frac{B \sum_{k=1}^{K} \log_2(1 + \mathrm{SINR}_k)}{\sum_{k=1}^{K} \mu_k p_k + P_c}, \tag{2.2.26}$$

where the denominator excludes any amplification-related term since the RIS does not consume active RF power.

Optimization problem. The corresponding optimization problem becomes

$$\max_{\boldsymbol{\gamma}, \mathbf{p}, \mathbf{C}} \ \mathrm{GEE}(\boldsymbol{\gamma}, \mathbf{p}, \mathbf{C}) \quad \text{s.t.} \quad (2.2.25), \quad 0 \le p_k \le P_{\max,k}, \ \forall k. \tag{2.2.27}$$

Remark 2.2.7 (Global vs. local constraints). Nearly-passive operation governed by a global reflection rule should not be confused with the conventional element-wise unit-modulus condition. In the local formulation, each reflecting element is individually limited to $|\gamma_n| \le 1$. Under the global rule in (2.2.25), however, some elements may slightly exceed this limit ($|\gamma_n| > 1$) provided that others compensate by reflecting less energy, so that the overall radiated power remains physically consistent. This more flexible interpretation sheds light on the performance trends discussed later in Section 2.3. Also, broader formulation offers insight into the performance differences that will be discussed later in Section 2.3.

Remark 2.2.8 (Problem characteristics). Both the active and nearly passive cases described in Problems (2.2.24) and (2.2.27) fall under the category of fractional optimization problems, which are inherently non-convex. The numerator is non-concave with respect to $(\mathbf{p}, \boldsymbol{\gamma})$, and the global constraint couples these variables through $\mathbf{R}(\mathbf{p})$. In the active configuration, an additional dependence arises because the colored noise covariance also varies with $\boldsymbol{\gamma}$. These features justify the use of alternating optimization and sequential convex approximation strategies, which are developed in detail in Section 2.4.

2.3 RISs with Global Reflection Constraint

Before presenting the solution methods for Problems (2.2.24) and (2.2.27), it is useful to examine the effects of applying a *global* reflection constraint at the RIS and to compare it with the traditional *local*, element-wise formulation. The global model treats the metasurface as a *macro-reflector*, enforcing power

balance at the surface level rather than per element; this strictly enlarges the feasible set of reflection coefficients and can yield measurable gains. For analytical clarity and without losing the main insights, we consider first a single-user, single-antenna receiver assisted by a nearly-passive RIS. In this case, the surface lacks amplification capability and only reflects the energy incident upon it. Owing to this limitation, the received power remains relatively low, representing the most constrained operating condition. Nevertheless, analyzing this regime is valuable, as it offers more profound insight into RIS-assisted links' physical behavior and practical design limits. The same general behavior is observed when extending the framework to multi-user or multi-antenna networks.

2.3.1 From local to global

Recall that, in the nearly-passive regime, the RIS operates under a surface-level power balance condition, which states that the total energy re-radiated by the array must not exceed the energy it receives from incoming signals. Using the notation introduced in Section 2.2.3 and setting $\sigma_{\text{RIS}}^2 = 0$, this relationship can be expressed as

$$P_{\text{out}} - P_{\text{in}} \leq 0 \iff \operatorname{tr}\big((\boldsymbol{\gamma}\boldsymbol{\gamma}^H - \mathbf{I}_N)\mathbf{R}\big) \leq 0, \qquad \mathbf{R} \triangleq \sum_{k=1}^{K} p_k \mathbf{H}_k^H \mathbf{H}_k. \quad (2.3.1)$$

By expanding (2.3.1) element by element, we obtain

$$\sum_{k=1}^{K} p_k \sum_{n=1}^{N} |h_{n,k}|^2 \big(|\gamma_n|^2 - 1\big) \leq 0, \quad (2.3.2)$$

where $h_{n,k}$ represents the n-th entry of the channel vector $\mathbf{h}_k$. The conventional *local* constraint, $|\gamma_n| \leq 1$ for every reflecting element, always fulfills (2.3.2). However, the converse does not hold, because the global condition governs only the total reflected energy over the entire surface rather than the behavior of each element separately. This distinction implies that

$$\mathcal{F}_{\text{local}} \subsetneq \mathcal{F}_{\text{global}},$$

and therefore, some reflecting elements may temporarily reach $|\gamma_n| > 1$ as long as others compensate by reflecting less power, preserving the total energy balance across the surface. From an electromagnetic perspective, this behavior arises from near-field and surface-wave coupling among neighboring elements, which enables limited energy exchange across the array.

Viewed from a communication standpoint, the RIS functions as a unified macro-reflector instead of a collection of independent passive mirrors. A constructive proof of this inclusion and additional physical insight is provided in Appendix A.1.3.

2.3.2 Single-user optimization under the exact global constraint

Consider one single-antenna user and a single-antenna receiver assisted by an N-element nearly-passive RIS. Let $\mathbf{g}, \mathbf{h} \in \mathbb{C}^N$ denote the RIS–receiver and user–RIS channels, respectively, and let the user transmit with power p. With $\mathbf{\Gamma} = \mathrm{diag}(\gamma_1, \ldots, \gamma_N)$, the coherent gain after reflection is

$$\left|\mathbf{g}^H \mathbf{\Gamma} \mathbf{h}\right|^2 \;=\; \left|\sum_{n=1}^{N} \gamma_n \, h(n) \, g(n)^*\right|^2 . \tag{2.3.3}$$

In this single-user, nearly-passive case we have $\mathbf{R} = p\,\mathbf{H}^H\mathbf{H}$ with $\mathbf{H} = \mathrm{diag}(h(1), \ldots, h(N))$, so the exact global constraint (2.3.1) becomes

$$\gamma^H \mathbf{R} \gamma \;\le\; \mathrm{tr}(\mathbf{R}) \quad\Longleftrightarrow\quad \left\| \mathbf{R}^{1/2} \gamma \right\|_2^2 \;\le\; \mathrm{tr}(\mathbf{R}). \tag{2.3.4}$$

Define the exact change of variables

$$\boldsymbol{x} \triangleq \mathbf{R}^{1/2} \gamma, \qquad \mathbf{z}^H \triangleq \mathbf{g}^H \mathbf{H} \mathbf{R}^{-1/2}, \tag{2.3.5}$$

and write $x_n = \rho_n e^{j\phi_n}$, $z_n = |z_n| e^{j \angle z_n}$. Since $\gamma = \mathbf{R}^{-1/2}\boldsymbol{x}$, the optimization

$$\max_{\gamma} \; \left|\mathbf{g}^H \mathbf{\Gamma} \mathbf{h}\right|^2 \quad \text{s.t.} \quad \gamma^H \mathbf{R} \gamma \le \mathrm{tr}(\mathbf{R}) \tag{2.3.6}$$

is *exactly* equivalent to

$$\max_{\{\rho_n, \phi_n\}} \; \left|\sum_{n=1}^{N} \rho_n e^{j\phi_n} z_n\right|^2 \quad \text{s.t.} \quad \sum_{n=1}^{N} \rho_n^2 \le \mathrm{tr}(\mathbf{R}), \;\; \rho_n \ge 0, \;\; \phi_n \in [0, 2\pi). \tag{2.3.7}$$

Proposition 2.3.1 (Closed-form optimizer under the exact constraint)**.** *Problem* (2.3.7) *admits the closed-form solution*

$$\phi_n^\star = -\angle z_n, \tag{2.3.8}$$

$$\rho_n^\star = |z_n| \sqrt{\frac{\mathrm{tr}(\mathbf{R})}{\sum_{m=1}^N |z_m|^2}}, \qquad n = 1, \ldots, N. \tag{2.3.9}$$

Proof. With the optimal phase choices $\phi_n^\star$, the objective reduces to $\left(\sum_n \rho_n |z_n|\right)^2$. The constraint $\|\boldsymbol{\rho}\|_2^2 \le \mathrm{tr}(\mathbf{R})$ corresponds to a Euclidean ball in $\mathbb{R}^N$, which limits the feasible amplitude vector $\boldsymbol{\rho}$ to a region of bounded energy. By applying the Cauchy–Schwarz inequality, the optimal amplitude vector $\boldsymbol{\rho}$ must be collinear with $|\mathbf{z}|$, that is, $\boldsymbol{\rho} = \alpha|\mathbf{z}|$ for some scalar α. Imposing the equality condition $\sum_n \rho_n^2 = \mathrm{tr}(\mathbf{R})$ then determines the scaling factor and gives the amplitude values stated in the proposition. A complete derivation based on the Karush–Kuhn–Tucker (KKT) conditions is presented in Appendix A.1.4. ■

2.3.3 Performance comparison with local unit-modulus reflection

We define $\mathbf{d} \triangleq \mathbf{H}^H \mathbf{g}$, with the entries given by $d_n = h^*(n) g(n)$. Let σ^2 represent the noise variance at the receiver. Based on the optimal global-reflection configuration established in Proposition 2.3.1, the received signal-to-noise ratio (SNR) can be expressed as follows:

$$\mathrm{SNR}_{\mathrm{opt}} = \frac{p}{\sigma^2} \sum_{n=1}^N \delta_n |d_n|^2, \qquad \delta_n \triangleq \frac{\|\mathbf{h}\|^2}{|h(n)|^2} \ge 1, \tag{2.3.10}$$

where the coefficients δ_n measure the relative contribution of each RIS element with respect to the total channel gain and we used $\mathbf{R} = p\,\mathbf{H}^H\mathbf{H}$, $\mathrm{tr}(\mathbf{R}) = p\|\mathbf{h}\|^2$, and $\mathbf{R}^{-1} = p^{-1}\,\mathrm{diag}\big(1/|h(1)|^2, \ldots, 1/|h(N)|^2\big)$. Under the local unit-modulus allocation ($|\gamma_n| = 1$, phases matched), the SNR is

$$\mathrm{SNR}_{\mathrm{uni}} = \frac{p}{\sigma^2} \left(\sum_{n=1}^N |d_n| \right)^2. \tag{2.3.11}$$

Hence, the gain factor is

$$\eta \triangleq \frac{\mathrm{SNR}_{\mathrm{opt}}}{\mathrm{SNR}_{\mathrm{uni}}} = \frac{\sum_{n=1}^{N} \delta_n |d_n|^2}{\left(\sum_{n=1}^{N} |d_n|\right)^2} \geq 1. \tag{2.3.12}$$

Equality holds when the cascaded magnitudes are "flat" (e.g., $|h(n)|$ constant so that all δ_n equal), while the gain is larger when $\{|d_n|\}$ (and/or $\{|h(n)|\}$) are heterogeneous. Two useful regimes are illustrative:

- If $|g(n)| = 0$ for all $n \neq k$ and $|g(k)| > 0$, then $|d_n| = 0$ for $n \neq k$, and (2.3.12) yields $\eta = \delta_k = \|\mathbf{h}\|^2 / |h(k)|^2$. In particular, if $|h(n)| = |h|$ for all n, then $\eta = N$.
- If $|d_n|$ are all equal, then $\eta = 1$.

The gain thus scales with the "spread" of the cascaded magnitudes, consistent with the macro-reflector intuition. A complete derivation of the expression for η, including the introduction of the scaling factor β, the proof that $\eta = 1$ in the uniform channel case, and the demonstration of its linear growth with N under highly unbalanced channel conditions is presented in Appendix A.1.5.

2.3.4 Ordering and majorization insight

Let the set $\{|z_n|\}$ (equivalently, $\{|d_n|\}$) be ordered in non-increasing fashion. The following two lemmas formalize the intuition that the optimal amplitude vector follows this ordering of the cascaded magnitudes and that the corresponding objective function is Schur-convex over the ordered domain.

Lemma 2.3.1 (Monotone rearrangement)**.** *Let $\{z_n\}$ denote a sequence arranged in non-increasing order, and let $\boldsymbol{\rho}$ be any feasible amplitude vector. If $\boldsymbol{\rho}$ is reordered to follow the same ordering as $\{z_n\}$, the value of $\sum_n \rho_n z_n$ does not decrease.*

The detailed proof of Lemma 2.3.1, based on an exchange argument, is provided in Appendix A.5.1.

Lemma 2.3.2 (Schur-convexity on ordered sets)**.** *Over the ordered domain $\mathcal{D} = \{\boldsymbol{\rho} : \rho_1 \geq \cdots \geq \rho_N\}$, the mapping $\boldsymbol{\rho} \mapsto \sum_{n=1}^{N} \rho_n a_n$ is Schur-convex. As a result, the objective value grows with the degree of "spread" of $\boldsymbol{\rho}$ in the majorization sense.*

A rigorous proof of Lemma 2.3.2, using the derivative condition for Schur-convexity, is given in Appendix A.5.2.

Remark 2.3.1 (Physical interpretation). In the global reflection model, energy can flow between adjacent elements through near-field interactions, allowing some surface parts to radiate slightly more power. In contrast, others emit less, as long as the total energy across the RIS satisfies the balance condition in (2.3.1). This macro-reflector behavior strictly generalizes the local unit-modulus model and explains the gains in (2.3.12), which become pronounced when the cascaded magnitudes are heterogeneous.

The above analysis shows that global reflection enlarges the feasible RIS set and enables closed-form optimal allocations in the single-user case, with quantifiable gains over local unit-modulus reflection. In multi-user systems, the same coupling that drives these gains renders the GEE maximization *non-convex* and *fractional*, with variables $(\mathbf{p}, \gamma, \mathbf{C})$ entering both numerator and denominator and in the feasibility set. Section 2.4 develops alternating/sequential fractional optimization methods to efficiently address Problems (2.2.24) and (2.2.27).

2.4 GEE Maximization

This section focuses on maximizing the global energy efficiency (GEE) for the general multi-user uplink scenario, considering an *active* RIS that operates under the proposed *global reflection constraint*. The coupling among the RIS coefficients γ, the user powers $\mathbf{p}$ and the BS linear receive filters $\mathbf{C}$ makes the problem non-convex for several reasons: (i) γ appears nonlinearly in both the useful-signal terms and the *colored* noise covariance induced by active amplification; (ii) the global reflection constraint includes a non-convex inequality; and (iii) the objective is a fractional, non-pseudoconcave function of the decision variables. We propose two algorithmic solutions. In this section, we develop the *first* one, based on *alternating optimization* (AO) combined with *sequential fractional programming* (SFP). The second approach (based on a weighted-MMSE reformulation) will be presented later for completeness and benchmarking.

2.4.1 First Proposed Approach

The approach alternates over the three blocks $\{\gamma, \mathbf{p}, \mathbf{C}\}$:

(i) RIS vector update: optimize γ with $(\mathbf{p}, \mathbf{C})$ fixed;

(ii) Power update: optimize $\mathbf{p}$ with $(\boldsymbol{\gamma}, \mathbf{C})$ fixed;

(iii) Receiver update: optimize $\mathbf{C}$ (decoupled across users) with $(\boldsymbol{\gamma}, \mathbf{p})$ fixed.

SFP handles each subproblem to obtain a concave–over–convex fractional form amenable to standard fractional programming (e.g., Dinkelbach). The resulting outer AO loop monotonically increases the GEE and stops when the improvement is below a prescribed tolerance.

2.4.1.1 Optimization of $\boldsymbol{\gamma}$

For fixed transmit powers $(\mathbf{p})$ and receive filters $(\mathbf{C})$, the RIS-update subproblem can be formulated as

$$\max_{\boldsymbol{\gamma}} \quad \frac{\sum_{k=1}^{K} \log\left(1 + \dfrac{p_k \, |\mathbf{c}_k^H \mathbf{A}_k \boldsymbol{\gamma}|^2}{\mathbf{c}_k^H \mathbf{W} \, \mathbf{c}_k + \sum_{m \neq k} p_m \, |\mathbf{c}_k^H \mathbf{A}_m \boldsymbol{\gamma}|^2}\right)}{\mathrm{tr}(\mathbf{R} \, \boldsymbol{\gamma}\boldsymbol{\gamma}^H) + P_{c,eq}} \tag{2.4.1a}$$

$$\text{s.t.} \quad \mathrm{tr}(\mathbf{R}) \leq \mathrm{tr}(\mathbf{R} \, \boldsymbol{\gamma}\boldsymbol{\gamma}^H) \leq \mathrm{tr}(\mathbf{R}) + P_{R,\max}, \tag{2.4.1b}$$

where $P_{c,eq} \triangleq \sum_k \mu_k p_k + P_c - \mathrm{tr}(\mathbf{R})$, and the colored noise covariance matrix is given by

$$\mathbf{W} = \sigma^2 \mathbf{I}_{N_R} + \sigma_{\mathrm{RIS}}^2 \, \mathbf{G}\boldsymbol{\Gamma}\boldsymbol{\Gamma}^H \mathbf{G}^H, \qquad \boldsymbol{\Gamma} = \mathrm{diag}(\boldsymbol{\gamma}).$$

Introducing $\mathbf{u}_k = \mathbf{G}^H \mathbf{c}_k$ and $\widetilde{\mathbf{U}}_k = \mathrm{diag}(|u_k(1)|^2, \ldots, |u_k(N)|^2)$ leads to

$$\mathbf{c}_k^H \mathbf{W} \, \mathbf{c}_k = \sigma^2 \|\mathbf{c}_k\|^2 + \sigma_{\mathrm{RIS}}^2 \, \boldsymbol{\gamma}^H \widetilde{\mathbf{U}}_k \boldsymbol{\gamma}. \tag{2.4.2}$$

To handle the non-convexity of the numerator in (2.4.1a), a sequential fractional programming (SFP) bound is constructed. For each user k, define

$$x = p_k |\mathbf{c}_k^H \mathbf{A}_k \boldsymbol{\gamma}|^2, \qquad y = \mathbf{c}_k^H \mathbf{W} \, \mathbf{c}_k + \sum_{m \neq k} p_m |\mathbf{c}_k^H \mathbf{A}_m \boldsymbol{\gamma}|^2,$$

and let $\bar{\boldsymbol{\gamma}}$ be a feasible reference point. The logarithmic term $\log(1 + \frac{x}{y})$ admits the following tight first-order lower bound, exact at ($x = \bar{x}$ and $y = \bar{y}$) [2]:

$$\log\left(1 + \frac{x}{y}\right) \geq \log\left(1 + \frac{\bar{x}}{\bar{y}}\right) + \frac{\bar{x}}{\bar{y}} \left(\frac{2\sqrt{x}}{\sqrt{\bar{x}}} - \frac{x + y}{\bar{x} + \bar{y}} - 1\right),$$

[2] A detailed derivation specific to the RIS-aided formulation can be found in Appendix A.1.6, while a broader discussion of the underlying principles is available in [95].

This bound stems from the concave–convex formulation, which guarantees exactness at the selected reference point. It underpins the Sequential Fractional Programming (SFP) framework adopted in this work and also serves as a locally concave approximation of the rate function whose value and gradient coincide with those of the original expression at the current iteration.

Substituting (3.3.2) into the rate expression yields, for each user k, the concave approximation

$$\bar{R}_k(\boldsymbol{\gamma}) = \bar{A}_k + \bar{B}_k\left(\bar{D}_k\,|\mathbf{c}_k^H\mathbf{A}_k\boldsymbol{\gamma}| - \bar{F}_k - \bar{E}_k\left[\sigma_{\mathrm{RIS}}^2\,\boldsymbol{\gamma}^H\widetilde{\mathbf{U}}_k\boldsymbol{\gamma} + \sum_{m=1}^{K} p_m|\mathbf{c}_k^H\mathbf{A}_m\boldsymbol{\gamma}|^2\right]\right), \tag{2.4.3}$$

where the coefficients, evaluated at the current iterate $\bar{\boldsymbol{\gamma}}$, are given by

$$\bar{A}_k = \log\left(1 + \frac{p_k|\mathbf{c}_k^H\mathbf{A}_k\bar{\boldsymbol{\gamma}}|^2}{\sigma^2\|\mathbf{c}_k\|^2 + \sigma_{\mathrm{RIS}}^2\bar{\boldsymbol{\gamma}}^H\widetilde{\mathbf{U}}_k\bar{\boldsymbol{\gamma}} + \sum_{m\neq k} p_m|\mathbf{c}_k^H\mathbf{A}_m\bar{\boldsymbol{\gamma}}|^2}\right),$$

$$\bar{B}_k = \frac{p_k|\mathbf{c}_k^H\mathbf{A}_k\bar{\boldsymbol{\gamma}}|^2}{\sigma^2\|\mathbf{c}_k\|^2 + \sigma_{\mathrm{RIS}}^2\bar{\boldsymbol{\gamma}}^H\widetilde{\mathbf{U}}_k\bar{\boldsymbol{\gamma}} + \sum_{m\neq k} p_m|\mathbf{c}_k^H\mathbf{A}_m\bar{\boldsymbol{\gamma}}|^2}, \qquad \bar{D}_k = \frac{2}{|\mathbf{c}_k^H\mathbf{A}_k\bar{\boldsymbol{\gamma}}|},$$

$$\bar{E}_k = \frac{1}{\sigma^2\|\mathbf{c}_k\|^2 + \sigma_{\mathrm{RIS}}^2\bar{\boldsymbol{\gamma}}^H\widetilde{\mathbf{U}}_k\bar{\boldsymbol{\gamma}} + \sum_{m=1}^{K} p_m|\mathbf{c}_k^H\mathbf{A}_m\bar{\boldsymbol{\gamma}}|^2}, \qquad \bar{F}_k = \bar{E}_k\sigma^2\|\mathbf{c}_k\|^2 + 1.$$

The only non-concave term in (2.4.3) is $|\mathbf{c}_k^H\mathbf{A}_k\boldsymbol{\gamma}|$, which is convex in $\boldsymbol{\gamma}$ and can therefore be lower-bounded by its first-order Taylor expansion around $\bar{\boldsymbol{\gamma}}$, giving

$$|\mathbf{c}_k^H\mathbf{A}_k\boldsymbol{\gamma}| \geq |\mathbf{c}_k^H\mathbf{A}_k\bar{\boldsymbol{\gamma}}| + \Re\left\{\frac{\mathbf{A}_k^H\mathbf{c}_k\,\mathbf{c}_k^H\mathbf{A}_k\bar{\boldsymbol{\gamma}}}{|\mathbf{c}_k^H\mathbf{A}_k\bar{\boldsymbol{\gamma}}|}(\boldsymbol{\gamma}-\bar{\boldsymbol{\gamma}})\right\}. \tag{2.4.4}$$

This leads to a concave surrogate, denoted $\widetilde{R}_k(\boldsymbol{\gamma})$. The right-hand inequality in (2.4.1b) is convex, while the left-hand one is not. However, since $\boldsymbol{\gamma}^H\mathbf{R}\boldsymbol{\gamma}$ is convex, it can be replaced by its affine lower bound at $\bar{\boldsymbol{\gamma}}$, expressed as

$$\boldsymbol{\gamma}^H\mathbf{R}\boldsymbol{\gamma} \geq \bar{\boldsymbol{\gamma}}^H\mathbf{R}\bar{\boldsymbol{\gamma}} + 2\,\Re\{\bar{\boldsymbol{\gamma}}^H\mathbf{R}(\boldsymbol{\gamma}-\bar{\boldsymbol{\gamma}})\}. \tag{2.4.5}$$

Algorithm 1 First approach — RIS update via SFP

Choose tolerance $\epsilon > 0$ and a feasible initializer $\bar{\gamma} = \gamma_0$;
repeat
  Solve (2.4.6) for γ (e.g., Dinkelbach);
  Set $\bar{\gamma} \leftarrow \gamma$;
until $\|\bar{\gamma} - \gamma\| < \epsilon$

At each iteration of the SFP procedure, the resulting subproblem becomes

$$\max_{\gamma} \quad \frac{\sum_{k=1}^{K} \widetilde{R}_k(\gamma)}{\gamma^H \mathbf{R} \gamma + P_{c,eq}} \tag{2.4.6a}$$

$$\text{s.t.} \quad \gamma^H \mathbf{R} \gamma \;\leq\; P_{R,\max} + \mathrm{tr}(\mathbf{R}), \tag{2.4.6b}$$

$$\bar{\gamma}^H \mathbf{R} \bar{\gamma} + 2\,\Re\{\bar{\gamma}^H \mathbf{R}(\gamma - \bar{\gamma})\} \;\geq\; \mathrm{tr}(\mathbf{R}), \tag{2.4.6c}$$

which represents a concave-over-convex fractional program subject to convex constraints. This problem can therefore be solved efficiently using fractional programming methods such as Dinkelbach's algorithm. The inner RIS update procedure is summarized in Algorithm 1.

Proposition 2.4.1. *Algorithm 1 increases or preserves the global energy efficiency (GEE) value with each iteration. The sequence generated by the algorithm therefore converges to a stationary solution of Problem (2.4.1) that satisfies the necessary first-order optimality conditions.*

Proof. By construction, at each SFP step, the surrogate objective is a tight (value- and gradient-matching) lower bound of the true objective at $\bar{\gamma}$, and the affine support in (2.4.6c) is a tight lower bound of the left global constraint; see Appendix A.1.6. Standard SFP arguments (e.g., [60], [95]) imply monotonic ascent and convergence to a stationary point. ■

2.4.1.2 Optimization of p

In this subproblem, the parameters $(\gamma, \mathbf{C})$ are kept fixed, and several auxiliary terms are introduced to simplify notation. Specifically, we define

$$a_{k,m} \triangleq |\mathbf{c}_k^H \mathbf{A}_m \gamma|^2, \qquad d_k \triangleq \mathbf{c}_k^H \mathbf{W}\, \mathbf{c}_k, \qquad P_{c,eq} \triangleq \sigma_{\mathrm{RIS}}^2(\|\gamma\|^2 - N) + P_c,$$

and

$$\mu_{k,eq} \triangleq \mu_k - \|\mathbf{h}_k\|^2 + \|\mathbf{H}_k \gamma\|^2.$$

These parameters capture, respectively, the effective user–interference coupling through the RIS, the contribution of colored noise at the receiver, the

equivalent static power offset due to RIS amplification, and the adjusted amplifier efficiency term associated with each user. Using these definitions, the power-allocation subproblem can be written as

$$\max_{\mathbf{p}} \quad \frac{\sum_{k=1}^{K} \log\left(1 + \frac{p_k a_{k,k}}{d_k + \sum_{m \neq k} p_m a_{k,m}}\right)}{\sum_{k=1}^{K} \mu_{k,eq}\, p_k + P_{c,eq}} \tag{2.4.7a}$$

$$\text{s.t.} \quad 0 \leq p_k \leq P_{\max,k}, \quad \forall k. \tag{2.4.7b}$$

The numerator of (2.4.7a) is non-concave in $\mathbf{p}$, making direct optimization intractable. To handle this, the objective can be expressed as a difference of two concave functions, $\mathrm{GEE}(\mathbf{p}) = g_1(\mathbf{p}) - g_2(\mathbf{p})$, where

$$g_1(\mathbf{p}) = \frac{\sum_k \log\left(d_k + \sum_m p_m a_{k,m}\right)}{\sum_i \mu_{i,eq} p_i + P_{c,eq}}, \qquad g_2(\mathbf{p}) = \frac{\sum_k \log\left(d_k + \sum_{m \neq k} p_m a_{k,m}\right)}{\sum_i \mu_{i,eq} p_i + P_{c,eq}}.$$

Letting $f_2(\mathbf{p}) \triangleq \sum_k \log\left(d_k + \sum_{m \neq k} p_m a_{k,m}\right)$, which is concave, its first-order Taylor approximation at $\bar{\mathbf{p}}$ provides a tight affine lower bound. This yields the inequality

$$\mathrm{GEE}(\mathbf{p}) \;\geq\; g_1(\mathbf{p}) - g_2(\bar{\mathbf{p}}) - \frac{\nabla f_2(\bar{\mathbf{p}})^T (\mathbf{p} - \bar{\mathbf{p}})}{\sum_i \mu_{i,eq} p_i + P_{c,eq}} \;\triangleq\; \widetilde{\mathrm{GEE}}(\mathbf{p}),$$

where the gradient components are

$$\frac{\partial f_2}{\partial p_i} = \sum_{k \neq i} \frac{a_{k,i}}{d_k + \sum_{m \neq k,i} p_m a_{k,m}}.$$

At each step of the sequential fractional programming (SFP) procedure, the problem reduces to

$$\max_{\mathbf{p}} \quad \widetilde{\mathrm{GEE}}(\mathbf{p}) \tag{2.4.8a}$$

$$\text{s.t.} \quad 0 \leq p_k \leq P_{\max,k}, \quad \forall k, \tag{2.4.8b}$$

which forms a pseudo-concave fractional program with convex constraints. This problem can be solved efficiently using Dinkelbach's algorithm, leading to the iterative power-update routine summarized in Algorithm 2.

Proposition 2.4.2. *Each iteration of Algorithm 2 either increases or preserves the value of the global energy efficiency (GEE). Consequently, the generated sequence is*

Algorithm 2 First approach — Power update via SFP

Choose $\epsilon > 0$ and a feasible initializer $\bar{\mathbf{p}} = \mathbf{p}_0$;
repeat
  Solve (2.4.8) for $\mathbf{p}$ (e.g., Dinkelbach);
  Set $\bar{\mathbf{p}} \leftarrow \mathbf{p}$;
until $\|\bar{\mathbf{p}} - \mathbf{p}\| < \epsilon$

monotonic and converges to a stationary point of Problem (2.4.7) *that satisfies the first-order optimality conditions.*

Proof. The result follows from the same line of argument used in Proposition 3.4.1. In particular, the convergence behavior is guaranteed by the fundamental properties of the sequential fractional programming (SFP) framework: (i) the surrogate functions constructed at each step are tight at the current iterate, and (ii) their gradients coincide with those of the original objective. These properties ensure monotonic improvement of the GEE value and convergence to a stationary (first-order optimal) solution. (see Appendix A.1.6.) ■

2.4.1.3 Optimization of C (Linear Detection)

When the RIS configuration γ and the transmit power vector $\mathbf{p}$ are fixed, the optimization over the receive filters $\mathbf{C} = [\mathbf{c}_1, \ldots, \mathbf{c}_K]$ influences only the numerator of the GEE objective, i.e., the aggregate sum-rate. Because the users are decoded independently, the problem separates across the K links. For each user, the optimal linear receiver that maximizes the individual SINR under colored noise conditions is given by the well-known *minimum mean-squared error* (MMSE) or Wiener filter, expressed as

$$\mathbf{c}_k^\star = \sqrt{p_k}\,\mathbf{M}_k^{-1}\mathbf{A}_k\boldsymbol{\gamma}, \qquad \mathbf{M}_k \triangleq \sum_{m\neq k} p_m\,\mathbf{A}_m\boldsymbol{\gamma}\boldsymbol{\gamma}^H\mathbf{A}_m^H + \mathbf{W}, \tag{2.4.9}$$

where $\mathbf{M}_k$ represents the interference-plus-noise covariance matrix experienced by user k, which naturally incorporates the colored noise induced by the active RIS. This formulation follows directly from the Wiener filtering criterion, and a detailed derivation together with the simplification obtained through the matrix inversion lemma is provided in Appendix A.1.1.

2.4.1.4 Overall AO–SFP Algorithm, Convergence, and Complexity

The outer loop alternates the three blocks and terminates when the GEE improvement is below a tolerance:

Algorithm 3 Solution algorithm for Problem (2.2.24)

Set tolerance $\epsilon > 0$; initialize $(\tilde{\mathbf{p}}, \tilde{\boldsymbol{\gamma}})$ to feasible values.
Compute $\mathbf{c}_k = \sqrt{p_k}\,\mathbf{M}_k^{-1}\mathbf{A}_k\boldsymbol{\gamma}$ for all k.
repeat
  $\mathrm{GEE}_{\mathrm{in}} \leftarrow \mathrm{GEE}(\tilde{\mathbf{p}}, \tilde{\boldsymbol{\gamma}}, \mathbf{C})$;
  Given $\tilde{\mathbf{p}}$, run Algorithm 1 to update $\tilde{\boldsymbol{\gamma}}$;
  Given $\tilde{\boldsymbol{\gamma}}$, run Algorithm 2 to update $\tilde{\mathbf{p}}$;
  Update $\mathbf{c}_k = \sqrt{p_k}\,\mathbf{M}_k^{-1}\mathbf{A}_k\boldsymbol{\gamma}$ for all k;
  $\mathrm{GEE}_{\mathrm{out}} \leftarrow \mathrm{GEE}(\tilde{\mathbf{p}}, \tilde{\boldsymbol{\gamma}}, \mathbf{C})$;
until $|\mathrm{GEE}_{\mathrm{out}} - \mathrm{GEE}_{\mathrm{in}}| < \epsilon$

Convergence (value) and stationarity. By Propositions 3.4.1–2.4.2 and the optimality of MMSE filters, Algorithm 3 *monotonically increases* the GEE and is *convergent in value*. Generally, AO methods do not guarantee convergence to a local optimum unless additional uniqueness conditions hold for each block update (cf. [7]); see the discussion note in the main text. We consistently observe convergence to high-quality stationary points and significant gains over local-constraint baselines.

Computational complexity. A concave-over-convex fractional program involving n real variables can be reformulated as a concave maximization problem in $n+1$ variables, solvable in polynomial-time [95]. From this observation, the computational effort needed to solve problems (2.4.6) and (2.4.8) grows roughly with $(N+1)^{\alpha}$ and $(K+1)^{\beta}$, respectively. The values of α and β typically fall between $[1, 4]$, depending on the specific convex optimization method applied [5]. The overall complexity is given by

$$\mathcal{C}_1 = \mathcal{O}\Big(I_1\big(I_{\gamma,1}(N+1)^{\alpha} + I_{p,1}(K+1)^{\beta}\big)\Big),$$

where I_1 denotes the number of outer iterations, and $I_{\gamma,1}$ and $I_{p,1}$ represent the iteration counts for the RIS and power updates, respectively.

Remark 2.4.1 (Sum-rate specialization). Replacing the fractional objective in (2.4.6a) and (2.4.8a) with their numerators (sum-rate) yields concave maximization subproblems that can be solved by standard convex programming.

2.4.2 Second proposed approach: embedded MMSE receivers

In Section 2.4.1, the problem was addressed through an iterative strategy that alternately refines three key components of the system: the RIS reflection vector $\boldsymbol{\gamma}$, the transmit power allocation $\mathbf{p}$, and the set of linear receive filters

$\mathbf{C} = [\mathbf{c}_1, \ldots, \mathbf{c}_K]$. While effective, the approach treats the receive filters as independent variables, thereby enlarging the search space and reducing the potential to exploit the problem's structural properties. In this section, we take a complementary approach by removing the explicit dependence on the receive filters and directly embedding their optimal Wiener (linear-MMSE) forms into the objective function. This reformulation reduces the decision space to the pair $(\boldsymbol{\gamma}, \mathbf{p})$ and leads to a tighter coupling with the information-theoretic nature of the system. While this modification strengthens the optimization framework and typically yields better performance, it also gives rise to a more intricate fractional program that remains tractable within the proposed solution method.

Recall that for each user k, the cascaded baseband channel seen through the RIS can be written as $\mathbf{A}_k \triangleq \mathbf{G}\mathbf{H}_k$. The corresponding noise at the BS is spatially colored and has covariance

$$\mathbf{W} \;=\; \sigma^2 \mathbf{I}_{N_R} + \sigma_{\mathrm{RIS}}^2\, \mathbf{G}\boldsymbol{\Gamma}\boldsymbol{\Gamma}^H \mathbf{G}^H \;=\; \sigma^2 \mathbf{I}_{N_R} + \sigma_{\mathrm{RIS}}^2\, \mathbf{G}\, \mathrm{diag}(\boldsymbol{\gamma}\boldsymbol{\gamma}^H)\, \mathbf{G}^H,$$

where the second equality arises from the diagonal form of $\boldsymbol{\Gamma} = \mathrm{diag}(\boldsymbol{\gamma})$. For a fixed power allocation $\mathbf{p}$, the interference–plus–noise covariance matrix associated with the detection of the k-th user stream is

$$\mathbf{M}_k \;=\; \mathbf{W} + \sum_{m \neq k} p_m\, \mathbf{A}_m \boldsymbol{\gamma}\boldsymbol{\gamma}^H \mathbf{A}_m^H.$$

If user k employs a linear receive filter $\mathbf{c}_k$, its instantaneous SINR takes the form

$$\mathrm{SINR}_k(\mathbf{c}_k) \;=\; \frac{p_k |\mathbf{c}_k^H \mathbf{A}_k \boldsymbol{\gamma}|^2}{\mathbf{c}_k^H \mathbf{M}_k \mathbf{c}_k}.$$

Maximizing this Rayleigh quotient with respect to $\mathbf{c}_k$ yields the Wiener solution. Setting $\mathbf{s}_k = \mathbf{A}_k \boldsymbol{\gamma}$ and normalizing such that $\mathbf{c}_k^H \mathbf{M}_k \mathbf{c}_k = 1$, the problem reduces to $\max_{\mathbf{c}_k} p_k |\mathbf{c}_k^H \mathbf{s}_k|^2$, whose optimum follows directly from the Cauchy–Schwarz inequality. The optimal linear MMSE receiver is therefore

$$\mathbf{c}_k^\star = \sqrt{p_k}\, \mathbf{M}_k^{-1} \mathbf{A}_k \boldsymbol{\gamma},$$

which coincides with the rigorous derivation reported in Appendix A.1.1. Substituting $\mathbf{c}_k^\star$ into the achievable rate expression, the system sum-rate can be expressed as

$$\mathrm{SR} = \sum_{k=1}^{K} \log\!\left(1 + p_k\, \mathbf{s}_k^H \mathbf{M}_k^{-1} \mathbf{s}_k\right).$$

Applying the matrix determinant lemma,

$$|\mathbf{M}_k + p_k \mathbf{s}_k \mathbf{s}_k^H| = |\mathbf{M}_k|\big(1 + p_k \mathbf{s}_k^H \mathbf{M}_k^{-1} \mathbf{s}_k\big),$$

leads to the equivalent relation

$$\log\big(1 + p_k \mathbf{s}_k^H \mathbf{M}_k^{-1} \mathbf{s}_k\big) = \log\big|\mathbf{M}_k + p_k \mathbf{s}_k \mathbf{s}_k^H\big| - \log|\mathbf{M}_k|.$$

Noting that $\mathbf{M}_k + p_k \mathbf{s}_k \mathbf{s}_k^H$ corresponds to the total covariance $\mathbf{W} + \sum_{m=1}^{K} p_m \mathbf{A}_m \boldsymbol{\gamma}\boldsymbol{\gamma}^H \mathbf{A}_m^H$, whereas $\mathbf{M}_k$ excludes the k-th term, summing across all users yields the exact log–det representation

$$\mathrm{SR}_{\mathrm{MMSE}} = \sum_{k=1}^{K} \log\Big|\mathbf{W} + \textstyle\sum_{m=1}^{K} p_m \mathbf{A}_m \boldsymbol{\gamma}\boldsymbol{\gamma}^H \mathbf{A}_m^H\Big| - \sum_{k=1}^{K} \log\big|\mathbf{W} + \textstyle\sum_{m\neq k} p_m \mathbf{A}_m \boldsymbol{\gamma}\boldsymbol{\gamma}^H \mathbf{A}_m^H\big|\,. \tag{2.4.10}$$

Equation (2.4.10) is an exact closed-form expression that requires no approximation and entirely removes the receive-filter variables from the optimization. Embedding the MMSE receivers in this way reduces the dimensionality of the alternating procedure and results in a tighter, more efficient optimization framework, a point that will be confirmed by the numerical analysis presented later.

Having embedded the MMSE receivers into the rate expression, we now set up the energy–efficiency maximization under the active-RIS power model of Sec. 2.2.2. An active surface reflects the incident field and draws extra power through reflection-type amplifiers and control circuits. Accordingly, the total power consumption includes three components: (i) the net RF energy supplied by the surface amplifiers, (ii) the transmit powers of the users, scaled by their respective amplifier inefficiencies, and (iii) the static hardware consumption associated with the base station and the RIS control circuitry. Formally, for given $(\boldsymbol{\gamma}, \mathbf{p})$,

$$P_{\mathrm{tot}}(\boldsymbol{\gamma}, \mathbf{p}) = \mathrm{tr}\Big(\big(\boldsymbol{\gamma}\boldsymbol{\gamma}^H - \mathbf{I}_N\big)\,\mathbf{R}(\mathbf{p})\Big) + \sum_{k=1}^{K} \mu_k p_k + P_c, \qquad \mathbf{R}(\mathbf{p}) = \sum_{k=1}^{K} p_k \mathbf{H}_k^H \mathbf{H}_k + \sigma_{\mathrm{RIS}}^2 \mathbf{I}_N,$$

where $\mathbf{R}(\mathbf{p})$ collects the spatial covariance of the field impinging on the RIS (user signals plus amplifier noise). The first term is the *incremental* RF draw: it vanishes when $|\gamma_n| = 1$ for all n, recovering purely reflective operation. The second term accounts for PA inefficiencies ($\mu_k \geq 1$), and P_c groups static costs.

The global energy efficiency (GEE) problem is a fractional program

$$\max_{\boldsymbol{\gamma},\mathbf{p}} \quad \frac{\mathrm{SR}_{\mathrm{MMSE}}(\boldsymbol{\gamma},\mathbf{p})}{\mathrm{tr}\big((\boldsymbol{\gamma}\boldsymbol{\gamma}^H-\mathbf{I}_N)\mathbf{R}(\mathbf{p})\big)+\sum_{k=1}^{K}\mu_k p_k+P_c} \tag{2.4.11a}$$

$$\text{s.t.} \quad \mathrm{tr}(\mathbf{R}(\mathbf{p})) \le \mathrm{tr}(\mathbf{R}(\mathbf{p})\boldsymbol{\gamma}\boldsymbol{\gamma}^H) \le \mathrm{tr}(\mathbf{R}(\mathbf{p})) + P_{R,\max}, \tag{2.4.11b}$$

$$0 \le p_k \le P_{max,k}, \quad k=1,\dots,K. \tag{2.4.11c}$$

Constraint (2.4.11b) enforces the global power balance at the surface: the reflected power cannot be smaller than the impinging power in the active regime and cannot exceed it by more than the amplifier budget $P_{R,\max}$. The nearly-passive specialization is obtained by setting $\sigma^2_{\mathrm{RIS}}=0$ and $P_{R,\max}=0$, which reduces (2.4.11b) to $\mathrm{tr}(\mathbf{R}\boldsymbol{\gamma}\boldsymbol{\gamma}^H) \le \mathrm{tr}(\mathbf{R})$ (with equality holding whenever $|\gamma_n|=1$ for all n).

Problem (2.4.11) is non-convex for two reasons: $\mathrm{SR}_{\mathrm{MMSE}}(\boldsymbol{\gamma},\mathbf{p})$ is not concave in either block, as it involves log–det differences coupled through bilinear terms and the feasibility band couples $\boldsymbol{\gamma}$ and $\mathbf{p}$ through $\mathbf{R}(\mathbf{p})$. We therefore adopt a block-alternating scheme. The troublesome numerator is replaced at each step by a concave, first-order-tight surrogate at the current iterate (which belongs to the class of *sequential fractional programming* (SFP) methods). This guarantees a non-decreasing GEE sequence and reduces each block to a pseudo-concave fractional problem solvable to global optimality (e.g., by Dinkelbach's method). All technical details of the surrogate construction, including the gradient expressions of the concave parts, are provided in Appendix A.1.6.

2.4.2.1 RIS update via lifting and sequential fractional programming

By keeping the transmit power vector $\mathbf{p}$ fixed, the optimization with respect to the RIS reflection vector $\boldsymbol{\gamma}$ can be reformulated through a *lifting* technique. In this formulation, we introduce a Hermitian positive semidefinite matrix that captures the quadratic structure of the reflection coefficients, defined as

$$\mathbf{X} \triangleq \boldsymbol{\gamma}\boldsymbol{\gamma}^H \succeq \mathbf{0}, \qquad \mathrm{rank}(\mathbf{X})=1,$$

which linearizes the otherwise bilinear dependence on $\boldsymbol{\gamma}$. Since $\mathrm{diag}(\mathbf{X})$ is an affine function of $\mathbf{X}$, this substitution allows the colored noise covariance to be expressed as

$$\mathbf{W}(\mathbf{X}) = \sigma^2\mathbf{I}_{N_R} + \sigma^2_{\mathrm{RIS}}\,\mathbf{G}\,\mathrm{diag}(\mathbf{X})\,\mathbf{G}^H.$$

Substituting this form into the MMSE-embedded rate expression (2.4.10) gives

$$\mathrm{SR}_{\mathrm{MMSE}}(\mathbf{X}) = \underbrace{\sum_{k=1}^{K} \log\left|\sigma^2\mathbf{I}_{N_R} + \sigma^2_{\mathrm{RIS}}\mathbf{G}\,\mathrm{diag}(\mathbf{X})\mathbf{G}^H + \sum_{m=1}^{K} p_m\mathbf{A}_m\mathbf{X}\mathbf{A}_m^H\right|}_{\triangleq F_1(\mathbf{X})} - \underbrace{\sum_{k=1}^{K} \log\left|\sigma^2\mathbf{I}_{N_R} + \sigma^2_{\mathrm{RIS}}\mathbf{G}\,\mathrm{diag}(\mathbf{X})\mathbf{G}^H + \sum_{m\neq k} p_m\mathbf{A}_m\mathbf{X}\mathbf{A}_m^H\right|}_{\triangleq F_2(\mathbf{X})}. \tag{2.4.12}$$

Both F_1 and F_2 are concave in $\mathbf{X}$, since they are compositions of the concave $\log|\cdot|$ function with affine matrix mappings. When the power allocation is fixed, the RIS subproblem becomes

$$\max_{\mathbf{X}\succeq\mathbf{0}} \quad \frac{F_1(\mathbf{X}) - F_2(\mathbf{X})}{\mathrm{tr}(\mathbf{R}\mathbf{X}) + P_{c,eq}} \tag{2.4.13a}$$

$$\text{s.t.} \quad \mathrm{tr}(\mathbf{R}) \le \mathrm{tr}(\mathbf{R}\mathbf{X}) \le \mathrm{tr}(\mathbf{R}) + P_{R,\max}, \tag{2.4.13b}$$

where $\mathbf{R}$ is constant in this step and $P_{c,eq} = \sum_k \mu_k p_k + P_c - \mathrm{tr}(\mathbf{R})$. As indicated above, objective numerator in (2.4.13a) is a difference of concave functions making it non-concave overall.

Lemma 2.4.1 (Concave surrogate for F_2)**.** *Let $\bar{\mathbf{X}}$ be a feasible point of* (2.4.13)*. Then $F_2(\mathbf{X})$ satisfies the affine majorization*

$$F_2(\mathbf{X}) \;\le\; F_2(\bar{\mathbf{X}}) + \Re\Big\{\,\mathrm{tr}\big(\nabla F_2(\bar{\mathbf{X}})^H(\mathbf{X}-\bar{\mathbf{X}})\big)\Big\},$$

where the gradient is given by

$$\nabla F_2(\bar{\mathbf{X}}) = \sum_{k=1}^{K}\left(\sigma^2_{RIS}\big(\mathbf{G}^H\bar{\mathbf{T}}_k^{-1}\mathbf{G}\big)\odot\mathbf{I}_N + \sum_{m\neq k} p_m\mathbf{A}_m^H\bar{\mathbf{T}}_k^{-1}\mathbf{A}_m\right),$$

with

$$\bar{\mathbf{T}}_k = \sigma^2\mathbf{I}_{N_R} + \sigma^2_{RIS}\mathbf{G}\,\mathrm{diag}(\bar{\mathbf{X}})\mathbf{G}^H + \sum_{m\neq k} p_m\mathbf{A}_m\bar{\mathbf{X}}\mathbf{A}_m^H.$$

Proof. Since F_2 is concave, the right-hand side corresponds to its first-order Taylor expansion, which globally upper-bounds F_2. The explicit gradient follows standard matrix differential identities applied to log–det functions. ■

Algorithm 4 RIS update via lifting and SFP (Second approach)

Input: Powers $\mathbf{p}$, tolerance $\epsilon > 0$.
Initialize $\bar{\mathbf{X}} \succeq \mathbf{0}$ feasible for (2.4.14b).
repeat
  Solve (2.4.14) for $\mathbf{X}^\star$ (e.g., by Dinkelbach).
  $\Delta \leftarrow \|\mathbf{X}^\star - \bar{\mathbf{X}}\|_F$; $\bar{\mathbf{X}} \leftarrow \mathbf{X}^\star$.
until $\Delta < \epsilon$
if $\mathrm{rank}(\bar{\mathbf{X}}) > 1$ **then**
  Apply rank reduction (e.g., randomization) to obtain $\boldsymbol{\gamma}$ with $\boldsymbol{\gamma}\boldsymbol{\gamma}^H \approx \bar{\mathbf{X}}$.
else
  Extract $\boldsymbol{\gamma}$ from the principal eigenvector of $\bar{\mathbf{X}}$.
Output: Updated RIS vector $\boldsymbol{\gamma}$.

Applying Lemma 2.4.1, the achievable rate satisfies

$$\mathrm{SR}_{\mathrm{MMSE}}(\mathbf{X}) \geq \widetilde{\mathrm{SR}}_{\mathrm{MMSE}}(\mathbf{X};\bar{\mathbf{X}}) = F_1(\mathbf{X}) - \Big(F_2(\bar{\mathbf{X}}) + \Re\{\mathrm{tr}(\nabla F_2(\bar{\mathbf{X}})^H(\mathbf{X}-\bar{\mathbf{X}}))\}\Big),$$

which is concave in $\mathbf{X}$. Hence, each sequential fractional programming (SFP) iteration solves

$$\max_{\mathbf{X}\succeq\mathbf{0}} \quad \frac{\widetilde{\mathrm{SR}}_{\mathrm{MMSE}}(\mathbf{X};\bar{\mathbf{X}})}{\mathrm{tr}(\mathbf{R}\mathbf{X}) + P_{c,eq}} \tag{2.4.14a}$$

$$\text{s.t.} \quad \mathrm{tr}(\mathbf{R}) \leq \mathrm{tr}(\mathbf{R}\mathbf{X}) \leq \mathrm{tr}(\mathbf{R}) + P_{R,\max}, \tag{2.4.14b}$$

a pseudo-concave fractional problem, since its numerator is concave, the denominator is affine and positive, and the feasible set is convex. Such problems admit globally optimal solutions using fractional programming techniques such as Dinkelbach's algorithm.[3] Finally, because the rank constraint $\mathrm{rank}(\mathbf{X}) = 1$ is non-convex, we employ a standard semidefinite relaxation (SDR). The relaxed problem (2.4.14) is solved first; if the resulting matrix $\mathbf{X}^\star$ has rank one, the exact optimum is recovered. Otherwise, a feasible $\boldsymbol{\gamma}$ can be reconstructed through Gaussian randomization or eigenvector-based rank reduction, as detailed in Appendix A.1.7.

Proposition 2.4.3 (Convergence of RIS update)**.** *Algorithm 4 produces a non-decreasing sequence of GEE values and converges in terms of the objective function. If the limiting point $\bar{\mathbf{X}}$ is rank one, the corresponding vector $\boldsymbol{\gamma}$ obtained from $\bar{\mathbf{X}}$ constitutes a first-order stationary solution of the RIS subproblem* (2.4.13).

[3] Each inner Dinkelbach iteration reduces to a concave maximization problem, which can be efficiently tackled by standard convex solvers.

Proof. According to Lemma 2.4.1, the surrogate formulation in (2.4.14) is both tight at the current point $\bar{\mathbf{X}}$ and consistent in gradient with the original non-concave objective. These two properties meet the essential requirements of the SFP framework, which ensures that each iteration produces a non-decreasing GEE value and that the sequence of objective values converges. Additionally, when the limiting matrix $\bar{\mathbf{X}}$ is of rank one, the relationship $\mathbf{X} = \boldsymbol{\gamma}\boldsymbol{\gamma}^H$ guarantees that the recovered $\boldsymbol{\gamma}$ satisfies the first-order stationarity conditions of the original RIS optimization problem. ■

2.4.2.2 Power update via sequential fractional programming

When the RIS vector $\boldsymbol{\gamma}$ is fixed, the MMSE-embedded sum-rate (2.4.10) reduces to a function of the user transmit powers $\mathbf{p}$. This dependence is nonlinear, and the numerator of the GEE objective is not concave in $\mathbf{p}$. To make the problem tractable, we exploit the *difference-of-concave* (DC) structure.

Define

$$\mathrm{SR}_{\mathrm{MMSE}}(\mathbf{p}) = G_1(\mathbf{p}) - G_2(\mathbf{p}),$$

with

$$G_1(\mathbf{p}) = \sum_{k=1}^{K} \log \left| \mathbf{W} + \sum_{m=1}^{K} p_m \mathbf{A}_m \boldsymbol{\gamma}\boldsymbol{\gamma}^H \mathbf{A}_m^H \right|,$$

$$G_2(\mathbf{p}) = \sum_{k=1}^{K} \log \left| \mathbf{W} + \sum_{m \neq k} p_m \mathbf{A}_m \boldsymbol{\gamma}\boldsymbol{\gamma}^H \mathbf{A}_m^H \right|.$$

Both G_1 and G_2 are concave in $\mathbf{p}$, hence $\mathrm{SR}_{\mathrm{MMSE}}$ is DC.

Lemma 2.4.2 (Affine majorization of G_2)**.** *Let $\bar{\mathbf{p}}$ be any feasible power vector. Then $G_2(\mathbf{p})$ admits the affine upper bound*

$$G_2(\mathbf{p}) \;\leq\; G_2(\bar{\mathbf{p}}) + \nabla G_2(\bar{\mathbf{p}})^\top (\mathbf{p} - \bar{\mathbf{p}}),$$

where the gradient entries are

$$\left[\nabla G_2(\bar{\mathbf{p}})\right]_i = \sum_{k \neq i} \mathrm{tr}\left(\left(\mathbf{W} + \sum_{m \neq k} \bar{p}_m \mathbf{A}_m \boldsymbol{\gamma}\boldsymbol{\gamma}^H \mathbf{A}_m^H \right)^{-1} \mathbf{A}_i \boldsymbol{\gamma}\boldsymbol{\gamma}^H \mathbf{A}_i^H \right), \qquad i = 1, \ldots, K.$$

Proof. Since G_2 is concave, its first-order Taylor approximation evaluated at $\bar{\mathbf{p}}$ always serves as a global upper bound for the function. The gradient expression follows directly from applying the matrix derivative rule

Algorithm 5 Second approach — Power update with SFP

Input: RIS vector γ, tolerance $\epsilon > 0$. Initialize feasible $\bar{\mathbf{p}}$.
repeat
Solve (2.4.15) for $\mathbf{p}^\star$ (e.g., Dinkelbach + convex solver).
$\Delta \leftarrow \|\mathbf{p}^\star - \bar{\mathbf{p}}\|_2$; $\bar{\mathbf{p}} \leftarrow \mathbf{p}^\star$.
until $\Delta < \epsilon$
Output: Updated power vector $\mathbf{p}$.

$\nabla_x \log|\mathbf{M}(x)| = \mathrm{tr}\big(\mathbf{M}(x)^{-1}\nabla_x \mathbf{M}(x)\big)$ to the affine matrix argument inside the logarithm. ■

Applying Lemma 2.4.2, the MMSE sum-rate satisfies

$$\mathrm{SR}_{\mathrm{MMSE}}(\mathbf{p}) \;\geq\; \widetilde{\mathrm{SR}}_{\mathrm{MMSE}}(\mathbf{p};\bar{\mathbf{p}}) = G_1(\mathbf{p}) - \Big(G_2(\bar{\mathbf{p}}) + \nabla G_2(\bar{\mathbf{p}})^\top(\mathbf{p}-\bar{\mathbf{p}})\Big),$$

where $\widetilde{\mathrm{SR}}_{\mathrm{MMSE}}(\mathbf{p};\bar{\mathbf{p}})$ is concave in $\mathbf{p}$.

Let the denominator be

$$D(\mathbf{p}) = \sum_{k=1}^{K} \mu_{k,eq} p_k + P_{c,eq},$$

with

$$\mu_{k,eq} = \mu_k - \|\mathbf{h}_k\|^2 + \|\mathbf{H}_k\gamma\|^2, \qquad P_{c,eq} = \sigma_{\mathrm{RIS}}^2(\|\gamma\|^2 - N) + P_c.$$

Since $D(\mathbf{p})$ is affine and positive, the power subproblem at each iteration of SFP is

$$\max_{\mathbf{p}} \quad \frac{\widetilde{\mathrm{SR}}_{\mathrm{MMSE}}(\mathbf{p};\bar{\mathbf{p}})}{D(\mathbf{p})} \tag{2.4.15a}$$

$$\text{s.t.} \quad 0 \leq p_k \leq P_{\max,k}, \qquad k = 1,\ldots,K. \tag{2.4.15b}$$

Problem (2.4.15) constitutes a pseudo-concave fractional program, where the surrogate numerator is concave, the denominator is positive and affine, and the feasible region is convex. As a result, each SFP iteration can attain the global optimum efficiently by employing Dinkelbach's algorithm.

Proposition 2.4.4 (Convergence of power update)**.** *Algorithm 5 generates a sequence of GEE values that is monotonically non-decreasing and convergent. The limiting point reached by the algorithm satisfies the first-order optimality conditions of the power subproblem* (2.4.15)*.*

Proof. The approximation used in (2.4.15) remains locally tight and preserves the gradient of the original objective at the reference point $\bar{\mathbf{p}}$. These features meet the requirements of the sequential fractional programming framework, which guarantees that each iteration produces an improvement (or leaves the value unchanged) in the objective function. Because every fractional subproblem is solved to global optimality, the sequence of objective values converges, and the final iterate naturally satisfies the first-order optimality conditions of the original power optimization problem. ■

2.4.2.3 Overall procedure, convergence, and complexity

The embedded-MMSE algorithm alternates between optimizing the RIS coefficients (Algorithm 4) and updating the transmit powers (Algorithm 5). At each outer iteration, one variable block is optimized while the other remains fixed, and each subproblem is solved to global optimality within its concave surrogate through sequential fractional programming. As a result, the global energy efficiency (GEE) value obtained at each iteration never decreases. Because the GEE is naturally upper-bounded by system limitations such as finite bandwidth and transmit power budgets, the sequence of objective values generated by the algorithm is guaranteed to converge. Let $\{J^{(t)}\}$ denote the sequence of GEE values produced by Algorithm 6. Then, for all iterations t,

$$J^{(t+1)} \geq J^{(t)},$$

with $\{J^{(t)}\}$ converging to a finite limit point $J^{\star}$. It is also important to note that, while the alternating structure does not guarantee global optimality due to the inherent non-convexity of Problem (2.4.11), it does ensure a monotonic improvement and convergence in the objective value. The final point reached by the algorithm satisfies the first-order optimality conditions of the embedded-MMSE GEE maximization problem. The computational complexity of the overall framework can be expressed as

$$\mathcal{C}_2 = \mathcal{O}\Big(I_2\big(I_{\gamma,2}(N+1)^{\alpha} + I_{p,2}(K+1)^{\beta}\big)\Big),$$

where I_2 is the number of outer iterations, $I_{\gamma,2}$ and $I_{p,2}$ are the iteration counts for the RIS and power updates, and $\alpha, \beta \in [1,4]$ describe the polynomial order of the inner convex solvers.[4]

[4] As discussed in Sec. 2.4.1.4, these exponents depend on the chosen solver type (e.g., interior-point versus first-order methods) and on the sparsity of the optimization structure. In practice, the number of iterations reported in Table 2.5.3 remains modest, confirming that the method is computationally practical.

Algorithm 6 GEE maximization with embedded MMSE (overall procedure)

Input: Feasible initialization $(\tilde{\gamma}, \tilde{\mathbf{p}})$; tolerance $\epsilon > 0$.
repeat
  $J_{\text{in}} \leftarrow \text{GEE}(\tilde{\gamma}, \tilde{\mathbf{p}})$.
  RIS step: Run Algorithm 4 with $\mathbf{p} = \tilde{\mathbf{p}}$ to obtain $\tilde{\gamma}$.
  Power step: Run Algorithm 5 with $\gamma = \tilde{\gamma}$ to obtain $\tilde{\mathbf{p}}$.
  $J_{\text{out}} \leftarrow \text{GEE}(\tilde{\gamma}, \tilde{\mathbf{p}})$.
until $|J_{\text{out}} - J_{\text{in}}| < \epsilon$
Post-processing: Compute MMSE filters $\mathbf{c}_k^\star = \sqrt{p_k}\,\mathbf{M}_k^{-1}\mathbf{A}_k\gamma$ for all k.

The complete algorithm is summarized in Algorithm 6. After both the RIS and power variables have been optimized, the corresponding MMSE receive filters are recovered in closed form from (2.4.9), preserving the consistency between the embedded formulation and the original system model.

Proposition 2.4.5 (Convergence of Algorithm 6)**.** *The GEE values obtained through Algorithm 6 form a monotonically increasing sequence that converges to a finite limit. At convergence, the pair* $(\gamma^\star, \mathbf{p}^\star)$ *fulfills the first-order stationarity conditions of Problem* (2.4.11)*. Additionally, the MMSE receive filters* $\mathbf{c}_k^\star$ *calculated in the final stage are fully compatible with the embedded formulation, ensuring that the algorithm's results align with the original signal model.*

Remark 2.4.2 (Sum-rate specialization). If the denominator terms in (2.4.14a) and (2.4.15a) are omitted, Algorithm 6 specializes to the case of sum-rate maximization under global reflection constraints. In this scenario, each subproblem features a concave objective with affine constraints and can therefore be solved to global optimality using standard convex optimization techniques.

2.5 Numerical Results

This section provides an in-depth numerical evaluation of the proposed global energy efficiency (GEE) optimization frameworks, considering both single-user and multi-user uplink scenarios. The numerical simulations follow the system and channel models detailed in Sections 2.2–2.2.1, which account for distance-dependent path loss, Rician block fading, and the global reflection behavior of the RIS.

Unless otherwise stated, each reported value represents an average over a large number of independent realizations of small-scale fading and randomly generated user positions within the coverage area. This approach

ensures statistical reliability of the presented results. Also, the iterative algorithms are initialized using the *random RIS configuration and uniform power allocation* schemes, which guarantee feasibility while avoiding bias toward specific channel conditions. In selected cases, a *warm-start strategy* is also employed, using the converged solution from a previous setup as the starting point to accelerate convergence.

Two representative scenarios are examined. First, a single-user configuration isolates the inherent effects of global reflection and highlights the fundamental differences between global and local reflection models regarding received SNR, achievable rate, and overall energy efficiency. This baseline eliminates multi-user interference and clarifies the physical implications of global reflection in a controlled setting. The second scenario analyzed involves a multi-user uplink, where multiple users communicate with a multi-antenna base station through an RIS. This setup creates an interference-limited environment, serving as a realistic testbed to evaluate the convergence, scalability, and performance of the resource allocation algorithms (Algorithms 3–6). The parameters used in the simulation are outlined in Table 2.5.1. In addition, the noise power over the system bandwidth B is given by

$$P_{\mathrm{n}} = N_0 B \times \mathrm{NF}, \tag{2.5.1}$$

where $N_0 = -174$ dBm/Hz denotes the thermal noise power spectral density at room temperature, and NF is the receiver noise figure, which accounts for both thermal and circuit-related contributions. We also modeled the large-scale fading as

$$L(d) = \beta_0 \left(\frac{d}{d_0} \right)^{-n}, \tag{2.5.2}$$

where d is the propagation distance, d_0 the reference distance, β_0 the path-loss at d_0, and n the path-loss exponent. Distinct path-loss exponents are used for the user–RIS and RIS–BS links in the single-user scenario, while a common exponent η is adopted in the multi-user case. Small-scale fading follows a block Rician model. In line with typical deployment layouts, the RIS–BS link is characterized by a stronger line-of-sight (LoS) component than the user–RIS links, with Rician factors $(K_t, K_r) = (4, 2)$. This asymmetry accounts for the fixed, mutually visible positions of the RIS and BS in contrast to mobile users affected by shadowing. It is worth noting, however, that the RIS–BS channel is not constrained to be purely LoS and may display a higher effective rank depending on the propagation environment.

TABLE 2.5.1: Simulation parameters for single-user and multi-user scenarios.

Parameter	Single-User	Multi-User
Setup	$K = 1$, $N_R = 1$, $N = 100$	$K = 4$, $N_R = 4$, $N = 100$
Bandwidth	$B = 20\,\text{MHz}$	$B = 20\,\text{MHz}$
Noise	$-174\,\text{dBm/Hz}$, NF$= 5\,\text{dB}$	$-174\,\text{dBm/Hz}$, NF$= 10\,\text{dB}$
Topology	RIS–BS 50 m; user $\leq 30\,\text{m}$ from RIS; heights: user $[0, 2.5]$ m, RIS 10 m, BS 10 m	RIS–BS 50 m; users $\leq 100\,\text{m}$ from RIS; heights: users $[0, 5]$ m, RIS 15 m, BS 10 m
Path-loss	$n_h = 4$ (UE$\rightarrow$RIS), $n_g = 2$ (RIS$\rightarrow$BS)	$\eta = 4$ (unless varied)
Rician	$K_t = 4$, $K_r = 2$	$K_t = 4$, $K_r = 2$; also $K_t = K_r \in \{2, 4\}$
RIS type	Nearly-passive (global)	Active / Nearly-passive (global); local (unit-modulus) baseline
Active RIS power	–	$P_{R,\max} = 10\,\text{dBW}$; $P_{0,\text{RIS}}^{(a)} = 30\,\text{dBm}$; $P_{c,n}^{(a)} = 20\,\text{dBm}$ (swept)
Passive RIS power	$P_{0,\text{RIS}}^{(p)} = 20\,\text{dBm}$; $P_{c,n}^{(p)} = 0\,\text{dBm}$	$P_{0,\text{RIS}}^{(p)} = 20\,\text{dBm}$; $P_{c,n}^{(p)} = 0\,\text{dBm}$
Other static	$P_0 = 40\,\text{dBm}$	$P_0 = 40\,\text{dBm}$
Algorithms	SNR/EE/SE global vs. local	Alg. 2.1, Alg. 2.2; sum-rate variants

2.5.1 Single-User Insights: Global versus Local Reflection

To build intuition before addressing the multi-user setting, we first isolate the single-user case with $K = 1$ and $N_R = 1$. This simplified configuration removes the effect of multi-user interference and allows us to directly quantify the physical gains afforded by global reflection in comparison with the conventional local (unit-modulus) model. Unless otherwise specified, the simulation parameters follow Table 2.5.1.

Energy efficiency and spectral efficiency versus transmit budget. Figures 2.5.5 and 2.5.2 illustrate the behavior of the global energy efficiency (GEE) and spectral efficiency (SE) as functions of the maximum user transmit power $P_{t,\max}$. As anticipated, the GEE initially rises with increasing transmit

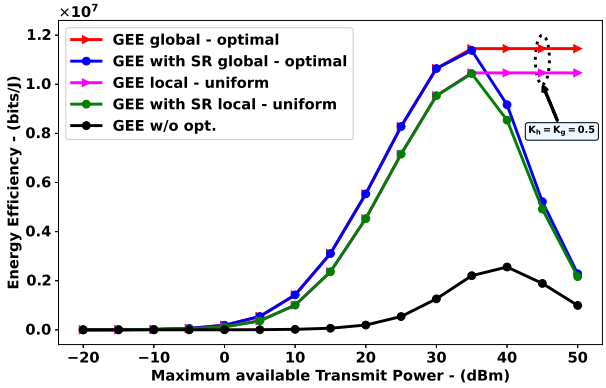

FIGURE 2.5.1: Achieved GEE versus $P_{t,\max}$. Single-user case with K=1, N_R=1, N=100, n_h=4, n_g=2.

power but eventually reaches a plateau, reflecting the well-known unimodal nature of energy efficiency: once the transmit power exceeds a certain threshold, additional power primarily increases consumption without yielding a comparable gain in rate. By contrast, the SE grows monotonically with $P_{t,\max}$. In both cases, the configuration based on global reflection provides consistently higher performance than the local model. This advantage stems from the relaxed feasibility region of the global constraint, which treats the RIS as a single energy-balanced surface rather than a collection of independent unit-modulus elements. This means that it allows for the flexible redistribution of reflection amplitudes across surface elements, enabling the RIS to better adapt to variations in cascaded channel gains. The results obtained under practical propagation conditions align with the theoretical analysis in Section 2.3.

SNR gain versus Rician factor. The SNR gain factor η, defined in (2.3.12), is depicted in Figure 2.5.3 and measures the ratio of achievable SNR between global and local reflection in relation to the Rician factor. The simulations indicate that the benefits of global reflection are most apparent at low Rician factors, where multipath fading causes greater variability among the RIS elements. In this regime, the cascaded magnitudes $\{z_n\}$ are highly uneven, and the global reflection model can reallocate amplitude toward the dominant components, enhancing the overall received power. As the Rician factor increases, the channel magnitudes become more uniform and the propagation tends toward a deterministic LoS condition; consequently, the relative benefit of global reflection diminishes and η approaches unity.

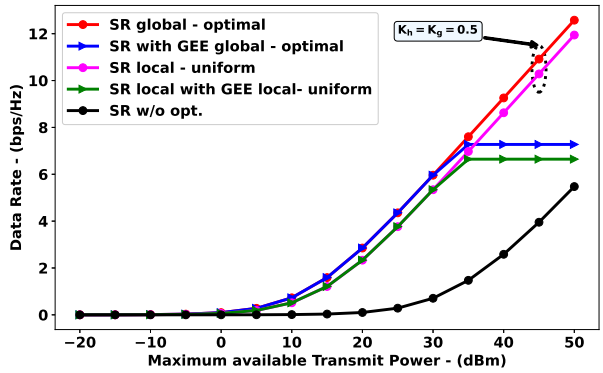

FIGURE 2.5.2: Achieved spectral efficiency (SE) versus $P_{t,\max}$. Same setup as Fig. 2.5.5.

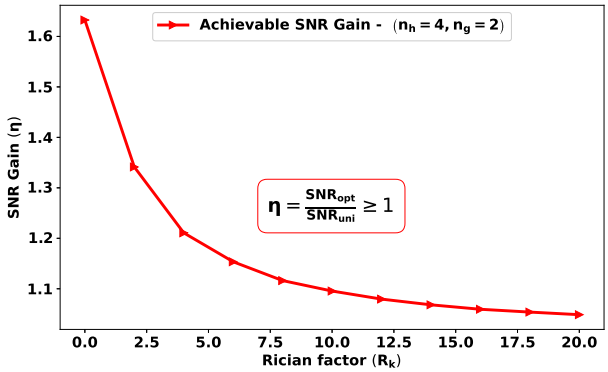

FIGURE 2.5.3: SNR gain η (§2.3) versus Rician factor K. $K = 1$, $N_R = 1$, $N = 100$, $P_{t,\max} = 40$ dBm.

These findings fully agree with the majorization-based theoretical analysis presented in Section 2.3.

Impact of RIS placement. Figure 2.5.4 illustrates the impact of RIS placement along the BS–UE axis on the overall system performance. Two operational regimes can be clearly distinguished. When the user–RIS link is subject to stronger attenuation, positioning the RIS closer to the user helps counteract the higher path-loss and leads to a noticeable improvement in energy efficiency. Conversely, when the RIS–BS link dominates the total attenuation, placing the surface nearer to the BS leads to better performance.

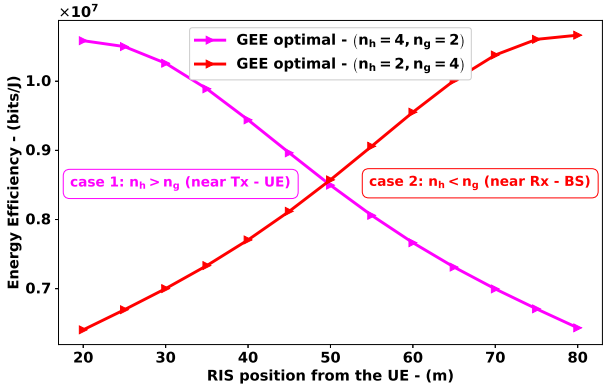

FIGURE 2.5.4: Achieved GEE versus RIS position x_{ris} along the BS–UE axis. $K = 1$, $N_R = 1$, $N = 100$, $P_{t,\max} = 40\,\text{dBm}$.

The observed trend arises from how the two path-loss components, L_{UR} and L_{RB}, combine multiplicatively, as noted in Remark 2.2.2. Hence, the best placement of the RIS cannot be described by a fixed geometric proportion; it varies according to the relative propagation behaviour of the two links. Furthermore, the global reflection model increases this adaptability: by redistributing reflection amplitudes across the surface, the RIS can dynamically adjust to different placements, thereby enlarging the performance advantage over the local reflection scheme.

To conclude, the single-user study indicates that RISs governed by global reflection constraints achieve superior performance compared with those restricted by local rules, regardless of the transmit power range, fading environment, or deployment geometry. The benefit of global reflection is most evident under challenging conditions—such as channels with small Rician factors or unbalanced path-loss, where traditional RIS designs tend to lose efficiency. The results closely align with the theoretical insights presented in Section 2.3 and offer practical recommendations for configuring and placing RISs in real-world systems.

2.5.2 Multi-User Results: Active versus Nearly-Passive RIS

We now focus on the multi-user uplink scenario with $K = 4$ users, $N_R = 4$ receive antennas at the base station, and a reconfigurable intelligent surface (RIS) consisting of $N = 100$ reflecting elements, as detailed in Table 2.5.1. The goal here is to evaluate and compare the two proposed optimization

strategies: Algorithm 3, which relies on alternating optimization, and Algorithm 6, which embeds the MMSE receiver design under both active and nearly-passive RIS operation, while enforcing the global reflection constraint.

Unless noted otherwise, all results represent averages over many random realizations of user positions and Rician fading conditions.

Energy and spectral efficiency versus transmit power. Figures 2.5.5 and 2.5.6 show how the global energy efficiency (GEE) and spectral efficiency (SE) vary with the maximum per-user transmit power $P_{\max}$. Five strategies are examined: (a) Algorithm 3 optimized for GEE, (b) Algorithm 6 optimized for GEE, (c) Algorithm 3 optimized for sum-rate, (d) Algorithm 6 optimized for sum-rate, and (e) a baseline with uniform power allocation and random RIS phases.

The results point to several trends. Algorithm 6 achieves higher efficiency than Algorithm 3, showing that embedding the MMSE structure directly in the optimization strengthens the interaction between transmission and reception. Both GEE-oriented methods (a) and (b) also deliver clear gains over the baseline (e), highlighting the benefit of jointly optimizing transmit powers, RIS coefficients, and receive filters. When sum-rate maximization is used instead, the achievable data rate improves, but at the cost of noticeably lower energy efficiency as $P_{\max}$ increases. This outcome demonstrates the non-linear behavior of the GEE. Once the transmit power exceeds a specific threshold, the increase in energy consumption outweighs the improvements in data rate, resulting in a plateau in efficiency.

The flattening of the GEE curves at high $P_{\max}$ indicates the operational limit, beyond which any further increases in power yield minimal benefits.

Active versus nearly-passive RISs. Figure 2.5.7 compares the global energy efficiency achieved by active and nearly-passive RISs using Algorithm 6. The analysis varies the per-element static consumption $P_{c,n}^{(a)}$ of active elements, while the passive case is fixed at $P_{c,n}^{(p)} = 0\,\text{dBm}$. When the static cost $P_{c,n}^{(a)}$ is low, active RISs provide clear advantages by compensating for the double-fading loss through analog amplification. As $P_{c,n}^{(a)}$ increases, however, the additional circuit power gradually offsets these gains, and the nearly-passive configuration becomes more energy-efficient. As the number of reflecting elements N grows, the point at which active and nearly-passive RISs achieve the same efficiency shifts to lower values of $P_{c,n}^{(a)}$. This behavior is intuitive: larger surfaces require a greater number of active components, which in turn raises the overall static power consumption. A comparable

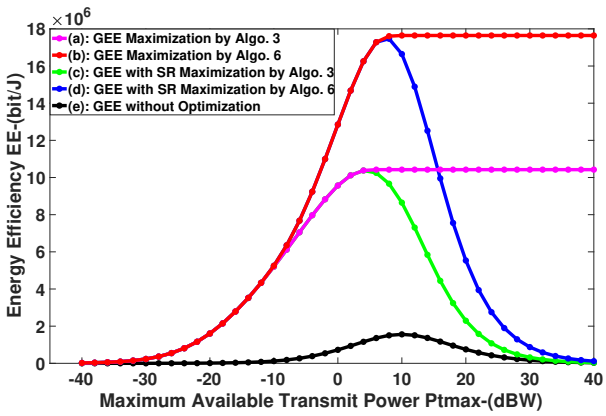

FIGURE 2.5.5: Achieved GEE versus $P_{\max}$ in the multi-user setting (K=4, N_R=4, N=100, B=20 MHz). Curves compare: (a) Alg. 3 (GEE-max), (b) Alg. 6 (GEE-max with embedded MMSE), (c) Alg. 3 (sum-rate max), (d) Alg. 6 (sum-rate max), and (e) uniform power + random RIS phases.

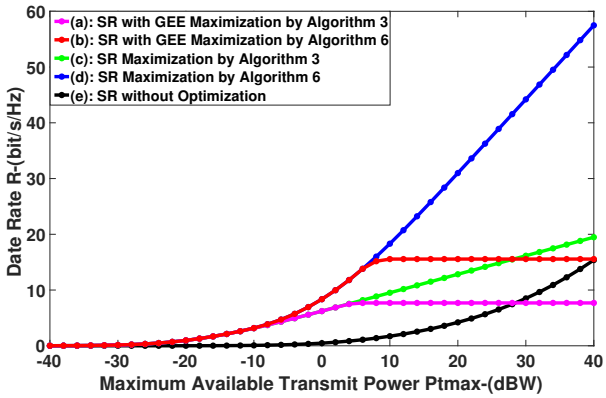

FIGURE 2.5.6: Achieved spectral efficiency versus $P_{\max}$ (K=4, N_R=4, N=100, B=20 MHz). Same schemes as Fig. 2.5.5.

pattern is observed in Figure 2.5.8. When $P_{c,n}^{(a)}$ is fixed, the energy efficiency of active RISs shows a gradual drop as the number of reflecting elements N increases. In comparison, nearly-passive configurations maintain a steadier performance as the array grows. From a design standpoint, active RISs are generally preferable for medium-sized deployments or in scenarios where efficient, low-power amplifiers can be used. In contrast, nearly-passive surfaces become more suitable for larger installations, where low circuit power

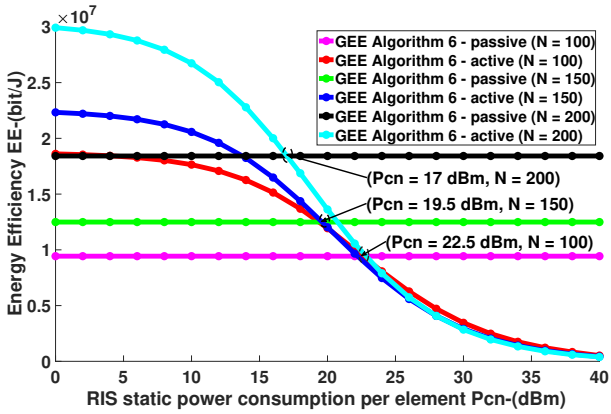

FIGURE 2.5.7: GEE versus per-element static power $P_{c,n}^{(a)}$ for active RIS and passive RIS baselines. K=4, N_R=4, $N \in \{100, 150, 200\}$, with $P_{c,n}^{(p)}$=0 dBm, $P_{0,\text{RIS}}^{(p)}$=20 dBm, $P_{0,\text{RIS}}^{(a)}$=30 dBm.

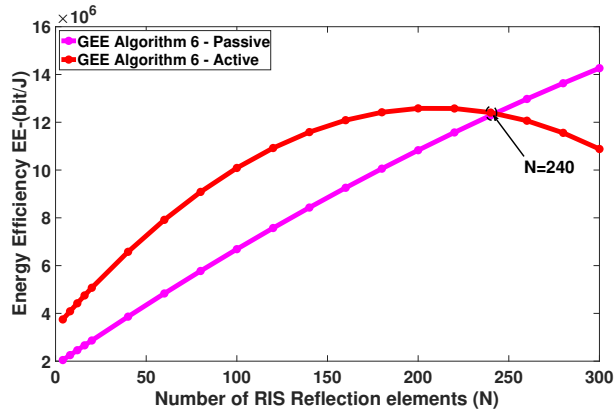

FIGURE 2.5.8: GEE versus number of RIS elements N under active and nearly-passive operation. K=4, N_R=4, $P_{c,n}^{(a)}$=20 dBm; other parameters as in Fig. 2.5.7.

consumption is a significant consideration.

Global versus local reflection. Figure 2.5.9 compares how the proposed global reflection approach performs against the standard local (unit-modulus) model for two Rician factor cases, $(K_t, K_r) = (2, 2)$ and $(K_t, K_r) = (4, 4)$. The global model yields higher global energy efficiency (GEE) since it relaxes the element-wise amplitude limits and provides a broader range of feasible reflection coefficients. The advantage becomes more noticeable when

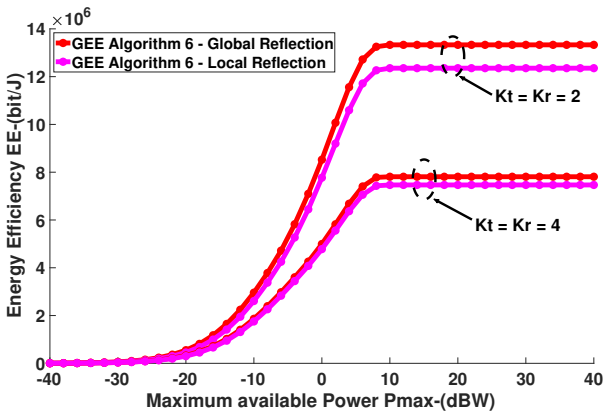

FIGURE 2.5.9: GEE versus $P_{\max}$ with global reflection constraint (nearly-passive RIS) versus local unit-modulus constraint. K=4, N_R=4, N=100. Curves shown for Rician factors K_t=$K_r \in \{2, 4\}$.

the Rician factors are small, as more substantial variations appear across the cascaded user–RIS–BS channels. As discussed in Section 2.3, the same advantage of global reflection observed in single-user cases also appears in multi-user systems, even when interference is present. Both active and nearly-passive RISs show similar trends, with performance gains mainly resulting from replacing individual element constraints with a single condition on the total reflected power across the surface.

Algorithmic convergence and complexity. Tables 2.5.2 and 2.5.3 report the average convergence times and iteration counts obtained for Algorithms 3 and 6 under both active and nearly-passive RIS setups. All simulations were executed on a workstation running an AMD Ryzen 9 processor, with convex subproblems handled through the CVX toolbox. The numerical results reveal two notable tendencies. Active RIS configurations take noticeably longer to converge, mainly because the associated optimization problem (2.2.24) involves more coupled variables and a higher computational load. While the two algorithms converge in roughly the same number of iterations, each iteration of Algorithm 6 is computationally heavier and therefore takes longer. This added effort is a direct consequence of the MMSE embedding: each iteration requires handling larger matrices and solving more involved convex problems, as described in Sections 2.4.1.4–2.4.2.3. In terms of practical use, Algorithm 3 offers a good balance between speed and performance, making it suitable for time-sensitive applications. When accuracy and energy

TABLE 2.5.2: Convergence time ratios of Alg. 3 and Alg. 6 with active and nearly-passive RIS.

$P_{\max}$ [dBW]	$T_{3,a}/T_{3,p}$	$T_{6,a}/T_{6,p}$	$T_{6,p}/T_{3,p}$	$T_{6,a}/T_{3,a}$
-35	1.89	2.27	18.3	21.9
-20	1.41	2.01	24.5	23.9
5	1.18	2.42	22.4	45.9
10	1.19	1.14	30.44	27.81

TABLE 2.5.3: Average number of iterations to converge for Alg. 3 and Alg. 6.

$P_{\max}$ [dBW]	Alg. 3 (Passive)	Alg. 3 (Active)	Alg. 6 (Passive)	Alg. 6 (Active)
-35	1.3	1.8	1.3	1.6
-20	2	2	2	2
-5	2	2	2	2
10	2	2	2	2

efficiency are the primary concerns, Algorithm 6 provides better overall results, albeit at a higher computational expense.

Initialization strategies. All algorithms were initialized with random RIS coefficients and uniform power allocation to ensure feasible starting points while maintaining statistical fairness across different channel realizations. Furthermore, we investigated a warm-start approach for the alternating optimization process, utilizing outcomes from a previous experiment as the starting point for the subsequent one. This approach notably reduced the number of iterations required for convergence, without influencing the final energy efficiency, and proved particularly effective in large or repeated simulation runs.

Overall, the multi-user results point to three central insights. The first is that including the MMSE receiver directly within the optimization framework (Algorithm 6) yields the highest global energy efficiency, though it requires additional computational resources. Second, the advantage of active RISs over nearly-passive ones depends strongly on hardware efficiency, i.e., amplification is beneficial only when the associated circuitry operates with low power consumption. Third, using a global reflection constraint yields a clear performance advantage over the conventional local model, and this improvement remains evident even under interference-limited multi-user conditions.

Chapter 3

Secrecy Energy Efficiency in RIS-Aided Networks

This chapter refers to articles published in the *2024 IEEE 25th International Workshop on Signal Processing Advances in Wireless Communications (SPAWC)*, in the *2024 IEEE International Conference on Communications (ICC)*, and in the *IEEE Transactions on Information Forensics and Security (TIFS)*, (Early Access, doi: 10.1109/TIFS.2025.3620227) 2025.

3.1 Introduction

This chapter focuses on *secrecy energy efficiency* (SEE), defined as the amount of confidential information transmitted per unit of consumed energy. In RIS-assisted wireless networks, secrecy is a critical concern due to the broadcast nature of the wireless medium and the potential presence of passive or active eavesdroppers. While physical-layer security (PLS) techniques can enhance confidentiality at the waveform level, they often incur additional power consumption (e.g., artificial noise generation), which directly impacts energy efficiency and motivates the use of SEE as a joint performance metric.

Although nearly-passive RISs are inherently energy-efficient, their effectiveness in secure communications is often limited by the multiplicative fading of cascaded channels, which can severely weaken the received signal at legitimate users. Active RIS architectures have recently been proposed to mitigate this limitation by enabling reflection-type amplification at the surface elements. However, such amplification introduces additional power consumption and noise, raising the fundamental question of whether and under which operating conditions active RISs can provide higher secrecy energy efficiency than nearly-passive designs.

To address this question, this chapter develops a unified SEE maximization framework under global reflection constraints, encompassing both active and nearly-passive RIS architectures as special cases. The proposed formulation enables a fair and systematic comparison of different RIS operating regimes while explicitly accounting for transmit power, circuit power, and RIS-related energy consumption.

3.1.1 Prior Works

The concept of *secrecy energy efficiency* (SEE) captures the trade-off between confidential throughput and total energy consumption and has recently attracted growing interest in RIS-assisted wireless networks.

Early studies primarily focused on secrecy rate or secrecy outage optimization, often neglecting the impact of circuit power and RIS-related energy consumption. As a result, these works provide limited insight into the net energy efficiency of secure RIS-assisted systems. These include STAR-RIS [48], [64], [98], discrete phase-shift RISs [78], [87], and configurations involving aerial eavesdroppers or wireless-powered nodes [15], [40], [49], [82], [88], [101]. Although previous studies have enhanced the understanding of secure transmission through Reconfigurable Intelligent Surfaces (RISs), they mainly concentrated on secrecy capacity and largely overlooked the associated energy expenditure. More recent research has started explicitly investigating the Secrecy Energy Efficiency (SEE) by employing techniques such as deep reinforcement learning and alternating optimization frameworks. Despite these advances, the existing analyses remain confined to nearly-passive RIS designs, leaving the role of active RIS architectures in SEE optimization largely unexplored. Only a few studies have investigated secrecy performance with active RISs, for instance, in wiretap or satellite communication settings [57], [81]. In summary, while RIS-assisted systems have been widely studied from both secrecy and energy-efficiency perspectives, a unified treatment of secrecy energy efficiency that explicitly compares active and nearly-passive RIS architectures under a common power-consumption and reflection model remains largely unexplored. This chapter addresses this gap by developing a global-reflection-based SEE optimization framework that enables a fair and systematic comparison across different RIS operating regimes.

3.1.2 Contributions

Motivated by the above gaps, this chapter investigates the uplink of a cellular network in which multiple users communicate with a base station (BS) through an RIS in the presence of a potential eavesdropper. The objective is to maximize the system SEE, jointly capturing energy efficiency and physical layer security under global reflection constraints. The main contributions of this chapter can be summarized as follows:

- Two resource-allocation algorithms are proposed to jointly optimize the users' transmit powers, the RIS reflection coefficients, and the BS receive filters to maximize the system-wide secrecy energy efficiency (SEE).
- Both perfect and statistical channel state information (CSI) for the eavesdropper's link are investigated, thereby addressing ideal and practically relevant operating conditions.
- The developed framework includes both *active* and *nearly-passive* RIS architectures as specific cases of a unified formulation, enabling a fair comparison of their performance in terms of SEE.
- Unlike many current studies, we adopt the global reflection model [21], broadening conventional per-element constraints and offering better design flexibility.

Chapter Roadmap

The remainder of this chapter is organized as follows. Section 4.2 presents the system model and formulates the secrecy energy efficiency (SEE) maximization problem. Section 3.3 develops the proposed optimization framework under the assumption of perfect channel state information (CSI) for the eavesdropper, while Section 3.4 extends the analysis to scenarios with statistical CSI. Finally, Section 3.5 reports numerical results and discusses the main trade-offs between active and nearly-passive RIS architectures in terms of secrecy energy efficiency.

3.2 System Model and Problem Formulation

3.2.1 System Model

We consider the uplink of a cellular network where K single-antenna users transmit information to a legitimate receiver, for instance, a base station (BS), equipped with N_B antennas. The transmission is assisted by a reconfigurable intelligent surface (RIS) composed of N reflecting elements. Within the same coverage area, a single-antenna eavesdropper is considered. This node may correspond to a legitimate terminal that inadvertently receives the transmitted signals, or to a malicious device intentionally attempting to intercept the confidential information. The overall system configuration is shown in Fig. 3.2.1.

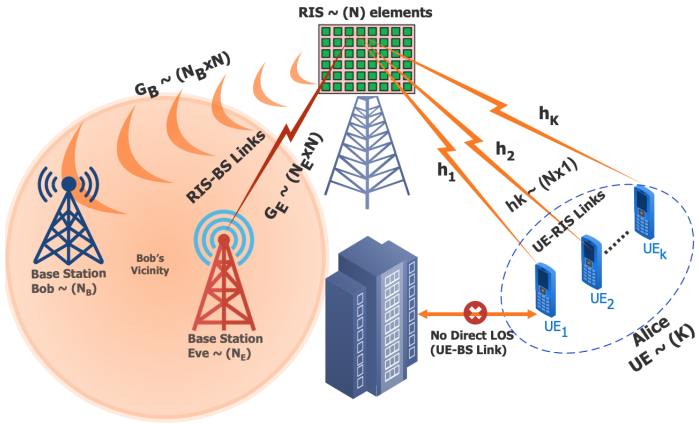

FIGURE 3.2.1: RIS-aided wireless network scenario with K users, a multi-antenna legitimate receiver, and a single-antenna eavesdropper.

Each user k transmits with power p_k. The RIS is described by its reflection-coefficient vector $\boldsymbol{\gamma} = (\gamma_1, \ldots, \gamma_N)^T \in \mathbb{C}^{N\times 1}$. The channel between the k-th user and the RIS is denoted by $\boldsymbol{h}_k \in \mathbb{C}^{N\times 1}$, that between the RIS and the BS by $\boldsymbol{G}_B \in \mathbb{C}^{N_B\times N}$, and that between the RIS and the eavesdropper by $\boldsymbol{g} \in \mathbb{C}^{N\times 1}$.

Under this notation, the received signal-to-interference-plus-noise ratios

(SINRs) for user k at the legitimate receiver and the eavesdropper are respectively expressed as

$$\mathrm{SINR}_{k,B} = \frac{p_k \left|\boldsymbol{c}_k^H \boldsymbol{A}_k \boldsymbol{\gamma}\right|^2}{\boldsymbol{c}_k^H \boldsymbol{W} \boldsymbol{c}_k + \sum_{m \neq k} p_m \left|\boldsymbol{c}_k^H \boldsymbol{A}_m \boldsymbol{\gamma}\right|^2}, \tag{3.2.1}$$

$$\mathrm{SINR}_{k,E} = \frac{p_k \left|\boldsymbol{g}^H \boldsymbol{H}_k \boldsymbol{\gamma}\right|^2}{\sigma_E^2 + \sigma_{RIS}^2 \boldsymbol{g}^H \boldsymbol{\Gamma} \boldsymbol{\Gamma}^H \boldsymbol{g} + \sum_{m \neq k} p_m \left|\boldsymbol{g}^H \boldsymbol{H}_m \boldsymbol{\gamma}\right|^2}, \tag{3.2.2}$$

where $\boldsymbol{A}_k = \boldsymbol{G}_B \boldsymbol{H}_k$ with $\boldsymbol{H}_k = \mathrm{diag}(\boldsymbol{h}_k)$, and $\boldsymbol{c}_k$ denotes the linear receive filter applied by the BS for user k. The covariance matrix representing the overall noise at the base station (BS) is expressed as follows:

$$\boldsymbol{W} = \sigma_B^2 \boldsymbol{I}_{N_B} + \sigma_{RIS}^2 \boldsymbol{G}_B \boldsymbol{\Gamma} \boldsymbol{\Gamma}^H \boldsymbol{G}_B^H, \tag{3.2.3}$$

where $\boldsymbol{\Gamma} = \mathrm{diag}(\boldsymbol{\gamma})$ and σ_{RIS}^2 denotes the noise variance introduced by the active RIS.

The system *secrecy sum-rate* (SSR) is then defined as

$$\mathrm{SSR} = \sum_{k=1}^{K} \left[\log_2\left(1 + \mathrm{SINR}_{k,B}\right) - \log_2\left(1 + \mathrm{SINR}_{k,E}\right)\right], \tag{3.2.4}$$

where the operating point is assumed to ensure non-negative secrecy rates for all users, since otherwise the system would be of limited practical significance.

Active versus nearly-passive RIS: This work considers active and nearly-passive RISs under a *global reflection constraint*. Active RISs are equipped with analog amplifiers that can increase the incident signal's radio-frequency (RF) power. In contrast, nearly-passive RISs adjust only the signal phase with negligible static power consumption. The constraint applies to the entire surface rather than individual elements within the global reflection model. Specifically,

- **Nearly-passive RIS:** $P_{\text{out}} \leq P_{\text{in}}$, i.e., the total reflected power cannot exceed the incident power.
- **Active RIS:** $P_{\text{out}} \leq P_{\text{in}} + P_{R,\max}$, where $P_{R,\max}$ represents the maximum additional RF power supplied by the RIS amplifiers.

This model generalizes the traditional *local reflection constraint*, which limits each element individually, e.g., $|\gamma_n|^2 \leq 1$.

For an active RIS, the net RF power consumption corresponds to the difference between its output and input powers, which can be expressed as [28]

$$\begin{aligned} P_{\text{out}} - P_{\text{in}} &= \text{tr}\left(\sum_{k=1}^{K} p_k \boldsymbol{\Gamma} \boldsymbol{h}_k \boldsymbol{h}_k^H \boldsymbol{\Gamma}^H + \sigma_{RIS}^2 \boldsymbol{\Gamma}\boldsymbol{\Gamma}^H\right) - \sum_{k=1}^{K} p_k \|\boldsymbol{h}_k\|^2 - \sigma_{RIS}^2 N \\ &= \text{tr}\Big[\big(\boldsymbol{\gamma}\boldsymbol{\gamma}^H - \boldsymbol{I}_N\big)\boldsymbol{R}\Big], \end{aligned} \tag{3.2.5}$$

where $\boldsymbol{R} = \sum_{k=1}^{K} p_k \boldsymbol{H}_k^H \boldsymbol{H}_k + \sigma_{RIS}^2 \boldsymbol{I}_N$. Accordingly, the total system power consumption is given by

$$P_{\text{tot}} = \text{tr}\Big[\big(\boldsymbol{\gamma}\boldsymbol{\gamma}^H - \boldsymbol{I}_N\big)\boldsymbol{R}\Big] + \sum_{k=1}^{K} p_k + P_c, \tag{3.2.6}$$

where $P_c = NP_{c,n} + P_{0,\text{RIS}} + P_0$ accounts for the static hardware power consumption.

Remark 3.2.1. For nearly-passive RISs, (3.2.6) simplifies to

$$P_{\text{tot}} = \sum_{k=1}^{K} p_k + P_c,$$

as $P_{\text{out}} \leq P_{\text{in}}$ and no amplification occurs. In this case, both $P_{c,n}$ and $P_{0,\text{RIS}}$ assume smaller values than in the active configuration, reflecting the reduced hardware complexity.

Finally, the system *secrecy energy efficiency* (SEE) is defined as

$$\text{SEE} = \frac{\text{SSR}}{\text{tr}\Big[\big(\boldsymbol{\gamma}\boldsymbol{\gamma}^H - \boldsymbol{I}_N\big)\boldsymbol{R}\Big] + \sum_{k=1}^{K} \mu_k p_k + P_c}, \tag{3.2.7}$$

where μ_k represents the inverse of the power amplifier efficiency for user k.

3.2.2 Problem Formulation

The objective of this chapter is to maximize the SEE of the described system. Two scenarios regarding channel state information (CSI) are considered.

3.2.2.1 Perfect CSI

All wireless channels are assumed to be perfectly known at the BS. The user–RIS and RIS–BS channels can be accurately estimated using conventional pilot-based training procedures. In contrast, perfect CSI for the RIS-eavesdropper channel reflects a scenario in which the eavesdropper is not a concealed adversary but instead a legitimate terminal within the network (for example, a cell-edge user served by another BS) that unintentionally intercepts part of the transmitted signal. Based on this premise, we can outline the task of optimizing secrecy energy efficiency (SEE) in the following way:

$$\max_{\boldsymbol{\gamma},\boldsymbol{p},\boldsymbol{C}} \ \mathrm{SEE}(\boldsymbol{\gamma},\boldsymbol{p},\boldsymbol{C}) \tag{3.2.8a}$$

$$\text{s.t. } \mathrm{tr}\left(\boldsymbol{R}\right) \leq \mathrm{tr}(\boldsymbol{R}\boldsymbol{\gamma}\boldsymbol{\gamma}^H) \leq P_{R,max} + \mathrm{tr}\left(\boldsymbol{R}\right), \tag{3.2.8b}$$

$$0 \leq p_k \leq P_{max,k}, \quad \forall k = 1,\ldots,K, \tag{3.2.8c}$$

where $\boldsymbol{C} = [\boldsymbol{c}_1,\ldots,\boldsymbol{c}_K]$ collects the BS receive filters. Feasibility is always guaranteed, since setting $|\gamma_n| = 1$ for all n satisfies the constraints.

3.2.2.2 Statistical CSI

In more adversarial or realistic scenarios, the RIS–eavesdropper channel cannot be estimated perfectly. However, it can be statistically estimated, with the statistical expectation following a mean-feedback model described below as:

$$\boldsymbol{g} = \widehat{\boldsymbol{g}} + \boldsymbol{\delta}, \tag{3.2.9}$$

where $\widehat{\boldsymbol{g}}$ denotes the estimated mean channel, and $\boldsymbol{\delta} \sim \mathcal{CN}(\boldsymbol{0}, \sigma_g^2 \boldsymbol{I}_N)$ captures the random estimation error. The variance σ_g^2 reflects the level of uncertainty: higher values indicate less accurate channel knowledge, whereas $\sigma_g^2 = 0$ corresponds to the perfect CSI case.

Remark 3.2.2 (Colored estimation errors). The isotropic error model $\boldsymbol{\delta} \sim \mathcal{CN}(\boldsymbol{0}, \sigma_g^2 \boldsymbol{I}_N)$ is adopted for analytical clarity and to capture the average impact of channel uncertainty. Nevertheless, the proposed framework readily extends to the more general case of *colored* estimation errors, where $\boldsymbol{\delta} \sim \mathcal{CN}(\boldsymbol{0}, \boldsymbol{C}_\delta)$ with a non-diagonal covariance matrix $\boldsymbol{C}_\delta$ reflecting spatially correlated uncertainty (e.g., due to angular correlation, hardware impairments, or biased estimation).

In this case, the expectation operators involved in the SEE formulation remain tractable, since the relevant terms depend on second-order moments of quadratic forms in complex Gaussian vectors. The resulting expressions

can be obtained by replacing $\sigma_g^2 \boldsymbol{I}_N$ with $\boldsymbol{C}_\delta$ in the corresponding derivations, without altering the structure of the optimization problem or the solution methodology developed in the following sections.

Under this model, the secrecy energy efficiency (SEE) maximization problem is formulated as

$$\max_{\boldsymbol{\gamma}, \boldsymbol{p}, \boldsymbol{C}} \ \mathbb{E}_\delta[\mathrm{SEE}(\boldsymbol{\gamma}, \boldsymbol{p}, \boldsymbol{C})]\,, \tag{3.2.10a}$$

$$\text{s.t. } \mathrm{tr}(\boldsymbol{R}) \leq \mathrm{tr}\left(\boldsymbol{R}\boldsymbol{\gamma}\boldsymbol{\gamma}^H\right) \leq P_{R,\max} + \mathrm{tr}(\boldsymbol{R})\,, \tag{3.2.10b}$$

$$0 \leq p_k \leq P_{\max,k}, \quad \forall k = 1, \ldots, K. \tag{3.2.10c}$$

In this formulation, the objective function is represented as the expected value of the SEE, averaged over the random channel error $\boldsymbol{\delta}$.

Remark 3.2.3. The proposed framework can be extended to multi-cell scenarios where inter-cell interference is treated as additional noise. In such cases, the only modification involves including the out-of-cell interference terms in the summations defining $\mathrm{SINR}_{k,B}$, $\mathrm{SINR}_{k,E}$, and P_{tot}. The optimization strategies introduced in the following sections remain directly applicable without structural changes.

3.3 Optimization with Perfect CSI

This section addresses Problem (3.2.8) under the assumption that all wireless channels are perfectly known at the BS. Owing to the intrinsic non-convexity of the fractional objective function and the strong coupling among the optimization variables, the problem is tackled using an alternating maximization strategy. Specifically, the optimization is performed cyclically over three variable blocks: the RIS reflection coefficients $\boldsymbol{\gamma}$, the users' transmit power vector $\boldsymbol{p}$, and the linear receive filter matrix $\boldsymbol{C}$. Each subproblem is solved

within the framework of *sequential fractional programming* (SFP), which iteratively replaces the original non-convex objective with locally tight concave or pseudo-concave lower bounds. This approach guarantees monotonic improvement of the objective value across iterations and convergence to a stationary point that satisfies the Karush–Kuhn–Tucker (KKT) optimality conditions.

3.3.1 Optimization of γ

With $(\boldsymbol{p}, \boldsymbol{C})$ held fixed, the RIS design subproblem reads

$$\max_{\gamma} \frac{\sum_{k=1}^{K} \Big(\log_2\big(1+\mathrm{SINR}_{k,B}\big) - \log_2\big(1+\mathrm{SINR}_{k,E}\big) \Big)}{\mathrm{tr}\big(\boldsymbol{R}\boldsymbol{\gamma}\boldsymbol{\gamma}^H\big) + P_{c,\mathrm{eq}}} \tag{3.3.1a}$$

$$\text{s.t.} \quad \mathrm{tr}\big(\boldsymbol{R}\big) \le \mathrm{tr}\big(\boldsymbol{R}\boldsymbol{\gamma}\boldsymbol{\gamma}^H\big) \le P_{R,\max} + \mathrm{tr}\big(\boldsymbol{R}\big), \tag{3.3.1b}$$

where $P_{c,\mathrm{eq}} = \sum_k \mu_k p_k + P_c - \mathrm{tr}\big(\boldsymbol{R}\big)$. The problem is non-convex because the objective is not concave in γ and the lower global-reflection bound in (3.3.1b) is itself non-convex.

To make the dependence on γ explicit, note that

$$\boldsymbol{c}_k^H \boldsymbol{W} \boldsymbol{c}_k = \sigma_B^2 \|\boldsymbol{c}_k\|^2 + \sigma_{RIS}^2\, \boldsymbol{\gamma}^H \widetilde{\boldsymbol{U}}_k \boldsymbol{\gamma}, \qquad \boldsymbol{g}^H \boldsymbol{\Gamma}\boldsymbol{\Gamma}^H \boldsymbol{g} = \|\boldsymbol{G}\boldsymbol{\gamma}\|^2, \tag{3.3.2}$$

with $\boldsymbol{u}_k = \boldsymbol{G}_B^H \boldsymbol{c}_k$, $\widetilde{\boldsymbol{U}}_k = \mathrm{diag}(|u_{k,1}|^2, \ldots, |u_{k,N}|^2)$, and $\boldsymbol{G} = \mathrm{diag}(g_1, \ldots, g_N)$. Define

$$x_B = p_k \big|\boldsymbol{c}_k^H \boldsymbol{A}_k \boldsymbol{\gamma}\big|^2, \qquad x_E = p_k \big|\boldsymbol{g}^H \boldsymbol{H}_k \boldsymbol{\gamma}\big|^2, \tag{3.3.3}$$

$$y_B = \sigma_B^2 \|\boldsymbol{c}_k\|^2 + \sigma_{RIS}^2 \|\widetilde{\boldsymbol{U}}_k^{1/2} \boldsymbol{\gamma}\|^2 + \sum_{m \ne k} p_m \big|\boldsymbol{c}_k^H \boldsymbol{A}_m \boldsymbol{\gamma}\big|^2, \tag{3.3.4}$$

$$y_E = \sum_{m \ne k} p_m \big|\boldsymbol{g}^H \boldsymbol{H}_m \boldsymbol{\gamma}\big|^2 + \sigma_{RIS}^2 \|\boldsymbol{G}\boldsymbol{\gamma}\|^2. \tag{3.3.5}$$

Hence, the k-th secrecy rate can be written as

$$\begin{aligned} R_{s,k}^{\mathrm{PCSI}} &= \log_2\!\left(1 + \frac{x_B}{y_B}\right) - \log_2\!\left(1 + \frac{x_E}{y_E + \sigma_E^2}\right) \\ &= \log_2\!\left(1 + \frac{x_B}{y_B}\right) + \log_2\!\left(1 + \frac{y_E}{\sigma_E^2}\right) + \log_2(\sigma_E^2) - \log_2(\sigma_E^2 + x_E + y_E). \end{aligned} \tag{3.3.6}$$

The second expression in (3.3.6) enables the use of the tight bounds (proved in Appendix A.1.6: Lemmas A.1.1 & A.1.2).

$$\log_2\!\left(1 + \frac{x}{y}\right) \ge \log_2\!\left(1 + \frac{\bar{x}}{\bar{y}}\right) + \frac{\bar{x}}{\bar{y}}\left(\frac{2\sqrt{x}}{\sqrt{\bar{x}}} - \frac{x+y}{\bar{x}+\bar{y}} - 1\right), \tag{3.3.7}$$

$$\log_2(\sigma_E^2 + x + y) \le \log_2(\sigma_E^2 + \bar{x} + \bar{y}) + \frac{1}{\ln 2}\, \frac{x + y - \bar{x} - \bar{y}}{\sigma_E^2 + \bar{x} + \bar{y}}, \tag{3.3.8}$$

which are exact at $(x, y) = (\bar{x}, \bar{y})$. Given a feasible reference point $\bar{\gamma}$, let

$$\bar{x}_B = p_k \left| \boldsymbol{c}_k^H \boldsymbol{A}_k \bar{\boldsymbol{\gamma}} \right|^2, \qquad \bar{x}_E = p_k \left| \boldsymbol{g}^H \boldsymbol{H}_k \bar{\boldsymbol{\gamma}} \right|^2, \tag{3.3.9}$$

$$\bar{y}_B = \sigma_B^2 \|\boldsymbol{c}_k\|^2 + \sigma_{RIS}^2 \|\widetilde{\boldsymbol{U}}_k^{1/2} \bar{\boldsymbol{\gamma}}\|^2 + \sum_{m \neq k} p_m \left| \boldsymbol{c}_k^H \boldsymbol{A}_m \bar{\boldsymbol{\gamma}} \right|^2, \tag{3.3.10}$$

$$\bar{y}_E = \sum_{m \neq k} p_m \left| \boldsymbol{g}^H \boldsymbol{H}_m \bar{\boldsymbol{\gamma}} \right|^2 + \sigma_{RIS}^2 \|\boldsymbol{G} \bar{\boldsymbol{\gamma}}\|^2. \tag{3.3.11}$$

Substituting (3.3.3)–(3.3.11) into (3.3.6) and applying (3.3.7)–(3.3.8) yields

$$\begin{aligned} R_{s,k}^{\mathrm{PCSI}}(\boldsymbol{\gamma}) \geq\ & \log_2\left(1 + \frac{\bar{x}_B}{\bar{y}_B}\right) + \log_2\left(1 + \frac{\bar{y}_E}{\sigma_E^2}\right) \\ & + \frac{\bar{x}_B}{\bar{y}_B}\left(\frac{2\sqrt{x_B}}{\sqrt{\bar{x}_B}} - \frac{x_B + y_B}{\bar{x}_B + \bar{y}_B} - 1\right) \\ & + \frac{\bar{y}_E}{\sigma_E^2}\left(\frac{2\sqrt{y_E}}{\sqrt{\bar{y}_E}} - \frac{y_E + \sigma_E^2}{\bar{y}_E + \sigma_E^2} - 1\right) \\ & + \log_2\left(\frac{\sigma_E^2}{\sigma_E^2 + \bar{x}_E + \bar{y}_E}\right) - \frac{x_E + y_E - \bar{x}_E - \bar{y}_E}{\sigma_E^2 + \bar{x}_E + \bar{y}_E} \\ =\ & \overline{R}_{s,k}^{\mathrm{PCSI}}(\boldsymbol{\gamma}). \end{aligned} \tag{3.3.12}$$

The only remaining non-concave terms are $\sqrt{x_B}$ and $\sqrt{y_E}$, both convex in $\boldsymbol{\gamma}$ and admit first-order lower approximations at $\bar{\boldsymbol{\gamma}}$. By Introducing the Hermitian PSD matrices

$$\boldsymbol{M}_{k,B} = \boldsymbol{A}_k^H \boldsymbol{c}_k \boldsymbol{c}_k^H \boldsymbol{A}_k, \qquad \boldsymbol{M}_{k,E} = \sum_{m \neq k} p_m \boldsymbol{H}_m^H \boldsymbol{g} \boldsymbol{g}^H \boldsymbol{H}_m + \sigma_{RIS}^2 \boldsymbol{G} \boldsymbol{G}^H. \tag{3.3.13}$$

and linearizing them at $\bar{\boldsymbol{\gamma}}$ yields

$$\sqrt{x_B} = \sqrt{p_k}\sqrt{\boldsymbol{\gamma}^H \boldsymbol{M}_{k,B} \boldsymbol{\gamma}} \ \geq\ \sqrt{p_k}\left(\sqrt{\bar{\boldsymbol{\gamma}}^H \boldsymbol{M}_{k,B} \bar{\boldsymbol{\gamma}}} + \frac{\Re\{\bar{\boldsymbol{\gamma}}^H \boldsymbol{M}_{k,B}(\boldsymbol{\gamma} - \bar{\boldsymbol{\gamma}})\}}{\sqrt{\bar{\boldsymbol{\gamma}}^H \boldsymbol{M}_{k,B} \bar{\boldsymbol{\gamma}}}}\right) = \widetilde{x}_B(\bar{\boldsymbol{\gamma}}), \tag{3.3.14}$$

$$\sqrt{y_E} = \sqrt{\boldsymbol{\gamma}^H \boldsymbol{M}_{k,E} \boldsymbol{\gamma}} \ \geq\ \sqrt{\bar{\boldsymbol{\gamma}}^H \boldsymbol{M}_{k,E} \bar{\boldsymbol{\gamma}}} + \frac{\Re\{\bar{\boldsymbol{\gamma}}^H \boldsymbol{M}_{k,E}(\boldsymbol{\gamma} - \bar{\boldsymbol{\gamma}})\}}{\sqrt{\bar{\boldsymbol{\gamma}}^H \boldsymbol{M}_{k,E} \bar{\boldsymbol{\gamma}}}} = \widetilde{y}_E(\bar{\boldsymbol{\gamma}}). \tag{3.3.15}$$

Replacing $\sqrt{x_B}$ and $\sqrt{y_E}$ in (3.3.12) gives the concave surrogate

$$R_{s,k}^{\mathrm{PCSI}}(\boldsymbol{\gamma}) \geq \overline{R}_{s,k}^{\mathrm{PCSI}}(\boldsymbol{\gamma}) \geq \log_2\!\left(1+\frac{\bar{x}_B}{\bar{y}_B}\right) + \frac{\bar{x}_B}{\bar{y}_B}\left(\frac{2\widetilde{x}_B}{\sqrt{\bar{x}_B}} - \frac{x_B+y_B}{\bar{x}_B+\bar{y}_B} - 1\right) + \log_2\!\left(1+\frac{\bar{y}_E}{\sigma_E^2}\right) + \frac{\bar{y}_E}{\sigma_E^2}\left(\frac{2\widetilde{y}_E}{\sqrt{\bar{y}_E}} - \frac{y_E+\sigma_E^2}{\bar{y}_E+\sigma_E^2} - 1\right) + \log_2\!\left(\frac{\sigma_E^2}{\sigma_E^2+\bar{x}_E+\bar{y}_E}\right) - \frac{x_E+y_E-\bar{x}_E-\bar{y}_E}{\sigma_E^2+\bar{x}_E+\bar{y}_E} = \widetilde{R}_{s,k}^{\mathrm{PCSI}}(\boldsymbol{\gamma}). \quad (3.3.16)$$

The non-convex lower global-reflection constraint is convexified via the first-order bound of $\mathrm{tr}\big(\boldsymbol{R}\boldsymbol{\gamma}\boldsymbol{\gamma}^H\big)$ at $\bar{\boldsymbol{\gamma}}$:

$$\mathrm{tr}\big(\boldsymbol{R}\boldsymbol{\gamma}\boldsymbol{\gamma}^H\big) \geq \bar{\boldsymbol{\gamma}}^H\boldsymbol{R}\bar{\boldsymbol{\gamma}} + 2\,\Re\{\bar{\boldsymbol{\gamma}}^H\boldsymbol{R}(\boldsymbol{\gamma}-\bar{\boldsymbol{\gamma}})\}. \quad (3.3.17)$$

Therefore, each SFP iteration solves

$$\max_{\boldsymbol{\gamma}} \ \frac{\sum_{k=1}^{K}\widetilde{R}_{s,k}^{\mathrm{PCSI}}(\boldsymbol{\gamma})}{\mathrm{tr}\big(\boldsymbol{R}\boldsymbol{\gamma}\boldsymbol{\gamma}^H\big)+P_{c,\mathrm{eq}}^{(a)}} \quad (3.3.18a)$$

$$\text{s.t.} \ \ \boldsymbol{\gamma}^H\boldsymbol{R}\boldsymbol{\gamma} \leq P_{R,\max} + \mathrm{tr}\big(\boldsymbol{R}\big), \quad (3.3.18b)$$

$$\bar{\boldsymbol{\gamma}}^H\boldsymbol{R}\bar{\boldsymbol{\gamma}} + 2\,\Re\{\bar{\boldsymbol{\gamma}}^H\boldsymbol{R}(\boldsymbol{\gamma}-\bar{\boldsymbol{\gamma}})\} \geq \mathrm{tr}\big(\boldsymbol{R}\big). \quad (3.3.18c)$$

The numerator of (3.3.18a) is concave in $\boldsymbol{\gamma}$, the denominator is convex (since $\boldsymbol{R} \succeq \sigma_{RIS}^2\boldsymbol{I} \succ 0$), and the constraints are convex. Hence, (3.3.18) is a *pseudo-concave* fractional program, solvable by parametric (Dinkelbach) iterations. Introducing $\eta \geq 0$, the inner loop solves

$$\max_{\boldsymbol{\gamma}} \ \Phi_\eta(\boldsymbol{\gamma}) \triangleq \sum_{k=1}^{K}\widetilde{R}_{s,k}^{\mathrm{PCSI}}(\boldsymbol{\gamma}) - \eta\left(\mathrm{tr}\big(\boldsymbol{R}\boldsymbol{\gamma}\boldsymbol{\gamma}^H\big)+P_{c,\mathrm{eq}}^{(a)}\right) \quad \text{s.t. (3.3.18b)–(3.3.18c)}, \quad (3.3.19)$$

and updates

$$\eta \ \leftarrow \ \frac{\sum_k \widetilde{R}_{s,k}^{\mathrm{PCSI}}(\boldsymbol{\gamma}^\star)}{\mathrm{tr}\big(\boldsymbol{R}\boldsymbol{\gamma}^\star\boldsymbol{\gamma}^{\star H}\big)+P_{c,\mathrm{eq}}^{(a)}}$$

until convergence (see Appendix A.6.1). Problem (3.3.19) is a concave maximization over a convex set and can be handled by standard solvers. For

implementation, one may use the Wirtinger gradient

$$\nabla_{\gamma^*}\Phi_\eta(\gamma) = \sum_{k=1}^{K} \nabla_{\gamma^*}\widetilde{R}_{s,k}^{\mathrm{PCSI}}(\gamma) - \eta\, \boldsymbol{R}\gamma, \tag{3.3.20}$$

where $\nabla_{\gamma^*}\widetilde{R}_{s,k}^{\mathrm{PCSI}}(\gamma)$ follows directly from (3.3.16) (closed-form expressions are provided in Appendix A.1.8), and $\boldsymbol{R}\gamma$ is the derivative of $\mathrm{tr}\big(\boldsymbol{R}\gamma\gamma^H\big)$ with respect to γ^*.

Algorithm 7 RIS optimization under perfect CSI

Input: feasible $\bar{\gamma}$ (e.g., $|\gamma_n| = 1$), tolerances $\epsilon, \varepsilon > 0$.
repeat
Surrogate construction: build $\widetilde{R}_{s,k}^{\mathrm{PCSI}}(\gamma)$ via (3.3.16) at $\bar{\gamma}$; linearize (3.3.17).
Parametric FP: initialize $\eta \geq 0$; **repeat** solve (3.3.19) for $\gamma^\star$ and update $\eta \leftarrow \dfrac{\sum_k \widetilde{R}_{s,k}^{\mathrm{PCSI}}(\gamma^\star)}{\mathrm{tr}(\boldsymbol{R}\gamma^\star\gamma^{\star H}) + P_{c,\mathrm{eq}}^{(a)}}$ **until** $|\Delta\eta| < \varepsilon$.
Major update: set $T = \big|\mathrm{SEE}(\gamma^\star) - \mathrm{SEE}(\bar{\gamma})\big|$ and $\bar{\gamma} \leftarrow \gamma^\star$.
until $T < \epsilon$

Proposition 3.3.1. *Algorithm 7 produces a non-decreasing sequence of SEE values and converges to a KKT point of* (3.3.1). *The claim follows from the SFP conditions (tightness and first-order agreement of the surrogates, convex feasible set at each step) and the optimality of Dinkelbach's inner loop for pseudo-concave fractional programs (Appendix A.6.1).*

Remark 3.3.1 (Global-reflection feasibility and nearly-passive specialization). Feasibility of (3.3.1) is ensured by selecting any γ that satisfies the global reflection constraint. For example, choosing $|\gamma_n| = 1$ for all n trivially guarantees feasibility since it yields $\mathrm{tr}\big(\boldsymbol{R}\gamma\gamma^H\big) = \mathrm{tr}\big(\boldsymbol{R}\big)$. The nearly-passive case is obtained by setting $P_{R,\max} = 0$, for which (3.3.1b) reduces to

$$\mathrm{tr}\big(\boldsymbol{R}\gamma\gamma^H\big) \leq \mathrm{tr}\big(\boldsymbol{R}\big).$$

Under this global constraint, the magnitudes of the individual reflection coefficients are not restricted to unity; some elements may exhibit $|\gamma_n| > 1$ as long as others satisfy $|\gamma_n| < 1$ such that the total reflected power remains below or equal to the total incident power. This flexibility distinguishes the global reflection model from the conventional local one, where each element is constrained by $|\gamma_n|^2 \leq 1$. □

3.3.2 Optimization of $\boldsymbol{p}$

For fixed $(\boldsymbol{\gamma}, \boldsymbol{C})$, optimizing the transmit powers constitutes the second block of the alternating maximization. Because the secrecy rate and the total consumed power depend nonlinearly on $\boldsymbol{p}$, the problem is not concave in its native form. To simplify the notation and clarify the structure, we introduce below the auxiliary terms:

$$a_{k,m}^{(B)} = |\boldsymbol{c}_k^H \boldsymbol{A}_m \boldsymbol{\gamma}|^2, \qquad d_k^{(B)} = \boldsymbol{c}_k^H \boldsymbol{W} \boldsymbol{c}_k, \tag{3.3.21}$$

$$a_k^{(E)} = |\boldsymbol{g}^H \boldsymbol{H}_k \boldsymbol{\gamma}|^2, \qquad d^{(E)} = \sigma_E^2 + \sigma_{RIS}^2 \boldsymbol{g}^H \boldsymbol{\Gamma} \boldsymbol{\Gamma}^H \boldsymbol{g}, \tag{3.3.22}$$

$$\mu_k = 1 + \mathrm{tr}\big[(\boldsymbol{\gamma}\boldsymbol{\gamma}^H - \boldsymbol{I}_N)\boldsymbol{H}_k^H \boldsymbol{H}_k\big], \quad P_{c,\mathrm{eq}} = \sigma_{RIS}^2 \big(\|\boldsymbol{\gamma}\|^2 - N\big) + P_c. \tag{3.3.23}$$

Here, $a_{k,m}^{(B)}$ and $a_k^{(E)}$ represent the effective channel gains at the legitimate receiver and at the eavesdropper, respectively. $d_k^{(B)}$ and $d^{(E)}$ are the corresponding interference-plus-noise powers; μ_k collects the effective per-user power cost and $P_{c,\mathrm{eq}}$ gathers circuit-related terms (including RIS-amplification noise).

With these definitions, the power-allocation subproblem is

$$\max_{\boldsymbol{p}} \; \frac{\displaystyle\sum_{k=1}^{K} \log_2\Big(1 + \frac{p_k a_{k,k}^{(B)}}{d_k^{(B)} + \sum_{m \neq k} p_m a_{k,m}^{(B)}}\Big) - \sum_{k=1}^{K} \log_2\Big(1 + \frac{p_k a_k^{(E)}}{d^{(E)} + \sum_{m \neq k} p_m a_m^{(E)}}\Big)}{\sum_{k=1}^{K} \mu_k p_k + P_{c,\mathrm{eq}}} \tag{3.3.24a}$$

$$\text{s.t.} \quad 0 \leq p_k \leq P_{\max,k}, \; \forall k. \tag{3.3.24b}$$

Due to the coupled interference terms, the objective function is non-concave in $\boldsymbol{p}$, so directly applying fractional programming is not feasible. We rewrite the SEE as a difference of four terms:

$$\mathrm{SEE}(\boldsymbol{p}) = g_{1,B}(\boldsymbol{p}) - g_{2,B}(\boldsymbol{p}) - g_{1,E}(\boldsymbol{p}) + g_{2,E}(\boldsymbol{p}), \tag{3.3.25}$$

where

$$g_{1,B}(\boldsymbol{p}) = \frac{\sum_{k=1}^{K} \log_2\left(d_k^{(B)} + \sum_{m=1}^{K} p_m a_{k,m}^{(B)}\right)}{\sum_{k=1}^{K} \mu_k p_k + P_{c,\mathrm{eq}}}, \tag{3.3.26}$$

$$g_{2,B}(\boldsymbol{p}) = \frac{\sum_{k=1}^{K} \log_2\left(d_k^{(B)} + \sum_{m\neq k} p_m a_{k,m}^{(B)}\right)}{\sum_{k=1}^{K} \mu_k p_k + P_{c,\mathrm{eq}}}, \tag{3.3.27}$$

$$g_{1,E}(\boldsymbol{p}) = \frac{\sum_{k=1}^{K} \log_2\left(d^{(E)} + \sum_{m=1}^{K} p_m a_m^{(E)}\right)}{\sum_{k=1}^{K} \mu_k p_k + P_{c,\mathrm{eq}}}, \tag{3.3.28}$$

$$g_{2,E}(\boldsymbol{p}) = \frac{\sum_{k=1}^{K} \log_2\left(d^{(E)} + \sum_{m\neq k} p_m a_m^{(E)}\right)}{\sum_{k=1}^{K} \mu_k p_k + P_{c,\mathrm{eq}}}. \tag{3.3.29}$$

Here, $g_{1,B}$ and $g_{2,E}$ are concave in $\boldsymbol{p}$, whereas $-g_{2,B}$ and $-g_{1,E}$ are not. Within the SFP framework, the non-concave parts are replaced by first-order (tight) approximations around the current iterate $\bar{\boldsymbol{p}}$. Let $f_{2,B}$ and $f_{1,E}$ denote the numerators of $g_{2,B}$ and $g_{1,E}$, respectively. Then

$$\frac{\partial f_{2,B}}{\partial p_j} = \sum_{k\neq j} \frac{a_{k,j}^{(B)}}{d_k^{(B)} + \sum_{m\neq k} p_m a_{k,m}^{(B)}}, \tag{3.3.30}$$

$$\frac{\partial f_{1,E}}{\partial p_j} = \frac{a_j^{(E)}}{d^{(E)} + \sum_{m=1}^{K} p_m a_m^{(E)}}. \tag{3.3.31}$$

Substituting the linearizations at $\bar{\boldsymbol{p}}$ into (3.3.25) yields the pseudo-concave lower bound

$$\begin{aligned}\mathrm{SEE}(\boldsymbol{p}) \geq\ & g_{1,B}(\boldsymbol{p}) + g_{2,E}(\boldsymbol{p}) - g_{2,B}(\bar{\boldsymbol{p}}) - g_{1,E}(\bar{\boldsymbol{p}}) \\ & - \frac{\left(\nabla f_{2,B}(\bar{\boldsymbol{p}})\right)^T(\boldsymbol{p}-\bar{\boldsymbol{p}})}{\sum_{k=1}^{K} \mu_k p_k + P_{c,\mathrm{eq}}} - \frac{\left(\nabla f_{1,E}(\bar{\boldsymbol{p}})\right)^T(\boldsymbol{p}-\bar{\boldsymbol{p}})}{\sum_{k=1}^{K} \mu_k p_k + P_{c,\mathrm{eq}}} \ =\ \widetilde{\mathrm{SEE}}(\boldsymbol{p}),\end{aligned} \tag{3.3.32}$$

which is globally valid and tight at $\boldsymbol{p} = \bar{\boldsymbol{p}}$. Thus, the SFP update solves

$$\max_{\boldsymbol{p}} \ \widetilde{\mathrm{SEE}}(\boldsymbol{p}) \tag{3.3.33a}$$

$$\text{s.t.} \quad 0 \leq p_k \leq P_{\max,k}, \ \forall k. \tag{3.3.33b}$$

The numerator of $\widetilde{\mathrm{SEE}}(\boldsymbol{p})$ is concave and the denominator is affine, so (3.3.33) is a pseudo-concave fractional program that can be solved efficiently and

globally using standard fractional programming routines (see Appendix A.6.1).

Algorithm 8 Power optimization under perfect CSI

Input: feasible $\bar{\boldsymbol{p}}$, tolerance $\epsilon > 0$.
repeat
  Solve (3.3.33) to obtain $\boldsymbol{p}^\star$;
  $T = \left|\mathrm{SEE}(\boldsymbol{p}^\star) - \mathrm{SEE}(\bar{\boldsymbol{p}})\right|$;
  Update $\bar{\boldsymbol{p}} \leftarrow \boldsymbol{p}^\star$;
until $T < \epsilon$

Proposition 3.3.2. *Algorithm 8 yields a non-decreasing sequence of SEE values and converges to a Karush–Kuhn–Tucker (KKT) point of problem (3.3.24). This behavior arises from the standard properties of sequential fractional programming: At each iteration, the constructed surrogate provides a global lower approximation of the true objective while matching its value and local gradient at the current iterate. In addition, the feasible region preserved by the update remains convex, which ensures that the resulting sequence of iterates is well defined and monotonic. Appendix A.6.1 includes a formal justification of these claims.*

Remark 3.3.2 (Practical implications). The proposed method allocates the available transmit power among users, while explicitly considering the eavesdropper's channel. In practice, the BS optimizes centrally in (3.3.33) and communicates the resulting powers p_k to each user. The overall computational effort scales polynomially with the number of users K; further complexity considerations are discussed at the end of Sec. 3.3. □

3.3.3 Optimization of $\boldsymbol{C}$

For fixed $(\boldsymbol{\gamma}, \boldsymbol{p})$, the receive filters influence only the numerator of the SEE, that is, the achievable rates of the legitimate users. Because the received signals are linearly separable across users, each user k can optimize its filter independently. The optimal receive filter follows the linear minimum mean-square error (LMMSE) design, which achieves the maximum signal-to-interference-plus-noise ratio (SINR) among all linear receivers. A detailed derivation of this result is given in Appendix A.1.1. The optimal filter is expressed as

$$\boldsymbol{c}_k^\star = \sqrt{p_k}\left(\sum_{m\neq k} p_m \boldsymbol{A}_m \boldsymbol{\gamma}\boldsymbol{\gamma}^H \boldsymbol{A}_m^H + \boldsymbol{W}\right)^{-1} \boldsymbol{A}_k \boldsymbol{\gamma}. \tag{3.3.34}$$

Substituting $\boldsymbol{c}_k^\star$ into the SINR expression gives the corresponding closed-form optimal SINR:

$$\mathrm{SINR}_{k,B}^\star = p_k \boldsymbol{\gamma}^H \boldsymbol{A}_k^H \left(\sum_{m \neq k} p_m \boldsymbol{A}_m \boldsymbol{\gamma} \boldsymbol{\gamma}^H \boldsymbol{A}_m^H + \boldsymbol{W} \right)^{-1} \boldsymbol{A}_k \boldsymbol{\gamma}, \tag{3.3.35}$$

which is subsequently employed in the evaluation of the system SEE.

3.3.4 Overall Algorithm, Convergence, Complexity, and Implementation

The three optimization modules developed in the previous sections—namely, the RIS reflection coefficients, the user transmit powers, and the LMMSE receive filters—are now integrated into an alternating maximization framework. Each block update guarantees a non-decreasing trend in secrecy energy efficiency (SEE) by following these steps:

(i) The optimization of the RIS is achieved using the SFP method. This method creates a locally tight surrogate at each iteration.

(ii) The power allocation update also utilizes SFP, resulting in a pseudo-concave subproblem.

(iii) The LMMSE filters are designed to maximize the legitimate SINR in closed form.

As a result, iteratively cycling through these updates guarantees that the overall SEE does not decrease. Algorithm 9 summarizes the complete resource allocation procedure.

Algorithm 9 Overall resource allocation under perfect CSI

Input: feasible $(\tilde{\boldsymbol{p}}, \tilde{\boldsymbol{\gamma}})$, tolerance $\epsilon > 0$.
Compute $\boldsymbol{C}$ (LMMSE).
repeat
  $\mathrm{SEE}_{\mathrm{in}} \leftarrow \mathrm{SEE}(\tilde{\boldsymbol{p}}, \tilde{\boldsymbol{\gamma}}, \boldsymbol{C})$;
  Update $\tilde{\boldsymbol{\gamma}}$ using Algorithm 7;
  Update $\tilde{\boldsymbol{p}}$ using Algorithm 8;
  Recompute $\boldsymbol{C}$ (LMMSE);
  $\mathrm{SEE}_{\mathrm{out}} \leftarrow \mathrm{SEE}(\tilde{\boldsymbol{p}}, \tilde{\boldsymbol{\gamma}}, \boldsymbol{C})$;
until $|\mathrm{SEE}_{\mathrm{out}} - \mathrm{SEE}_{\mathrm{in}}| < \epsilon$

Proposition 3.3.3. *Algorithm 9 yields a sequence of SEE values that is monotonically non-decreasing and converges to a finite limit. This behavior follows directly from Propositions 3.3.1 and 3.3.2, as each block update either increases or preserves the current SEE. At the same time, the overall sequence is bounded above*

by the physical power constraints of the system. A complete convergence analysis is presented in Appendix A.6.2.

Remark 3.3.3 (SSR specialization). By setting the denominator in equation (3.2.8a) to one, Algorithm 9 simplifies to maximizing the secrecy sum-rate (SSR). This shows that the proposed framework integrates traditional SSR optimization with the broader problem of maximizing the SEE. □

Computational complexity. Apart from the negligible cost of the closed-form LMMSE update, the computational burden of Algorithm 9 is dominated by the RIS and power-optimization stages. A pseudo-concave maximization in n variables can be reformulated as a concave maximization in $n+1$ variables, with polynomial complexity $\mathcal{O}((n+1)^{\alpha})$, where $\alpha \in [1,4]$ depends on the chosen convex solver [6]. Hence, the overall complexity of Algorithm 9 can be expressed as

$$\mathcal{C}_1 = \mathcal{O}\Big(I_1\Big(I_{\gamma,1}(N+1)^{\alpha} + I_{p,1}(K+1)^{\beta}\Big)\Big), \tag{3.3.36}$$

where $I_{\gamma,1}$, $I_{p,1}$, and I_1 denote the iteration counts associated with the RIS, power, and outer loops, respectively.

Practical implementation. Algorithm 9 is executed centrally at the BS. Once convergence is reached, the BS communicates the optimized reflection vector (N coefficients) to the RIS controller over the dedicated control link and distributes the optimized power levels (K values) to the users through the uplink control channel. Thus, the signaling overhead grows linearly with the number of RIS elements and users.

Prior to execution, the BS must obtain the relevant channel state information. For the legitimate links, standard RIS-aided estimation techniques can be used. These include blind or pilot-assisted schemes for acquiring the composite channels $\boldsymbol{A}_k$ for $k = 1, \ldots, K$ (see, e.g., [13], [94]) and the BS–RIS channel $\boldsymbol{G}_B$, which is static since both nodes are fixed. Once $\boldsymbol{A}_k$ and $\boldsymbol{G}_B$ are known, the diagonal user-to-RIS channel $\boldsymbol{H}_k$ can be reconstructed from the relation $\boldsymbol{A}_k = \boldsymbol{G}_B\boldsymbol{H}_k$. Regarding the eavesdropper's channel $\boldsymbol{g}$, under the perfect-CSI assumption adopted here, the eavesdropper is modeled as a legitimate terminal within the network (for example, a cell-edge user served by a neighboring BS). Consequently, its channel can also be estimated through standard procedures, ensuring that this node cannot decode the confidential information. The total estimation overhead depends on the

adopted training strategy but scales approximately with the number of coefficients to be estimated, i.e., $\mathcal{O}(NN_BK)$. Such scaling is typical of RIS-aided systems and represents the main bottleneck in deploying very large surfaces. Nevertheless, once the channels are acquired, the alternating optimization in Algorithm 9 can be executed at moderate computational cost and updated within the channel coherence interval.

3.4 Optimization with Statistical CSI

We now consider the practical scenario in which the BS does not have perfect instantaneous CSI of the eavesdropper's link. The design problem is given by (3.2.10), where the numerator involves the expectation $\mathbb{E}_\delta[\log_2(1+\mathrm{SINR}_{k,E})]$. Since no closed-form expression is available in general, a tractable approximation is obtained via Jensen's inequality. Because $x \mapsto \log_2(1+x)$ is concave for $x > -1$, we have

$$\mathbb{E}[\log_2(1+X)] \le \log_2(1+\mathbb{E}[X])\,.$$

Replacing $\mathbb{E}[\log_2(1+\mathrm{SINR}_{k,E})]$ with $\log_2(1+\mathbb{E}[\mathrm{SINR}_{k,E}])$ therefore yields an *upper bound* on the eavesdropper term. Consequently, the resulting secrecy rate becomes a *conservative* estimate of the achievable performance, which is desirable from a security standpoint.

Starting from

$$\begin{aligned}
&\mathbb{E}_\delta[\log_2(1+\mathrm{SINR}_{k,E})] \qquad (3.4.1)\\
&= \mathbb{E}_\delta\left[\log_2\left(\sigma_E^2+\sigma_{RIS}^2\boldsymbol{g}_E^H\boldsymbol{\Gamma}\boldsymbol{\Gamma}^H\boldsymbol{g}_E+\sum_{m=1}^{K}p_m\left|\boldsymbol{g}_E^H\boldsymbol{H}_m\boldsymbol{\gamma}\right|^2\right)\right]\\
&\quad-\mathbb{E}_\delta\left[\log_2\left(\sigma_E^2+\sigma_{RIS}^2\boldsymbol{g}_E^H\boldsymbol{\Gamma}\boldsymbol{\Gamma}^H\boldsymbol{g}_E+\sum_{m\neq k}p_m\left|\boldsymbol{g}_E^H\boldsymbol{H}_m\boldsymbol{\gamma}\right|^2\right)\right],
\end{aligned}$$

and substituting $\boldsymbol{g}_E = \widehat{\boldsymbol{g}}_E + \boldsymbol{\delta}$ with $\boldsymbol{\delta}\sim\mathcal{CN}(\boldsymbol{0},\sigma_g^2\boldsymbol{I})$, we move the expectation inside the logarithm to obtain

$$\begin{aligned}
(3.4.1) \approx\ &\log_2\left(\sigma_E^2+\mathbb{E}_\delta\left[\sigma_{RIS}^2\boldsymbol{g}_E^H\boldsymbol{\Gamma}\boldsymbol{\Gamma}^H\boldsymbol{g}_E+\sum_{m=1}^{K}p_m\left|\boldsymbol{g}_E^H\boldsymbol{H}_m\boldsymbol{\gamma}\right|^2\right]\right)\\
&-\log_2\left(\sigma_E^2+\mathbb{E}_\delta\left[\sigma_{RIS}^2\boldsymbol{g}_E^H\boldsymbol{\Gamma}\boldsymbol{\Gamma}^H\boldsymbol{g}_E+\sum_{m\neq k}p_m\left|\boldsymbol{g}_E^H\boldsymbol{H}_m\boldsymbol{\gamma}\right|^2\right]\right).
\end{aligned}$$

For $m = 1, \ldots, K$, direct computation gives

$$\begin{aligned}\mathbb{E}\left[\left|\boldsymbol{g}_E^H \boldsymbol{H}_m \boldsymbol{\gamma}\right|^2\right] &= \widehat{\boldsymbol{g}}_E^H \boldsymbol{H}_m \boldsymbol{\gamma}\boldsymbol{\gamma}^H \boldsymbol{H}_m^H \widehat{\boldsymbol{g}}_E + \sigma_g^2 \|\boldsymbol{H}_m \boldsymbol{\gamma}\|^2 \\ &= \boldsymbol{\gamma}^H \boldsymbol{H}_m^H \left(\widehat{\boldsymbol{g}}_E \widehat{\boldsymbol{g}}_E^H + \sigma_g^2 \boldsymbol{I}_N\right) \boldsymbol{H}_m \boldsymbol{\gamma} = \left\|\boldsymbol{R}_E^{1/2} \boldsymbol{H}_m \boldsymbol{\gamma}\right\|^2, \quad (3.4.2)\\ \mathbb{E}\left[\boldsymbol{g}_E^H \boldsymbol{\Gamma}\boldsymbol{\Gamma}^H \boldsymbol{g}_E\right] &= \boldsymbol{\gamma}^H \left(\widehat{\boldsymbol{g}}_E \widehat{\boldsymbol{g}}_E^H + \sigma_g^2 \boldsymbol{I}_N\right) \boldsymbol{\gamma} = \left\|\boldsymbol{R}_E^{1/2} \boldsymbol{\gamma}\right\|^2, \quad (3.4.3)\end{aligned}$$

where $\boldsymbol{R}_E \triangleq \widehat{\boldsymbol{g}}_E \widehat{\boldsymbol{g}}_E^H + \sigma_g^2 \boldsymbol{I}_N$. Hence,

$$\mathbb{E}_\delta[\log_2(1 + \mathrm{SINR}_{k,E})] \approx \log_2\left(1 + \widetilde{\mathrm{SINR}}_{k,E}\right), \quad (3.4.4)$$

with

$$\widetilde{\mathrm{SINR}}_{k,E} = \frac{p_k \left\|\boldsymbol{R}_E^{1/2} \boldsymbol{H}_k \boldsymbol{\gamma}\right\|^2}{\sum_{m \neq k} p_m \left\|\boldsymbol{R}_E^{1/2} \boldsymbol{H}_m \boldsymbol{\gamma}\right\|^2 + \sigma_{RIS}^2 \left\|\boldsymbol{R}_E^{1/2} \boldsymbol{\gamma}\right\|^2 + \sigma_E^2}. \quad (3.4.5)$$

Accordingly, the SEE in (3.2.10a) can be approximated as

$$\widetilde{\mathrm{SEE}} = \frac{\sum_{k=1}^{K} \left[\log_2(1 + \mathrm{SINR}_{k,B}) - \log_2\left(1 + \widetilde{\mathrm{SINR}}_{k,E}\right)\right]}{\mathrm{tr}\left(\left(\boldsymbol{\gamma}\boldsymbol{\gamma}^H - \boldsymbol{I}_N\right) \boldsymbol{R}\right) + \sum_{k=1}^{K} p_k + P_c}. \quad (3.4.6)$$

The corresponding optimization problem becomes

$$\begin{aligned}&\max_{\boldsymbol{\gamma}, \boldsymbol{p}, \boldsymbol{C}} \ \widetilde{\mathrm{SEE}}(\boldsymbol{\gamma}, \boldsymbol{p}, \boldsymbol{C}) && (3.4.7a)\\ &\text{s.t.} \quad \mathrm{tr}(\boldsymbol{R}) \leq \mathrm{tr}(\boldsymbol{R}\boldsymbol{\gamma}\boldsymbol{\gamma}^H) \leq P_{R,\max} + \mathrm{tr}(\boldsymbol{R}), && (3.4.7b)\\ &\qquad 0 \leq p_k \leq P_{\max,k}, \quad \forall k. && (3.4.7c)\end{aligned}$$

Problem (3.4.7) is solved through alternating optimization over the variables $\boldsymbol{\gamma}$, $\boldsymbol{p}$, and $\boldsymbol{C}$, reusing the same sequential fractional programming framework developed for the perfect-CSI case, with the substitution of $\widetilde{\mathrm{SINR}}_{k,E}$ for $\mathrm{SINR}_{k,E}$.

3.4.1 RIS Optimization (sCSI)

For fixed $(\boldsymbol{p}, \boldsymbol{C})$, the RIS-design subproblem reads

$$\max_{\boldsymbol{\gamma}} \quad \frac{\sum_{k=1}^{K}\Big[\log_2\big(1+\mathrm{SINR}_{k,B}\big)-\log_2\big(1+\widetilde{\mathrm{SINR}}_{k,E}\big)\Big]}{\mathrm{tr}\big(\boldsymbol{R}\boldsymbol{\gamma}\boldsymbol{\gamma}^H\big)+P_{c,\mathrm{eq}}} \tag{3.4.8a}$$

$$\text{s.t.} \quad \mathrm{tr}\big(\boldsymbol{R}\big) \le \mathrm{tr}\big(\boldsymbol{R}\boldsymbol{\gamma}\boldsymbol{\gamma}^H\big) \le P_{R,\max}+\mathrm{tr}\big(\boldsymbol{R}\big), \tag{3.4.8b}$$

where $P_{c,\mathrm{eq}} = \sum_k \mu_k p_k + P_c - \mathrm{tr}\big(\boldsymbol{R}\big)$. As before, we have $\boldsymbol{c}_k^H \boldsymbol{W} \boldsymbol{c}_k = \sigma_B^2\|\boldsymbol{c}_k\|^2 + \sigma_{RIS}^2\|\widetilde{\boldsymbol{U}}_k^{1/2}\boldsymbol{\gamma}\|^2$ and we reuse $x_B, y_B, \bar{x}_B, \bar{y}_B$ from (3.3.3)–(3.3.10). On the eavesdropper side (statistical CSI), we define

$$x_E = p_k\big\|\boldsymbol{R}_E^{1/2}\boldsymbol{H}_k\boldsymbol{\gamma}\big\|^2, \qquad \bar{x}_E = p_k\big\|\boldsymbol{R}_E^{1/2}\boldsymbol{H}_k\bar{\boldsymbol{\gamma}}\big\|^2, \tag{3.4.9}$$

$$y_E = \sum_{m\neq k} p_m\big\|\boldsymbol{R}_E^{1/2}\boldsymbol{H}_m\boldsymbol{\gamma}\big\|^2 + \sigma_{RIS}^2\big\|\boldsymbol{R}_E^{1/2}\boldsymbol{\gamma}\big\|^2, \tag{3.4.10}$$

$$\bar{y}_E = \sum_{m\neq k} p_m\big\|\boldsymbol{R}_E^{1/2}\boldsymbol{H}_m\bar{\boldsymbol{\gamma}}\big\|^2 + \sigma_{RIS}^2\big\|\boldsymbol{R}_E^{1/2}\bar{\boldsymbol{\gamma}}\big\|^2. \tag{3.4.11}$$

Following the same steps used for the perfect-CSI case (cf. (3.3.6)–(3.3.8)), the k-th secrecy term admits the lower-bound structure

$$\begin{aligned} R_{s,k}^{\mathrm{SCSI}}(\boldsymbol{\gamma}) \ge{}& \log_2\!\left(1+\frac{\bar{x}_B}{\bar{y}_B}\right) + \log_2\!\left(1+\frac{\bar{y}_E}{\sigma_E^2}\right) \\ &+ \frac{\bar{x}_B}{\bar{y}_B}\left(\frac{2\sqrt{x_B}}{\sqrt{\bar{x}_B}} - \frac{x_B+y_B}{\bar{x}_B+\bar{y}_B} - 1\right) \\ &+ \frac{\bar{y}_E}{\sigma_E^2}\left(\frac{2\sqrt{y_E}}{\sqrt{\bar{y}_E}} - \frac{y_E+\sigma_E^2}{\bar{y}_E+\sigma_E^2} - 1\right) \\ &+ \log_2\!\left(\frac{\sigma_E^2}{\sigma_E^2+\bar{x}_E+\bar{y}_E}\right) - \frac{x_E+y_E-\bar{x}_E-\bar{y}_E}{\sigma_E^2+\bar{x}_E+\bar{y}_E} \;=:\; \overline{R}_{s,k}^{\mathrm{SCSI}}(\boldsymbol{\gamma}). \end{aligned} \tag{3.4.12}$$

As in the perfect-CSI derivation, $\sqrt{x_B}$ and $\sqrt{y_E}$ are convex in $\boldsymbol{\gamma}$ and we linearize them at a feasible reference point $\bar{\boldsymbol{\gamma}}$:

$$\sqrt{x_B} \ge \widetilde{x}_B(\bar{\boldsymbol{\gamma}}) \quad \text{as in (3.3.14)}, \tag{3.4.13}$$

$$\sqrt{y_E} = \sqrt{\boldsymbol{\gamma}^H\boldsymbol{M}_{k,E}\boldsymbol{\gamma}} = \big\|\boldsymbol{M}_{k,E}^{1/2}\boldsymbol{\gamma}\big\| \;\ge\; \widetilde{y}_E(\bar{\boldsymbol{\gamma}}) \quad \text{as in (3.3.15)}, \tag{3.4.14}$$

with the sCSI matrix

$$\boldsymbol{M}_{k,E} = \sum_{m \neq k} p_m \boldsymbol{H}_m^H \boldsymbol{R}_E \boldsymbol{H}_m + \sigma_{RIS}^2 \boldsymbol{R}_E. \tag{3.4.15}$$

These redefinitions yield, for any feasible $\bar{\boldsymbol{\gamma}}$, the following concave surrogate (tight at $\boldsymbol{\gamma} = \bar{\boldsymbol{\gamma}}$):

$$\begin{aligned} R_{s,k}^{\mathrm{SCSI}}(\boldsymbol{\gamma}) &\geq \overline{R}_{s,k}^{\mathrm{SCSI}}(\boldsymbol{\gamma}) \\ &\geq \log_2\!\left(1 + \frac{\bar{x}_B}{\bar{y}_B}\right) + \frac{\bar{x}_B}{\bar{y}_B}\left(\frac{2\,\widetilde{x}_B}{\sqrt{\bar{x}_B}} - \frac{x_B + y_B}{\bar{x}_B + \bar{y}_B} - 1\right) \\ &\quad + \log_2\!\left(1 + \frac{\bar{y}_E}{\sigma_E^2}\right) + \frac{\bar{y}_E}{\sigma_E^2}\left(\frac{2\,\widetilde{y}_E}{\sqrt{\bar{y}_E}} - \frac{y_E + \sigma_E^2}{\bar{y}_E + \sigma_E^2} - 1\right) \\ &\quad + \log_2\!\left(\frac{\sigma_E^2}{\sigma_E^2 + \bar{x}_E + \bar{y}_E}\right) - \frac{x_E + y_E - \bar{x}_E - \bar{y}_E}{\sigma_E^2 + \bar{x}_E + \bar{y}_E} \;\triangleq\; \widetilde{R}_{s,k}^{\mathrm{SCSI}}(\boldsymbol{\gamma}). \end{aligned} \tag{3.4.16}$$

The bound in (3.4.16) preserves both value and gradient at the expansion point and is jointly concave in $\boldsymbol{\gamma}$, which enables the ensuing fractional-programming step.

By replacing (3.4.12) with its linearized counterpart (cf. (3.3.16)) and convexifying the lower global-reflection constraint as in (3.3.17), the RIS update at each SFP iteration becomes

$$\max_{\boldsymbol{\gamma}} \quad \frac{\sum_{k=1}^{K} \widetilde{R}_{s,k}^{\mathrm{SCSI}}(\boldsymbol{\gamma})}{\mathrm{tr}\big(\boldsymbol{R}\boldsymbol{\gamma}\boldsymbol{\gamma}^H\big) + P_{c,\mathrm{eq}}} \tag{3.4.17a}$$

$$\text{s.t.} \quad \boldsymbol{\gamma}^H \boldsymbol{R} \boldsymbol{\gamma} \;\leq\; P_{R,\max} + \mathrm{tr}\big(\boldsymbol{R}\big), \tag{3.4.17b}$$

$$\bar{\boldsymbol{\gamma}}^H \boldsymbol{R} \bar{\boldsymbol{\gamma}} + 2\,\Re\{\bar{\boldsymbol{\gamma}}^H \boldsymbol{R}(\boldsymbol{\gamma} - \bar{\boldsymbol{\gamma}})\} \geq \mathrm{tr}\big(\boldsymbol{R}\big). \tag{3.4.17c}$$

Problem (3.4.17) is a pseudo-concave fractional program with convex constraints and is solved by Dinkelbach iterations, exactly as in (3.3.19), upon replacing $\widetilde{R}_{s,k}^{\mathrm{PCSI}}$ with $\widetilde{R}_{s,k}^{\mathrm{SCSI}}$.

Proposition 3.4.1. *Algorithm 10 produces a non-decreasing sequence of objective values for (3.4.8) and converges to a Karush–Kuhn–Tucker (KKT) point. The proof mirrors the perfect-CSI case and follows from the SFP conditions (tightness and first-order agreement of the surrogates, convex feasible set) together with the optimality of Dinkelbach's inner loop; see Appendix A.6.1.*

Algorithm 10 RIS optimization under statistical CSI

Input: tolerance $\epsilon > 0$, feasible $\bar{\gamma}$.
repeat
Build $\widetilde{R}_{s,k}^{\mathrm{SCSI}}(\gamma)$ at $\bar{\gamma}$; solve (3.4.17) (via Dinkelbach) for $\gamma^\star$;
$T = \left|\widetilde{\mathrm{SEE}}(\gamma^\star) - \widetilde{\mathrm{SEE}}(\bar{\gamma})\right|$; $\quad \bar{\gamma} \leftarrow \gamma^\star$;
until $T < \epsilon$

3.4.2 Power Optimization (sCSI)

With $(\gamma, \boldsymbol{C})$ fixed, the power-update subproblem resembles the form of (3.3.24), but the quantities related to the eavesdropper are substituted with their statistical-CSI equivalents. By introducing

$$a_{k,m}^{(B)} = \left|\boldsymbol{c}_k^H \boldsymbol{A}_m \gamma\right|^2, \qquad d_k^{(B)} = \boldsymbol{c}_k^H \boldsymbol{W} \boldsymbol{c}_k, \tag{3.4.18}$$

$$\tilde{a}_k^{(E)} = \left\|\boldsymbol{R}_E^{1/2} \boldsymbol{H}_k \gamma\right\|^2, \qquad \tilde{d}^{(E)} = \sigma_E^2 + \sigma_{RIS}^2 \left\|\boldsymbol{R}_E^{1/2} \gamma\right\|^2, \tag{3.4.19}$$

$$\mu_k = 1 + \mathrm{tr}\left[(\gamma\gamma^H - \boldsymbol{I}_N)\boldsymbol{H}_k^H \boldsymbol{H}_k\right], \quad P_{c,\mathrm{eq}} = \sigma_{RIS}^2\left(\|\gamma\|^2 - N\right) + P_c. \tag{3.4.20}$$

The sCSI power-allocation problem reads.

$$\max_{\boldsymbol{p}} \; \frac{\sum_{k=1}^{K} \log_2\!\left(1 + \dfrac{p_k a_{k,k}^{(B)}}{d_k^{(B)} + \sum_{m \neq k} p_m a_{k,m}^{(B)}}\right) - \sum_{k=1}^{K} \log_2\!\left(1 + \dfrac{p_k \tilde{a}_k^{(E)}}{\tilde{d}^{(E)} + \sum_{m \neq k} p_m \tilde{a}_m^{(E)}}\right)}{\sum_{k=1}^{K} \mu_k p_k + P_{c,\mathrm{eq}}} \tag{3.4.21a}$$

$$\text{s.t.} \quad 0 \leq p_k \leq P_{\max,k}, \; \forall k. \tag{3.4.21b}$$

As in the perfect-CSI case, we can write.

$$\mathrm{SEE}(\boldsymbol{p}) = g_{1,B}(\boldsymbol{p}) - g_{2,B}(\boldsymbol{p}) - \tilde{g}_{1,E}(\boldsymbol{p}) + \tilde{g}_{2,E}(\boldsymbol{p}), \qquad g_\bullet(\boldsymbol{p}) \triangleq \frac{f_\bullet(\boldsymbol{p})}{D(\boldsymbol{p})},$$

with a common denominator

$$D(\boldsymbol{p}) = \sum_{k=1}^{K} \mu_k p_k + P_{c,\mathrm{eq}},$$

and numerators

$$f_{1,B}(\boldsymbol{p}) = \sum_{k=1}^{K} \log_2\Big(d_k^{(B)} + \sum_{i=1}^{K} p_i a_{k,i}^{(B)}\Big), \quad f_{2,B}(\boldsymbol{p}) = \sum_{k=1}^{K} \log_2\Big(d_k^{(B)} + \sum_{m\neq k} p_m a_{k,m}^{(B)}\Big),$$

$$\tilde{f}_{1,E}(\boldsymbol{p}) = \sum_{k=1}^{K} \log_2\Big(\tilde{d}^{(E)} + \sum_{i=1}^{K} p_i \tilde{a}_i^{(E)}\Big), \quad \tilde{f}_{2,E}(\boldsymbol{p}) = \sum_{k=1}^{K} \log_2\Big(\tilde{d}^{(E)} + \sum_{m\neq k} p_m \tilde{a}_m^{(E)}\Big).$$

The non-concave parts are $-f_{2,B}$ and $-\tilde{f}_{1,E}$. By linearizing these two numerators at a feasible reference point $\bar{\boldsymbol{p}}$ gives the SFP surrogate

$$\widetilde{\mathrm{SEE}}(\boldsymbol{p}) = \frac{f_{1,B}(\boldsymbol{p}) + \tilde{f}_{2,E}(\boldsymbol{p}) - \Big(f_{2,B}(\bar{\boldsymbol{p}}) + \nabla f_{2,B}(\bar{\boldsymbol{p}})^T(\boldsymbol{p}-\bar{\boldsymbol{p}})\Big) - \Big(\tilde{f}_{1,E}(\bar{\boldsymbol{p}}) + \nabla \tilde{f}_{1,E}(\bar{\boldsymbol{p}})^T(\boldsymbol{p}-\bar{\boldsymbol{p}})\Big)}{D(\boldsymbol{p})} \tag{3.4.22}$$

with gradient components (evaluated at $\bar{\boldsymbol{p}}$)

$$\big[\nabla f_{2,B}(\bar{\boldsymbol{p}})\big]_j = \sum_{k\neq j} \frac{a_{k,j}^{(B)}}{d_k^{(B)} + \sum_{m\neq k} \bar{p}_m a_{k,m}^{(B)}}, \tag{3.4.23}$$

$$\big[\nabla \tilde{f}_{1,E}(\bar{\boldsymbol{p}})\big]_j = \sum_{k=1}^{K} \frac{\tilde{a}_j^{(E)}}{\tilde{d}^{(E)} + \sum_{m=1}^{K} \bar{p}_m \tilde{a}_m^{(E)}}. \tag{3.4.24}$$

Note. The derivative of $\tilde{f}_{1,E}$ w.r.t. p_j depends on $\tilde{a}_j^{(E)}$ and is replicated across the sum over k, since the inner argument of each logarithm is identical.

The sCSI power-update step solves

$$\max_{\boldsymbol{p}} \ \widetilde{\mathrm{SEE}}(\boldsymbol{p}) \tag{3.4.25a}$$

$$\text{s.t.} \quad 0 \le p_k \le P_{\max,k}, \ \forall k, \tag{3.4.25b}$$

which is a pseudo-concave fractional program and can be solved globally by standard fractional-programming methods (see Appendix A.6.1).

Algorithm 11 Power optimization under statistical CSI

Input: feasible $\bar{\boldsymbol{p}}$, tolerance $\epsilon > 0$.
repeat
  Solve (3.4.25) to obtain $\boldsymbol{p}^\star$;
  $T = \big|\widetilde{\mathrm{SEE}}(\boldsymbol{p}^\star) - \widetilde{\mathrm{SEE}}(\bar{\boldsymbol{p}})\big|$; $\bar{\boldsymbol{p}} \leftarrow \boldsymbol{p}^\star$;
until $T < \epsilon$

Proposition 3.4.2. *Algorithm 11 generates a monotonically non-decreasing sequence of objective values for Problem (3.4.21) and converges to a solution that satisfies the Karush–Kuhn–Tucker (KKT) conditions of (3.4.21).*

Proof. The claim is a direct consequence of the properties of sequential fractional programming (see Appendix A.6.1). At each iteration, the surrogate in (3.4.22) is a global underestimator of the original objective, is tight at the current iterate $\bar{\boldsymbol{p}}$, and matches the first-order behavior there. These properties guarantee monotonic improvement and ensure that any limit point fulfills the KKT conditions of (3.4.21). ■

3.4.3 Optimization of C (sCSI)

In the statistical-CSI case, the receive combiners $\boldsymbol{C}$ influence only the legitimate users' rates and have no impact on the (approximated) eavesdropper term. As a result, the optimization again decouples across users, allowing each user k to determine its own filter independently. Under these conditions, the LMMSE filter derived in Appendix A.1.1 remains the optimal choice. Its expression is

$$\boldsymbol{c}_k^\star = \sqrt{p_k}\left(\sum_{m\neq k} p_m \boldsymbol{A}_m \boldsymbol{\gamma}\boldsymbol{\gamma}^H \boldsymbol{A}_m^H + \boldsymbol{W}\right)^{-1} \boldsymbol{A}_k \boldsymbol{\gamma}. \tag{3.4.26}$$

3.4.4 Overall Algorithm, Convergence, Complexity, and Practical Implementation

The AO framework established for the perfect-CSI scenario can be successfully applied to the statistical-CSI scenario. The main adjustment lies in replacing the instantaneous secrecy-rate terms with their expected-value approximations derived in Section 3.4. Although the overall structure of the algorithm remains unchanged, i.e., by alternating between the RIS coefficients, transmit powers, and receive filters, the optimization now operates on the surrogate objective $\widetilde{\mathrm{SEE}}$, which captures the ergodic secrecy performance.

The essential difference arises in the handling of the eavesdropper's channel. Rather than depending on instantaneous CSI, which is rarely available in practice, the optimization relies solely on the statistical characterization of the channel. This substantially reduces the estimation burden and makes the algorithm well-suited to scenarios with passive or hidden eavesdroppers,

where perfect CSI cannot be acquired. The resulting iterative procedure is summarized in Algorithm 12 below.

Algorithm 12 Overall resource allocation under statistical CSI

Input: feasible $(\tilde{\boldsymbol{p}}, \tilde{\boldsymbol{\gamma}})$, tolerance $\epsilon > 0$.
Compute $\boldsymbol{C}$ (LMMSE, see Appendix A.1.1).
repeat
  $\widetilde{\mathrm{SEE}}_{\mathrm{in}} \leftarrow \widetilde{\mathrm{SEE}}(\tilde{\boldsymbol{p}}, \tilde{\boldsymbol{\gamma}}, \boldsymbol{C})$;
  Update $\tilde{\boldsymbol{\gamma}}$ using Algorithm 1;
  Update $\tilde{\boldsymbol{p}}$ using Algorithm 11;
  Recompute $\boldsymbol{C}$ (LMMSE);
  $\widetilde{\mathrm{SEE}}_{\mathrm{out}} \leftarrow \widetilde{\mathrm{SEE}}(\tilde{\boldsymbol{p}}, \tilde{\boldsymbol{\gamma}}, \boldsymbol{C})$;
until $|\widetilde{\mathrm{SEE}}_{\mathrm{out}} - \widetilde{\mathrm{SEE}}_{\mathrm{in}}| < \epsilon$

Proposition 3.4.3. *Algorithm 12 generates a non-decreasing sequence of $\widetilde{SEE}$ values and converges to a finite limit.*

Proof. Propositions 3.4.1 and 3.4.2 ensure that every update step in Algorithm 12 yields a surrogate objective value that never decreases. The sequence of $\widetilde{\mathrm{SEE}}$ values is monotone and remains bounded above, owing to the finite transmit-power and RIS-reflection limits. Consequently, the iterations converge to a stationary point of Problem (3.4.7). ■

Remark 3.4.1 (Ergodic SSR specialization). By setting the denominator in (3.2.10a) to unity, Algorithm 12 reduces to an ergodic secrecy sum-rate (SSR) maximization procedure. In this way, the proposed formulation subsumes conventional SSR optimization as a particular instance of the more general SEE framework. □

Computational Complexity. The complexity analysis closely follows that of the perfect-CSI counterpart. Each pseudo-concave fractional subproblem can be reformulated as a concave maximization with one additional variable and solved in polynomial time [95]. Let $I_{\gamma,2}$, $I_{p,2}$, and I_2 denote the iteration counts of the RIS, power, and outer loops, respectively. The overall computational complexity is then expressed as follows.

$$\mathcal{C}_2 = \mathcal{O}\Big(I_2\big(I_{\gamma,2}(N+1)^{\alpha} + I_{p,2}(K+1)^{\beta}\big)\Big), \tag{3.4.27}$$

where $\alpha, \beta \in [1, 4]$ depend on the underlying convex solver. As in the perfect-CSI case, the total cost scales polynomially with both the number of RIS elements N and the number of users K.

Practical Implementation. The execution of Algorithm 12 is centralized at the BS. Once convergence is reached, the BS forwards the optimized reflection vector to the RIS controller and the transmit-power settings to the users. Under the statistical-CSI model, the BS no longer needs an exact estimate of the eavesdropper's channel $\boldsymbol{g}$; it only requires its mean $\widehat{\boldsymbol{g}}$ and variance σ_g^2. This assumption is realistic in networks where the eavesdropper is passive or only approximately located. In the limiting regime where $\sigma_g^2 \gg \|\widehat{\boldsymbol{g}}\|^2$, no specific channel knowledge is needed at all, which eliminates any estimation overhead and still maintains robustness in the SEE optimization.

Discussion. The perfect-CSI and statistical-CSI frameworks should be regarded as complementary baselines. The first framework represents an optimistic setting, providing an upper bound on achievable SEE performance when the eavesdropper's channel is perfectly known. In contrast, the second framework reflects a more realistic condition in which only statistical or partial knowledge is available; it accounts for the uncertainties that typically arise in practical wireless environments. Taken together, Algorithms 9 and 12 provide a unified optimization framework that bridges idealized and real-world conditions. The following section will explore their relative performance and associated trade-offs through numerical results.

3.5 Numerical Analysis

This section evaluates the proposed algorithms' performance under perfect and statistical channel state information (CS) conditions. Unless indicated otherwise, the main simulation parameters are given in Table 4.4.1. The selected values correspond to a realistic cellular configuration, with a moderately sized RIS and a multi-antenna BS, chosen so that both energy efficiency and secrecy aspects remain non-trivial. The scenario is motivated by the fact that the RIS and the BS are fixed and strategically placed to guarantee favorable propagation conditions toward the legitimate receiver. By contrast, the eavesdropper is modeled as another mobile node of the network, or as an external intruder, which, owing to its random position and lower elevation, is assumed to be in less favorable propagation conditions than the legitimate receiver. This modeling choice reflects practical deployments, where the legitimate infrastructure can be optimized while potential eavesdroppers cannot. To guarantee statistical reliability, all numerical results are averaged over 10^3 independent realizations of user positions and channel fading. In the case of statistical CSI, the accuracy of the RIS–eavesdropper channel

estimate is quantified through the normalized error variance (NEV), defined as

$$\mathrm{NEV} = \frac{\mathbb{E}[\|\boldsymbol{\delta}\|^2]}{\mathbb{E}[\|\boldsymbol{g}\|^2]},$$

where $\boldsymbol{\delta}$ denotes the estimation error. Unless explicitly stated otherwise, we adopt $\mathrm{NEV} = 0\,\mathrm{dB}$ as the default operating condition.

3.5.1 SEE and SSR versus Transmit Power

The first set of experiments examines how the secrecy energy efficiency (SEE) and secrecy sum-rate (SSR) vary with the maximum transmit power $P_{t,\max}$. To provide a comprehensive comparison, several resource-allocation strategies are evaluated:

(a) **Algorithm 9** (perfect CSI, SEE maximization): optimized for maximum SEE with complete channel knowledge.

(b) **Algorithm 12** (statistical CSI, SEE maximization): the RIS coefficients, transmit powers, and receive filters are optimized using only statistical knowledge of $\boldsymbol{g}$, whereas the achieved SEE is computed using the actual channel realizations.

(c) **Algorithm 9** (perfect CSI, SSR maximization): specialized for secrecy sum-rate optimization, as described in Remark 3.3.3.

(d) **Algorithm 12** (statistical CSI, ergodic SSR maximization): adapted for ergodic SSR maximization according to Remark 3.4.1. Here, the optimization relies on statistical CSI, but performance evaluation uses the true channel states.

(e)–(f) **Modified versions of Algorithms 9–12**: the RIS reflection vector $\boldsymbol{\gamma}$ is refined through per-element alternating optimization following [86]. For each reflecting element n, both amplitude and phase of γ_n are tuned via exhaustive search.

(g) **Heuristic approach:** random RIS phases, uniform reflection amplitudes, and uniform transmit-power allocation, i.e., $|\gamma_n|^2 = 1 + P_{R,\max}/\operatorname{tr}(\boldsymbol{R})$ for all n, and $p_k = P_{t,\max}/K$ for all k.

The corresponding results are depicted in Fig. 3.5.1. Designs that rely on statistical CSI, namely schemes (b) and (d), attain slightly lower SEE compared with their perfect-CSI counterparts (a) and (c). This reduction stems

TABLE 3.5.1: Simulation parameters used in Section 3.5. Unless otherwise stated, these values are fixed across experiments.

Symbol	Description	Value
Network sizes and bandwidth		
K	Number of users	4
N_B	BS antennas	4
N	RIS elements	100
B	System bandwidth	20 MHz
Geometry and placement		
RIS/BS height	Heights of RIS and BS	10 m (each)
User height	User elevation range	[1.5, 2.5] m
Eavesdropper height	Eavesdropper elevation range	[1.5, 2.5] m
User area	User drop radius	50 m
RIS guard distance	Min user–RIS distance	$R_n = 20$ m
RIS–BS distance	Horizontal distance	20 m
Eavesdropper area	Radius from BS	30 m
Propagation (path loss and fading)		
n_h	Path-loss exp. (user→RIS)	4
$n_{g,E}$	Path-loss exp. (eve→RIS)	4
$n_{g,B}$	Path-loss exp. (RIS→BS)	2
K_t	Rician K-factor (RIS→BS)	4
K_r	Rician K-factor (user/eve→RIS)	2
Noise and RF front-end		
N_0	Noise PSD	−174 dBm/Hz
NF	Receiver noise figure	5 dB
Power budgets and static consumptions		
$P_{t\,\max}$	Per-user max TX power	swept in figures
P_0	Static (TX/RX other)	20 dBm
$P_{0,\mathrm{RIS}}$	RIS static (base)	30 dBm
$P_{c,n}$	RIS per-element static (base)	0 dBm
$P_{R,\max}$	RIS RF amp. budget (active RIS)	as specified per figure
Eavesdropper CSI (statistical case)		
$\widehat{\mathbf{g}}$, σ_g^2	Mean/channel error variance	model in Sec. 3.4
NEV	Normalized error variance	0 dB (default)
Monte Carlo and evaluation		
N_{MC}	Number of trials	10^3
Metric	Reported objective	SEE (3.2.7), SSR (3.3.6)

Notes: (i) In active vs. nearly-passive comparisons (Figs. 3.5.3–3.5.4), we set $P_{c,n}^{(p)} = 0$ dBm, $P_{c,n}^{(a)} \in [0, 40]$ dBm, $P_{0,\mathrm{RIS}}^{(a)} = 20$ dBm, and $P_{0,\mathrm{RIS}}^{(p)} = 10$ dBm. (ii) In quantization experiments (Figs. 3.5.6–3.5.9), RIS phase/amplitude quantizers use 1–4 bits over the amplitude interval derived from the global reflection constraint.

from the uncertainty in the RIS–eavesdropper channel; however, the performance loss remains minor. Even with statistical CSI, the SEE stays well above 10 Mb/J across the examined power range, confirming that secure and energy-efficient operation is preserved despite imperfect information.

It is also evident that the SEE-driven schemes (a) and (b) consume considerably less power than the SSR-oriented ones (c) and (d), especially at higher $P_{t,\max}$. Maximizing SSR alone encourages excessive use of transmit power, improving the achievable rates but degrading efficiency. In contrast, SEE-oriented optimization promotes a more balanced operating point that sustains high secrecy and low energy costs.

Finally, the heuristic and partially optimized baselines (e)–(g) exhibit much poorer performance, often by a significant margin. These outcomes demonstrate the necessity of a coordinated optimization across all design variables. When the RIS coefficients, transmit powers, and receive filters are not jointly optimized, energy efficiency and secrecy performance drop sharply, underscoring the advantage of the proposed framework.

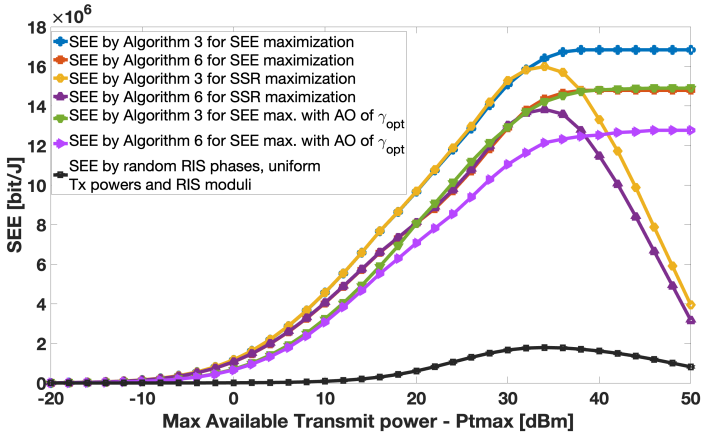

FIGURE 3.5.1: SEE versus $P_{t\,\max}$ for the schemes (a)–(g). $K = 4$, $N_B = 4$, $N = 100$, $n_h = n_{g,E} = 4$, $n_{g,B} = 2$.

Figure 3.5.2 presents the secrecy sum-rate (SSR) obtained for the same resource-allocation strategies considered in Fig. 3.5.1. As expected, when the optimization directly targets SSR, the achievable rate increases steadily with transmit power for both perfect and statistical CSI, showing the characteristic monotonic growth typical of power-limited systems. In contrast, the SSR curves corresponding to SEE-oriented designs exhibit an early saturation: since these schemes limit the transmit power to maximize energy efficiency, the rate eventually flattens once the optimum power balance is reached. This

behavior explains why the gap between SSR- and SEE-driven allocations becomes smaller at high $P_{t,\max}$, even though the underlying design objectives differ.

A further observation is that all proposed optimization frameworks substantially outperform the heuristic baseline (g), which relies on random RIS phases and uniform transmit power. That simple configuration yields markedly lower SSR and SEE values across the entire range of transmit powers, confirming the importance of coordinated resource allocation among the RIS, the users, and the BS.

Finally, the modified algorithmic variants (e)–(f), which refine the RIS coefficients via exhaustive per-element search, attain performance levels very close to those of the main proposed methods but at a considerably higher computational cost. This trade-off highlights the efficiency of the proposed optimization framework, which achieves nearly optimal results without resorting to costly brute-force tuning.

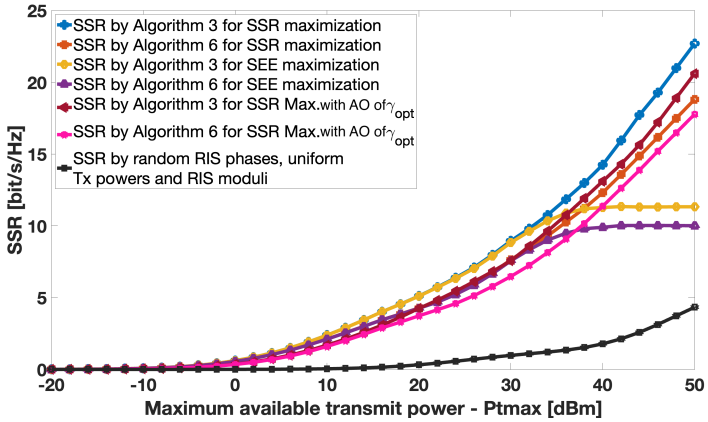

FIGURE 3.5.2: SSR versus $P_{t\max}$ for the schemes (a)–(g). Parameters as in Fig. 3.5.1.

3.5.2 Active versus Nearly-Passive RIS

Figures 3.5.3 and 3.5.4 present a comparison of the secrecy energy efficiency (SEE) obtained with active and nearly-passive RIS architectures under perfect and statistical CSI, respectively. In the nearly-passive case, each reflecting element operates with a fixed static power of $P_{c,n}^{(p)} = 0$ dBm.

For the active RIS, $P_{c,n}^{(a)}$ varies from 0 to 40 dBm, reflecting the extra consumption introduced by the analog reflection amplifiers. The residual

static power is set to $P_{0,\mathrm{RIS}}^{(a)} = 20$ dBm for the active case and $P_{0,\mathrm{RIS}}^{(p)} = 10$ dBm for the nearly-passive one, reflecting the additional circuitry required by the amplification hardware. Simulations are performed for two surface sizes, $N = 100$ and $N = 200$ elements.

The results highlight a distinct trade-off between amplification benefits and circuit-related costs. At low values of $P_{c,n}^{(a)}$, the active RIS achieves superior SEE, since the additional reflected signal power more than compensates for the slight increase in static consumption. As $P_{c,n}^{(a)}$ grows, this advantage gradually diminishes: the circuit losses start to dominate the energy budget, and cause the overall efficiency of the active surface to fall below that of its nearly-passive counterpart eventually.

The point at which this crossover occurs depends on the surface size: for larger N, the threshold appears at lower values of $P_{c,n}^{(a)}$ because the total static cost grows roughly linearly with the number of elements, making active operation increasingly inefficient in very large arrays.

From a design standpoint, these findings emphasize the need to align the RIS architecture with both the deployment scale and the underlying hardware efficiency. Active RISs are especially attractive for compact or medium-scale deployments, where their amplification capability can extend coverage and improve secrecy. When implemented with highly efficient low-power amplifiers, they deliver these gains without significantly burdening the energy budget.

In contrast, as the array size increases, nearly-passive RISs become the more attractive option—their negligible per-element power consumption maintains superior SEE even without amplification. In conclusion, the optimal RIS setup depends on the hardware's efficiency and the deployment's scale. Designing the system with energy awareness is key to unlocking the full advantages of active and nearly-passive RISs.

3.5.3 Impact of Channel Uncertainty

Figure 3.5.5 shows how channel uncertainty influences the secrecy energy efficiency (SEE). The quality of the RIS–eavesdropper channel estimate is measured by the normalized error variance (NEV). The analysis includes Algorithm 9 (perfect CSI) and Algorithm 12 (statistical CSI), each tested with RISs having $N = 100$ and $N = 200$ reflecting elements.

When perfect CSI is available, the SEE remains nearly constant across all NEV values, resulting in flat curves that act as reference points. However, when only statistical CSI is utilized, the SEE gradually decreases as the

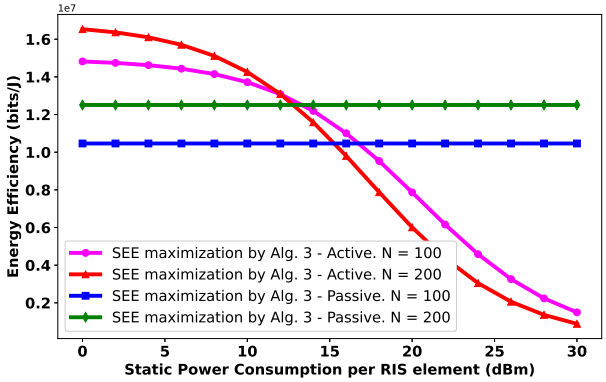

FIGURE 3.5.3: SEE (Algorithm 9, perfect CSI) for active and nearly-passive RISs versus static element consumption. $N \in \{100, 200\}$, $P_{t\,\max} = 30\,\text{dBm}$.

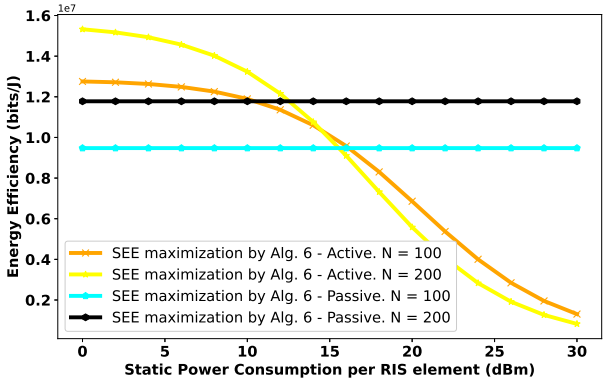

FIGURE 3.5.4: SEE (Algorithm 12, statistical CSI) for active and nearly-passive RISs versus static element consumption. $N \in \{100, 200\}$, $P_{t\,\max} = 30\,\text{dBm}$.

NEV increases. This decline occurs because the accuracy of the surrogate SINR model diminishes at higher NEV values. For small or moderate uncertainty levels (up to NEV $= 0$ dB), this degradation is barely visible, and Algorithm 12 performs nearly the same as its perfect-CSI counterpart. This confirms that the statistical design remains reliable under realistic estimation errors. When the uncertainty becomes larger, the SEE declines faster, with a stronger impact observed for $N = 200$. This suggests that bigger RIS arrays are more exposed to channel mismatches. In practice, statistical CSI still performs well under moderate uncertainty, but its advantage quickly fades as

estimation errors grow. Accurate statistical modeling of the eavesdropper's channel is essential to preserve the benefits of secure and energy-efficient operation.

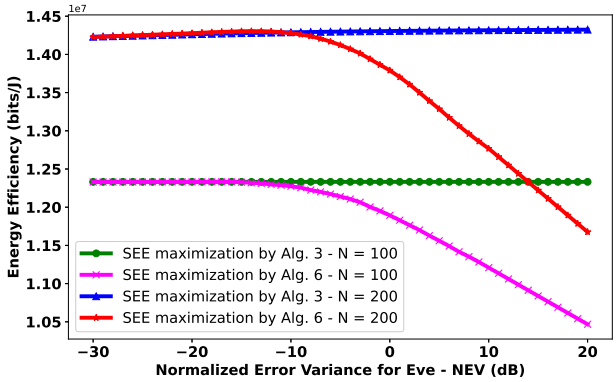

FIGURE 3.5.5: SEE versus NEV: Algorithms 9–12, $N \in \{100, 200\}$. $P_{t\,\max} = 30\,\text{dBm}$.

3.5.4 Relaxation and Projection

In practice, RIS hardware cannot realize reflection coefficients with continuous phase and amplitude values. This constraint stems from the use of finite-resolution phase shifters and discrete gain amplifiers, which together create a gap between the continuous-domain optimization model and what the hardware can actually implement. Bridging this gap is crucial for achieving RIS designs that are theoretically sound and feasible for practical deployment.

A widely used remedy is the *relaxation and projection* approach. Here, the optimization is first carried out in the continuous domain—as in Algorithms 9 and 12 to exploit the analytical tractability of convex approximations and sequential fractional programming. Once the continuous solution is obtained, the reflection coefficients are projected onto the discrete feasible set by quantizing both their amplitude and phase. This two-step process offers a practical middle ground, preserving the efficiency of convex optimization while remaining consistent with hardware limitations.

An added advantage of this approach lies in its computational scalability. Because each of the N reflecting elements is quantized independently, the complexity of the projection step grows only linearly with N.

Combined with the fact that the proposed algorithms already scale polynomially with surface size, the overall complexity remains polynomial. By contrast, tackling the discrete resource-allocation problem directly would lead to exponential complexity in N, making it impractical for large RIS deployments.

Quantization strategy. Each reflection coefficient γ_n, for $n = 1, \ldots, N$, has its phase uniformly quantized over the range $[0, 2\pi)$. The amplitude $|\gamma_n|$, however, must be quantized more carefully to ensure that the overall configuration satisfies the feasibility constraint

$$\operatorname{tr}\left(\mathbf{R}\boldsymbol{\gamma}\boldsymbol{\gamma}^H\right) \in \left[\operatorname{tr}(\mathbf{R}),\, P_{R,\max} + \operatorname{tr}(\mathbf{R})\right]. \tag{3.5.1}$$

which links all RIS coefficients through the global reflection constraint. A naïve setting such as $|\gamma_n|^2 \in [0,\, \operatorname{tr}(\mathbf{R}) + P_{R,\max}]$ would create an unnecessarily wide dynamic range and, as a result, lower the accuracy of the quantization.

To derive a tighter bound, let $\mathbf{R}$ be diagonal with diagonal entries r_n. It follows that

$$R_{\min}\|\boldsymbol{\gamma}\|^2 \leq \operatorname{tr}\left(\mathbf{R}\boldsymbol{\gamma}\boldsymbol{\gamma}^H\right) \leq R_{\max}\|\boldsymbol{\gamma}\|^2, \tag{3.5.2}$$

where $R_{\min}$ and $R_{\max}$ corresponds to the smallest and largest diagonal elements of $\mathbf{R}$, respectively. Substituting this expression into (3.5.1) gives

$$\frac{\operatorname{tr}(\mathbf{R})}{R_{\max}} \leq \|\boldsymbol{\gamma}\|^2 \leq \frac{\operatorname{tr}(\mathbf{R}) + P_{R,\max}}{R_{\min}}. \tag{3.5.3}$$

If the reflection coefficients are approximately uniform, so that $\|\boldsymbol{\gamma}\|^2 \approx N|\gamma_n|^2$, then under this assumption, the admissible range for the amplitude can be written as

$$|\gamma_n| \in \left[\sqrt{\frac{\operatorname{tr}(\mathbf{R})}{R_{\max}N}},\, \sqrt{\frac{\operatorname{tr}(\mathbf{R}) + P_{R,\max}}{R_{\min}N}}\right], \qquad n = 1, \ldots, N. \tag{3.5.4}$$

This interval is then uniformly quantized according to the desired number of bits for amplitude control.

Performance evaluation. Figures 3.5.6 and 3.5.7 display the resulting SEE performance under perfect and statistical CSI, respectively, when the coefficients obtained from Algorithms 9 and 12 are quantized with 1, 2, 3, and 4 bits. The unquantized (continuous) outcome is also a reference upper bound.

Across both CSI regimes, quantization with at least three bits yields the same performance as the continuous solution, providing an effective balance between energy efficiency and hardware cost. A modest but acceptable degradation is observed with two bits, whereas one-bit quantization causes a pronounced SEE loss. Interestingly, the performance loss due to quantization is smaller under statistical CSI, since precise RIS tuning becomes less critical when only statistical information about the eavesdropper's channel is available.

Figures 3.5.8 and 3.5.9 report the corresponding secrecy sum-rate (SSR) results. The overall trend is similar: using three or more quantization bits yields an SSR performance close to the continuous case, whereas a single-bit resolution proves insufficient.

A small but measurable performance gap persists even with four-bit quantization, especially at high $P_{t,\max}$ values in the perfect-CSI case. This confirms that SSR maximization is inherently more sensitive to quantization errors than SEE optimization, as secrecy rates depend more heavily on accurate interference management.

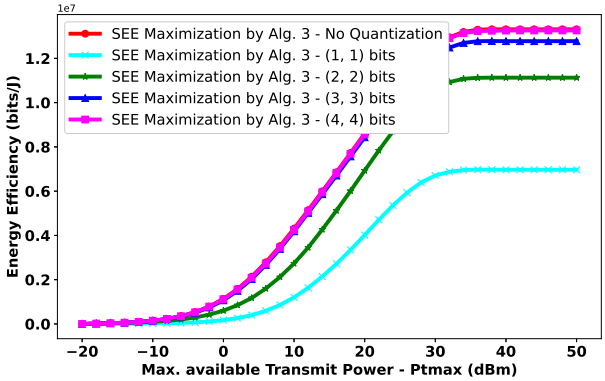

FIGURE 3.5.6: Quantized SEE (Algorithm 9, perfect CSI) versus $P_{t\,\max}$.

3.5.5 GEE–SR Operating Frontier

Figure 3.5.10 depicts the relationship between global energy efficiency (GEE) and the achievable sum-rate (SR), obtained by jointly considering the allocations that are optimal for SEE and for SSR. Each data point corresponds to a specific value of the maximum transmit power $P_{t,\max}$. For that power level, Algorithm 9 (perfect CSI) or Algorithm 12 (statistical CSI) is executed

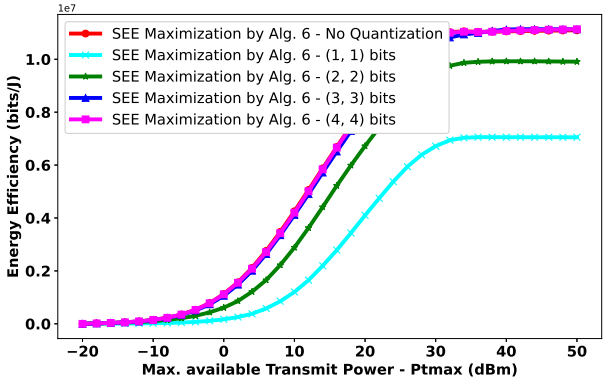

FIGURE 3.5.7: Quantized SEE (Algorithm 12, statistical CSI) versus $P_{t\max}$.

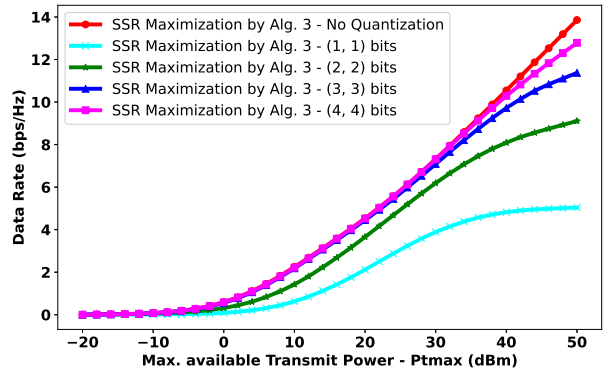

FIGURE 3.5.8: Quantized SSR (Algorithm 9, perfect CSI) versus $P_{t\max}$.

twice—first to maximize the SEE and then to maximize the SSR. The resulting GEE from the SEE-optimal allocation is plotted on the vertical axis, while the SR of the corresponding SSR-optimal solution is shown on the horizontal axis.

As the transmit-power limit increases, the SR grows monotonically, since the SSR-oriented design always exploits the entire available power budget. The GEE, however, exhibits a different trend: it rises initially and then levels off once the power surpasses the value that maximizes the SEE. Beyond this point, additional transmit power does not change the optimal resource allocation, and both the SEE and the resulting GEE remain nearly constant.

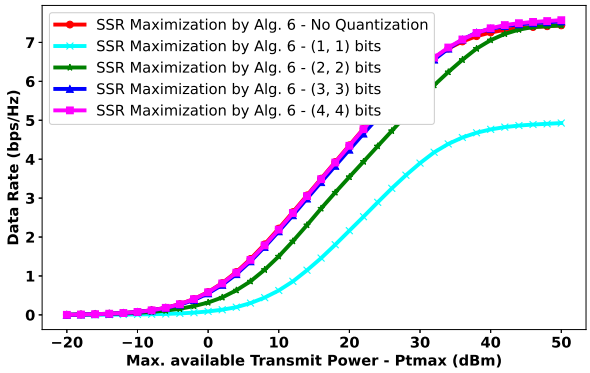

FIGURE 3.5.9: Quantized SSR (Algorithm 12, statistical CSI) versus $P_{t\,\max}$.

This plateau behavior reflects the intrinsic unimodality of the SEE function with respect to transmit power.

The obtained frontier makes the trade-off between energy-focused and rate-focused operation explicit. Allocations that pursue higher rates continue to improve SR but do so at the expense of energy efficiency. At the same time, energy-optimal operation provides no further benefit once the SEE peak has been reached. In practical terms, this curve offers guidance for network operators. Depending on the traffic load and the available power budget, they can choose to emphasize throughput or operate closer to the energy-efficient point of the trade-off.

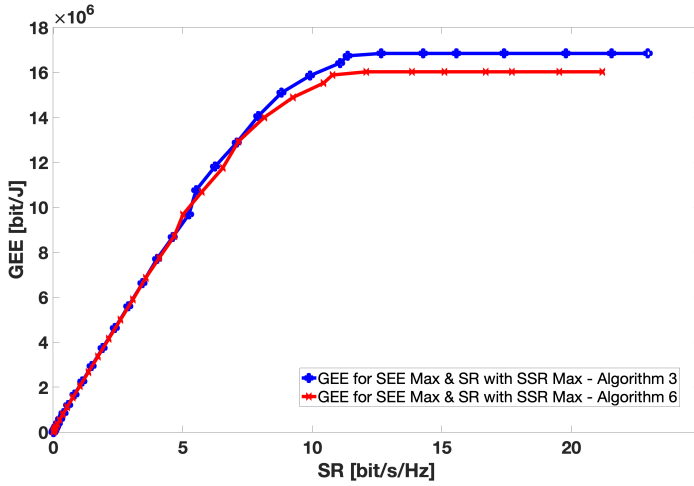

FIGURE 3.5.10: GEE (SEE design) vs. SR (SSR design) for Algorithms 9–12, $P_{t\,\max} \in [-20, 50]$ dBm. $K = 4$, $N_B = 4$, $N = 100$.

Chapter 4

Dual-Metasurface-Aided Networks: Secure Energy Efficiency Maximization

This chapter refers to articles published in the *EURASIP Journal on Advances in Signal Processing* (Open Access), 2025. https://rdcu.be/eJURW

4.1 Introduction

Building upon the unified modeling framework and energy- and secrecy-oriented design principles developed in the previous chapters, this chapter investigates a dual-metasurface architecture for secure and energy-efficient wireless communications. In particular, the focus is on combining a *reconfigurable holographic surface* (RHS) integrated in the near field of the base station (BS) with an environmental *reconfigurable intelligent surface* (RIS), thereby enabling joint spatial control in both the transmitter domain and the propagation environment.

Metasurface-assisted wireless systems have emerged as a promising alternative to fully digital massive MIMO architectures, primarily due to their ability to manipulate electromagnetic waves directly in the analog domain while significantly reducing the number of energy-intensive RF chains. This feature is particularly relevant in light of the growing energy consumption of current 5G infrastructures, where large digital antenna arrays have led to substantial static power overheads. By contrast, metasurfaces offer fine-grained spatial control with a much lower energy footprint, making them attractive candidates for sustainable 6G deployments.

Within this context, two complementary metasurface technologies have attracted considerable attention. Environmental RISs are typically deployed to create or enhance propagation paths, while RHSs are integrated in the near field of the BS antenna array to enable holographic beamforming with reduced digital complexity. The operating characteristics of these surfaces depend on their hardware realization: nearly-passive designs consume minimal control power but are affected by multiplicative fading over cascaded links, whereas active metasurfaces can partially mitigate this effect through reflection-type amplification at the cost of additional power consumption and noise. The dual-metasurface architecture considered in this chapter leverages the strengths of both approaches by jointly shaping the transmitted wavefront and the wireless environment.

In addition to energy efficiency, secure communication is a fundamental requirement for future wireless networks. Physical-layer security (PLS) provides an attractive complement to conventional cryptographic techniques by exploiting the physical properties of the wireless channel to ensure confidentiality with limited processing overhead. When combined with metasurface-assisted transmission, PLS techniques enable spatially selective enhancement of legitimate links while suppressing information leakage toward unintended receivers.

Motivated by these considerations, this chapter studies a downlink multiuser multiple-input single-output (MISO) system in which a BS communicates with multiple legitimate users through a dual-metasurface configuration comprising an RHS at the transmitter and an RIS deployed in the environment, in the presence of a passive eavesdropper. The objective is to maximize the minimum *secrecy energy efficiency* (SEE) across users, defined as the number of securely transmitted bits per unit of consumed energy, subject to constraints on transmit power, quality of service, and metasurface reflection coefficients. This formulation enables a unified evaluation of the trade-offs between energy efficiency, secrecy performance, and hardware complexity in dual-metasurface-assisted networks.

4.1.1 Prior Works

To jointly account for energy efficiency and physical-layer security, the notion of *secrecy energy efficiency* (SEE) has been introduced. It measures how much confidential information can be reliably transmitted for each joule of consumed energy [92]. Despite this unified perspective, most studies on metasurface-aided wireless networks have addressed either secrecy or energy efficiency in isolation.

Secrecy-oriented research. The study of RIS-assisted physical-layer security has gained significant attention. Prior work includes secrecy-outage analyses for RIS-based NOMA systems [48], [64] and investigations of discrete-phase RIS architectures [78]. Scenarios with multiple eavesdroppers were investigated in [87], and worst-case secrecy formulations for NOMA-based schemes were proposed in [98]. Beyond these, several works have focused on specific scenarios: secrecy-outage analysis with wireless power transfer [101], secrecy-rate optimization for space–ground communications [40], and multi-user secrecy improvement [49]. In addition, the authors of [88] examined how different channel conditions influence RIS-aided secrecy.

Energy-efficiency-oriented research. Most investigations targeting EE have not incorporated secrecy constraints. Examples include vehicular networks assisted by omnidirectional RISs [16], and joint power minimization and sum-rate maximization in RIS-aided MISO systems [103]. The study in [51] explored how different interconnection structures — fully connected versus sub-connected affect the performance of active RISs. Building on this line of work, [59] focused on multi-user EE optimization with QoS guarantees, applying fractional programming techniques [73]. In [65], the authors investigated hybrid metasurface architectures that integrate both passive and active elements to improve design flexibility and efficiency. In [35], the authors developed resource-allocation methods that improve multi-user energy efficiency in RIS-assisted systems. The study in [81] examined how bounded channel uncertainties affect the secrecy of satellite networks employing active RISs.

Secrecy energy efficiency (SEE). Only a few studies have treated SEE explicitly. Recent efforts such as [39], [55], [97] have focused mainly on nearly-passive RIS architectures, adopting machine-learning or alternating-optimization methods to maximize SEE. However, these contributions do not account for hybrid setups combining RIS and RHS, nor do they incorporate active metasurfaces. Evidence from visible-light communication studies [74] indicates that RISs can enhance secrecy and authentication, reflecting the broad applicability of metasurface-based secure links.

4.1.2 Contributions

In light of the above, this work presents a unified framework that jointly address both energy efficiency and physical-layer security in a dual-metasurface MISO system. The main contributions are summarized as follows:

- A downlink MISO configuration is investigated in which a multi-antenna base station (BS) serves multiple single-antenna users through two distinct metasurfaces. A reconfigurable intelligent surface (RIS) is placed in the propagation environment to improve the channel conditions. In contrast, a reconfigurable holographic surface (RHS) is integrated in the near field of the BS array to provide additional analog beamforming control. The BS transmits artificial noise further to reduce information leakage toward potential eavesdroppers [37].

- The optimization goal is to maximize the minimum secrecy energy efficiency (SEE) across users. This requires the joint design of the BS beamforming vectors, the covariance matrix of the artificial noise, and the reflection coefficients of both metasurfaces. Because the resulting formulation is non-convex and fractional in nature, it cannot be solved directly. A convergent algorithmic framework is therefore developed, combining the generalized Dinkelbach method with sequential convex approximation, Schur complement transformations, and an alternating optimization structure.

- The performance of the proposed dual-metasurface system is examined through a set of numerical experiments. The analysis compares the design with two benchmark configurations: one incorporating a single RIS and another relying on conventional digital beamforming. The results show that coordinated operation of the RHS and RIS provides marked gains in secrecy energy efficiency (SEE), particularly under practical power constraints.

Chapter Roadmap

The remainder of this chapter is divided into three main parts. Section 4.2 outlines the dual-metasurface downlink MISO system, describing the channel setup, the signal representation, and the main sources of power consumption. It also introduces the formulation of the secrecy energy-efficiency (SEE) maximization problem and its related constraints. Section 4.3 outlines how the optimization problem is solved. The method brings together the generalized Dinkelbach approach, sequential convex approximation, and Schur-complement tools, which are applied within an alternating optimization loop. Section 4.4 follows with the simulation outcomes, highlighting the main SEE performance trends and concluding the chapter with a brief discussion of the key observations.

4.2 System Model and Problem Formulation

This study examine a downlink multiple-input single-output (MISO) setup in which a base station (BS) equipped with M antennas transmits confidential information to K legitimate single-antenna users, while a passive eavesdropper attempts to intercept the communication. To enhance the received signal quality and reinforce physical-layer security, the BS operates together with two metasurfaces:

- A *reconfigurable holographic surface* (RHS) is installed close to the BS antenna array, operating in its near field. It contains N_t tunable elements that allow the transmitted wavefront to be shaped before it leaves the array.
- A *reconfigurable intelligent surface* (RIS) is placed farther away, along the wireless path between the BS and the users and it is loaded with N_r adjustable reflectors that modify the path and timing of incoming signals, enhancing the channel conditions for users.

The overall arrangement is shown in Figure 4.2.1, which offers a schematic representation. The RHS, positioned directly in front of the BS array, interacts with the outgoing electromagnetic field immediately after transmission, providing an additional layer of analog beam control in the near field. The RIS, situated at a strategically chosen location, redirects the incident waves to improve the effective propagation paths toward the intended receivers. In this dual-surface arrangement, both legitimate receivers and the eavesdropper observe superimposed signals that may experience one or two reflections. Each transmitted waveform can either (i) pass through the RHS alone before reaching its destination, or (ii) be successively reflected by both metasurfaces. Through joint control of the RHS and RIS, the BS can focus energy toward the legitimate users while weakening the signal intercepted by the eavesdropper, thereby improving both efficiency and confidentiality.

Channel Model

Let $\mathbf{Q}_t \in \mathbb{C}^{N_t \times M}$ denote the channel between the BS and the RHS, and $\mathbf{Q}_r \in \mathbb{C}^{N_r \times N_t}$ the channel from the RHS to the RIS. The channels from the RHS and the RIS to the k-th legitimate user are denoted by $\mathbf{h}_{t,k} \in \mathbb{C}^{N_t \times 1}$ and $\mathbf{h}_{r,k} \in \mathbb{C}^{N_r \times 1}$, respectively. In the same way, $\mathbf{g}_t \in \mathbb{C}^{N_t \times 1}$ and $\mathbf{g}_r \in \mathbb{C}^{N_r \times 1}$ describe the corresponding channels leading to the eavesdropper.

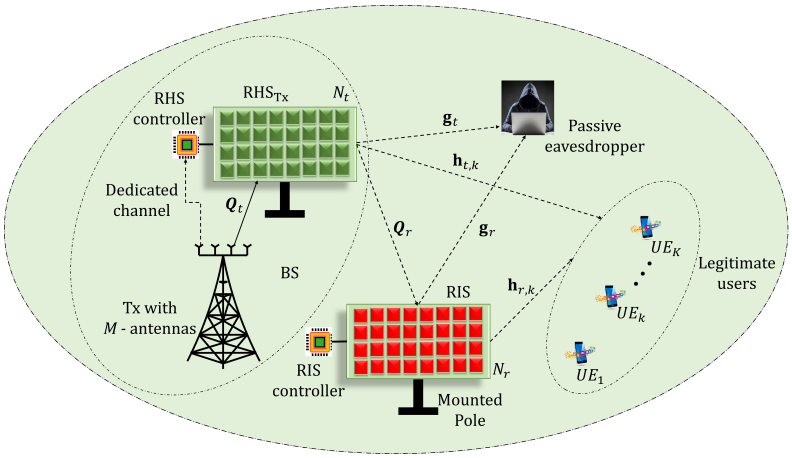

FIGURE 4.2.1: Dual-metasurface system model: an RHS is co-located with the BS antenna array to provide near-field holographic beamforming, while an RIS is deployed in the environment to further shape the propagation toward the users. Both the legitimate users and the eavesdropper are affected by signals reflected from the RHS and RIS.

Both metasurfaces work in a nearly passive configuration where each element changes only the phase of the incident signal and does not introduce any active amplification. The overall behavior of the two surfaces can be represented by the following diagonal reflection matrices:

$$\boldsymbol{\Gamma}_t = \mathrm{diag}(\beta_{t,1}, \ldots, \beta_{t,N_t}), \tag{4.2.1}$$

$$\boldsymbol{\Gamma}_r = \mathrm{diag}(\beta_{r,1}, \ldots, \beta_{r,N_r}), \tag{4.2.2}$$

with the elements satisfying the unit-modulus conditions

$$|\beta_{t,n}| = 1,\ n = 1, \ldots, N_t, \qquad |\beta_{r,n}| = 1,\ n = 1, \ldots, N_r. \tag{4.2.3}$$

Based on these definitions, the effective downlink channel seen by user k can be expressed as

$$\mathbf{h}_k^{\mathrm{eff}} = \left(\mathbf{h}_{t,k}^H \boldsymbol{\Gamma}_t \mathbf{Q}_t + \mathbf{h}_{r,k}^H \boldsymbol{\Gamma}_r \mathbf{Q}_r \boldsymbol{\Gamma}_t \mathbf{Q}_t\right)^H, \tag{4.2.4}$$

and the corresponding effective channel at the eavesdropper is given by

$$\mathbf{g}^{\mathrm{eff}} = \left(\mathbf{g}_t^H \boldsymbol{\Gamma}_t \mathbf{Q}_t + \mathbf{g}_r^H \boldsymbol{\Gamma}_r \mathbf{Q}_r \boldsymbol{\Gamma}_t \mathbf{Q}_t\right)^H. \tag{4.2.5}$$

Transmit Signal Model

For additional protection against eavesdropping, the base station includes artificial noise (AN) along with the useful information signals [37]. The transmitted signal is written as

$$\mathbf{x} = \sum_{k=1}^{K} \mathbf{w}_k s_k + \mathbf{z}, \tag{4.2.6}$$

where $\mathbf{w}_k \in \mathbb{C}^{M\times 1}$ denotes the beamforming vector of user k, s_k is the data symbol with $\mathbb{E}[|s_k|^2] = 1$, and $\mathbf{z}$ represents the artificial noise, whose covariance is given by $\mathbf{C}_z = \mathbb{E}[\mathbf{z}\mathbf{z}^H]$.

Because both the BS–RHS and BS–RHS–RIS links carry the artificial noise, it appears in all effective channels, including that of the eavesdropper. When the transmit beamformers, metasurface reflection coefficients, and artificial-noise covariance are optimized together, most of the unwanted energy can be directed toward the eavesdropper while its influence on legitimate users remains small. The use of two metasurfaces gives the system extra spatial degrees of freedom compared with a conventional single-RIS design, making it possible to reinforce the intended signals and at the same time disturb the eavesdropper's reception.

Achievable Rates and Secrecy Rate

For user k, the received waveform is corrupted by signals from other users, the intentionally injected artificial noise, and thermal noise $n_{u,k} \sim \mathcal{CN}(0, \sigma_{u,k}^2)$. Taking these effects into account, the achievable rate of user k is expressed as

$$R_k^{(u)} = \log_2\left(\frac{S_k^{(u)}}{I_k^{(u)}}\right), \tag{4.2.7}$$

where

$$S_k^{(u)} = \sum_{j=1}^{K} |\mathbf{h}_k^{\text{eff},H}\mathbf{w}_j|^2 + \mathbf{h}_k^{\text{eff},H}\mathbf{C}_z\mathbf{h}_k^{\text{eff}} + \sigma_{u,k}^2, \tag{4.2.8}$$

$$I_k^{(u)} = \sum_{j\neq k} |\mathbf{h}_k^{\text{eff},H}\mathbf{w}_j|^2 + \mathbf{h}_k^{\text{eff},H}\mathbf{C}_z\mathbf{h}_k^{\text{eff}} + \sigma_{u,k}^2. \tag{4.2.9}$$

The eavesdropper receives all transmitted signals together with the artificial noise and its own disturbance $n_e \sim \mathcal{CN}(0, \sigma_e^2)$. Its achievable rate when

trying to decode user k is

$$R_k^{(e)} = \log_2\left(\frac{S^{(e)}}{I_k^{(e)}}\right), \tag{4.2.10}$$

with

$$S^{(e)} = \sum_{j=1}^{K} |\mathbf{g}^{\text{eff},H}\mathbf{w}_j|^2 + \mathbf{g}^{\text{eff},H}\mathbf{C}_z\mathbf{g}^{\text{eff}} + \sigma_e^2, \tag{4.2.11}$$

$$I_k^{(e)} = \sum_{j\neq k} |\mathbf{g}^{\text{eff},H}\mathbf{w}_j|^2 + \mathbf{g}^{\text{eff},H}\mathbf{C}_z\mathbf{g}^{\text{eff}} + \sigma_e^2. \tag{4.2.12}$$

The achievable secrecy rate for user k is then given by

$$R_{\text{sec},k} = [\, R_k^{(u)} - R_k^{(e)} \,]^+, \tag{4.2.13}$$

where the operator $[\,\cdot\,]^+$ enforces that the secrecy rate remains non-negative. For clarity in later derivations, this operator is omitted, assuming that after optimization all users achieve positive secrecy rates.

Power Consumption Model

Recall that the SEE for user k is defined as the ratio between its achievable secrecy rate and the total power consumed during transmission, which can be expressed as:

$$\eta_k = \frac{R_{\text{sec},k}}{P_{\text{total},k}}. \tag{4.2.14}$$

Here, the total consumed power comprises two main components: the radiated transmit power and the static hardware power. The transmit power associated with user k can be written as

$$\|\mathbf{w}_k\|^2 + w_k \,\text{Tr}(\mathbf{C}_z), \tag{4.2.15}$$

where w_k denotes the fraction of artificial-noise (AN) power allocated to user k. Therefore, to distribute the artificial-noise (AN) power fairly among users, a softmax-based weighting function is adopted:

$$w_k = \frac{\exp(\lambda R_{\min,k})}{\sum_{j=1}^{K} \exp(\lambda R_{\min,j})}, \tag{4.2.16}$$

where $\lambda > 0$ controls the sensitivity of the power allocation to each user's minimum rate target.

The static part of the overall power consumption is modeled as follows:

$$P_{\text{static}} = MP_{\text{Tx,static}} + N_t P_{\text{RHS,static}} + N_r P_{\text{RIS,static}} + P_{\text{other}}, \tag{4.2.17}$$

where $P_{\text{Tx,static}}$ is the per-antenna static power at the BS, $P_{\text{RHS,static}}$ and $P_{\text{RIS,static}}$ denote the per-element static power consumptions of the RHS and RIS, respectively, and P_{other} accounts for additional circuitry and control overhead.

By combining the radiated and static contributions, the total power associated with user k becomes

$$P_{\text{total},k} = \|\mathbf{w}_k\|^2 + w_k(P_{\text{static}} + \text{Tr}(\mathbf{C}_z)) \,. \tag{4.2.18}$$

Substituting (4.2.18) into (4.2.14), the SEE expression is obtained as

$$\eta_k = \frac{R_{\text{sec},k}}{\|\mathbf{w}_k\|^2 + w_k(P_{\text{static}} + \text{Tr}(\mathbf{C}_z))}. \tag{4.2.19}$$

Optimization Problem

The design objective here is to maximize the minimum secrecy energy efficiency (SEE) among all users, while satisfying the system's quality-of-service (QoS) requirements, transmit-power limitations, and metasurface reflection constraints. The resulting optimization problem is then formulated as:

$$\max_{\{\mathbf{w}_k\},\mathbf{C}_z,\mathbf{\Gamma}_t,\mathbf{\Gamma}_r} \quad \min_k \ \eta_k \tag{4.2.20a}$$

$$\text{s.t.} \quad R_k^{(u)} \geq R_{\min,k}, \quad \forall k, \tag{4.2.20b}$$

$$\sum_{k=1}^{K} \|\mathbf{w}_k\|^2 + \text{Tr}(\mathbf{C}_z) \leq P_{\max}, \tag{4.2.20c}$$

$$|\beta_{t,n}| = 1, \quad n = 1, \ldots, N_t, \tag{4.2.20d}$$

$$|\beta_{r,n}| = 1, \quad n = 1, \ldots, N_r. \tag{4.2.20e}$$

Problem (4.2.20) is inherently non-convex due to the fractional SEE objective and the coupling among the beamforming vectors, artificial-noise covariance, and metasurface reflection coefficients. To obtain an efficient and

convergent solution, the following sections develop a structured optimization framework that combines fractional programming, sequential convex approximation, and alternating optimization techniques.

4.3 Proposed Solution Method

Solving Problem (4.2.20) directly is challenging due to several structural factors that render the optimization problem highly non-convex:

- The objective (4.2.20a) is a *non-differentiable* max–min fractional expression. As a result, traditional fractional programming cannot be applied directly because the design variables' secrecy-rate terms (numerators) are non-concave.
- The coexistence of *two metasurfaces* (RHS and RIS) further complicates the optimization. The reflection matrices are coupled through the intermediate channel $\mathbf{Q}_r$, so the overall response cannot be reduced to a single equivalent surface variable.
- The quality-of-service (QoS) constraints are *non-convex*, since the achievable rates of the legitimate users are not concave functions of the optimization parameters.

To address these challenges, an alternating-optimization framework is developed. The procedure iteratively updates three blocks of variables:

(i) the transmit covariances, including the beamforming vectors and artificial-noise covariance;

(ii) the reflection coefficients of the RHS;

(iii) the reflection coefficients of the RIS.

Each subproblem is reformulated using appropriate convex-approximation techniques to ensure tractable updates. The remainder of this section focuses on step (i), while the optimization of the metasurface reflections is presented in the subsequent subsections.

4.3.1 Optimization of Beamforming Vectors and AN Covariance

In this subproblem, the metasurface reflection matrices $\mathbf{\Gamma}_t$ and $\mathbf{\Gamma}_r$ remain fixed, while the optimization focuses on the transmit beamforming vectors

$\{\mathbf{w}_k\}$ and the artificial noise (AN) covariance $\mathbf{C}_z$. The problem can then be formulated as

$$\max_{\{\mathbf{w}_k\},\mathbf{C}_z} \quad \min_k \ \eta_k \tag{4.3.1a}$$

$$\text{s.t.} \quad R_k^{(u)} \geq R_{\min,k}, \quad \forall k, \tag{4.3.1b}$$

$$\sum_{k=1}^{K} \|\mathbf{w}_k\|^2 + \mathrm{Tr}(\mathbf{C}_z) \leq P_{\max}, \qquad \mathbf{C}_z \succeq \mathbf{0}. \tag{4.3.1c}$$

Generalized Dinkelbach reformulation. Let

$$f_k(\{\mathbf{w}_j\},\mathbf{C}_z) \triangleq R_{\text{sec},k}, \qquad g_k(\{\mathbf{w}_j\},\mathbf{C}_z) \triangleq \|\mathbf{w}_k\|^2 + w_k(P_{\text{static}} + \mathrm{Tr}(\mathbf{C}_z)).$$

The optimization in (4.3.1) involves maximizing the minimum across a set of fractional objectives. To handle this class of problems, the generalized Dinkelbach procedure [95] extends the well-known single-ratio approach to the multi-ratio case. At iteration i, the method solves

$$\max_{\{\mathbf{w}_k\},\mathbf{C}_z} \quad \min_k \Big\{ f_k(\{\mathbf{w}_j\},\mathbf{C}_z) - \lambda^{(i)}\, g_k(\{\mathbf{w}_j\},\mathbf{C}_z) \Big\} \tag{4.3.2a}$$

$$\text{s.t.} \quad R_k^{(u)} \geq R_{\min,k},\ \forall k, \qquad \sum_k \|\mathbf{w}_k\|^2 + \mathrm{Tr}(\mathbf{C}_z) \leq P_{\max},\ \mathbf{C}_z \succeq \mathbf{0}, \tag{4.3.2b}$$

and updates the parameter

$$\lambda^{(i+1)} = \min_k \frac{f_k(\{\mathbf{w}_j^\star\},\mathbf{C}_z^\star)}{g_k(\{\mathbf{w}_j^\star\},\mathbf{C}_z^\star)}. \tag{4.3.3}$$

Algorithm 13 Generalized Dinkelbach Algorithm for (4.3.1)

Input: tolerance $\varepsilon > 0$; feasible initialization $(\{\mathbf{w}_k^{(0)}\},\mathbf{C}_z^{(0)})$; set $\lambda^{(0)} = 0$.
repeat
  Solve (4.3.2) $\rightarrow (\{\mathbf{w}_k^\star\},\mathbf{C}_z^\star)$.
  Update $\lambda^{(i+1)}$ using (4.3.3); set $\Delta \leftarrow \lambda^{(i+1)} - \lambda^{(i)}$.
until $|\Delta| \leq \varepsilon$ or no further improvement is observed.

Discussion. At every iteration, Algorithm 13 replaces the fractional structure with a difference formulation parameterized by $\lambda^{(i)}$. The parameter $\lambda^{(i)}$

represents the current estimate of the minimum SEE that can be attained under the existing beamforming and AN configuration. In this sense, it acts simultaneously as an optimization variable and a running lower bound on the achievable SEE.

Remark 4.3.1 (Monotonic behavior). When each instance of subproblem (4.3.2) is solved exactly, the sequence $\{\lambda^{(i)}\}$ produced by the generalized Dinkelbach method increases monotonically and converges to the optimal solution of (4.3.1). In practical implementations, where the inner problems are solved approximately, the same upward trend persists until the numerical tolerance is reached; at this point, successive updates naturally flatten out.

Proposition 4.3.1 (Convergence of the generalized Dinkelbach method)**.** *If Problem* (4.3.2) *is solved to global optimality at every iteration, Algorithm 13 attains the global solution of* (4.3.1) *within a finite number of iterations. In cases where the subproblems are solved only approximately, the sequence* $\{\lambda^{(i)}\}$ *remains monotonic and the procedure converges to a stationary point of the relaxed formulation.*

Implementation notes.

- **Initialization:** setting $\lambda^{(0)} = 0$ ensures that the procedure starts from a feasible point and establishes a valid lower bound for the SEE metric.
- **Stopping rule:** the algorithm's progress can be tracked through the quantity $\Delta = \lambda^{(i+1)} - \lambda^{(i)}$. Since the sequence $\{\lambda^{(i)}\}$ is non-decreasing, Δ provides a simple and reliable indicator of convergence.
- **Computational aspects:** relative to bisection-based search methods, the generalized Dinkelbach procedure generally converges in fewer iterations and does not require multiple feasibility evaluations at each step.

Despite this reformulation, the inner problem (4.3.2) remains non-convex because the optimization variables' secrecy-rate functions are not concave. To address this difficulty, a concave surrogate is constructed using matrix lifting and first-order majorization, as discussed in the following section.

Lifting and DC structure. To simplify the non-convex beamforming subproblem, a lifting reformulation is adopted. In this approach, each transmit beamforming vector is replaced by a Hermitian positive semidefinite matrix $\mathbf{W}_k = \mathbf{w}_k \mathbf{w}_k^H \succeq \mathbf{0}$, which captures the second-order structure of the transmitted signal. For convenience, we also define the rank-one channel matrices

$$\mathbf{H}_k^{\text{eff}} = \mathbf{h}_k^{\text{eff}} \mathbf{h}_k^{\text{eff}H}, \qquad \mathbf{G}^{\text{eff}} = \mathbf{g}^{\text{eff}} \mathbf{g}^{\text{eff}H}.$$

These matrices represent the effective channels seen by the legitimate users and the eavesdropper, respectively. Based on these definitions, the received signal and interference components can be written as

$$S_k^{(u)} = \sum_j \mathrm{Tr}\big(\mathbf{H}_k^{\mathrm{eff}}(\mathbf{W}_j + \mathbf{C}_z)\big) + \sigma_{u,k}^2, \quad I_k^{(u)} = \sum_{j\neq k} \mathrm{Tr}\big(\mathbf{H}_k^{\mathrm{eff}}(\mathbf{W}_j + \mathbf{C}_z)\big) + \sigma_{u,k}^2,$$
$$S^{(e)} = \sum_j \mathrm{Tr}\big(\mathbf{G}^{\mathrm{eff}}(\mathbf{W}_j + \mathbf{C}_z)\big) + \sigma_e^2, \quad I_k^{(e)} = \sum_{j\neq k} \mathrm{Tr}\big(\mathbf{G}^{\mathrm{eff}}(\mathbf{W}_j + \mathbf{C}_z)\big) + \sigma_e^2. \tag{4.3.4}$$

The corresponding user and eavesdropper rates can then be rewritten as

$$R_k^{(u)} = \underbrace{\log_2 S_k^{(u)}}_{g_{1,k}^{(u)}} - \underbrace{\log_2 I_k^{(u)}}_{g_{2,k}^{(u)}}, \qquad R_k^{(e)} = \underbrace{\log_2 S^{(e)}}_{g_1^{(e)}} - \underbrace{\log_2 I_k^{(e)}}_{g_{2,k}^{(e)}}, \tag{4.3.5}$$

$$R_{\mathrm{sec},k} = \big(g_{1,k}^{(u)} + g_{2,k}^{(e)}\big) - \big(g_{2,k}^{(u)} + g_1^{(e)}\big), \tag{4.3.6}$$

which reveals a difference-of-concave (DC) structure in the variables $(\{\mathbf{W}_j\}, \mathbf{C}_z)$.

Let $(\{\mathbf{W}_j^{(n)}\}, \mathbf{C}_z^{(n)})$ denote the current iterate. Since $-g_{2,k}^{(u)}$ and $-g_1^{(e)}$ are convex functions, their first-order Taylor expansions act as global underestimators:

$$\begin{aligned} -g_{2,k}^{(u)} \;=\; -\log_2 I_k^{(u)} \;\geq\; -\log_2 I_k^{(u)(n)} - \frac{1}{I_k^{(u)(n)}\ln 2}\Bigg[2\,\Re\Bigg\{\sum_{j\neq k}\mathrm{Tr}\Big(\mathbf{H}_k^{\mathrm{eff}}(\mathbf{W}_j - \mathbf{W}_j^{(n)})\Big)\Bigg\} \\ +\; 2\,\Re\Bigg\{\mathrm{Tr}\Big(\mathbf{H}_k^{\mathrm{eff}}(\mathbf{C}_z - \mathbf{C}_z^{(n)})\Big)\Bigg\}\Bigg] \;\triangleq\; \widetilde{g}_{2,k}^{(u)}, \end{aligned} \tag{4.3.7}$$

$$\begin{aligned} -g_1^{(e)} \;=\; -\log_2 S^{(e)} \;\geq\; -\log_2 S^{(e)(n)} - \frac{1}{S^{(e)(n)}\ln 2}\Bigg[2\,\Re\Bigg\{\sum_{j}\mathrm{Tr}\Big(\mathbf{G}^{\mathrm{eff}}(\mathbf{W}_j - \mathbf{W}_j^{(n)})\Big)\Bigg\} \\ +\; 2\,\Re\Bigg\{\mathrm{Tr}\Big(\mathbf{G}^{\mathrm{eff}}(\mathbf{C}_z - \mathbf{C}_z^{(n)})\Big)\Bigg\}\Bigg] \;\triangleq\; \widetilde{g}_1^{(e)}. \end{aligned} \tag{4.3.8}$$

Based on these approximations, the secrecy rate can be bounded as

$$\widetilde{R}_{\mathrm{sec},k} = g_{1,k}^{(u)} + g_{2,k}^{(e)} + \widetilde{g}_{2,k}^{(u)} + \widetilde{g}_1^{(e)} \;\leq\; R_{\mathrm{sec},k},$$

and likewise $\widetilde{R}_k^{(u)} = g_{1,k}^{(u)} - \widetilde{g}_{2,k}^{(u)} \leq R_k^{(u)}$.

Lemma 4.3.1 (Tightness at the expansion point)**.** *For every user k, the surrogate functions satisfy $\widetilde{R}_{\mathrm{sec},k} = R_{\mathrm{sec},k}$ and $\widetilde{R}_k^{(u)} = R_k^{(u)}$ at the expansion point*

$(\{\mathbf{W}_j^{(n)}\}, \mathbf{C}_z^{(n)})$. *Furthermore,* $\widetilde{R}_{\mathrm{sec},k} \le R_{\mathrm{sec},k}$ *and* $\widetilde{R}_k^{(u)} \le R_k^{(u)}$ *hold for all feasible* $(\{\mathbf{W}_j\}, \mathbf{C}_z)$.

Replacing the secrecy-rate and QoS terms with their concave surrogates yields the following optimization problem:

$$\max_{\{\mathbf{W}_k \succeq \mathbf{0}\}, \mathbf{C}_z \succeq \mathbf{0}} \quad \min_k \left\{ \widetilde{R}_{\mathrm{sec},k}(\{\mathbf{W}_j\}, \mathbf{C}_z) - \lambda_{\mathrm{old}} \left[\mathrm{Tr}(\mathbf{W}_k) + w_k \left(P_{\mathrm{static}} + \mathrm{Tr}(\mathbf{C}_z) \right) \right] \right\} \tag{4.3.9a}$$

$$\text{s.t.} \quad \widetilde{R}_k^{(u)}(\{\mathbf{W}_j\}, \mathbf{C}_z) \ge R_{\min,k}, \quad \forall k, \tag{4.3.9b}$$

$$\sum_{k=1}^{K} \mathrm{Tr}(\mathbf{W}_k) + \mathrm{Tr}(\mathbf{C}_z) \le P_{\max}, \tag{4.3.9c}$$

$$\mathrm{rank}(\mathbf{W}_k) = 1, \quad k = 1, \ldots, K. \tag{4.3.9d}$$

Problem (4.3.9) would be convex were it not for the rank-one restrictions in (4.3.9d), which ensure that each $\mathbf{W}_k$ corresponds to a valid beamforming vector $\mathbf{w}_k$. Because these constraints make the problem non-convex and challenging to solve directly, a spectral penalty method is introduced in the following section to handle them efficiently.

Rank-one enforcement via spectral penalty. The lifted variables $\mathbf{W}_k = \mathbf{w}_k \mathbf{w}_k^H \succeq \mathbf{0}$ must satisfy the implicit rank-one condition $\mathrm{rank}(\mathbf{W}_k) = 1$ in order to represent valid beamforming vectors. Enforcing this property directly makes the optimization problem non-convex and challenging to solve. A common workaround involves the use of semidefinite relaxation (SDR). In this approach, the explicit rank constraint in the original formulation is relaxed, and the resulting convex problem is solved to obtain a feasible approximation of the optimal solution. After obtaining the resulting high-rank covariance matrices, we recover the rank-one solutions through post-processing techniques, such as Gaussian randomization or eigenvalue-based rank reduction.

Although simple to implement, this method provides no optimality guarantee and can lead to significant performance loss, especially when the underlying channels are highly correlated.

To address this limitation, a penalty-based method is adopted instead. Rather than explicitly forcing the matrices to be rank-one, a continuous penalty term is added to the objective so that, as the penalty weight increases, the feasible matrices automatically converge toward a rank-one structure.

For a Hermitian positive semidefinite matrix $\mathbf{W}_k$ with eigenvalues $\mu_1 \geq \mu_2 \geq \cdots \geq \mu_M \geq 0$, a useful measure of its deviation from rank-one is

$$\rho(\mathbf{W}_k) = \mathrm{Tr}(\mathbf{W}_k) - \lambda_{\max}(\mathbf{W}_k) = \sum_{i=2}^{M} \mu_i(\mathbf{W}_k). \tag{4.3.10}$$

By definition, $\rho(\mathbf{W}_k) \geq 0$ becomes zero only when all eigenvalues except the largest vanish. Hence $\rho(\mathbf{W}_k)$ can be interpreted as a smooth indicator of how far $\mathbf{W}_k$ is from being rank-one.

Lemma 4.3.2 (Rank-one penalty)**.** *Let* $\mathbf{W}_k \succeq 0$*. Then* $\rho(\mathbf{W}_k) = 0$ *if and only if* $\mathrm{rank}(\mathbf{W}_k) = 1$*. Moreover,* $\rho(\mathbf{W}_k)$ *is convex and* 1*-Lipschitz continuous.*

Sketch of proof. Since $\mathrm{Tr}(\mathbf{W}_k) = \sum_i \mu_i(\mathbf{W}_k)$, the difference $\rho(\mathbf{W}_k) = \mathrm{Tr}(\mathbf{W}_k) - \lambda_{\max}(\mathbf{W}_k)$ reduces to $\sum_{i\geq 2} \mu_i(\mathbf{W}_k)$. This term is nonnegative and equals zero only when all eigenvalues except the largest are zero, corresponding to $\mathbf{W}_k$ having a single nonzero eigenvalue (i.e., rank one). The convexity and Lipschitz continuity of $\rho(\mathbf{W}_k)$ follow directly from the convexity of the spectral norm $\lambda_{\max}(\mathbf{W}_k)$ and the linearity of the trace operator. ■

Including $\rho(\mathbf{W}_k)$ in the objective, weighted by a coefficient $\alpha_k > 0$, yields a differentiable penalty term that progressively drives the solution toward the rank-one manifold. For sufficiently large α_k, the matrices $\mathbf{W}_k$ obtained from the optimization are practically rank-one, allowing the corresponding beamforming vectors to be recovered by eigen-decomposition.

Convex surrogate formulation. The penalized subproblem becomes

$$\max_{\{\mathbf{W}_k \succeq 0\}, \mathbf{C}_z \succeq 0} \quad \min_k \left\{ \widetilde{R}_{\mathrm{sec},k}(\{\mathbf{W}_j\}, \mathbf{C}_z) - \lambda_{\mathrm{old}} \Big(\mathrm{Tr}(\mathbf{W}_k) + w_k \big(P_{\mathrm{static}} + \mathrm{Tr}(\mathbf{C}_z) \big) \Big) \right\}$$
$$+ \sum_{k=1}^{K} \alpha_k \big(\lambda_{\max}(\mathbf{W}_k) - \mathrm{Tr}(\mathbf{W}_k) \big) \tag{4.3.11a}$$

$$\text{s.t.} \quad \widetilde{R}_k^{(u)}(\{\mathbf{W}_j\}, \mathbf{C}_z) \geq R_{\min,k}, \ \forall k, \tag{4.3.11b}$$

$$\sum_{k=1}^{K} \mathrm{Tr}(\mathbf{W}_k) + \mathrm{Tr}(\mathbf{C}_z) \leq P_{\max}.$$

The only non-convex element in (4.3.11a) is the spectral norm $\lambda_{\max}(\mathbf{W}_k)$. To preserve the concavity of the objective, this term is replaced by its first-order Taylor approximation evaluated at the current iterate $\mathbf{W}_k^{(n)}$:

$$\lambda_{\max}(\mathbf{W}_k) \geq \lambda_{\max}(\mathbf{W}_k^{(n)}) + 2\,\Re\Big\{ \mathrm{Tr}\big(\mathbf{u}_{\max}^{(n)} \mathbf{u}_{\max}^{(n)H} (\mathbf{W}_k - \mathbf{W}_k^{(n)}) \big) \Big\} \triangleq \widetilde{G}_k(\mathbf{W}_k), \tag{4.3.12}$$

where $\mathbf{u}_{\max}^{(n)}$ is the principal eigenvector of $\mathbf{W}_k^{(n)}$. Substituting $\widetilde{G}_k(\mathbf{W}_k)$ into (4.3.11) produces the convex surrogate

$$\max_{\{\mathbf{W}_k \succeq 0\}, \mathbf{C}_z \succeq 0} \quad \min_k \left\{ \widetilde{R}_{\text{sec},k}(\{\mathbf{W}_j\}, \mathbf{C}_z) - \lambda_{\text{old}} \Big(\text{Tr}(\mathbf{W}_k) + w_k \big(P_{\text{static}} + \text{Tr}(\mathbf{C}_z) \big) \Big) \right\}$$
$$+ \sum_{k=1}^{K} \alpha_k \big(\widetilde{G}_k(\mathbf{W}_k) - \text{Tr}(\mathbf{W}_k) \big) \tag{4.3.13a}$$

$$\text{s.t.} \quad \widetilde{R}_k^{(u)}(\{\mathbf{W}_j\}, \mathbf{C}_z) \geq R_{\min,k}, \ \forall k, \tag{4.3.13b}$$
$$\sum_{k=1}^{K} \text{Tr}(\mathbf{W}_k) + \text{Tr}(\mathbf{C}_z) \leq P_{\max}.$$

At this stage, the optimization becomes convex, which means it can be solved directly with standard semidefinite programming tools. In practice, the optimization problem is solved iteratively. After each iteration, the variables $\{\mathbf{W}_k\}$, $\mathbf{C}_z$, and the expansion point $\mathbf{W}_k^{(n)}$ are updated, and the problem is addressed again using these new values. As the iterations continue, the matrices gradually approach a rank-one structure, while the overall SEE keeps increasing until it reaches convergence.

Remark 4.3.2 (Convexity of the surrogate). The optimization problem in (4.3.13) is convex. Its objective is the minimum of several concave functions combined with linear terms, while all constraints preserve convexity. As a result, the problem admits a globally optimal solution that can be obtained using conventional semidefinite or conic optimization solvers. The associated computational cost grows polynomially with the system dimensions, making the approach tractable for practical problem sizes.

Although (4.3.13) provides a convex formulation, it remains a *local surrogate* of the original non-convex problem (4.3.2). This stems from the fact that the concave lower bounds $\widetilde{R}_{\text{sec},k}$ and $\widetilde{R}_k^{(u)}$ are constructed through first-order linearization at the current operating point. To gradually tighten these approximations and approach a stationary solution of the original difference-of-convex (DC) formulation, the convex surrogate is placed within a *Sequential Fractional Programming (SFP)* loop. In each iteration of the SFP process, the surrogate model is updated around the latest estimate, solved to optimality, and then used as the basis for the next linearization step. The process is repeated until the improvement between consecutive steps becomes negligible. The resulting procedure is outlined in Algorithm 14.

Algorithm 14 Sequential Fractional Programming (inner loop for (4.3.2))

Input: tolerance $\varepsilon > 0$, initial feasible point $(\{\mathbf{W}_k^{(0)}\}, \mathbf{C}_z^{(0)})$, and corresponding eigenvectors $\mathbf{u}_{\max}^{(0)}$.
repeat
Solve (4.3.13) to obtain $(\{\mathbf{W}_k^\star\}, \mathbf{C}_z^\star)$;
Update the dominant eigenvectors $\mathbf{u}_{\max}^{(n+1)}$ from $\{\mathbf{W}_k^\star\}$;
Compute the change Err $\leftarrow |F(\{\mathbf{W}_k^\star\}, \mathbf{C}_z^\star) - F(\{\mathbf{W}_k^{(n)}\}, \mathbf{C}_z^{(n)})|$, where F denotes the objective in (4.3.13);
Set $\{\mathbf{W}_k^{(n+1)}\} \leftarrow \{\mathbf{W}_k^\star\}$, $\mathbf{C}_z^{(n+1)} \leftarrow \mathbf{C}_z^\star$;
until Err $\leq \varepsilon$
Recover beamformers $\mathbf{w}_k$ as the principal components of $\mathbf{W}_k^\star$.

Remark 4.3.3 (Gradients in (4.3.7)–(4.3.8)). The gradients used for the first-order expansions are $\nabla_{\mathbf{W}_j} S_k^{(u)} = \mathbf{H}_k^{\text{eff}}$, $\nabla_{\mathbf{W}_j} I_k^{(u)} = \mathbf{H}_k^{\text{eff}} \mathbf{1}_{\{j \neq k\}}$, $\nabla_{\mathbf{W}_j} S^{(e)} = \mathbf{G}^{\text{eff}}$, and $\nabla_{\mathbf{W}_j} I_k^{(e)} = \mathbf{G}^{\text{eff}} \mathbf{1}_{\{j \neq k\}}$. Similarly, $\nabla_{\mathbf{C}_z} S_k^{(u)} = \mathbf{H}_k^{\text{eff}}$ and $\nabla_{\mathbf{C}_z} S^{(e)} = \mathbf{G}^{\text{eff}}$. These expressions lead directly to the trace formulations in (4.3.7)–(4.3.8).

Proposition 4.3.2 (Monotonicity and convergence of the inner loop)**.** *If the surrogate functions are tight at their respective linearization points (as stated in Lemma 4.3.1) and each subproblem in* (4.3.13) *is solved exactly, then Algorithm 14 produces a non-decreasing sequence of the minimum SEE surrogate values which converges to a stationary solution for the DC-approximated problem. Combined with the outer Dinkelbach iterations in Algorithm 13, the resulting SEE sequence remains non-decreasing until convergence.*

Remark 4.3.4 (Implementation considerations). To enhance numerical stability and improve convergence behavior, it is often beneficial to include a small regularization term in the initialization of $\mathbf{C}_z$. In practical implementations, initializing the covariance matrices with heuristic precoders such as maximum-ratio transmission (MRT) or zero-forcing (ZF) generally provides a good starting point. Furthermore, gradually increasing the penalty weights α_k whenever the rank-one indicator $\rho(\mathbf{W}_k)$ ceases to decrease has been found to yield faster convergence and more stable updates. Detailed parameter settings and numerical configurations used in the simulations are provided in Appendix A.2.

4.3.2 Optimization of the RHS Reflection $\mathbf{\Gamma}_t$

In this stage, the reflection matrix of the RHS is optimized while keeping the transmit covariances and the RIS configuration fixed. Let the matrices $\{\mathbf{W}_k\}_{k=1}^K$, $\mathbf{C}_z$, and $\mathbf{\Gamma}_r$ be given. The RHS reflection matrix is given as $\mathbf{\Gamma}_t = \mathrm{diag}(\beta_{t,1}, \ldots, \beta_{t,N_t})$, where each element satisfies $|\beta_{t,n}| = 1$. The corresponding effective channels depend on $\mathbf{\Gamma}_t$ as

$$\mathbf{h}_k^{\mathrm{eff}H} = \mathbf{h}_{t,k}^H \mathbf{\Gamma}_t \mathbf{Q}_t + \mathbf{h}_{r,k}^H \mathbf{\Gamma}_r \mathbf{Q}_r \mathbf{\Gamma}_t \mathbf{Q}_t, \qquad \mathbf{g}^{\mathrm{eff}H} = \mathbf{g}_t^H \mathbf{\Gamma}_t \mathbf{Q}_t + \mathbf{g}_r^H \mathbf{\Gamma}_r \mathbf{Q}_r \mathbf{\Gamma}_t \mathbf{Q}_t.$$

Since the denominator of the SEE expression does not depend on $\mathbf{\Gamma}_t$, the RHS update reduces to maximizing the secrecy rate under QoS and unit-modulus constraints:

$$\max_{\mathbf{\Gamma}_t} \quad \min_k \; R_{\mathrm{sec},k} \tag{4.3.14a}$$

$$\text{s.t.} \quad R_k^{(u)} \geq R_{\min,k}, \quad \forall k, \tag{4.3.14b}$$

$$|\beta_{t,n}| = 1, \quad n = 1, \ldots, N_t. \tag{4.3.14c}$$

Problem (4.3.14) is non-convex, as neither $R_{\mathrm{sec},k}$ nor $R_k^{(u)}$ is concave in $\mathbf{\Gamma}_t$. To proceed, we introduce a lifted formulation that replaces the unit-modulus variables with a Hermitian semidefinite matrix representation. Let $\gamma_t = [\beta_{t,1}, \ldots, \beta_{t,N_t}]^T$ and define $\mathbf{X}_t = \gamma_t^* \gamma_t^T \in \mathbb{C}^{N_t \times N_t}$. The unit-modulus conditions imply $[\mathbf{X}_t]_{nn} = 1$ and $\mathrm{rank}(\mathbf{X}_t) = 1$.

Next, define the auxiliary matrices

$$\mathbf{B}_e \triangleq \mathbf{Q}_t^H \,\mathrm{diag}\big(\mathbf{g}_t + \mathbf{Q}_r^H \mathbf{\Gamma}_r^H \mathbf{g}_r\big), \qquad \mathbf{B}_k \triangleq \mathbf{Q}_t^H \,\mathrm{diag}\big(\mathbf{h}_{t,k} + \mathbf{Q}_r^H \mathbf{\Gamma}_r^H \mathbf{h}_{r,k}\big).$$

These matrices compactly describe how the reflected signals depend on the RHS coefficients. The received signal power terms can then be written as quadratic forms in $\mathbf{X}_t$; for instance, $\left|\mathbf{h}_k^{\mathrm{eff}H} \mathbf{w}_j\right|^2 = \mathrm{Tr}(\mathbf{B}_k \mathbf{X}_t \mathbf{B}_k^H \mathbf{W}_j)$ and $\mathbf{h}_k^{\mathrm{eff}H} \mathbf{C}_z \mathbf{h}_k^{\mathrm{eff}} = \mathrm{Tr}(\mathbf{B}_k \mathbf{X}_t \mathbf{B}_k^H \mathbf{C}_z)$, with similar expressions for the eavesdropper using $\mathbf{B}_e$.

Substituting these relations into the rate definitions gives

$$R_k^{(u)} = \underbrace{\log_2\Big(\sum_{j=1}^{K}\mathrm{Tr}(\mathbf{B}_k\mathbf{X}_t\mathbf{B}_k^H\mathbf{W}_j)+\mathrm{Tr}(\mathbf{B}_k\mathbf{X}_t\mathbf{B}_k^H\mathbf{C}_z)+\sigma_{u,k}^2\Big)}_{f_{1,k}^{(u)}(\mathbf{X}_t)} - \underbrace{\log_2\Big(\sum_{j\neq k}\mathrm{Tr}(\mathbf{B}_k\mathbf{X}_t\mathbf{B}_k^H\mathbf{W}_j)+\mathrm{Tr}(\mathbf{B}_k\mathbf{X}_t\mathbf{B}_k^H\mathbf{C}_z)+\sigma_{u,k}^2\Big)}_{f_{2,k}^{(u)}(\mathbf{X}_t)}, \tag{4.3.15}$$

and similarly for the eavesdropper,

$$R_k^{(e)} = \underbrace{\log_2\Big(\sum_{j=1}^{K}\mathrm{Tr}(\mathbf{B}_e\mathbf{X}_t\mathbf{B}_e^H\mathbf{W}_j)+\mathrm{Tr}(\mathbf{B}_e\mathbf{X}_t\mathbf{B}_e^H\mathbf{C}_z)+\sigma_e^2\Big)}_{f_1^{(e)}(\mathbf{X}_t)} - \underbrace{\log_2\Big(\sum_{j\neq k}\mathrm{Tr}(\mathbf{B}_e\mathbf{X}_t\mathbf{B}_e^H\mathbf{W}_j)+\mathrm{Tr}(\mathbf{B}_e\mathbf{X}_t\mathbf{B}_e^H\mathbf{C}_z)+\sigma_e^2\Big)}_{f_{2,k}^{(e)}(\mathbf{X}_t)}. \tag{4.3.16}$$

Hence, $R_{\mathrm{sec},k} = R_k^{(u)} - R_k^{(e)} = (f_{1,k}^{(u)} + f_{2,k}^{(e)}) - (f_{2,k}^{(u)} + f_1^{(e)})$ can be expressed as a difference of concave functions in $\mathbf{X}_t$. This motivates the use of a sequential convex approximation strategy, where the convex parts are linearized at the current iterate $\mathbf{X}_t^{(n)}$. The resulting first-order approximations are

$$-f_{2,k}^{(u)}(\mathbf{X}_t) \;\geq\; -\log_2 I_k^{(u)(n)} - \frac{2}{I_k^{(u)(n)}\ln 2}\,\Re\Big\{\mathrm{Tr}\Big(\big(\nabla_{I_k}^{(u)(n)}\big)^H(\mathbf{X}_t-\mathbf{X}_t^{(n)})\Big)\Big\} \;\triangleq\; \widetilde{f}_{2,k}^{(u)}(\widehat{\mathbf{X}}_t), \tag{4.3.17}$$

$$-f_1^{(e)}(\mathbf{X}_t) \;\geq\; -\log_2 S^{(e)(n)} - \frac{2}{S^{(e)(n)}\ln 2}\,\Re\Big\{\mathrm{Tr}\Big(\big(\nabla_{S}^{(e)(n)}\big)^H(\mathbf{X}_t-\mathbf{X}_t^{(n)})\Big)\Big\} \;\triangleq\; \widetilde{f}_1^{(e)}(\widehat{\mathbf{X}}_t) \tag{4.3.18}$$

where the gradients are given by

$$\nabla_{I_k}^{(u)(n)} = \sum_{j\neq k}\mathbf{B}_k^H\mathbf{W}_j\mathbf{B}_k + \mathbf{B}_k^H\mathbf{C}_z\mathbf{B}_k, \tag{4.3.19}$$

$$\nabla_{S}^{(e)(n)} = \sum_{j=1}^{K}\mathbf{B}_e^H\mathbf{W}_j\mathbf{B}_e + \mathbf{B}_e^H\mathbf{C}_z\mathbf{B}_e. \tag{4.3.20}$$

Defining $\widetilde{R}_{\mathrm{sec},k}(\mathbf{X}_t) = f_{1,k}^{(u)} + f_{2,k}^{(e)} + \widetilde{f}_{2,k}^{(u)} + \widetilde{f}_1^{(e)}$ and $\widetilde{R}_k^{(u)}(\mathbf{X}_t) = f_{1,k}^{(u)} + \widetilde{f}_{2,k}^{(u)}$, we obtain the following convex surrogate problem:

$$\begin{aligned}
\max_{\mathbf{X}_t} \quad & \min_k \ \widetilde{R}_{\mathrm{sec},k}(\mathbf{X}_t) && \text{(4.3.21a)}\\
\text{s.t.} \quad & \widetilde{R}_k^{(u)}(\mathbf{X}_t) \geq R_{\min,k}, \quad \forall k, && \text{(4.3.21b)}\\
& [\mathbf{X}_t]_{nn} = 1, \quad n = 1, \ldots, N_t, && \text{(4.3.21c)}\\
& \mathrm{rank}(\mathbf{X}_t) = 1. && \text{(4.3.21d)}
\end{aligned}$$

To handle the rank constraint, a spectral penalty formulation is used instead of standard semidefinite relaxation. Let

$$\rho(\mathbf{X}_t) = \mathrm{Tr}(\mathbf{X}_t) - \lambda_{\max}(\mathbf{X}_t) = \sum_{i \geq 2} \lambda_i(\mathbf{X}_t) \geq 0,$$

which equals zero if and only if $\mathbf{X}_t$ has rank one. Using the convexity of $\lambda_{\max}(\cdot)$, its affine lower bound at $\mathbf{X}_t^{(n)}$ is

$$\lambda_{\max}(\mathbf{X}_t) \geq \lambda_{\max}(\mathbf{X}_t^{(n)}) + 2\,\Re\Big\{\mathrm{Tr}\big(\mathbf{v}_{\max}^{(n)}\mathbf{v}_{\max}^{(n)H}(\mathbf{X}_t - \mathbf{X}_t^{(n)})\big)\Big\} \triangleq F_t(\mathbf{X}_t), \tag{4.3.22}$$

where $\mathbf{v}_{\max}^{(n)}$ is the principal eigenvector of $\mathbf{X}_t^{(n)}$. Adding this term as a penalty with weight $\alpha > 0$ yields the convex subproblem

$$\begin{aligned}
\max_{\mathbf{X}_t} \quad & \min_k \Big\{\widetilde{R}_{\mathrm{sec},k}(\mathbf{X}_t) + \alpha\big(F_t(\mathbf{X}_t) - \mathrm{Tr}(\mathbf{X}_t)\big)\Big\} && \text{(4.3.23a)}\\
\text{s.t.} \quad & \widetilde{R}_k^{(u)}(\mathbf{X}_t) \geq R_{\min,k}, \ \forall k, && \text{(4.3.23b)}\\
& [\mathbf{X}_t]_{nn} = 1, \quad n = 1, \ldots, N_t. && \text{(4.3.23c)}
\end{aligned}$$

This subproblem is convex and can be efficiently solved with semidefinite programming solvers. The overall RHS optimization is carried out through the sequential convex approximation (SCA) procedure summarized below.

Algorithm 15 SCA for RHS reflection (surrogate of (4.3.14))

Input: tolerance $\varepsilon > 0$; feasible $\mathbf{X}_t^{(0)}$ with $[\mathbf{X}_t^{(0)}]_{nn} = 1$.
repeat
Compute gradients (4.3.19)–(4.3.20) at $\mathbf{X}_t^{(n)}$; build $F_t(\mathbf{X}_t)$ via (4.3.22).
Solve convex program (4.3.23) $\rightarrow \mathbf{X}_t^{\star}$.
Err $\leftarrow |T(\mathbf{X}_t^{\star}) - T(\mathbf{X}_t^{(n)})|$, where $T(\cdot)$ is the objective in (4.3.23).
$\mathbf{X}_t^{(n+1)} \leftarrow \mathbf{X}_t^{\star}$.
until Err $\leq \varepsilon$
Recover RHS phases: $\boldsymbol{\gamma}_t \leftarrow e^{j\angle(\mathbf{v}_{\max}(\mathbf{X}_t^{\star}))}$; set $\boldsymbol{\Gamma}_t = \mathrm{diag}(\boldsymbol{\gamma}_t)$.

Remark 4.3.5 (Unit-modulus recovery). The diagonal constraints ensure $[\mathbf{X}_t]_{nn} = 1$, so taking the dominant eigenvector of $\mathbf{X}_t^{\star}$ and extracting its element-wise phases always produces a feasible reflection vector with $|\beta_{t,n}| = 1$ for all n.

Lemma 4.3.3 (Per-iteration complexity)**.** *When the matrices $\mathbf{B}_k$ and $\mathbf{B}_e$ are precomputed, evaluating the gradients in (4.3.19)–(4.3.20) requires $\mathcal{O}(KN_t^2)$ operations. The semidefinite program (4.3.23) can be solved in polynomial time using interior-point methods, and the eigenvector recovery step has a worst-case cost of $\mathcal{O}(N_t^3)$, which can be reduced with iterative eigensolvers.*

4.3.3 Optimization of the RIS Reflection $\boldsymbol{\Gamma}_r$

This subsection addresses the optimization of the RIS reflection matrix while keeping the transmit covariances and the RHS configuration fixed. Let $\{\mathbf{W}_k\}_{k=1}^K$, $\mathbf{C}_z$, and $\boldsymbol{\Gamma}_t$ be given. The RIS is expressed as

$$\boldsymbol{\Gamma}_r = \mathrm{diag}(\beta_{r,1}, \ldots, \beta_{r,N_r}),$$

where each reflection element satisfies the unit-modulus constraint $|\beta_{r,n}| = 1$ for all n.
Under these definitions, the RIS subproblem can be expressed as

$$\max_{\boldsymbol{\Gamma}_r} \quad \min_k \; R_{\mathrm{sec},k} \tag{4.3.24a}$$

$$\text{s.t.} \quad R_k^{(u)} \geq R_{\min,k}, \quad \forall k, \tag{4.3.24b}$$

$$|\beta_{r,n}| = 1, \quad n = 1, \ldots, N_r. \tag{4.3.24c}$$

This formulation mirrors the RHS optimization problem, but the coupling introduced by $\mathbf{Q}_r$ between $\boldsymbol{\Gamma}_t$ and $\boldsymbol{\Gamma}_r$ prevents the two metasurfaces from

being combined into a single equivalent reflection matrix. As a result, the RIS must be optimized separately.

Lifting and quadratic reformulation. To derive a tractable surrogate, we lift the RIS coefficients. Define the augmented vector $\widehat{\gamma}_r = [\gamma_r^T \ 1]^T \in \mathbb{C}^{(N_r+1)\times 1}$, where the last entry serves as a normalization factor to resolve global phase ambiguity. Let $\mathbf{X}_r = \gamma_r^* \gamma_r^T$ and $\widehat{\mathbf{X}}_r = \widehat{\gamma}_r^* \widehat{\gamma}_r^T$. The user and eavesdropper channel matrices are defined as

$$\mathbf{C}_k = \Big[\mathbf{Q}_t^H \mathbf{\Gamma}_t^H \mathbf{Q}_r^H \mathrm{diag}(\mathbf{h}_{r,k}) \quad \mathbf{Q}_t^H \mathbf{\Gamma}_t^H \mathbf{h}_{t,k}\Big], \qquad \mathbf{C}_e = \Big[\mathbf{Q}_t^H \mathbf{\Gamma}_t^H \mathbf{Q}_r^H \mathrm{diag}(\mathbf{g}_r) \quad \mathbf{Q}_t^H \mathbf{\Gamma}_t^H \mathbf{g}_t\Big].$$

Using these definitions, the achievable rates can be rewritten as Hermitian quadratic forms in $\widehat{\mathbf{X}}_r$:

$$\begin{aligned} R_k^{(u)} = & \underbrace{\log_2\Big(\sum_{j=1}^{K} \mathrm{Tr}(\mathbf{C}_k \widehat{\mathbf{X}}_r \mathbf{C}_k^H \mathbf{W}_j) + \mathrm{Tr}(\mathbf{C}_k \widehat{\mathbf{X}}_r \mathbf{C}_k^H \mathbf{C}_z) + \sigma_{u,k}^2\Big)}_{f_{1,k}^{(u)}(\widehat{\mathbf{X}}_r)} \\ & - \underbrace{\log_2\Big(\sum_{j\neq k} \mathrm{Tr}(\mathbf{C}_k \widehat{\mathbf{X}}_r \mathbf{C}_k^H \mathbf{W}_j) + \mathrm{Tr}(\mathbf{C}_k \widehat{\mathbf{X}}_r \mathbf{C}_k^H \mathbf{C}_z) + \sigma_{u,k}^2\Big)}_{f_{2,k}^{(u)}(\widehat{\mathbf{X}}_r)}, \end{aligned} \tag{4.3.25}$$

$$\begin{aligned} R_k^{(e)} = & \underbrace{\log_2\Big(\sum_{j=1}^{K} \mathrm{Tr}(\mathbf{C}_e \widehat{\mathbf{X}}_r \mathbf{C}_e^H \mathbf{W}_j) + \mathrm{Tr}(\mathbf{C}_e \widehat{\mathbf{X}}_r \mathbf{C}_e^H \mathbf{C}_z) + \sigma_e^2\Big)}_{f_1^{(e)}(\widehat{\mathbf{X}}_r)} \\ & - \underbrace{\log_2\Big(\sum_{j\neq k} \mathrm{Tr}(\mathbf{C}_e \widehat{\mathbf{X}}_r \mathbf{C}_e^H \mathbf{W}_j) + \mathrm{Tr}(\mathbf{C}_e \widehat{\mathbf{X}}_r \mathbf{C}_e^H \mathbf{C}_z) + \sigma_e^2\Big)}_{f_{2,k}^{(e)}(\widehat{\mathbf{X}}_r)}. \end{aligned} \tag{4.3.26}$$

It follows that

$$R_{\mathrm{sec},k} = R_k^{(u)} - R_k^{(e)} = \big(f_{1,k}^{(u)} + f_{2,k}^{(e)}\big) - \big(f_{2,k}^{(u)} + f_1^{(e)}\big),$$

which has the structure of a difference of concave (DC) functions in $\widehat{\mathbf{X}}_r$.

Concave surrogate construction. To handle this DC structure, the convex terms $-\big(f_{2,k}^{(u)} + f_1^{(e)}\big)$ are linearized around the current point $\widehat{\mathbf{X}}_r^{(n)}$. This leads to concave lower bounds:

$$-f_{2,k}^{(u)}(\widehat{\mathbf{X}}_r) \geq -\log_2 I_k^{(u)(n)} - \frac{2}{I_k^{(u)(n)} \ln 2} \Re\Big\{ \mathrm{Tr}\big(\big(\nabla_{I_k}^{(u)(n)}\big)^H (\widehat{\mathbf{X}}_r - \widehat{\mathbf{X}}_r^{(n)}) \big) \Big\} \triangleq \widetilde{f}_{2,k}^{(u)}(\widehat{\mathbf{X}}_r), \tag{4.3.27}$$

$$-f_1^{(e)}(\widehat{\mathbf{X}}_r) \geq -\log_2 S^{(e)(n)} - \frac{2}{S^{(e)(n)} \ln 2} \Re\Big\{ \mathrm{Tr}\big(\big(\nabla_{S}^{(e)(n)}\big)^H (\widehat{\mathbf{X}}_r - \widehat{\mathbf{X}}_r^{(n)}) \big) \Big\} \triangleq \widetilde{f}_{1}^{(e)}(\widehat{\mathbf{X}}_r), \tag{4.3.28}$$

where the gradients are defined similarly to (4.3.19)–(4.3.20). Using these bounds, we define the concave surrogates $\widetilde{R}_{\mathrm{sec},k} = f_{1,k}^{(u)} + f_{2,k}^{(e)} + \widetilde{f}_{2,k}^{(u)} + \widetilde{f}_1^{(e)}$ and $\widetilde{R}_k^{(u)} = f_{1,k}^{(u)} + \widetilde{f}_{2,k}^{(u)}$. The corresponding convexified problem becomes

$$\max_{\widehat{\mathbf{X}}_r \succeq 0} \quad \min_k \ \widetilde{R}_{\mathrm{sec},k}(\widehat{\mathbf{X}}_r) \tag{4.3.29a}$$

$$\text{s.t.} \quad \widetilde{R}_k^{(u)}(\widehat{\mathbf{X}}_r) \geq R_{\min,k}, \quad \forall k, \tag{4.3.29b}$$

$$[\widehat{\mathbf{X}}_r]_{nn} = 1, \quad n = 1, \ldots, N_r + 1, \tag{4.3.29c}$$

$$\mathrm{rank}(\widehat{\mathbf{X}}_r) = 1. \tag{4.3.29d}$$

Spectral penalty and convex relaxation. As in the RHS optimization, the rank-one constraint is promoted through a spectral penalty term $\rho(\widehat{\mathbf{X}}_r) = \mathrm{Tr}(\widehat{\mathbf{X}}_r) - \lambda_{\max}(\widehat{\mathbf{X}}_r)$. Linearizing $\lambda_{\max}(\cdot)$ at $\widehat{\mathbf{X}}_r^{(n)}$ gives

$$F_r(\widehat{\mathbf{X}}_r) = \lambda_{\max}(\widehat{\mathbf{X}}_r^{(n)}) + 2\,\Re\Big\{ \mathrm{Tr}\left(\mathbf{v}_{\max}^{(n)} \mathbf{v}_{\max}^{(n)H} (\widehat{\mathbf{X}}_r - \widehat{\mathbf{X}}_r^{(n)}) \right) \Big\},$$

where $\mathbf{v}_{\max}^{(n)}$ is the dominant eigenvector of $\widehat{\mathbf{X}}_r^{(n)}$. This leads to the following convex subproblem:

$$\max_{\widehat{\mathbf{X}}_r} \quad \min_k \ \widetilde{R}_{\mathrm{sec},k}(\widehat{\mathbf{X}}_r) + \alpha \big(F_r(\widehat{\mathbf{X}}_r) - \mathrm{Tr}(\widehat{\mathbf{X}}_r) \big) \tag{4.3.30a}$$

$$\text{s.t.} \quad \widetilde{R}_k^{(u)}(\widehat{\mathbf{X}}_r) \geq R_{\min,k}, \quad \forall k, \tag{4.3.30b}$$

$$[\widehat{\mathbf{X}}_r]_{nn} = 1, \quad n = 1, \ldots, N_r + 1. \tag{4.3.30c}$$

Sequential optimization procedure. The Sequential Convex Approximation (SCA) algorithm used for updating the RIS reflection coefficients follows the same structure as in the RHS case and its algorithm is outlined below.

Algorithm 16 SCA for RIS reflection (surrogate of (4.3.24))

Input: tolerance $\varepsilon > 0$; feasible $\widehat{\mathbf{X}}_r^{(0)}$ with $[\widehat{\mathbf{X}}_r^{(0)}]_{nn} = 1$.
repeat
Compute gradients and $F_r(\widehat{\mathbf{X}}_r)$ at $\widehat{\mathbf{X}}_r^{(n)}$.
Solve convex program (4.3.30) to obtain $\widehat{\mathbf{X}}_r^{\star}$.
Evaluate error Err $\leftarrow |R(\widehat{\mathbf{X}}_r^{\star}) - R(\widehat{\mathbf{X}}_r^{(n)})|$, where $R(\cdot)$ is the objective in (4.3.30).
Update $\widehat{\mathbf{X}}_r^{(n+1)} \leftarrow \widehat{\mathbf{X}}_r^{\star}$.
until Err $\leq \varepsilon$
Recover $\widehat{\gamma}_r$ from $\widehat{\mathbf{X}}_r^{\star}$ via the principal eigenvector, enforce $\widehat{\gamma}_r(N_r+1) = 1$, and set $\mathbf{\Gamma}_r = \mathrm{diag}(\gamma_r)$.

Remark 4.3.6 (On coupling and phase ambiguity). Due to the presence of $\mathbf{Q}_r$ between $\mathbf{\Gamma}_t$ and $\mathbf{\Gamma}_r$, the two metasurfaces cannot be merged into a single equivalent phase vector. The alternating optimization strategy captures this interaction by recomputing the effective channels after each update. Furthermore, $\widehat{\gamma}_r$ is only determined up to a global phase factor, since both $\widehat{\gamma}_r$ and $e^{j\theta}\widehat{\gamma}_r$ yield the same $\widehat{\mathbf{X}}_r$. To remove this ambiguity, the normalization $\widehat{\gamma}_r(N_r+1) = 1$ is enforced.

Lemma 4.3.4 (Per-iteration complexity)**.** *With precomputed $\mathbf{C}_k$ and $\mathbf{C}_e$, the gradient computations in (4.3.30) require $\mathcal{O}\big(K\,(N_r+1)^2\big)$ operations. Solving the convex subproblem via an interior-point method scales polynomially with N_r+1, while eigenvector recovery has complexity $\mathcal{O}\big((N_r+1)^3\big)$ in the worst case (lower for iterative eigensolvers). Thus, each RIS update remains computationally feasible for moderately large surfaces.*

4.3.4 Overall Algorithm and Convergence Analysis

This section combines the individual update procedures developed earlier into a unified alternating optimization framework for solving Problem (4.2.20). The algorithm proceeds iteratively by updating three groups of variables:

(A) the transmit covariance matrices, including the user beamformers $\{\mathbf{W}_k\}$ and the artificial-noise covariance $\mathbf{C}_z$;

(B) the reflection matrix of the reconfigurable holographic surface (RHS), $\mathbf{\Gamma}_t$;

(C) the reflection matrix of the reconfigurable intelligent surface (RIS), $\mathbf{\Gamma}_r$.

At each step, the other variable blocks are held constant, and the corresponding subproblem is solved using the sequential convex-approximation techniques introduced in Sections 4.3.1, 4.3.2, and 4.3.3.

Algorithmic structure. The complete alternating routine is summarized in Algorithm 17. The outer loop cycles through the three update blocks until the overall change in the minimum SEE objective becomes smaller than a predefined tolerance. Within each iteration, block (A) is handled using the generalized Dinkelbach method (Algorithm 13) combined with the SFP routine (Algorithm 14), while blocks (B) and (C) are updated according to the Majorization–Minimization (MM) principle, or equivalently, through SCA-based procedures as implemented in Algorithms 15 and 16, respectively.

Algorithm 17 Alternating optimization for Problem (4.2.20)

Set tolerance $\varepsilon > 0$, iteration index $n = 0$.
Initialize feasible $\{\mathbf{W}_k^{(0)}\}_{k=1}^K$, $\mathbf{C}_z^{(0)}$, $\mathbf{\Gamma}_t^{(0)}$, and $\mathbf{\Gamma}_r^{(0)}$.
repeat
$n \leftarrow n + 1$.
(A) Covariance update: Given $\mathbf{\Gamma}_t^{(n-1)}$ and $\mathbf{\Gamma}_r^{(n-1)}$, run Algorithm 13 (with inner SFP, Algorithm 14) to obtain $\{\mathbf{W}_k^{(n)}\}$ and $\mathbf{C}_z^{(n)}$.
(B) RHS update: With $\{\mathbf{W}_k^{(n)}\}$, $\mathbf{C}_z^{(n)}$, and $\mathbf{\Gamma}_r^{(n-1)}$ fixed, apply Algorithm 15 to obtain $\mathbf{\Gamma}_t^{(n)}$.
(C) RIS update: Using $\{\mathbf{W}_k^{(n)}\}$, $\mathbf{C}_z^{(n)}$, and $\mathbf{\Gamma}_t^{(n)}$, execute Algorithm 16 to update $\mathbf{\Gamma}_r^{(n)}$.
(Outer convergence check):

$$\text{Err} \leftarrow \left| O(\{\mathbf{W}_k^{(n)}\}, \mathbf{C}_z^{(n)}, \mathbf{\Gamma}_t^{(n)}, \mathbf{\Gamma}_r^{(n)}) - O(\{\mathbf{W}_k^{(n-1)}\}, \mathbf{C}_z^{(n-1)}, \mathbf{\Gamma}_t^{(n-1)}, \mathbf{\Gamma}_r^{(n-1)}) \right|,$$

where $O(\cdot)$ denotes the objective of Problem (4.2.20).
until Err $\leq \varepsilon$

Convergence behavior. The convergence of Algorithm 17 is a direct consequence of the monotonic nature of its block updates. Each subproblem is solved using a convex surrogate that satisfies three key properties: (i) it forms a global lower bound of the true objective; (ii) it is tight at the current iterate; and (iii) it is maximized at each step. This guarantees non-decreasing improvement of the surrogate objective, placing the method within the framework of *majorization–minimization* (MM) algorithms. Since the SEE

is bounded above by the feasible power budget, the sequence of objective values is monotone and convergent.

Theorem 1 (Monotonic improvement and convergence)**.** *If each subproblem (A)–(C) is solved using the sequential convex-approximation procedures described in Sections 4.3.1–4.3.3, the sequence of minimum SEE values generated by Algorithm 17 is monotonically non-decreasing. Moreover, every accumulation point of this sequence corresponds to a block-wise stationary point of Problem* (4.2.20).

Sketch of proof. Each update step solves a convex surrogate whose objective majorizes the true non-convex function at the current iterate. Because the surrogate is tight at the expansion point, the updated variables cannot reduce the value of the true objective. Thus, monotonicity follows directly from the MM principle. The transmit-power and reflection constraints guarantee the boundedness of the SEE sequence, and standard results on block-MM convergence ensure that any limit point is a block-wise stationary solution. ■

Numerical stability. For numerical robustness, all effective channels are normalized at each iteration, and the QoS constraints are evaluated using a logarithmic (dB) scale to improve conditioning. To mitigate potential ill-conditioning in the covariance-related log-determinant expressions, a small regularization term is added to the artificial-noise covariance matrix:

$$\mathbf{C}_z \succeq \delta \mathbf{I}, \qquad 0 < \delta \ll 1.$$

This adjustment improves numerical stability during matrix inversion operations, while its effect on the overall system performance remains negligible.

Remark 4.3.7 (Extension to secrecy-rate maximization). The alternating optimization framework presented here can be directly applied to secrecy-rate maximization. By omitting the power-consumption term in the denominator of (4.2.19), the objective function reduces to the minimum secrecy rate. At the same time, the structure of all subproblems and their corresponding solution methods remain unchanged. As a result, Algorithm 17 preserves both its procedural form and convergence guarantees under this alternative formulation.

Computational Complexity

The total computational load of Algorithm 17 can be expressed as

$$\mathcal{C}_{\text{alt}} = \mathcal{O}\Big(I_{\text{alt}}\big(\mathcal{C}_{\text{Dink}} + \mathcal{C}_{\text{T}} + \mathcal{C}_{\text{R}}\big)\Big), \tag{4.3.31}$$

where I_{alt} denotes the number of outer iterations required for convergence, and $\mathcal{C}_{\text{Dink}}$, $\mathcal{C}_{\text{T}}$, and $\mathcal{C}_{\text{R}}$ represent the computational costs of the covariance, RHS, and RIS updates, respectively.

Complexity of inner blocks. Each sub-algorithm requires solving a series of convex optimization problems through interior-point methods. The computational effort of these solvers grows polynomially with the number of optimization variables and approximately linearly with the number of iterations needed for convergence. Following standard complexity estimates from [6], the computational cost of each update block can be approximated as:

$$\mathcal{C}_{\text{Dink}} = \mathcal{O}\Big(I_{\text{Dink}}\, I_{\text{seq}}\, [M(M+1)]^4\Big), \tag{4.3.32}$$

$$\mathcal{C}_{\text{T}} \leq \mathcal{O}\Big(I_{\text{T}}\, [N_t(N_t-1)/2]^4\Big), \tag{4.3.33}$$

$$\mathcal{C}_{\text{R}} \leq \mathcal{O}\Big(I_{\text{R}}\, [(N_r+1)N_r/2]^4\Big). \tag{4.3.34}$$

Here, I_{Dink} and I_{seq} denote the iteration counts of the generalized Dinkelbach algorithm (Algorithm 13) and its inner sequential-fractional routine (Algorithm 14), respectively. Each instance of Problem (4.3.13) optimizes two $M \times M$ Hermitian matrices—$\{\mathbf{W}_k\}$ and $\mathbf{C}_z$—which yield $M(M+1)$ real variables after symmetry reduction. The terms $\mathcal{C}_{\text{T}}$ and $\mathcal{C}_{\text{R}}$ correspond to the RHS and RIS updates, whose main variables are Hermitian matrices of dimensions $N_t \times N_t$ and $(N_r{+}1) \times (N_r{+}1)$, respectively, each with unit-diagonal constraints.

Discussion. Therefore, the overall complexity of Algorithm 17 grows polynomially in the system dimensions M, N_t, and N_r. This starkly contrasts with the exponential complexity resulting from brute-force joint optimization. In typical configurations, the iteration counts I_{alt}, I_{Dink}, I_{seq}, I_{T}, and I_{R} remain moderate, making the algorithm practically viable even for large-scale 6G deployments.

4.4 Numerical Results

This section evaluates the performance of the proposed optimization framework through extensive simulations in a multiuser downlink scenario. The scenario is supported by two metasurfaces: a reconfigurable holographic surface (RHS) integrated with the base station (BS) and an environmental reconfigurable intelligent surface (RIS). The study aims to accomplish three main objectives: (i) to quantify the secrecy energy efficiency (SEE) gains achieved by metasurface-assisted transmission relative to conventional architectures; (ii) to examine how transmit power and quality of service (QoS) constraints shape the SEE–SR operating frontier; and (iii) to investigate the convergence behavior and robustness characteristics of the alternating optimization algorithm.

Simulation Environment

Unless stated otherwise, all simulations are based on the configuration summarized in Table 4.4.1. The scenario corresponds to a single-cell deployment with a 50 m radius. A four-antenna BS is placed at an elevation of 11 m and serves $K = 4$ single-antenna users randomly distributed within the coverage area, while one passive eavesdropper is also present. The RIS is mounted at a height of 10 m and positioned 50 m away from the BS, whereas the RHS is installed immediately adjacent to the BS antenna array.

The propagation environment follows a mixed deterministic–stochastic model. The BS–RHS channel is described using a spherical-wave formulation [19], [25], capturing near-field coupling effects. All other links experience distance-dependent path loss with exponent 2 and Rician fading. A Rician factor of $K = 10$ is assigned to the RHS–RIS link to represent its strong line-of-sight (LoS) condition, while a smaller factor of $K = 5$ is used for the remaining connections.

Thermal noise is computed from a power spectral density of $-174\,\mathrm{dBm/Hz}$ combined with a receiver noise figure of 5 dB, yielding a noise variance of approximately $\sigma^2 \approx -96\,\mathrm{dBm}$ per user. Static power consumption at each metasurface element is set to 1 mW, the BS radio-frequency chains draw 251 mW each, and an additional fixed overhead of 2.0 W accounts for digital processing and cooling. All these contributions are explicitly incorporated into the denominator of the SEE expression in (4.2.19).

TABLE 4.4.1: Simulation Parameters (Baseline unless otherwise stated)

Parameter	Symbol / Value	Notes
Cell radius	50 m	Uniform UE/eavesdropper drops
BS height / UE height	11 m / 1.5 m	–
RIS elevation / BS–RIS distance	10 m / 50 m	Building/rooftop mounting
Carrier frequency / Bandwidth	3.5 GHz / 20 MHz	Mid-band 5G setting
Noise PSD / NF	-174 dBm/Hz / 5 dB	Implies $\sigma^2 \approx -96$ dBm
RHS / RIS elements	$N_t = N_r = 64$	Unless varied
BS digital antennas	$M = 4$ (with RHS), $M = 32$ (no RHS)	Per scenario
Metasurface static power	$P_{\text{RHS,static}} = P_{\text{RIS,static}} = 0$ dBm	1 mW per element
BS per-chain static power	$P_{\text{Tx,static}} = 24$ dBm	≈ 251 mW per chain
Other static power	$P_{\text{other}} = 33$ dBm	≈ 2.0 W
Path-loss exponent	2	All links but BS$\rightarrow$RHS deterministic
Rician K-factors	$K = 5$ (general), $K = 10$ (RHS$\leftrightarrow$RIS)	Linear scale
QoS thresholds	$R_{\min,k}$	Common $R_{\min}$ when enforced

Baseline Policies

To assess the benefits of the proposed dual–metasurface architecture, its performance is compared with several alternative transmission and resource–allocation strategies. The comparison is designed to disentangle three key factors: (i) the contribution of using both metasurfaces jointly (RHS and RIS) versus relying on a single or no surface; (ii) the difference between optimizing for *secrecy energy efficiency* (SEE) and for *secrecy rate* (SR) alone; and (iii) the impact of the number of digital RF chains at the BS, which directly influences static power consumption.

Six representative baseline configurations are examined:

(a) **Dual metasurface, min-SEE (proposed):** This configuration corresponds to the complete version of Algorithm 17. It jointly optimizes the user beamforming matrices $\{\mathbf{W}_k\}$, the artificial–noise covariance $\mathbf{C}_z$, and the reflection matrices of both metasurfaces, $\mathbf{\Gamma}_t$ (RHS) and $\mathbf{\Gamma}_r$ (RIS). The BS employs a compact four–antenna digital array, while the RHS and RIS each contain $N_t = N_r = 64$ reflecting elements. This setup highlights how large, low–power metasurfaces can compensate for a smaller active array at the transmitter.

(b) **Dual metasurface, min-SR:** The same hardware configuration as in (a) is used, but the optimization objective is changed to maximize the minimum secrecy rate. This variant ignores the power–consumption denominator in (4.2.19), focusing purely on the achievable secrecy throughput. Comparing (a) and (b) shows that accounting for power consumption in the optimization changes the preferred operating point at high transmit powers.

(c) **RIS only, min-SEE:** Here, the RHS is deactivated, and only an environmental RIS is optimized along with $(\{\mathbf{W}_k\}, \mathbf{C}_z)$. To offset the missing near–field aperture, the BS array is expanded to $M = 32$ antennas, while the RIS retains $N_r = 64$ elements. The optimization follows the SEE criterion using Algorithm 17, excluding the RHS–update step. This configuration quantifies whether a dual–surface setup can replace a larger fully–digital array in terms of energy efficiency.

(d) **RIS only, min-SR:** This case uses the same hardware configuration as (c) but focuses on maximizing the secrecy–rate objective. The comparison with (b) helps assess how the absence of the RHS affects system performance when the design is purely rate–driven.

(e) **No metasurface, min-SEE:** In this benchmark, both metasurfaces are omitted, and the BS operates as a conventional fully digital array with $M = 32$ antennas. The optimization is limited to the beamforming vectors and artificial noise covariance, aiming to maximize the SEE. This configuration represents the traditional massive-MIMO baseline used to quantify the performance and energy-efficiency gains provided by metasurface-aided networks.

(f) **No metasurface, min-SR:** This case employs the same fully digital configuration as (e), but the optimization objective is changed to maximizing the minimum secrecy rate. It serves as a purely digital, SR-oriented

benchmark, providing a reference point for evaluating the benefits of metasurface-assisted designs.

Together, these six cases provide a comprehensive basis for comparison. Contrasting (a) with (c) and (e) highlights the incremental advantages of adding an RHS at the BS and/or an RIS in the environment. Comparing the SEE–oriented variants (a, c, e) with their SR–focused counterparts (b, d, f) exposes the effect of the chosen optimization metric. Finally, differences between (a) and (e) indicate how a small BS array combined with an RHS compares to a conventional large fully–digital system.

Implementation Complexity and Runtime Analysis

Implementation complexity is discussed in terms of the runtime required by the proposed optimization framework to reach convergence for the different architectures under consideration. The observed execution times for architectures supported by metasurfaces and fully digital baselines are shown in Fig. 4.4.1.

The runtime values refer to the total execution time of Algorithm 17. Identical channel realizations, secrecy constraints, and convergence tolerances are used throughout the comparison. For the fully digital configurations, the parametric baseband power and processing model described in Appendix A.2.2 is applied so that the computational effort reflects the scaling of digital processing with the number of RF chains and the adopted baseband optimization.

The figure considers three transmit-power levels, namely $P_{\max} = -30$ dBm, $P_{\max} = 0$ dBm, and $P_{\max} = 30$ dBm. For each operating point, the overall runtime is divided into the contributions associated with BS beamforming and artificial noise optimization, RHS updates, and RIS updates. This separation allows the contribution of digital processing to be examined separately from that of the metasurface updates.

The dual-metasurface configuration (RHS and RIS) has a higher computational load per iteration than the single-surface and small fully digital cases. Several optimization steps are carried out at each iteration. The transmit-side variables are updated first, followed by separate updates of the RHS and RIS reflection coefficients. All updates are handled within an alternating procedure, which increases the per-iteration workload when compared with simpler architectures.

The runtime measured for the dual-metasurface configuration is comparable to that of fully digital baselines with a larger number of RF chains, and

is lower in several cases. The computational cost increases at different rates for the architectures considered.

In fully digital systems, increasing the number of RF chains directly increases the size of the beamforming vectors and covariance matrices. As a result, the matrix operations required in the Dinkelbach and SCA updates become significantly more expensive as the number of antennas grows.

By contrast, the dual-metasurface architecture operates with a small digital front-end. Although the RHS and RIS introduce additional variables, their dimensions remain limited and do not grow with the number of BS antennas. The corresponding SCA updates therefore remain manageable, even when the transmit-power budget is increased. In practice, the reduction in BS-side digital dimensionality compensates for the additional metasurface-related computations.

The runtime trends also reflect the number of outer iterations required for convergence. In the dual-metasurface case, the coupling among the three variable blocks typically leads to a moderate increase in the number of iterations. This effect is reduced by using a warm-start strategy, where the solution obtained at a given transmit-power level initializes the optimization at the next power point. Warm-start initialization limits the growth in iteration count at higher values of $P_{\max}$ and avoids a sharp increase in total runtime.

In summary, these findings clearly demonstrate a trade-off. The dual-metasurface framework requires a more complex optimization process and has greater complexity per iteration, but it allows for operation with significantly fewer RF chains at the base station. In contrast, fully digital systems employ a simpler optimization framework; however, their computational demands increase sharply as the number of antennas rises. From this perspective, the combination of metasurface-assisted transmission and a compact digital front-end presents a scalable and efficient solution for secure and energy-saving wireless systems.

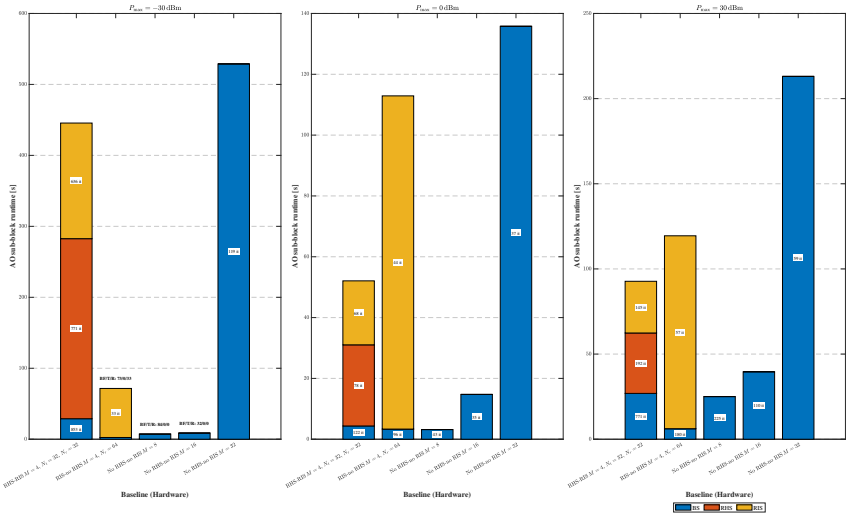

FIGURE 4.4.1: Average runtime of the alternating optimization algorithm for different architectural baselines and transmit-power regimes. The total runtime is decomposed into the contributions of the BS beamforming and artificial-noise optimization block, the RHS update block, and the RIS update block.

Global Energy Efficiency versus Transmit Power

Global energy efficiency is evaluated for different values of the maximum transmit power $P_{\max}$ and for the architectural configurations considered in this chapter. The numerical results corresponding to this study are presented in Figure 4.4.2.

Table 4.4.1 lists the parameters used in the simulations. Some values are changed when required. The dual-metasurface case uses $M = 4$ RF chains at the BS. Two metasurfaces are included, each with $N_t = N_r = 32$ elements. The RIS-only case also uses $M = 4$ RF chains. The RIS size is set to $N_r = 64$ elements. The fully digital cases do not use metasurfaces. Two configurations are considered, with $M = 8$ and $M = 16$ RF chains.

Rician fading is considered for all wireless links, with different K-factors assigned to each case. The link between the two metasurfaces uses $K_{Q_r} = 10$ dB. For the metasurface-to-user and metasurface-to-eavesdropper links, K-factors are set between 0 and 4 dB.

For fully digital configurations, the baseband power terms are taken from the formulation in Appendix A.2.2. A static baseband power of 33 dBm is used. Additional contributions arise from stream processing, RF-chain

interfacing, bandwidth-related processing, and linear precoding. The same parameter values are used for all fully digital configurations.

Figure 4.4.2 reveals a characteristic unimodal behavior of the GEE as a function of $P_{\max}$ for all architectures. At low values of $P_{\max}$, the GEE increases. As $P_{\max}$ becomes larger, the GEE reaches a maximum. For SEE-oriented optimization, the GEE does not increase further at higher transmit-power levels, whereas for SR-oriented optimization, the GEE decreases as the transmit power increases. This behavior is observed for all considered architectures.

Higher GEE values are observed for the dual-metasurface configuration under SEE-oriented optimization. This configuration operates with a limited number of RF chains at the BS and includes both the RHS and RIS, whereas lower GEE values are observed for fully digital baselines as the number of RF chains increases.

On the other hand, SR-oriented optimization favors higher transmit power levels. As a consequence, secrecy rates increase while GEE decreases, especially at large values of $P_{\max}$. This trend is common to both metasurface-assisted and fully digital configurations.

The comparison between SEE-oriented and SR-oriented designs further highlights the role of the optimization objective. SR-maximizing schemes tend to exploit the full transmit-power budget, which yields higher secrecy rates at large $P_{\max}$ but leads to a pronounced degradation in GEE. In contrast, SEE-oriented designs converge to an energy-efficient operating point and avoid unnecessary power expenditure, resulting in superior performance in terms of bits per joule.

A similar trend is observed for RIS-only and fully digital architectures. As the number of RF chains increases in fully digital systems, the improvement in GEE obtained by increasing $P_{\max}$ becomes progressively smaller, and the optimal operating point shifts toward lower transmit powers. This behavior reflects the growing dominance of static and baseband power consumption, as captured by the model in Appendix A.2.2. Metasurface-assisted architectures, on the other hand, maintain a higher GEE over a broader transmit-power range, demonstrating improved scalability with respect to hardware complexity.

Overall, Figure 4.4.2 shows higher GEE values for metasurface-assisted architectures with a small number of RF chains. Fully digital configurations exhibit a stronger sensitivity to hardware power consumption.

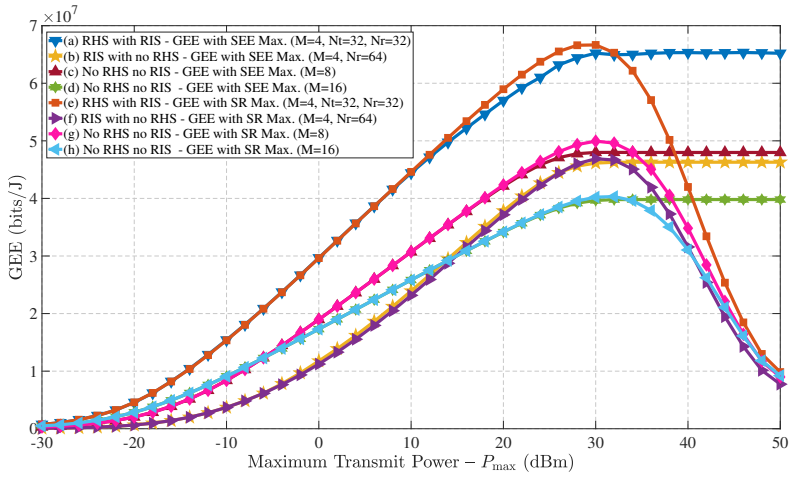

FIGURE 4.4.2: Global energy efficiency versus maximum transmit power for metasurface-assisted and fully digital architectures under SEE- and SR-oriented optimization.

Sum Rate versus Transmit Power

Figure 4.4.3 shows the achievable sum rate at the legitimate receivers as a function of the maximum transmit power $P_{\max}$ for the considered architectures. Results are reported for both secrecy-rate–oriented and secrecy energy efficiency–oriented optimization objectives.

At low values of $P_{\max}$, the sum rate increases for all configurations. As $P_{\max}$ becomes larger, the increase in sum rate gradually slows down. The same pattern appears across the considered architectures.

SR-oriented optimization produces larger sum-rate values over the considered transmit-power range. The difference becomes more pronounced in fully digital configurations with a greater number of RF chains. In these setups, the larger digital dimension is linked to higher achievable rates.

In optimization that focuses on SEE, there are limits on transmit power. As the maximum power, $P_{\max}$, is raised, the increase in the sum rate becomes gradual and ultimately levels off. This operating behavior differs from that observed under SR-oriented optimization.

Metasurface-assisted configurations are evaluated with a reduced number of RF chains at the BS. The dual-metasurface case achieves sum-rate values nearly reaching those of fully digital baselines while maintaining moderate antenna dimensions. Both the RHS and RIS are active in this configuration.

The RIS-only configuration provides higher sum-rate values than a no-metasurface baseline with the same number of RF chains. When compared with fully digital architectures employing a larger number of RF chains, however, the RIS-only configuration achieves lower sum rates. This difference arises from the double-fading characteristic of RIS-assisted links, which limits the multiplexing capability in comparison to fully digital systems with additional spatial degrees of freedom.

Differences are observed between SR-oriented and SEE-oriented operation, and between metasurface-assisted and fully digital architectures. Fully digital configurations with a larger number of RF chains exhibit higher sum-rate values at high transmit-power levels. Metasurface-assisted configurations operate with fewer RF chains and reach comparable sum-rate levels under lower hardware and power requirements. These trends complement the GEE results in Fig. 4.4.2, confirming that the operating points that maximize secrecy throughput do not, in general, coincide with those that optimize energy efficiency, particularly at high transmit-power levels. results shown in Fig. 4.4.2.

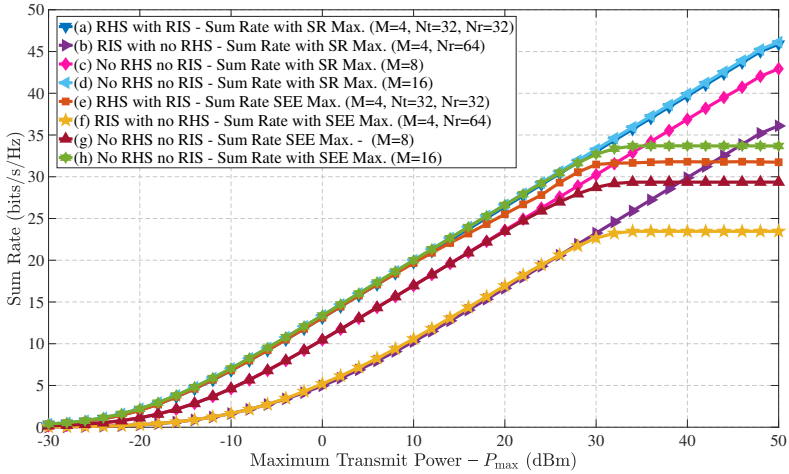

FIGURE 4.4.3: Achievable sum rate of the legitimate receivers versus maximum transmit power for metasurface-assisted and fully digital architectures under secrecy-oriented optimization objectives.

Performance versus Transmit Power

Figure 4.4.4 shows how the minimum secrecy energy efficiency (SEE) varies with the maximum BS transmit power $P_{\max}$, under the assumption of no QoS constraint ($R_{\min} = 0$). Several key trends can be observed.

First, the proposed *dual-metasurface, SEE-oriented* configuration (case (a)) consistently provides the highest performance across the entire transmit-power range. Notably, with only $M = 4$ digital antennas, the joint use of an RHS and an RIS achieves higher SEE than a fully digital BS with $M = 32$ antennas and no metasurface support (case (e)). This behavior arises from two complementary mechanisms: (i) the RHS increases the effective aperture of the transmitting array without incurring extra RF-chain power consumption, and (ii) the RIS provides an environmental degree of freedom that enhances spatial selectivity—concentrating energy toward the intended users while deflecting artificial noise from the eavesdropper.

Second, the comparison between cases (a) and (c) demonstrates the *benefit of including the RHS*. Although the RIS-only setup already improves energy efficiency relative to the no-metasurface baseline, jointly employing both surfaces yields additional gains—even when the BS operates with a substantially smaller digital array. This confirms that near-BS and environmental metasurfaces can act cooperatively: the RHS enhances the effective radiated power per RF chain, while the RIS exploits spatial diversity in the channel.

Third, *SR-oriented policies* (cases (b), (d), and (f)) show markedly lower SEE performance at medium-to-high transmit powers. This follows from the intrinsic behavior of the SEE metric, which is *unimodal* with respect to radiated power. Once the transmit power surpasses the level that maximizes the secrecy-rate-per-joule ratio, additional power increases primarily affect the denominator of (4.2.19), with only marginal rate gains. Consequently, the SEE declines—sometimes sharply—especially in fully digital configurations, where SR-oriented optimization keeps raising transmit power beyond the efficient operating point.

Finally, SEE-driven allocations (cases (a), (c), and (e)) exhibit the expected saturation pattern: after reaching the optimal operating point, the SEE stabilizes. This plateau indicates that the algorithm successfully balances radiated and static power consumption, preventing inefficient over-allocation. From a practical standpoint, this demonstrates that SEE-optimized designs sustain *stable and power-aware performance* even when the available transmit budget significantly exceeds the level required for optimal operation.

Impact of RF-Chain Hardware Power Consumption

Figure 4.4.5 shows the minimum secrecy energy efficiency (SEE) as a function of the RF-chain hardware power consumption P_{RF}. The results correspond to SEE-oriented optimization.

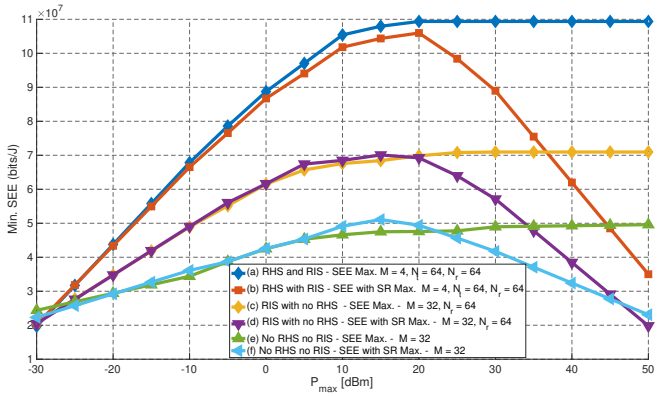

FIGURE 4.4.4: Minimum SEE versus maximum transmit power for different resource allocation policies.

Unless stated otherwise, the simulations use the baseline parameters in Table 4.4.1. The transmit power budget is fixed, and the RF chain power consumption is varied. The total power consumption includes RF-chain power, static overheads, and baseband processing power. Baseband power follows the formulation given in Appendix A.2.2.

For all configurations, the SEE decreases as P_{RF} increases. This behavior is observed across the full range of RF-chain power values considered.

Higher SEE values are observed for the dual-metasurface configuration over a broad range of P_{RF}. This configuration uses a limited number of RF chains at the BS and includes both the RHS and RIS.

The RIS-only architecture and the fully digital baseline with $M = 8$ RF chains exhibit an interesting trade-off behavior. At low values of P_{RF}, the fully digital configuration achieves a higher SEE, benefiting from its larger number of RF chains and enhanced spatial multiplexing capability. In this regime, the secrecy-rate gains provided by the additional digital degrees of freedom outweigh the associated circuit-power cost. As P_{RF} increases, however, a crossover point emerges at which the RIS-only architecture with $M = 4$ RF chains and $N_r = 64$ reflecting elements outperforms the fully digital baseline with $M = 8$. Beyond this point, the accumulated RF-chain and baseband power consumption of the fully digital system dominates the SEE denominator, leading to a faster efficiency degradation. By contrast, the RIS-only configuration benefits from its reduced number of RF chains and maintains a higher SEE despite the inherent double-fading nature of the RIS-assisted link.

For the fully digital configuration with $M = 16$ RF chains, the SEE

decreases more rapidly as P_{RF} increases. In this case, the total power consumption is dominated by RF-chain and baseband power terms.

Overall, the results in Fig. 4.4.5 show differences in SEE behavior across architectures as RF-chain power consumption varies. Metasurface-assisted configurations operate with fewer RF chains, while fully digital configurations exhibit stronger sensitivity to RF-chain power consumption.

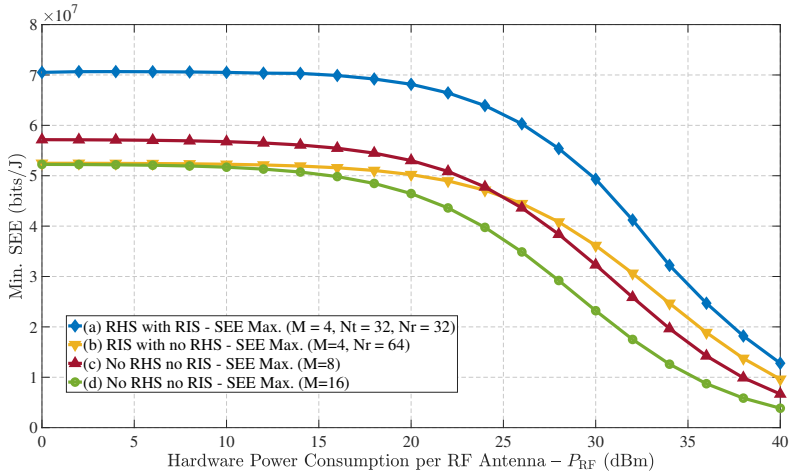

FIGURE 4.4.5: Minimum secrecy energy efficiency versus RF-chain hardware power consumption for SEE-oriented designs under different architectural configurations.

Performance versus QoS Constraints

The results in this section shows how enforcing minimum-rate constraints influences the minimum secrecy energy efficiency (SEE). As shown in Figure 4.4.6, the SEE is plotted against a uniform QoS target $R_{\min} = R_{\min,k}$ for all users, with a fixed BS transmit power of $P_{\max} = 40\,\mathrm{dBm}$.

To isolate the role of QoS, the comparison focuses on the *SEE-oriented* designs: the dual-metasurface configuration (case (a)), the RIS-only system (case (c)), and the no-metasurface baseline (case (e)).

The results reveal several key insights. First, the dual-metasurface setup consistently achieves the highest SEE across the entire QoS range, despite operating with only four RF chains at the BS. This outcome highlights the ability of the combined RHS–RIS architecture to preserve energy efficiency even under demanding rate constraints. The RHS effectively enlarges the transmit aperture, while the RIS refines the propagation environment, allowing user-rate targets to be met without significant power increases.

When the RHS is removed (case (c)), the SEE drops markedly—even though the BS array is expanded to $M = 32$ antennas and the RIS remains active. This demonstrates that the near-field contribution of the RHS cannot be entirely replaced by digital beamforming alone, underscoring the complementary benefits of combining both metasurfaces. In the extreme case without any metasurface (case (e)), the SEE deteriorates further, confirming the high energy cost of only meeting QoS requirements through digital transmission.

All three configurations display the same qualitative pattern: as $R_{\min}$ increases, the feasible design region for beamforming and reflection coefficients contracts. As a result, the minimum SEE declines and eventually vanishes once $R_{\min}$ exceeds the system's achievable secrecy-rate boundary. If infeasibility occurs, the algorithm terminates and reports the last feasible iterate as the final outcome. This outcome exemplifies the *feasibility–efficiency tradeoff* outlined in Chapter 4.2, since tighter QoS requirements reduce design flexibility and limit achievable efficiency.

Finally, the decline of SEE with growing $R_{\min}$ is noticeably slower in the dual-metasurface system than in the other two baselines. These results show that metasurfaces improve system performance in unconstrained and QoS-limited regimes, offering robustness that is especially valuable for 6G networks aiming to ensure efficiency, reliability, and fairness jointly.

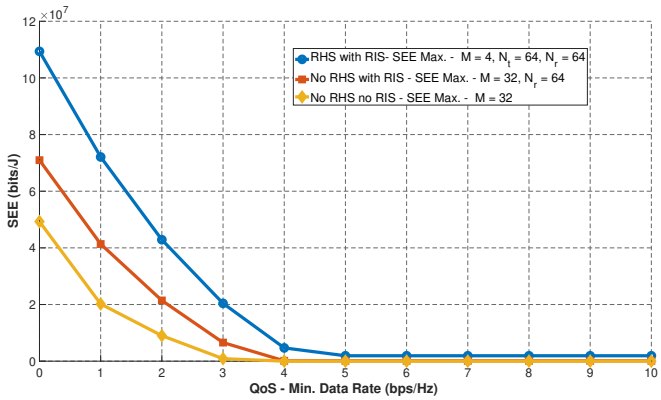

FIGURE 4.4.6: Minimum SEE versus QoS constraint for SEE-optimized policies.

Convergence Behavior

The convergence performance of the alternating optimization framework is evaluated in this section. Figure 4.4.7 presents the variation of the minimum secrecy energy efficiency (SEE) with the iteration count. The iteration count includes both the outer updates of Algorithm 17 and the inner loops carried out by the generalized Dinkelbach procedure (for transmit covariance optimization) and the SFP/SCA-based routines used to update the right-hand side (RHS) and reflections of the RIS. The evaluation focuses on the case $R_{\min} = 0$ and considers three representative configurations: a dual-metasurface setup (case (a)), a single-RIS arrangement (case (c)), and a fully digital baseline without metasurfaces (case (e)). For each setup, we report convergence under two transmit power limits: $P_{\max} = -30\,\text{dBm}$ (low-power) and $P_{\max} = 0\,\text{dBm}$ (moderate-power).

Across all scenarios, the proposed algorithm demonstrates *rapid and stable convergence*. In the RIS-only and no-metasurface baselines, the SEE reaches a steady value within only a few outer iterations, indicating that when fewer coupled variables are present, the update dynamics are almost immediate. For the dual metasurface configuration, convergence proceeds more gradually, as both $\mathbf{\Gamma}_t$ and $\mathbf{\Gamma}_r$ must be optimized jointly with the transmit covariances, creating stronger inter-block dependencies. Even so, the minimum SEE stabilizes after approximately 30 total iterations, a count that already includes all inner steps of the Dinkelbach and SFP/SCA procedures.

Two main conclusions can be drawn. First, the alternating optimization scheme is computationally efficient: despite the non-convex fractional structure and the coupling among multiple variable blocks, the use of convex surrogates and spectral penalties guarantees monotonic improvement and reliable stabilization. Second, the additional complexity introduced by optimizing both metasurfaces jointly remains modest. Although the dual metasurface setup requires more iterations than the RIS-only or fully-digital counterparts, the difference stays within a single order of magnitude, keeping the overall computational cost practical.

Overall, these results confirm that Algorithm 17 achieves consistent convergence behavior and can be deployed in dynamic wireless environments where rapid reconfiguration and periodic re-optimization are required.

Impact of Initialization

An important practical consideration is the sensitivity of the alternating optimization algorithm to its initial point. For this test, we set $N_t = N_r = 32$

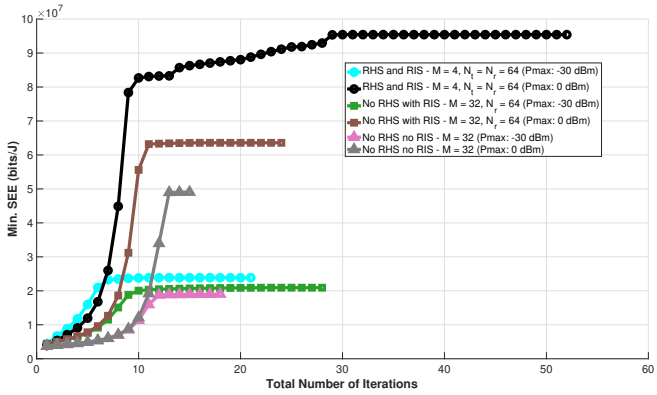

FIGURE 4.4.7: Convergence behavior of Algorithm 17: minimum SEE versus iteration count under different metasurface configurations and transmit power levels.

and $P_{\max} = 30\,\text{dBm}$, while the other parameters adhere to those specified in Table 4.4.1.

Figure 4.4.8 traces the evolution of the minimum SEE across the outer iterations of Algorithm 17 for eight different initialization strategies. These strategies are formed by combining three design choices:

- **Metasurface phases:** either random initialization with phases drawn uniformly from $[0, 2\pi]$, or SVD-based initialization where $\mathbf{\Gamma}_t$ and $\mathbf{\Gamma}_r$ are aligned with the dominant eigenmodes of the BS–RHS and RHS–RIS channels, respectively.
- **Beamforming:** maximum ratio transmission (MRT) or regularized zero-forcing (RZF).
- **Artificial noise (AN):** isotropic distribution (scaled identity) or projection into the null-space of the user precoder matrix $\mathbf{W} = [\mathbf{w}_1, \ldots, \mathbf{w}_K]$.

The complete set of initialization combinations is listed in Table 4.4.2.
Across all configurations, the algorithm converges quickly, typically within fewer than ten outer iterations, and the resulting SEE levels are nearly indistinguishable once convergence is reached. The only noticeable deviation occurs in Case 5 (*SVD, MRT, isotropic AN*). In this setting, aligning both metasurfaces with the dominant singular vectors, while simultaneously using MRT and isotropic artificial noise, concentrates transmit energy too narrowly and fails to suppress leakage toward the eavesdropper adequately.

TABLE 4.4.2: Initialization strategies used in Fig. 4.4.8.

Case	Metasurface phases	Beamforming	Artificial Noise (AN)
1	Random	MRT	Isotropic
2	Random	MRT	Null-space
3	Random	RZF	Isotropic
4	Random	RZF	Null-space
5	SVD-based	MRT	Isotropic
6	SVD-based	MRT	Null-space
7	SVD-based	RZF	Isotropic
8	SVD-based	RZF	Null-space

When null-space AN is employed instead (Cases 2, 4, 6, and 8), the leakage is effectively mitigated, and the optimal SEE is recovered.

Overall, the alternating framework demonstrates strong robustness with respect to initialization, with only minor variations in convergence speed or final SEE under specific configurations. This property is important for real-world implementations, where accurate or carefully engineered warm-starts are often impractical due to rapid channel variations. For reproducibility, the analytical expressions used to construct the initial metasurface phases, linear precoders, and AN covariances in Fig. 4.4.8 are provided in Appendix A.2.2.

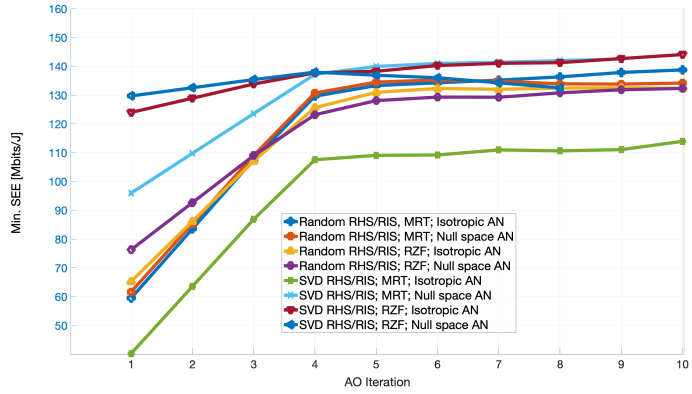

FIGURE 4.4.8: Minimum SEE versus outer iterations of Algorithm 17 under different initialization strategies (see Table 4.4.2).

Key Takeaways. The numerical analysis presented in this chapter provides several key insights that clarify the effects of dual metasurfaces and the efficiency of the proposed optimization algorithms.

- A base station equipped with only a **small number of RF chains**, when complemented by a transmit-side RHS and an environmental RIS, can achieve higher SEE than a considerably larger fully digital array. This demonstrates that metasurface assistance can substantially reduce hardware complexity and power demand without compromising performance.
- Explicitly **optimizing for SEE** proves essential. When the design targets only secrecy rate, the transmitter often operates near its power limit, which lowers overall efficiency at higher power levels. By contrast, SEE-oriented optimization naturally converges to an operating point that balances secrecy performance with power consumption, sustaining both energy efficiency and secure throughput.
- The proposed **alternating optimization framework** exhibits rapid and stable convergence across all scenarios tested. Typically, a few tens of iterations are sufficient for the objective to settle, even in cases with strong coupling between the metasurface and transmit variables, which makes the algorithm practical for real-time adaptation.
- The method also shows strong **robustness to initialization**. Only minor variations in performance appear under specific, unfavorable settings. Notably, employing **null-space artificial noise** improves robustness in line-of-sight conditions by suppressing unintended signal leakage toward the eavesdropper, while maintaining the data rates of legitimate users.

Taken together, the results establish the dual-metasurface configuration as a practical and effective solution for **energy-efficient and secure 6G wireless communication**. It enables a favorable balance between spectral efficiency, energy usage, and physical-layer confidentiality, making it a practical foundation for future green and secure wireless networks.

Chapter 5

Conclusions and Future Directions

5.1 Summary of Key Findings

This dissertation has explored optimizing *energy* and *secrecy energy efficiency* in wireless networks assisted by reconfigurable metasurfaces. Across three principal research axes, the thesis has contributed new models, algorithms, and insights that advance both the theoretical understanding and the practical viability of metasurface technologies for future 6G systems.

EE with Active and Nearly-Passive RISs (Chapter 2). The first line of investigation addressed the maximization of EE in uplink multi-user networks aided by *active* and *nearly-passive* RISs, under the novel framework of *global reflection constraints*. To this end, provably convergent and low-complexity algorithms were developed, revealing that global constraints enlarge the feasible design space of reflection coefficients and thus enable significant performance gains compared to classical local models. The numerical and theoretical analysis has shown that active reconfigurable intelligent surfaces (RISs) provide energy efficiency (EE) benefits only when the additional static power needed for amplification is kept moderate. In contrast, nearly-passive RISs present a more reliable and scalable energy profile. This distinction, therefore, provides a solid basis for evaluating different hardware options using realistic power consumption models.

SEE in RIS-Aided Networks (Chapter 3). The second contribution focused on the joint optimization of secrecy and energy efficiency in RIS-assisted networks. Under both perfect and statistical CSI assumptions, two algorithms were proposed for allocating user transmit powers, RIS reflection coefficients,

and receive filters. The findings indicated that: (i) active Reconfigurable Intelligent Surfaces (RISs) do not always surpass nearly-passive RISs, as the extra circuit power they demand can offset any potential gains in data rates; and (ii) statistical channel state information (CSI) is sufficient for sustaining high secrecy energy efficiency (SEE) performance, highlighting the resilience of the proposed approaches against imperfect knowledge of the eavesdropper's channel. These results confirm that integrating *physical-layer security* into energy-efficient metasurface-assisted architectures is feasible. [32].

Dual-Metasurface Architectures (Chapter 4). The final research focused on a downlink Multiple Input Single Output (MISO) system enhanced by a dual metasurface architecture. The objective was to solve the problem of a passive eavesdropper while optimizing the minimum users' SEE. This problem was solved using various methods, such as sequential convexification, generalized fractional programming, and alternating optimization. Numerical simulation results showed that dual metasurface designs significantly increase SEE while lowering the need for expensive RF chains at the base station. According to this, RHS–RIS collaboration is a prospective facilitator of *secure and sustainable 6G networks* [31].

These three research lines provide a coherent picture of how metasurfaces can be designed and optimized to deliver energy- and secrecy-efficient communication. They collectively advance the case for RISs and RHSs as practical foundations for the smart radio environments envisioned in beyond-5G and 6G systems.

5.2 The Big Picture: RIS Viability for 6G

The results of this dissertation collectively support the idea that reconfigurable metasurfaces, in both nearly passive and holographic forms, are not just minor improvements to existing technologies but rather *key architectural enablers* for the sixth generation of wireless systems. In contrast to the transition from 4G to 5G, which introduced massive MIMO technology that delivered unprecedented throughput gains but also significantly increased circuit and processing demands, the metasurface approach offers an entirely different pathway, i.e., it facilitates the development of wireless infrastructures that are greener, more secure, and more flexible.

The contributions highlighted in this work emphasize three key aspects of this paradigm shift. First, **global reflection engineering** shows that metasurfaces can be treated as a unified reflective entity instead of merely a collection

of separate elements. This approach expands the possible design options for reflection profiles and enables the system to achieve additional efficiency gains that are impossible with traditional local reflection models. In practical terms, this results in reduced transmission costs per bit and ultimately allows for the support of ultra-dense and heterogeneous networks without excessive energy consumption. Second, integrating physical-layer security with energy-efficient optimization illustrates that **security and efficiency need not be competing objectives**. By embedding secrecy constraints within the optimization of RIS-aided systems, this dissertation shows that metasurfaces can simultaneously enhance the reliability of confidential communications and sustain favorable bit-per-Joule operating points. This perspective is particularly relevant in the 6G context, where the proliferation of machine-type and IoT devices will exacerbate energy scarcity and exposure to adversarial threats.

Third, the investigation of **dual-surface cooperation** through the joint use of an RHS at the transmitter and an RIS in the environment reveals that metasurfaces are not confined to auxiliary roles. Instead of relying on large arrays of expensive and power-hungry RF chains, we can actively redesign transceivers. Dual-surface architectures can significantly reduce static power consumption while maintaining high performance levels by offloading some of the beamforming functionality to nearly passive holographic structures, which therefore presents a novel design principle: future systems could leverage metasurface technology as a substitute for the ongoing scaling of digital hardware, thereby attaining a more sustainable equilibrium between complexity and performance.

Taken together, these advances support the positioning of RISs and RHSs as *cornerstone technologies for smart radio environments* in beyond-5G and 6G networks [30], [33]. They point to a future where the radio environment becomes an active, programmable network infrastructure component. This shift aligns seamlessly with the vision of 6G as a platform for ubiquitous, secure, and sustainable connectivity.

5.3 Limitations and Assumptions

The findings presented in this thesis show that metasurfaces have the potential to improve significantly both energy efficiency and communication security in emerging 6G networks. Even so, the analytical framework developed here depends on simplifying assumptions introduced to keep the

mathematical analysis manageable. While these choices enabled the development of rigorous and convergent optimization methods, they also restrict the immediate transfer of the results to practical deployments.

To begin with, the designs presented throughout this dissertation assume *idealized control and synchronization* of the metasurface elements. This suggests that the reflection coefficients for Reconfigurable Intelligent Surfaces (RISs) and Reconfigurable Holographic Surfaces (RHSs) can be updated centrally, instantly, and without errors. However, in practice, control signaling demands bandwidth and energy resources, and dealing with reconfiguration delays and imperfections in hardware interfaces can adversely affect performance. Addressing such issues will be critical in assessing the real-world viability of global reflection control strategies.

Second, the electromagnetic models employed in this work adopt a *global reflection abstraction* that treats the metasurface as a perfectly programmable entity subject to energy conservation. The model explains how power is generally redistributed across the surface. However, it does not capture several practical effects—coupling losses, fabrication imperfections, and nonlinear behaviors often appearing in large metasurface arrays. It also leaves out hardware limits such as phase quantization and the restricted dynamic range of amplifiers used in active designs.

A significant drawback concerns the modeling of adversarial actions, since the analysis mainly focuses on a passive eavesdropper who experiences less favorable propagation conditions than the legitimate receiver. Although this assumption is consistent with much of the existing literature on physical-layer security, it does not account for more aggressive attack models that may arise in practical deployments. These include active eavesdropping strategies, pilot contamination attacks, and coordinated adversarial behaviors.

Moreover, while the thesis considers artificial noise generation as an effective means to impair eavesdropping, it does not explicitly address other *active* physical-layer security techniques such as intentional jamming or cooperative jamming by friendly nodes. Such approaches can further enhance secrecy by deliberately degrading the eavesdropper's reception at the cost of additional power consumption and potential interference to legitimate users. Incorporating active jamming strategies within an energy- or secrecy-energy-efficiency framework would therefore require a careful redesign of the optimization objectives to explicitly balance secrecy gains against the increased energy expenditure and interference footprint.

The analysis in this thesis also assumes the availability of ideal or statistical channel state information (CSI). While the inclusion of statistical CSI improves robustness, the cost associated with estimating and feeding back this information has not been explicitly modeled. In fast-varying networks, especially those operating in the near-field regime, obtaining accurate CSI can introduce substantial signaling overhead, which may reduce both the achievable data rate and the system's overall energy efficiency.

In this study, artificial noise improved the security of multi-user networks by making eavesdropping more difficult. Even so, an important area that remains only partially explored is how these techniques interact with other network layers. In reality, a base station must juggle limited resources among several coexisting services—such as enhanced mobile broadband, machine-type communications, and integrated sensing, naturally leading to new trade-offs. Understanding these interactions requires moving beyond the single-objective models used in this thesis and exploring them more thoroughly in future studies.

In summary, these limitations do not reduce the value of the work presented here; instead, they help define the boundaries within which the results should be interpreted. They also underscore the gap between theoretical modeling and practical implementation, pointing toward clear directions for future investigation.

5.4 Industrial Perspectives and Practical Use Cases

Beyond their theoretical interest, the results developed in this thesis provide concrete insights for the design and deployment of energy-efficient and secure wireless systems in practical industrial scenarios. By jointly accounting for realistic power-consumption models, propagation conditions, and physical-layer security requirements, the proposed frameworks yield actionable guidelines that support informed architectural choices rather than isolated algorithmic solutions.

Dense urban cellular networks. In dense urban environments, such as city centers and smart-city deployments, the results of Chapters 2 and 3 indicate that nearly-passive RISs can deliver substantial energy-efficiency gains when favorable propagation geometries are available (e.g., short Tx–RIS and RIS–Rx distances and moderate-to-strong line-of-sight components). In these scenarios, façade-mounted or lamppost-integrated RISs can be deployed to reshape propagation with minimal circuit power consumption,

offering a low-cost and scalable alternative to increasing the number of active base-station antennas. When secrecy constraints are present, the SEE-oriented designs developed in Chapter 3 further show that RIS-assisted spatial shaping can enhance confidentiality without incurring the energy overhead typical of purely transmit-side security mechanisms.

Coverage extension in energy-constrained or harsh environments. In scenarios characterized by weak cascaded channels or unfavorable geometries—such as rural areas, industrial plants, tunnels, or large indoor facilities—the double-fading bottleneck severely limits the effectiveness of nearly-passive RISs. The analysis in Chapter 2 demonstrates that active RISs can provide tangible energy-efficiency improvements in these regimes by partially compensating for severe path-loss through reflection-type amplification. These results suggest that active RISs are particularly suitable for targeted coverage extension, where modest amplification budgets can translate into significant performance gains, provided that the additional circuit power and noise are properly accounted for at the system level.

Secure wireless access for mission-critical services. The secrecy energy efficiency framework developed in Chapter 3 is directly applicable to mission-critical services requiring intrinsic confidentiality, such as industrial automation, healthcare monitoring, vehicular communications, and private wireless networks. The results show that RIS-assisted physical-layer security can achieve meaningful secrecy gains while controlling energy expenditure, enabling secure-by-design wireless access without relying exclusively on higher-layer cryptographic mechanisms. The comparative analysis between nearly-passive and active RISs further clarifies under which operating conditions enhanced security justifies the additional power consumption associated with active hardware.

Energy-aware base-station architectures with dual metasurfaces. The dual-metasurface architecture studied in Chapter 4 highlights a promising direction for reducing the energy footprint of future base stations. By combining a reconfigurable holographic surface (RHS) in the near field of the base station with an environmental RIS, the proposed design achieves fine-grained spatial control while significantly reducing reliance on energy-intensive digital RF chains. This architecture is particularly attractive for private 6G deployments and green cellular infrastructure, where operational expenditure and sustainability are primary concerns. The demonstrated

gains in both energy efficiency and secrecy energy efficiency suggest that dual-metasurface solutions can serve as practical enablers for scalable and sustainable high-capacity networks.

Overall, these use cases illustrate that the methodologies and insights developed in this thesis are not limited to abstract optimization problems but can directly inform real-world deployment strategies. By linking architectural choices to propagation conditions, power budgets, and security requirements, the proposed frameworks provide a valuable foundation for the design of energy-efficient and secure wireless systems beyond 5G.

5.5 Future Research Directions

The results of this dissertation open several promising avenues that extend beyond algorithmic optimality toward deployable, standards-oriented solutions. The prospective research agenda spans multiple levels of investigation, ranging from hardware and electromagnetic (EM) modeling to learning-driven resource orchestration and, ultimately, to integrating metasurface-assisted systems with sensing functions and large-scale cellular infrastructures.

(i) Hardware-realistic metasurfaces and EM-compliant modeling. One promising research avenue is to narrow the gap between abstract reflection theories and metasurface devices that can be built in practice. Making this transition calls for models that include real electromagnetic effects such as coupling between elements, material losses, discrete phase tuning, and the limited speed of tunable components. Promising approaches include the development of *hybrid active–passive* architectures with adaptive amplifier duty-cycling, as well as control interfaces constrained by bandwidth and quantization limits. At the same time, the development of *electromagnetically compliant global reflection models* is essential for accurately capturing non-ideal radiation efficiency and the coupling effects that occur among elements in dense metasurface arrays. Several recent works [20], [38], [72], [77] combine circuit modeling and full-wave simulations, allowing researchers to test analytical predictions against results obtained under real-world conditions. A practical next step for this line of research is hardware-in-the-loop testing, in which algorithmic updates are repeatedly evaluated against electromagnetic simulators or experimental prototypes to keep theoretical results aligned with physical behavior.

(ii) Reconfigurable holography under near-field operation. Reconfigurable holography plays a key role in lowering the number of required RF chains while maintaining the array gain offered by large apertures. Future work in this area should address two main priorities. Progress in this area depends first on near-field channel models that correctly represent array geometry and metasurface layout, minimizing errors in the Fresnel zone. It is equally important to develop practical algorithms for updating the RHS and RIS coefficients that remain stable under real hardware conditions—most notably, limited phase precision and nonlinear amplifier behavior [30], [33]. One direction worth exploring is the use of *stacked intelligent metasurfaces* (SIMs) in place of single-layer holographic panels. When multiple layers operate together, they can shape beams more precisely and increase spatial multiplexing near the transmitter, which also makes rank adaptation in MIMO links easier to manage. Recent studies [2], [3], [18], [63] highlight their potential and provide useful models for future holographic and codebook-based precoding work.

(iii) AI-driven resource allocation under partial and delayed CSI. In future wireless systems, channel state information (CSI) will frequently be incomplete, quantized, or outdated, especially in networks where multiple reconfigurable intelligent surfaces (RIS) or reconfigurable holographic surfaces (RHS) interact with mobile terminals that have limited energy resources. In such situations, conventional optimization methods that depend on perfect CSI become impractical. A promising research direction is using *learning-based controllers* capable of adapting to uncertain and time-varying environments. Using only limited feedback, model-based reinforcement learning and policy optimization with embedded safety mechanisms can effectively identify near-optimal operating points along the energy and secrecy efficiency tradeoff frontier. In this framework, RIS and RHS control can follow a two-timescale learning process: the surface parameters evolve gradually, whereas the digital beamforming and power allocation adjust more rapidly in response to channel variations. Prior knowledge derived from electromagnetic models or physics-informed neural surrogates can further guide the learning process toward physically consistent solutions [43], [91], [100].

(iv) Integration with ISAC: joint sensing, security, and efficiency. An immediate direction for future work lies in extending the SEE-oriented framework toward *Integrated Sensing and Communication* (ISAC). In such

systems, metasurfaces can be tuned to form beampatterns that detect and track targets and support secure data transmission. Work on RIS-aided ISAC has already shown that reliable sensing does not have to come at the expense of throughput, provided that the available degrees of freedom are carefully managed [17], [50]. Future research could extend this work by combining secrecy-oriented features like eavesdropper beam suppression with sensing metrics that capture detection reliability and estimation accuracy. Bringing these goals together with energy-efficiency optimization in a single framework would be a natural next step, building directly on the modular alternating algorithms established in this thesis.

(v) Network-level design and standardization alignment. At the network level, future studies need to examine RIS and RHS architectures operating in *multi-cell* settings. In such environments, user association, scheduling, and backhaul signaling interact in ways that can strongly affect control rates and energy budgets. To obtain an accurate understanding of system performance, future experiments and large-scale simulations should examine how energy and secrecy efficiency change once practical factors such as channel estimation, feedback signaling, and surface reconfiguration are considered, particularly in user mobility or signal blockage settings.

From a regulatory and societal perspective, *electromagnetic field (EMF) exposure constraints* are also expected to play a central role in the deployment of large-scale RIS- and RHS-assisted networks. Although metasurfaces are typically passive or low-power devices, dense deployments and active configurations may locally alter field distributions in ways that must comply with exposure limits defined by international guidelines and standardization bodies. Incorporating EMF-aware constraints into network-level optimization—such as exposure-aware beam shaping, surface activation policies, and user scheduling—represents an important direction for aligning metasurface-assisted systems with health, safety, and regulatory requirements in future 6G networks.

An IoT-oriented perspective on energy neutrality and self-organization [93] offers valuable insight into scalable, plug-and-play deployment models and control sparsification strategies such as clustering or hierarchical coordination among surfaces. In addition, bringing metasurface control in line with current communication standards is essential for practical adoption. This effort combines codebook-based precoding, numerology design, and control-plane signaling elements highlighted in [79] to help move metasurface technologies from laboratory experiments toward standardized and

scalable 6G systems.

In all these directions, the methodological pillars of this dissertation—global reflection engineering, dual-surface cooperation, and SEE-aware optimization remain central. While the optimization framework developed in this thesis primarily relies on alternating optimization and SCA/MM-based surrogate constructions, future research could explore complementary solution paradigms better suited to large-scale, uncertain, or decentralized deployments. These include stochastic optimization methods for long-term average SEE maximization, robust and chance-constrained formulations to account for CSI uncertainty, hardware impairments, and EMF exposure limits, as well as game-theoretic and distributed optimization approaches for multi-cell or multi-operator scenarios. In addition, learning-assisted and hybrid model-driven/data-driven techniques may enable fast, low-overhead adaptation of RIS and RHS configurations under partial or delayed CSI. Such paradigms would complement the analytical tools developed in this thesis and further enhance scalability, robustness, and real-time applicability in future 6G networks.

5.6 Concluding Remarks

This dissertation has shown that secure and energy-efficient wireless communication can be achieved and scaled through the intelligent use of reconfigurable metasurfaces. The research lays a foundation for developing 6G networks that are sustainable, secure, and adaptive to their environments through the combined study of global reflection design, physical-layer security, and holographic beamforming.

Some practical issues persist, such as non-ideal hardware and large-scale coordination among programmable surfaces. Nevertheless, the proposed models and optimization strategies advance how these networks can be analyzed and engineered. These findings are important for bridging electromagnetic modeling, algorithmic design, and system-level performance evaluation.

Looking ahead, RISs and RHSs should not be viewed merely as accessories to existing infrastructure but as core components of future smart radio environments. Once integrated, these technologies could turn wireless channels into programmable, energy-efficient entities that adapt to the environment. In doing so, they would guide the evolution of future communication systems toward sustainability, security, and ubiquitous connectivity.

Appendix A

Appendix: Technical Derivations and Proofs

This appendix collects detailed derivations, proofs, and complementary results that support the main analysis presented in Chapters 2– 4.

A.1 Derivations of Key Results

A.1.1 Derivation of the MMSE Receive Filter

For completeness, this section derives the closed-form expression of the linear minimum mean-square error (MMSE) receive filter used in Section 2.2.2 for detecting the symbol of user k.

System model recap. The received signal at the BS is:

$$\mathbf{r} \;=\; \sum_{m=1}^{K} \sqrt{p_m}\,\mathbf{A}_m \boldsymbol{\gamma}\, s_m \;+\; \mathbf{G}\boldsymbol{\Gamma}\mathbf{n} \;+\; \mathbf{w}, \tag{A.1.1}$$

where s_m denotes the normalized symbol of user m, $\mathbf{A}_m = \mathbf{G}\mathbf{H}_m$, and $\boldsymbol{\gamma}$ collects the RIS reflection coefficients. The vectors $\mathbf{n} \sim \mathcal{CN}(\mathbf{0}, \sigma^2_{\text{RIS}}\mathbf{I}_N)$ and $\mathbf{w} \sim \mathcal{CN}(\mathbf{0}, \sigma^2\mathbf{I}_{N_R})$ model the thermal noise introduced by the RIS and the BS, respectively.

MMSE criterion. Let $\mathbf{c}_k \in \mathbb{C}^{N_R}$ denote the linear combining vector employed to detect s_k. The decision variable is $r_k = \mathbf{c}_k^H \mathbf{r}$. The MMSE receive filter minimizes the mean-square error:

$$\mathbf{c}_k^\star = \arg\min_{\mathbf{c}_k} \; \mathbb{E}\Big[\,|s_k - \mathbf{c}_k^H \mathbf{r}|^2\Big]\,. \tag{A.1.2}$$

Error expansion. Expanding the objective in (A.1.2) gives

$$\begin{aligned}\mathbb{E}\Big[|s_k - \mathbf{c}_k^H \mathbf{r}|^2\Big] &= \mathbb{E}[|s_k|^2] - 2\,\Re\{\mathbf{c}_k^H \mathbb{E}[s_k \mathbf{r}]\} + \mathbf{c}_k^H \mathbb{E}[\mathbf{r}\mathbf{r}^H]\mathbf{c}_k \\ &= 1 - 2\,\Re\{\mathbf{c}_k^H \mathbf{d}_k\} + \mathbf{c}_k^H \mathbf{R}_{\mathbf{rr}} \mathbf{c}_k, \end{aligned} \tag{A.1.3}$$

where

$$\mathbf{d}_k \triangleq \mathbb{E}[s_k \mathbf{r}] = \sqrt{p_k}\,\mathbf{A}_k \boldsymbol{\gamma}, \tag{A.1.4}$$

$$\mathbf{R}_{\mathbf{rr}} \triangleq \mathbb{E}[\mathbf{r}\mathbf{r}^H] = \sum_{m=1}^{K} p_m\,\mathbf{A}_m \boldsymbol{\gamma}\boldsymbol{\gamma}^H \mathbf{A}_m^H + \sigma_{\mathrm{RIS}}^2 \mathbf{G}\boldsymbol{\Gamma}\boldsymbol{\Gamma}^H \mathbf{G}^H + \sigma^2 \mathbf{I}_{N_R}. \tag{A.1.5}$$

Wiener solution. Minimizing the quadratic form above yields the well-known Wiener filter

$$\mathbf{c}_k^\star = \mathbf{R}_{\mathbf{rr}}^{-1} \mathbf{d}_k = \sqrt{p_k}\,\mathbf{R}_{\mathbf{rr}}^{-1} \mathbf{A}_k \boldsymbol{\gamma}. \tag{A.1.6}$$

Simplified formulation. To obtain a more compact expression, the received covariance can be decomposed as

$$\mathbf{R}_{\mathbf{rr}} = p_k\,\mathbf{A}_k \boldsymbol{\gamma}\boldsymbol{\gamma}^H \mathbf{A}_k^H + \mathbf{M}_k, \tag{A.1.7}$$

where

$$\mathbf{M}_k = \sum_{m \neq k} p_m\,\mathbf{A}_m \boldsymbol{\gamma}\boldsymbol{\gamma}^H \mathbf{A}_m^H + \mathbf{W}, \qquad \mathbf{W} = \sigma^2 \mathbf{I}_{N_R} + \sigma_{\mathrm{RIS}}^2 \mathbf{G}\boldsymbol{\Gamma}\boldsymbol{\Gamma}^H \mathbf{G}^H. \tag{A.1.8}$$

Applying the matrix inversion lemma (Woodbury identity) gives

$$\left(\mathbf{M}_k + p_k\,\mathbf{A}_k \boldsymbol{\gamma}\boldsymbol{\gamma}^H \mathbf{A}_k^H\right)^{-1} = \mathbf{M}_k^{-1} - \mathbf{M}_k^{-1} \mathbf{A}_k \boldsymbol{\gamma} \Big(p_k^{-1} + \boldsymbol{\gamma}^H \mathbf{A}_k^H \mathbf{M}_k^{-1} \mathbf{A}_k \boldsymbol{\gamma}\Big)^{-1} \boldsymbol{\gamma}^H \mathbf{A}_k^H \mathbf{M}_k^{-1}. \tag{A.1.9}$$

Multiplying both sides by $\sqrt{p_k}\,\mathbf{A}_k \boldsymbol{\gamma}$ yields

$$\begin{aligned}\mathbf{c}_k^\star &= \sqrt{p_k}\Big[\mathbf{M}_k^{-1} \mathbf{A}_k \boldsymbol{\gamma} - \mathbf{M}_k^{-1} \mathbf{A}_k \boldsymbol{\gamma} \frac{\boldsymbol{\gamma}^H \mathbf{A}_k^H \mathbf{M}_k^{-1} \mathbf{A}_k \boldsymbol{\gamma}}{p_k^{-1} + \boldsymbol{\gamma}^H \mathbf{A}_k^H \mathbf{M}_k^{-1} \mathbf{A}_k \boldsymbol{\gamma}}\Big] \\ &= \sqrt{p_k}\,\frac{1}{1 + p_k\,\boldsymbol{\gamma}^H \mathbf{A}_k^H \mathbf{M}_k^{-1} \mathbf{A}_k \boldsymbol{\gamma}}\,\mathbf{M}_k^{-1} \mathbf{A}_k \boldsymbol{\gamma}. \end{aligned} \tag{A.1.10}$$

Since the scalar prefactor does not affect the SINR (it cancels in both numerator and denominator), the filter can be expressed up to a scaling

factor as

$$\boxed{\mathbf{c}_k^\star = \sqrt{p_k}\,\mathbf{M}_k^{-1}\mathbf{A}_k\boldsymbol{\gamma}.} \tag{A.1.11}$$

Remark A.1.1 (Scale invariance of the MMSE filter). The MMSE receiver derived from the Wiener solution is proportional to

$$\mathbf{c}_k^\star \propto \mathbf{M}_k^{-1}\mathbf{A}_k\boldsymbol{\gamma},$$

up to a positive scalar factor introduced by the matrix inversion lemma. However, since the signal-to-interference-plus-noise ratio is invariant to such scaling, i.e.,

$$\mathrm{SINR}_k(c\mathbf{c}_k) = \frac{p_k|c|^2|\mathbf{c}_k^H\mathbf{A}_k\boldsymbol{\gamma}|^2}{|c|^2\,\mathbf{c}_k^H\Big(\sum_{m\neq k} p_m\mathbf{A}_m\boldsymbol{\gamma}\boldsymbol{\gamma}^H\mathbf{A}_m^H + \mathbf{W}\Big)\mathbf{c}_k} = \mathrm{SINR}_k(\mathbf{c}_k),$$

the scalar can be omitted without loss of generality. For notational simplicity, the canonical representation

$$\mathbf{c}_k^\star = \sqrt{p_k}\,\mathbf{M}_k^{-1}\mathbf{A}_k\boldsymbol{\gamma}$$

is adopted throughout the thesis.

A.1.2 Derivation of the Net Amplification Power

The net amplification power at the RIS corresponds to the difference between the radiated and the incident powers. Starting from (2.2.14) and (2.2.15), this quantity can be written as

$$P_{\text{out}} - P_{\text{in}} = \sum_{k=1}^{K} p_k\Big(\operatorname{tr}(\mathbf{H}_k\boldsymbol{\gamma}\boldsymbol{\gamma}^H\mathbf{H}_k^H) - \operatorname{tr}(\mathbf{H}_k\mathbf{H}_k^H)\Big) + \sigma_{\text{RIS}}^2\Big(\operatorname{tr}(\boldsymbol{\gamma}\boldsymbol{\gamma}^H) - N\Big). \tag{A.1.12}$$

By applying the cyclic property of the trace operator, $\operatorname{tr}(\mathbf{AB}) = \operatorname{tr}(\mathbf{BA})$, we can move $\boldsymbol{\gamma}\boldsymbol{\gamma}^H$ to the left of $\mathbf{H}_k^H\mathbf{H}_k$, which gives

$$P_{\text{out}} - P_{\text{in}} = \sum_{k=1}^{K} p_k\,\operatorname{tr}\big[(\boldsymbol{\gamma}\boldsymbol{\gamma}^H - \mathbf{I}_N)\mathbf{H}_k^H\mathbf{H}_k\big] + \sigma_{\text{RIS}}^2\,\operatorname{tr}\big(\boldsymbol{\gamma}\boldsymbol{\gamma}^H - \mathbf{I}_N\big). \tag{A.1.13}$$

To simplify notation, define the positive-semidefinite matrix

$$\mathbf{R} \triangleq \sum_{k=1}^{K} p_k \, \mathbf{H}_k^H \mathbf{H}_k + \sigma_{\mathrm{RIS}}^2 \, \mathbf{I}_N. \tag{A.1.14}$$

Substituting this definition into (A.1.13) yields the compact form

$$\boxed{P_{\mathrm{out}} - P_{\mathrm{in}} = \mathrm{tr}\big[(\boldsymbol{\gamma}\boldsymbol{\gamma}^H - \mathbf{I}_N)\mathbf{R}\big].} \tag{A.1.15}$$

This expression shows that $\boldsymbol{\gamma}\boldsymbol{\gamma}^H - \mathbf{I}_N$ captures how far the surface operation departs from the purely passive case, where $|\gamma_n| = 1$ for all elements. When the trace in the boxed equation is positive, the RIS introduces a net amplification; when it is zero or negative, the surface behaves as a passive or lossy reflector.

A.1.3 Derivation and Projection for the Global-Reflection Constraint

This appendix develops the *global-reflection* formulation employed throughout the thesis and derives the corresponding Euclidean projection operator used in the $\boldsymbol{\gamma}$-block updates of the AO/SCA framework (see Sec. 1.4). The discussion proceeds in three parts: (i) derivation of the power-balance relation defining the constraint, (ii) comparison with the standard element-wise (local) model, and (iii) exact projection onto the resulting ellipsoidal feasible set. The material follows standard convex-optimization notation (cf. [12, Sec. 8.1.2]) but is restated here for completeness.

Power balance at the metasurface (global model). Let $\mathbf{R} \succeq \mathbf{0}$ denote the covariance of the impinging field at the surface, and let

$$\Gamma = \mathrm{diag}(\boldsymbol{\gamma}) \in \mathbb{C}^{N \times N}$$

collect the complex reflection coefficients. The incident and re-radiated (aperture) powers are

$$P_{\mathrm{in}} = \mathrm{tr}(\mathbf{R}), \tag{A.1.16}$$

$$P_{\mathrm{out}} = \mathrm{tr}\big(\mathbf{R}\Gamma\Gamma^H\big). \tag{A.1.17}$$

Energy conservation for a nearly-passive surface requires

$$P_{\text{out}} - P_{\text{in}} = \text{tr}\big[(\Gamma\Gamma^H - \mathbf{I})\mathbf{R}\big] \leq 0 \quad \Longleftrightarrow \quad \text{tr}\big(\mathbf{R}\Gamma\Gamma^H\big) \leq \text{tr}(\mathbf{R}), \tag{A.1.18}$$

whereas an active surface endowed with an RF amplification budget $P_{R,\max} \geq 0$ satisfies

$$\text{tr}(\mathbf{R}) \leq \text{tr}\big(\mathbf{R}\Gamma\Gamma^H\big) \leq \text{tr}(\mathbf{R}) + P_{R,\max}. \tag{A.1.19}$$

Since Γ is diagonal,

$$\text{tr}\big(\mathbf{R}\Gamma\Gamma^H\big) = \sum_{n=1}^{N} R_{nn}\,|\gamma_n|^2 = \boldsymbol{\gamma}^H \mathbf{D}\,\boldsymbol{\gamma}, \qquad \mathbf{D} \triangleq \text{diag}\big(\text{diag}(\mathbf{R})\big) \succeq \mathbf{0}. \tag{A.1.20}$$

Hence the feasible sets are origin-centred ellipsoids:

$$\mathcal{G}_{\text{pass}} = \Big\{\boldsymbol{\gamma} \in \mathbb{C}^N : \ \boldsymbol{\gamma}^H \mathbf{D}\,\boldsymbol{\gamma} \leq \text{tr}(\mathbf{R})\Big\}, \tag{A.1.21}$$

$$\mathcal{G}_{\text{act}} = \Big\{\boldsymbol{\gamma} \in \mathbb{C}^N : \ \boldsymbol{\gamma}^H \mathbf{D}\,\boldsymbol{\gamma} \leq \text{tr}(\mathbf{R}) + P_{R,\max}\Big\}. \tag{A.1.22}$$

From local to global: strict inclusion. Under per-element limits $|\gamma_n| \leq 1$, one obtains for each n

$$\sum_{k=1}^{K} p_k\,|h_k(n)|^2 |\gamma_n|^2 \leq \sum_{k=1}^{K} p_k\,|h_k(n)|^2,$$

and summing over all n gives $\text{tr}(\mathbf{R}\Gamma\Gamma^H) \leq \text{tr}(\mathbf{R})$. Thus, $\mathcal{F}_{\text{local}} \subseteq \mathcal{F}_{\text{global}}$.

Proposition A.1.1 (Global constraint strictly generalizes local)**.** *Let* $\mathcal{F}_{\text{local}} = \{\boldsymbol{\gamma} : \ |\gamma_n| \leq 1, \forall n\}$ *and* $\mathcal{F}_{\text{global}} = \{\boldsymbol{\gamma} : \ \text{tr}(\mathbf{R}\Gamma\Gamma^H) \leq \text{tr}(\mathbf{R})\}$*. Then* $\mathcal{F}_{\text{local}} \subsetneq \mathcal{F}_{\text{global}}$*.*

Proof. Inclusion follows by summation. For strictness, take $N = 3$, $K = 2$, $p_1 = p_2 = 1$, and

$$\mathbf{h}_1 = \begin{bmatrix} 1 \\ j \\ 0 \end{bmatrix}, \qquad \mathbf{h}_2 = \begin{bmatrix} 0 \\ 0 \\ 2e^{j\pi/5} \end{bmatrix}, \qquad \sigma^2_{\text{RIS}} = 0.$$

Then $\mathrm{diag}(\mathbf{R}) = (|1|^2, |j|^2, 0) + (0, 0, |2|^2) = (1, 1, 4)$, so $\mathbf{D} = \mathrm{diag}(1, 1, 4)$ and $\mathrm{tr}(\mathbf{R}) = 6$. Choose

$$\gamma = \begin{bmatrix} \sqrt{2}\, e^{j\pi/3} \\ 0 \\ e^{-j\pi/7} \end{bmatrix}.$$

Hence $\gamma^H \mathbf{D}\, \gamma = 1 \cdot 2 + 1 \cdot 0 + 4 \cdot 1 = 6 = \mathrm{tr}(\mathbf{R})$, so $\gamma \in \mathcal{F}_{\text{global}}$, while $|\gamma_1| = \sqrt{2} > 1$ implies $\gamma \notin \mathcal{F}_{\text{local}}$. Therefore $\mathcal{F}_{\text{local}} \subsetneq \mathcal{F}_{\text{global}}$. ■

Projection onto the global-reflection set

Given $\tilde{\gamma} \in \mathbb{C}^N$, the AO/SCA algorithm requires the Euclidean projection onto (A.1.21) or (A.1.22). The generic projection problem is

$$\min_{\gamma \in \mathbb{C}^N} \|\gamma - \tilde{\gamma}\|_2^2 \quad \text{s.t.} \quad \gamma^H \mathbf{D}\, \gamma \le B, \quad B \in \{\mathrm{tr}(\mathbf{R}),\, \mathrm{tr}(\mathbf{R}) + P_{R,\max}\}. \tag{A.1.23}$$

KKT solution (exact Euclidean projection). Introduce the Lagrangian multiplier $\lambda \ge 0$:

$$\mathcal{L}(\gamma, \lambda) = (\gamma - \tilde{\gamma})^H (\gamma - \tilde{\gamma}) + \lambda \big(\gamma^H \mathbf{D}\, \gamma - B\big). \tag{A.1.24}$$

Stationarity with respect to γ^* gives

$$(\mathbf{I} + \lambda \mathbf{D})\gamma = \tilde{\gamma}, \qquad \Rightarrow \quad \gamma(\lambda) = (\mathbf{I} + \lambda \mathbf{D})^{-1} \tilde{\gamma}. \tag{A.1.25}$$

Complementary slackness and feasibility require

$$\lambda \ge 0, \quad \gamma(\lambda)^H \mathbf{D}\, \gamma(\lambda) \le B, \quad \lambda \Big[\gamma(\lambda)^H \mathbf{D}\, \gamma(\lambda) - B\Big] = 0. \tag{A.1.26}$$

Let $\mathbf{D} = \mathrm{diag}(d_1, \ldots, d_N)$ and $\tilde{\gamma} = [\tilde{\gamma}_1, \ldots, \tilde{\gamma}_N]^T$. Equation (A.1.25) gives componentwise

$$\gamma_i(\lambda) = \frac{\tilde{\gamma}_i}{1 + \lambda d_i}, \qquad |\gamma_i(\lambda)|^2 = \frac{|\tilde{\gamma}_i|^2}{(1 + \lambda d_i)^2}. \tag{A.1.27}$$

If $\tilde{\gamma}$ already satisfies the constraint ($\tilde{\gamma}^H \mathbf{D} \tilde{\gamma} \le B$), then $\lambda^\star = 0$ and $\gamma^\star = \tilde{\gamma}$. Otherwise, the active-constraint case $\lambda^\star > 0$ is found from

$$\phi(\lambda) = \sum_{i=1}^{N} \frac{d_i |\tilde{\gamma}_i|^2}{(1 + \lambda d_i)^2} - B = 0. \tag{A.1.28}$$

The derivative

$$\phi'(\lambda) = -2\sum_{i=1}^{N} \frac{d_i^2 |\tilde{\gamma}_i|^2}{(1+\lambda d_i)^3} < 0 \quad (\lambda \geq 0, d_i \geq 0)$$

shows that $\phi(\lambda)$ is strictly decreasing, with

$$\phi(0) = \tilde{\gamma}^H \mathbf{D} \tilde{\gamma} - B > 0, \qquad \lim_{\lambda \to \infty} \phi(\lambda) = -B < 0.$$

Thus (A.1.28) admits a unique root $\lambda^\star > 0$, and the projection is

$$\boxed{\gamma^\star = (\mathbf{I} + \lambda^\star \mathbf{D})^{-1} \tilde{\gamma}.} \tag{A.1.29}$$

The complexity of evaluating (A.1.29) is linear in N, and $\lambda^\star$ can be found efficiently by bisection on (A.1.28).

Special cases. *(i) Spherical ellipsoid.* If $\mathbf{D} = d\,\mathbf{I}$, then

$$\gamma(\lambda) = \frac{1}{1+\lambda d} \tilde{\gamma} = \alpha(\lambda) \tilde{\gamma},$$

and the active constraint gives the closed-form scaling

$$\alpha^\star = \min\left\{1, \sqrt{\frac{B}{\tilde{\gamma}^H \mathbf{D} \tilde{\gamma}}}\right\}, \qquad \gamma^\star = \alpha^\star \tilde{\gamma}. \tag{A.1.30}$$

(ii) Ray-restricted update. If the algorithm restricts the correction to the ray $\{\alpha\,\tilde{\gamma} : \alpha \geq 0\}$, the one-dimensional projection also yields (A.1.30).

Summary. The global-reflection condition leads to the ellipsoidal feasible sets (A.1.21)–(A.1.22). Their Euclidean projection admits the diagonal KKT form (A.1.29), with a unique multiplier $\lambda^\star$ satisfying (A.1.28). In the spherical or ray-restricted cases, the projection reduces to the scalar rescaling (A.1.30). This operator is used in all AO/SCA iterations to maintain feasibility of the RIS coefficients under the global-reflection constraint.

A.1.4 Closed-Form Solution for the Single-User Problem (Proposition 2.3.1)

We derive the closed-form optimizer for the nearly-passive single-user case under the *exact* global-reflection constraint.

Setting and exact constraint. Let $\mathbf{h}, \mathbf{g} \in \mathbb{C}^N$ denote the user–RIS and RIS–receiver channels, and let the user transmit with power $p > 0$. With $\mathbf{\Gamma} = \operatorname{diag}(\gamma_1, \ldots, \gamma_N)$,

$$\left|\mathbf{g}^H \mathbf{\Gamma} \mathbf{h}\right|^2 \;=\; \Big| \sum_{n=1}^{N} \gamma_n \, h(n) \, g(n)^* \Big|^2. \tag{A.1.31}$$

Since the RIS is nearly-passive, $\sigma_{\mathrm{RIS}}^2 = 0$ and

$$\mathbf{R} \;=\; p \, \mathbf{H}^H \mathbf{H} \;=\; p \operatorname{diag}\big(|h(1)|^2, \ldots, |h(N)|^2\big), \tag{A.1.32}$$

so the exact global feasibility set is

$$\boldsymbol{\gamma}^H \mathbf{R} \boldsymbol{\gamma} \;\le\; \operatorname{tr}(\mathbf{R}) \quad \Longleftrightarrow \quad \sum_{n=1}^{N} p \, |h(n)|^2 \, |\gamma_n|^2 \;\le\; p \sum_{n=1}^{N} |h(n)|^2. \tag{A.1.33}$$

Exact change of variables and reduction to a ball. Define (on the support of $\mathbf{h}$)

$$\mathbf{R}^{1/2} = \sqrt{p} \operatorname{diag}\big(|h(1)|, \ldots, |h(N)|\big), \quad \mathbf{R}^{-1/2} = \tfrac{1}{\sqrt{p}} \operatorname{diag}\Big(\tfrac{1}{|h(1)|}, \ldots, \tfrac{1}{|h(N)|} \Big), \tag{A.1.34}$$

and introduce

$$\boldsymbol{x} \triangleq \mathbf{R}^{1/2} \boldsymbol{\gamma}, \qquad \mathbf{z}^H \triangleq \mathbf{g}^H \mathbf{H} \mathbf{R}^{-1/2}. \tag{A.1.35}$$

Then $\boldsymbol{\gamma} = \mathbf{R}^{-1/2} \boldsymbol{x}$ and

$$\mathbf{g}^H \mathbf{\Gamma} \mathbf{h} \;=\; \mathbf{g}^H \mathbf{H} \, \mathbf{R}^{-1/2} \boldsymbol{x} \;=\; \mathbf{z}^H \boldsymbol{x}, \tag{A.1.36}$$

whereas the constraint (A.1.33) becomes

$$\|\boldsymbol{x}\|_2^2 \;\le\; \operatorname{tr}(\mathbf{R}) \;=\; p \, \|\mathbf{h}\|_2^2. \tag{A.1.37}$$

Hence (A.1.31)–(A.1.33) are *exactly* equivalent to

$$\max_{\boldsymbol{x} \in \mathbb{C}^N} \; \left|\mathbf{z}^H \boldsymbol{x}\right|^2 \quad \text{s.t.} \quad \|\boldsymbol{x}\|_2^2 \le \operatorname{tr}(\mathbf{R}). \tag{A.1.38}$$

Optimal phases and amplitudes (Cauchy–Schwarz). Write $x_n = \rho_n e^{j\phi_n}$ and $z_n = |z_n| e^{j\angle z_n}$. For fixed $\{\rho_n\}$,

$$\phi_n^\star \;=\; -\angle z_n \quad \Rightarrow \quad \mathbf{z}^H \boldsymbol{x} = \sum_n \rho_n |z_n|. \tag{A.1.39}$$

By Cauchy–Schwarz and (A.1.37),

$$\sum_{n=1}^{N} \rho_n |z_n| \;\le\; \|\boldsymbol{\rho}\|_2 \, \||\mathbf{z}|\|_2 \;\le\; \sqrt{\mathrm{tr}(\mathbf{R})} \Big(\sum_{n=1}^{N} |z_n|^2 \Big)^{1/2}, \tag{A.1.40}$$

with equality iff $\boldsymbol{\rho} = \alpha \, |\mathbf{z}|$ and $\|\boldsymbol{\rho}\|_2^2 = \mathrm{tr}(\mathbf{R})$. Thus

$$\rho_n^\star \;=\; |z_n| \sqrt{\frac{\mathrm{tr}(\mathbf{R})}{\sum_{m=1}^{N} |z_m|^2}}, \qquad \phi_n^\star \;=\; -\angle z_n. \tag{A.1.41}$$

Alternative KKT derivation (for completeness). Under (A.1.39), (A.1.38) reduces to

$$\max_{\boldsymbol{\rho} \ge 0} \; \sum_{n=1}^{N} \rho_n |z_n| \quad \text{s.t.} \quad \sum_{n=1}^{N} \rho_n^2 \le \mathrm{tr}(\mathbf{R}). \tag{A.1.42}$$

The Lagrangian is

$$\mathcal{L}(\boldsymbol{\rho}, \lambda, \boldsymbol{\nu}) = \sum_{n=1}^{N} \rho_n |z_n| - \lambda \Big(\sum_{n=1}^{N} \rho_n^2 - \mathrm{tr}(\mathbf{R}) \Big) - \sum_{n=1}^{N} \nu_n \rho_n, \tag{A.1.43}$$

with $\lambda \ge 0$, $\nu_n \ge 0$. Stationarity yields $|z_n| - 2\lambda\rho_n - \nu_n = 0$. If $|z_n| > 0$, optimality forces $\nu_n = 0$ and $\rho_n^\star = |z_n|/(2\lambda)$; enforcing $\sum_n (\rho_n^\star)^2 = \mathrm{tr}(\mathbf{R})$ reproduces (A.1.41). If $|z_n| = 0$, any $\rho_n \ge 0$ is optimal; setting $\rho_n^\star = 0$ is consistent.

Mapping back to γ (explicit form). From (A.1.35) and (A.1.41),

$$\gamma_n^\star = \big[\mathbf{R}^{-1/2} \boldsymbol{x}^\star\big]_n = \frac{\rho_n^\star e^{j\phi_n^\star}}{\sqrt{p}\,|h(n)|} = \underbrace{\sqrt{\frac{\|\mathbf{h}\|_2^2}{\sum_{m=1}^{N} |z_m|^2}}}_{\alpha^\star} \cdot \frac{|z_n|}{|h(n)|} \, e^{-j\angle z_n}. \tag{A.1.44}$$

Using (A.1.35), $\mathbf{H} = \operatorname{diag}(\mathbf{h})$, and (A.1.36),

$$\begin{aligned}\mathbf{z}^H &= \mathbf{g}^H \mathbf{H} \mathbf{R}^{-1/2} \\ &= \frac{1}{\sqrt{p}}\, \mathbf{g}^H \operatorname{diag}\Big(\tfrac{h(1)}{|h(1)|}, \ldots, \tfrac{h(N)}{|h(N)|}\Big) \;\Rightarrow\; |z_n| = \tfrac{|g(n)|}{\sqrt{p}},\;\; \angle z_n = \angle h(n) - \angle g(n).\end{aligned} \tag{A.1.45}$$

Substitution into (A.1.44) gives the explicit optimizer:

$$\boxed{\gamma_n^\star = \sqrt{\frac{\|\mathbf{h}\|_2^2}{\|\mathbf{g}\|_2^2}}\, \frac{|g(n)|}{|h(n)|}\, e^{j\angle h(n) - j\angle g(n)}, \quad n \text{ with } |h(n)| > 0.} \tag{A.1.46}$$

Optimal value and SNR form. At optimum,

$$\max_{\|\boldsymbol{x}\|^2 \le \operatorname{tr}(\mathbf{R})} |\mathbf{z}^H \boldsymbol{x}|^2 = \operatorname{tr}(\mathbf{R}) \sum_{n=1}^{N} |z_n|^2. \tag{A.1.47}$$

Using (A.1.45) and $\operatorname{tr}(\mathbf{R}) = p\,\|\mathbf{h}\|_2^2$,

$$\left|\mathbf{g}^H \boldsymbol{\Gamma}^\star \mathbf{h}\right|^2 = p\,\|\mathbf{h}\|_2^2 \cdot \frac{\|\mathbf{g}\|_2^2}{p} = \|\mathbf{h}\|_2^2\, \|\mathbf{g}\|_2^2. \tag{A.1.48}$$

Let $\mathbf{d} \triangleq \mathbf{H}^H \mathbf{g}$ (so $d_n = h^*(n) g(n)$) and let σ^2 be the receiver noise variance. Then

$$\mathrm{SNR}_{\mathrm{opt}} = \frac{p}{\sigma^2} \left|\mathbf{g}^H \boldsymbol{\Gamma}^\star \mathbf{h}\right|^2 = \frac{p}{\sigma^2}\, \|\mathbf{h}\|_2^2\, \|\mathbf{g}\|_2^2 = \frac{p}{\sigma^2} \sum_{n=1}^{N} \delta_n\, |d_n|^2, \tag{A.1.49}$$

where

$$\sum_{n=1}^{N} \delta_n\, |d_n|^2 = \sum_{n=1}^{N} \frac{\|\mathbf{h}\|_2^2}{|h(n)|^2}\, |h(n)|^2\, |g(n)|^2 = \|\mathbf{h}\|_2^2\, \|\mathbf{g}\|_2^2, \qquad \delta_n \triangleq \frac{\|\mathbf{h}\|_2^2}{|h(n)|^2} \ge 1. \tag{A.1.50}$$

For the local unit-modulus allocation ($|\gamma_n| = 1$ with phase matching),

$$\mathrm{SNR}_{\mathrm{uni}} = \frac{p}{\sigma^2} \Big(\sum_{n=1}^{N} |d_n| \Big)^2 = \frac{p}{\sigma^2} \Big(\sum_{n=1}^{N} |h(n)|\, |g(n)| \Big)^2. \tag{A.1.51}$$

Hence the (exact-constraint) gain factor is

$$\eta \triangleq \frac{\mathrm{SNR}_{\mathrm{opt}}}{\mathrm{SNR}_{\mathrm{uni}}} = \frac{\|\mathbf{h}\|_2^2 \, \|\mathbf{g}\|_2^2}{\left(\sum_{n=1}^{N} |h(n)| \, |g(n)|\right)^2} \geq 1, \tag{A.1.52}$$

with equality iff $|h(n)|$ and $|g(n)|$ are proportional (Cauchy–Schwarz equality).

Remark A.1.2 (Zero entries and non-invertible $\mathbf{R}$). If $|h(n)| = 0$ for some n, the n-th element does not affect the objective (A.1.31) or the constraint (A.1.33). Remove such indices and apply the derivation on the reduced support; (A.1.46) then specifies $\gamma_n^\star$ for all $|h(n)| > 0$, while γ_n for $|h(n)| = 0$ can be set arbitrarily (e.g., $\gamma_n = 0$) without changing the optimum.

Remark A.1.3 (Feasibility saturation, uniqueness, and scale). (i) The constraint $\|\boldsymbol{x}\|_2^2 \leq \mathrm{tr}(\mathbf{R})$ is tight at the optimum whenever $\mathbf{z} \neq \mathbf{0}$. (ii) The optimizer (A.1.46) is unique up to a common phase rotation. (iii) The modulus $|\gamma_n^\star|$ increases with $|g(n)|/|h(n)|$, consistent with the global-reflection feasibility.

A.1.5 Further Expansion of the SNR Gain Factor

We detail the algebra leading from the compact form of η to its expansions and limiting cases (cf. Section 2.3.3).

Starting point. From Appendix A.1.4,

$$\eta \triangleq \frac{\mathrm{SNR}_{\mathrm{opt}}}{\mathrm{SNR}_{\mathrm{uni}}} = \frac{\sum_{n=1}^{N} \delta_n |d_n|^2}{\left(\sum_{n=1}^{N} |d_n|\right)^2}, \qquad d_n = h^*(n) g(n), \;\; \delta_n = \frac{\|\mathbf{h}\|_2^2}{|h(n)|^2}. \tag{A.1.53}$$

Expansion and auxiliary ratio. Since

$$\left(\sum_n |d_n|\right)^2 = \sum_n |d_n|^2 + 2 \sum_{n<m} |d_n||d_m|,$$

we may write

$$\eta = \frac{\sum_n \delta_n |d_n|^2}{\sum_n |d_n|^2 + 2\sum_{n<m} |d_n||d_m|} = \beta - \frac{2\sum_{n<m} \left(|d_n||d_m| - |d_n||d_m|\right)}{\sum_n |d_n|^2 + 2\sum_{n<m} |d_n||d_m|}, \tag{A.1.54}$$

where

$$\beta \triangleq \frac{\sum_n \delta_n |d_n|^2 + 2\sum_{n<m} |d_n||d_m|}{\sum_n |d_n|^2 + 2\sum_{n<m} |d_n||d_m|} \geq 1. \tag{A.1.55}$$

Equal-channel case. If $|h(n)| = |h|$ and $|g(n)| = |g|$ for all n, then $|d_n| = |h||g|$ and

$$\sum_n \delta_n = \sum_n \frac{\|\mathbf{h}\|_2^2}{|h|^2} = N \cdot \frac{N|h|^2}{|h|^2} = N^2,$$

so

$$\beta = \frac{N^2 + N(N-1)}{N + N(N-1)} = 2 - \frac{1}{N}, \qquad \Rightarrow \qquad \eta = 1.$$

Extreme heterogeneous case. If only one cascaded component is nonzero, say $|g_k| > 0$ and $|g_n| = 0$ for $n \neq k$, then

$$\eta = \beta = \delta_k = \frac{\|\mathbf{h}\|_2^2}{|h(k)|^2}.$$

If moreover $|h(n)| = |h|$ for all n, then $\eta = N$.

Summary. Thus $\eta = 1$ in the equal-channel case (no gain), $\eta > 1$ whenever the cascaded magnitudes are unequal, and η can scale as N in highly heterogeneous scenarios, quantifying how global reflection benefits from power-imbalance across surface elements.

A.1.6 Sequential Fractional Programming Surrogates for the RIS Update

We detail the surrogate used in the SFP step that updates the RIS vector γ (Chapter 2.4). For user k,

$$\begin{aligned} R_k(\gamma) &= \log\left(1 + \frac{x_k(\gamma)}{y_k(\gamma)}\right), \qquad x_k(\gamma) = p_k |\mathbf{c}_k^H \mathbf{A}_k \gamma|^2, \\ y_k(\gamma) &= \sigma^2 \|\mathbf{c}_k\|^2 + \sigma_{\mathrm{RIS}}^2 \, \gamma^H \widetilde{\mathbf{U}}_k \gamma + \sum_{m \neq k} p_m |\mathbf{c}_k^H \mathbf{A}_m \gamma|^2, \end{aligned} \tag{A.1.56}$$

where $\mathbf{A}_k = \mathbf{G}\mathbf{H}_k$, $\mathbf{u}_k = \mathbf{G}^H \mathbf{c}_k$, and $\widetilde{\mathbf{U}}_k = \mathrm{diag}(|u_{k,1}|^2, \ldots, |u_{k,N}|^2)$ so that $\mathbf{c}_k^H \mathbf{W} \mathbf{c}_k = \sigma^2 \|\mathbf{c}_k\|^2 + \sigma_{\mathrm{RIS}}^2 \, \gamma^H \widetilde{\mathbf{U}}_k \gamma$. Given a feasible reference $\bar{\gamma}$, set

$$\bar{x}_k \triangleq x_k(\bar{\gamma}), \qquad \bar{y}_k \triangleq y_k(\bar{\gamma}), \qquad \bar{\alpha}_k \triangleq \frac{\bar{x}_k}{\bar{y}_k}.$$

We construct a globally *valid* concave lower bound $\widetilde{R}_k(\gamma;\bar{\gamma})$ with $\widetilde{R}_k(\bar{\gamma};\bar{\gamma}) = R_k(\bar{\gamma})$ and $\nabla_\gamma \widetilde{R}_k|_{\bar{\gamma}} = \nabla_\gamma R_k|_{\bar{\gamma}}$.

A. Log–ratio identity

Lemma A.1.1 (Lagrangian dual transform [73])**.** *For $x \geq 0$, $y > 0$,*

$$\log\Big(1+\tfrac{x}{y}\Big) = \max_{\alpha\geq 0}\Big\{\log(1+\alpha) - \alpha + (1+\alpha)\tfrac{x}{x+y}\Big\},$$

attained at $\alpha^\star = x/y$.

Evaluating at the reference $\bar{\alpha} = \bar{x}/\bar{y}$ gives the tight global lower bound

$$\log\Big(1+\tfrac{x}{y}\Big) \;\geq\; \underbrace{\log(1+\bar{\alpha}) - \bar{\alpha}}_{\text{const.}} + (1+\bar{\alpha})\,\frac{x}{x+y}, \quad \text{with equality at } (x,y) = (\bar{x},\bar{y}). \tag{A.1.57}$$

It remains to lower bound $x/(x+y)$ by a concave expression.

B. A concave lower bound for $x/(x+y)$

Lemma A.1.2 (Concave minorant)**.** *For $x, y \geq 0$ and $\bar{x}, \bar{y} > 0$,*

$$\frac{x}{x+y} \;\geq\; \frac{2\sqrt{x\bar{x}} - (x+y)}{\bar{x}+\bar{y}} + \frac{\bar{x}}{\bar{x}+\bar{y}}, \qquad \textit{equality at } (x,y) = (\bar{x},\bar{y}). \tag{A.1.58}$$

The right-hand side is concave in $(\sqrt{x}, x, y)$.

Combining A and B (user k). With $x = x_k(\gamma)$, $y = y_k(\gamma)$, define

$$\bar{A}_k \triangleq \log(1+\bar{\alpha}_k) - \bar{\alpha}_k + (1+\bar{\alpha}_k)\frac{\bar{x}_k}{\bar{x}_k+\bar{y}_k}, \qquad \bar{B}_k \triangleq \frac{1+\bar{\alpha}_k}{\bar{x}_k+\bar{y}_k}. \tag{A.1.59}$$

By (A.1.57)–(A.1.58),

$$R_k(\gamma) \;\geq\; \bar{A}_k + \bar{B}_k\Big(2\sqrt{x_k(\gamma)\bar{x}_k} - x_k(\gamma) - y_k(\gamma)\Big), \quad \text{tight at } \gamma = \bar{\gamma}. \tag{A.1.60}$$

C. Linearizing the modulus

Let $v_k(\gamma) = \mathbf{c}_k^H \mathbf{A}_k \gamma$ (linear in γ), $\bar{v}_k = v_k(\bar{\gamma})$. Then

$$\sqrt{x_k(\gamma)} = \sqrt{p_k}\,|v_k(\gamma)|, \qquad x_k(\gamma) = p_k\,|v_k(\gamma)|^2.$$

Since $|v_k(\gamma)|$ is convex, its global affine lower bound at $\bar{\gamma}$ is

$$|v_k(\gamma)| \;\geq\; |\bar{v}_k| + \Re\left\{ \frac{\bar{v}_k^*}{|\bar{v}_k|} \left(v_k(\gamma) - \bar{v}_k\right) \right\} \quad (\bar{v}_k \neq 0), \tag{A.1.61}$$

and any subgradient at 0 if $\bar{v}_k = 0$. Plugging (A.1.61) into (A.1.60), and keeping $-x_k(\gamma)$ and $-y_k(\gamma)$ intact (both are concave, being negatives of convex quadratics), yields the concave, tight surrogate

$$\boxed{\begin{aligned}\widetilde{R}_k(\gamma;\bar{\gamma}) = \bar{A}_k + \bar{B}_k \Bigg(& \bar{D}_k \Big[|\bar{v}_k| + \Re\Big\{ \tfrac{\bar{v}_k^*}{|\bar{v}_k|} \left(v_k(\gamma) - \bar{v}_k\right) \Big\} \Big] \\ & - \bar{E}_k \Big(\sigma_{\mathrm{RIS}}^2 \, \gamma^H \widetilde{\mathbf{U}}_k \gamma + \sum_{m=1}^{K} p_m \, |\mathbf{c}_k^H \mathbf{A}_m \gamma|^2 \Big) - \bar{F}_k \Bigg)\end{aligned}} \tag{A.1.62}$$

with

$$\bar{D}_k = \frac{2\sqrt{\bar{x}_k}}{|\bar{v}_k|} \;=\; 2\sqrt{p_k}, \quad \bar{E}_k = \frac{1}{\sigma^2 \|\mathbf{c}_k\|^2 + \sigma_{\mathrm{RIS}}^2 \, \bar{\gamma}^H \widetilde{\mathbf{U}}_k \bar{\gamma} + \sum_{m=1}^{K} p_m \, |\mathbf{c}_k^H \mathbf{A}_m \bar{\gamma}|^2},$$
$$\bar{F}_k = \bar{E}_k \, \sigma^2 \|\mathbf{c}_k\|^2. \tag{A.1.63}$$

Concavity: (A.1.62) is the sum of an affine term (from (A.1.61)) and negatives of convex quadratics ($-x_k$, $-y_k$). *Tightness/gradient consistency:* $\widetilde{R}_k(\bar{\gamma};\bar{\gamma}) = R_k(\bar{\gamma})$ and $\nabla_\gamma \widetilde{R}_k|_{\bar{\gamma}} = \nabla_\gamma R_k|_{\bar{\gamma}}$.

RIS–numerator surrogate and SFP step. Summing over k gives a concave lower bound

$$\sum_{k=1}^{K} R_k(\gamma) \;\geq\; \sum_{k=1}^{K} \widetilde{R}_k(\gamma;\bar{\gamma}) \;\triangleq\; \widetilde{\mathcal{R}}(\gamma;\bar{\gamma}), \tag{A.1.64}$$

tight and gradient-matching at $\bar{\gamma}$. Using $\widetilde{\mathcal{R}}(\gamma;\bar{\gamma})$ as numerator and the convex denominator from the main text, the RIS subproblem is a *pseudo-concave* fractional program solvable to global optimality (e.g., by Dinkelbach). Since the surrogate is inner and reference-tight, each SFP iteration is non-decreasing in GEE, and limit points satisfy first-order stationarity (standard SCA/SFP guarantees; cf. [60], [73], [95]).

Remark A.1.4 (Zero reference field). If $\bar{v}_k = 0$, take any subgradient of $|v_k|$ with modulus ≤ 1, or regularize $|v_k| \approx \sqrt{|v_k|^2 + \varepsilon}$, $\varepsilon \downarrow 0$; both preserve global validity and tightness in the limit.

Remark A.1.5 (Numerical stability). Ensure $\bar{E}_k$ remains strictly positive by initializing from a feasible point and, if needed, adding a tiny $\varepsilon > 0$ to its denominator during early iterations; this does not alter convergence empirically.

A.1.7 MMSE-Embedded GEE: Identities, SDR Lifting, and SFP Details

This appendix collects the derivations used in Section 2.4.2: (i) the log–det sum-rate identity induced by the MMSE receiver; (ii) the semidefinite lifting $\mathbf{X} = \boldsymbol{\gamma}\boldsymbol{\gamma}^H$ with concavity and gradients; (iii) the SFP surrogate for the $\mathbf{X}$-update; (iv) the power-update surrogate and gradients; and (v) a rank-one recovery for $\boldsymbol{\gamma}$.

A. From the MMSE Filter to the Log–Det Sum-Rate Identity

The received signal is

$$\mathbf{r} \;=\; \sum_{m=1}^{K} \sqrt{p_m}\,\mathbf{A}_m \boldsymbol{\gamma}\, s_m \;+\; \mathbf{w}', \qquad \mathbf{w}' \triangleq \mathbf{G}\boldsymbol{\Gamma}\mathbf{n} + \mathbf{w}, \tag{A.1.65}$$

with $\mathbb{E}[s_m s_n^*] = \delta_{mn}$ and

$$\mathbf{W} \triangleq \mathbb{E}[\mathbf{w}'\mathbf{w}'^H] = \sigma^2 \mathbf{I}_{N_R} + \sigma_{\mathrm{RIS}}^2\, \mathbf{G}\boldsymbol{\Gamma}\boldsymbol{\Gamma}^H\mathbf{G}^H. \tag{A.1.66}$$

For user k, define the interference-plus-noise covariance

$$\mathbf{M}_k \;\triangleq\; \sum_{m\neq k} p_m\, \mathbf{A}_m \boldsymbol{\gamma}\boldsymbol{\gamma}^H \mathbf{A}_m^H \;+\; \mathbf{W} \;\succeq\; \mathbf{0}. \tag{A.1.67}$$

With a linear combiner $\mathbf{c}_k$, the SINR reads

$$\mathrm{SINR}_k(\mathbf{c}_k) = \frac{p_k\, |\mathbf{c}_k^H \mathbf{A}_k \boldsymbol{\gamma}|^2}{\mathbf{c}_k^H \mathbf{M}_k \mathbf{c}_k}. \tag{A.1.68}$$

The MMSE filter (Appendix A.1.1) is $\mathbf{c}_k^\star = \sqrt{p_k}\,\mathbf{M}_k^{-1}\mathbf{A}_k\boldsymbol{\gamma}$, which yields

$$\begin{aligned} 1 + \mathrm{SINR}_k(\mathbf{c}_k^\star) &= 1 + p_k\, \boldsymbol{\gamma}^H \mathbf{A}_k^H \mathbf{M}_k^{-1} \mathbf{A}_k \boldsymbol{\gamma} = \frac{\left|\mathbf{M}_k + p_k\, \mathbf{A}_k \boldsymbol{\gamma}\boldsymbol{\gamma}^H \mathbf{A}_k^H\right|}{|\mathbf{M}_k|} \\ &= \frac{\left|\mathbf{W} + \sum_{m=1}^{K} p_m\, \mathbf{A}_m \boldsymbol{\gamma}\boldsymbol{\gamma}^H \mathbf{A}_m^H\right|}{\left|\mathbf{W} + \sum_{m\neq k} p_m\, \mathbf{A}_m \boldsymbol{\gamma}\boldsymbol{\gamma}^H \mathbf{A}_m^H\right|}. \end{aligned} \tag{A.1.69}$$

Taking logarithms and summing over k gives

$$\mathrm{SR}_{\mathrm{MMSE}}(\boldsymbol{\gamma}, \mathbf{p}) = \sum_{k=1}^{K} \log\Big|\mathbf{W} + \sum_{m=1}^{K} p_m \, \mathbf{A}_m \boldsymbol{\gamma}\boldsymbol{\gamma}^H \mathbf{A}_m^H\Big| - \sum_{k=1}^{K} \log\Big|\mathbf{W} + \sum_{m\neq k} p_m \, \mathbf{A}_m \boldsymbol{\gamma}\boldsymbol{\gamma}^H \mathbf{A}_m^H\Big|, \tag{A.1.70}$$

which is (2.4.10) in the main text. *Sketch:* use $\mathbf{c}_k^\star$ and Woodbury to get $\mathrm{SINR}_k = p_k \, \boldsymbol{\gamma}^H \mathbf{A}_k^H \mathbf{M}_k^{-1} \mathbf{A}_k \boldsymbol{\gamma}$, then apply $|\mathbf{M} + \mathbf{u}\mathbf{u}^H| = |\mathbf{M}|(1 + \mathbf{u}^H \mathbf{M}^{-1} \mathbf{u})$ with $\mathbf{u} = \sqrt{p_k}\, \mathbf{A}_k \boldsymbol{\gamma}$.

B. Lifting to $\mathbf{X} = \boldsymbol{\gamma}\boldsymbol{\gamma}^H$, Concavity, and Gradients

Let

$$\mathbf{X} \triangleq \boldsymbol{\gamma}\boldsymbol{\gamma}^H \succeq \mathbf{0}, \qquad \mathrm{rank}(\mathbf{X}) = 1. \tag{A.1.71}$$

Then

$$\mathbf{W} = \sigma^2 \mathbf{I}_{N_R} + \sigma_{\mathrm{RIS}}^2 \, \mathbf{G} \, \mathrm{diag}(\mathbf{X}) \, \mathbf{G}^H, \qquad \mathbf{A}_m \boldsymbol{\gamma}\boldsymbol{\gamma}^H \mathbf{A}_m^H = \mathbf{A}_m \mathbf{X} \mathbf{A}_m^H. \tag{A.1.72}$$

Hence

$$\mathrm{SR}_{\mathrm{MMSE}}(\mathbf{X}) = F_1(\mathbf{X}) - F_2(\mathbf{X}), \tag{A.1.73}$$

with

$$F_1(\mathbf{X}) \triangleq \sum_{k=1}^{K} \log\left|\sigma^2 \mathbf{I}_{N_R} + \sigma_{\mathrm{RIS}}^2 \, \mathbf{G} \, \mathrm{diag}(\mathbf{X}) \mathbf{G}^H + \sum_{m=1}^{K} p_m \, \mathbf{A}_m \mathbf{X} \mathbf{A}_m^H\right|, \tag{A.1.74}$$

$$F_2(\mathbf{X}) \triangleq \sum_{k=1}^{K} \log\left|\sigma^2 \mathbf{I}_{N_R} + \sigma_{\mathrm{RIS}}^2 \, \mathbf{G} \, \mathrm{diag}(\mathbf{X}) \mathbf{G}^H + \sum_{m\neq k} p_m \, \mathbf{A}_m \mathbf{X} \mathbf{A}_m^H\right|. \tag{A.1.75}$$

Concavity. Each log–det argument is an affine function of $\mathbf{X}$ (both $\mathrm{diag}(\mathbf{X})$ and $\mathbf{A}_m \mathbf{X} \mathbf{A}_m^H$ are linear in $\mathbf{X}$). Since $\log|\cdot|$ is concave on $\mathbb{S}_{++}$, F_1 and F_2 are concave; thus $\mathrm{SR}_{\mathrm{MMSE}}$ is a *difference of concave* (DC) function.

Gradient of $F_2(\mathbf{X})$. Let

$$\mathbf{T}_k(\mathbf{X}) \triangleq \sigma^2 \mathbf{I}_{N_R} + \sigma_{\mathrm{RIS}}^2 \, \mathbf{G} \, \mathrm{diag}(\mathbf{X}) \mathbf{G}^H + \sum_{m\neq k} p_m \, \mathbf{A}_m \mathbf{X} \mathbf{A}_m^H \succ \mathbf{0}. \tag{A.1.76}$$

Using $\mathrm{d}\log|\mathbf{T}| = \mathrm{tr}(\mathbf{T}^{-1}\mathrm{d}\mathbf{T})$ and $\mathrm{diag}(\mathbf{X}) = \mathbf{X}\odot\mathbf{I}_N$, we get

$$\nabla_{\mathbf{X}}\log|\mathbf{T}_k(\mathbf{X})| = \sigma_{\mathrm{RIS}}^2\left(\mathbf{G}^H\mathbf{T}_k^{-1}\mathbf{G}\right)\odot\mathbf{I}_N + \sum_{m\neq k} p_m\,\mathbf{A}_m^H\mathbf{T}_k^{-1}\mathbf{A}_m. \tag{A.1.77}$$

Summing over k,

$$\boxed{\nabla F_2(\mathbf{X}) = \sum_{k=1}^{K}\left[\sigma_{\mathrm{RIS}}^2\left(\mathbf{G}^H\mathbf{T}_k^{-1}\mathbf{G}\right)\odot\mathbf{I}_N + \sum_{m\neq k} p_m\,\mathbf{A}_m^H\mathbf{T}_k^{-1}\mathbf{A}_m\right].} \tag{A.1.78}$$

An analogous expression holds for $\nabla F_1(\mathbf{X})$ with $\sum_{m=1}^{K}(\cdot)$ in place of $\sum_{m\neq k}(\cdot)$.

Lifted global-reflection constraints. With $\mathbf{R} \triangleq \sum_{k=1}^{K} p_k\,\mathbf{H}_k^H\mathbf{H}_k + \sigma_{\mathrm{RIS}}^2\mathbf{I}_N$,

$$\mathrm{tr}(\mathbf{R}) \;\le\; \mathrm{tr}(\mathbf{R}\mathbf{X}) \;\le\; \mathrm{tr}(\mathbf{R}) + P_{R,\max}, \qquad \mathbf{X}\succeq\mathbf{0}. \tag{A.1.79}$$

The rank constraint is relaxed (SDR), and γ is recovered in a post-processing step.

C. SFP Surrogate for the X-Update

For fixed $\mathbf{p}$,

$$\max_{\mathbf{X}\succeq\mathbf{0}} \quad \frac{\mathrm{SR}_{\mathrm{MMSE}}(\mathbf{X})}{\mathrm{tr}(\mathbf{R}\mathbf{X}) + P_{c,\mathrm{eq}}} \quad \text{s.t. (A.1.79).} \tag{A.1.80}$$

Linearize the concave part F_2 at a feasible $\bar{\mathbf{X}}$:

$$\widetilde{\mathrm{SR}}_{\mathrm{MMSE}}(\mathbf{X};\bar{\mathbf{X}}) = F_1(\mathbf{X}) - \Big(F_2(\bar{\mathbf{X}}) + \Re\{\mathrm{tr}(\nabla F_2(\bar{\mathbf{X}})^H(\mathbf{X}-\bar{\mathbf{X}}))\}\Big), \tag{A.1.81}$$

which is concave in $\mathbf{X}$. Each SFP iteration solves the concave-over-affine program

$$\max_{\mathbf{X}\succeq\mathbf{0}} \quad \frac{\widetilde{\mathrm{SR}}_{\mathrm{MMSE}}(\mathbf{X};\bar{\mathbf{X}})}{\mathrm{tr}(\mathbf{R}\mathbf{X}) + P_{c,\mathrm{eq}}} \quad \text{s.t. (A.1.79).} \tag{A.1.82}$$

Solution via Dinkelbach. For parameter $\eta \ge 0$, solve

$$\max_{\mathbf{X}\succeq\mathbf{0}} \quad \Phi_\eta(\mathbf{X}) \triangleq \widetilde{\mathrm{SR}}_{\mathrm{MMSE}}(\mathbf{X};\bar{\mathbf{X}}) - \eta\big(\mathrm{tr}(\mathbf{R}\mathbf{X}) + P_{c,\mathrm{eq}}\big) \quad \text{s.t. (A.1.79).} \tag{A.1.83}$$

For fixed η, (A.1.83) is a concave maximization with affine constraints. Set

$$\eta \leftarrow \frac{\widetilde{\mathrm{SR}}_{\mathrm{MMSE}}(\mathbf{X}^\star;\bar{\mathbf{X}})}{\mathrm{tr}(\mathbf{R}\mathbf{X}^\star)+P_{c,\mathrm{eq}}},$$

update $\bar{\mathbf{X}} \leftarrow \mathbf{X}^\star$, and iterate.

D. Rank-One Recovery of γ

If $\mathrm{rank}(\mathbf{X}^\star)=1$, factor $\mathbf{X}^\star=\gamma^\star(\gamma^\star)^H$. Otherwise, use Gaussian randomization:

1. Draw $\mathbf{v}^{(\ell)} \sim \mathcal{CN}(\mathbf{0},\mathbf{X}^\star)$, $\ell=1,\dots,L$.
2. Scale to feasibility:

$$\alpha^{(\ell)} \leftarrow \min\left\{\sqrt{\frac{\mathrm{tr}(\mathbf{R})+P_{R,\max}}{\mathrm{tr}(\mathbf{R}\,\mathbf{v}^{(\ell)}\mathbf{v}^{(\ell)H})}},\ \max\left\{1,\sqrt{\frac{\mathrm{tr}(\mathbf{R})}{\mathrm{tr}(\mathbf{R}\,\mathbf{v}^{(\ell)}\mathbf{v}^{(\ell)H})}}\right\}\right\},\quad \hat{\boldsymbol{\gamma}}^{(\ell)} \leftarrow \alpha^{(\ell)}\mathbf{v}^{(\ell)}.$$

3. Evaluate the true MMSE-embedded GEE for $\hat{\boldsymbol{\gamma}}^{(\ell)}$ and keep the best.

E. SFP Surrogate and Gradients for the Power Update

For fixed $\boldsymbol{\gamma}$, define

$$\mathbf{T}_k(\mathbf{p}) \triangleq \mathbf{W}+\sum_{m\neq k} p_m\,\mathbf{A}_m\boldsymbol{\gamma}\boldsymbol{\gamma}^H\mathbf{A}_m^H,\qquad \mathbf{S}(\mathbf{p}) \triangleq \mathbf{W}+\sum_{m=1}^{K} p_m\,\mathbf{A}_m\boldsymbol{\gamma}\boldsymbol{\gamma}^H\mathbf{A}_m^H. \tag{A.1.84}$$

Then

$$\mathrm{SR}_{\mathrm{MMSE}}(\mathbf{p})=\sum_{k=1}^{K}\log|\mathbf{S}(\mathbf{p})|-\sum_{k=1}^{K}\log|\mathbf{T}_k(\mathbf{p})|. \tag{A.1.85}$$

With amplifier coefficients $\mu_{k,\mathrm{eq}}$ and circuit term $P_{c,\mathrm{eq}}$,

$$\mathrm{GEE}_{\mathrm{MMSE}}(\mathbf{p})=\frac{\mathrm{SR}_{\mathrm{MMSE}}(\mathbf{p})}{\sum_{k=1}^{K}\mu_{k,\mathrm{eq}}p_k+P_{c,\mathrm{eq}}}. \tag{A.1.86}$$

Gradients. Let $F_2(\mathbf{p}) = \sum_{k=1}^{K} \log|\mathbf{T}_k(\mathbf{p})|$. Since $\partial \mathbf{T}_k / \partial p_i = \mathbf{A}_i \boldsymbol{\gamma}\boldsymbol{\gamma}^H \mathbf{A}_i^H$ for $i \neq k$ (and $\mathbf{0}$ for $i = k$),

$$\boxed{\frac{\partial F_2}{\partial p_i} = \sum_{k \neq i} \operatorname{tr}\Big(\mathbf{T}_k(\mathbf{p})^{-1}\, \mathbf{A}_i \boldsymbol{\gamma}\boldsymbol{\gamma}^H \mathbf{A}_i^H\Big).} \tag{A.1.87}$$

Similarly, for $F_1(\mathbf{p}) = \sum_{k=1}^{K} \log|\mathbf{S}(\mathbf{p})|$,

$$\frac{\partial F_1}{\partial p_i} = \sum_{k=1}^{K} \operatorname{tr}\Big(\mathbf{S}(\mathbf{p})^{-1}\, \mathbf{A}_i \boldsymbol{\gamma}\boldsymbol{\gamma}^H \mathbf{A}_i^H\Big). \tag{A.1.88}$$

Power SFP. Linearize the concave F_2 at $\bar{\mathbf{p}}$:

$$\widetilde{\mathrm{SR}}_{\mathrm{MMSE}}(\mathbf{p}; \bar{\mathbf{p}}) = F_1(\mathbf{p}) - \Big(F_2(\bar{\mathbf{p}}) + \nabla F_2(\bar{\mathbf{p}})^T(\mathbf{p} - \bar{\mathbf{p}})\Big), \tag{A.1.89}$$

and solve the concave-over-affine program

$$\max_{\mathbf{0} \le \mathbf{p} \le \mathbf{P}_{\max}} \quad \frac{\widetilde{\mathrm{SR}}_{\mathrm{MMSE}}(\mathbf{p}; \bar{\mathbf{p}})}{\sum_{k=1}^{K} \mu_{k,\mathrm{eq}} p_k + P_{c,\mathrm{eq}}}. \tag{A.1.90}$$

Using Dinkelbach yields the sequence

$$\max_{\mathbf{0} \le \mathbf{p} \le \mathbf{P}_{\max}} \quad \widetilde{\mathrm{SR}}_{\mathrm{MMSE}}(\mathbf{p}; \bar{\mathbf{p}}) - \eta\Big(\sum_{k=1}^{K} \mu_{k,\mathrm{eq}} p_k + P_{c,\mathrm{eq}}\Big), \tag{A.1.91}$$

with η updated by the current ratio.

F. KKT Conditions for the Concave-Over-Affine Subproblems

For either (A.1.83) or the power case above, KKT conditions are necessary and sufficient (concave objective, convex feasible set). For (A.1.83):

$$\nabla_{\mathbf{X}} \widetilde{\mathrm{SR}}_{\mathrm{MMSE}}(\mathbf{X}; \bar{\mathbf{X}}) - \eta\, \mathbf{R} - \boldsymbol{\Lambda} + \lambda_+\, \mathbf{R} - \lambda_-\, \mathbf{R} = \mathbf{0}, \tag{A.1.92}$$

with $\boldsymbol{\Lambda} \succeq \mathbf{0}$ the multiplier for $\mathbf{X} \succeq \mathbf{0}$, and $\lambda_+, \lambda_- \geq 0$ for the upper and lower global-reflection bounds in (A.1.79), plus feasibility and complementary slackness. The power case follows analogously.

A.1.8 Explicit Gradients for the RIS Surrogate

This subsection derives closed-form expressions for the gradients required by the parametric subproblem (3.3.19) in the RIS-update step (see Sec. 3.3). All

derivatives are taken in the Wirtinger sense with respect to γ^*. The following identities hold for constant matrices/vectors $(\boldsymbol{M}, \boldsymbol{A}, \boldsymbol{a})$ and complex variable γ:

$$\nabla_{\gamma^*}(\gamma^H \boldsymbol{M}\gamma) = \boldsymbol{M}\gamma, \qquad \nabla_{\gamma^*}\Re\{\boldsymbol{a}^H\gamma\} = \tfrac{1}{2}\boldsymbol{a}, \qquad \nabla_{\gamma^*}\|\boldsymbol{A}\gamma\|^2 = \boldsymbol{A}^H\boldsymbol{A}\gamma.$$

Throughout, the following Hermitian positive semidefinite (HPSD) matrices are used:

$$\boldsymbol{M}_{k,B} = \boldsymbol{A}_k^H \boldsymbol{c}_k \boldsymbol{c}_k^H \boldsymbol{A}_k, \qquad \boldsymbol{I}_{k,m}^{(B)} = \boldsymbol{A}_m^H \boldsymbol{c}_k \boldsymbol{c}_k^H \boldsymbol{A}_m, \qquad \boldsymbol{N}_{m,E} = \boldsymbol{H}_m^H \boldsymbol{g}\boldsymbol{g}^H \boldsymbol{H}_m,$$

with $\widetilde{\boldsymbol{U}}_k = \mathrm{diag}(|u_{k,1}|^2, \ldots, |u_{k,N}|^2)$ and

$$\boldsymbol{M}_{k,E} = \sum_{m \neq k} p_m \boldsymbol{N}_{m,E} + \sigma_{\mathrm{RIS}}^2 \boldsymbol{G}\boldsymbol{G}^H.$$

Basic differentials. From (3.3.3)–(3.3.5), one obtains

$$\begin{aligned}
x_B &= p_k\, \gamma^H \boldsymbol{M}_{k,B}\gamma, && \Rightarrow\ \nabla_{\gamma^*} x_B = p_k\, \boldsymbol{M}_{k,B}\gamma,\\
y_B &= \sigma_B^2\|\boldsymbol{c}_k\|^2 + \sigma_{\mathrm{RIS}}^2 \gamma^H \widetilde{\boldsymbol{U}}_k \gamma + \sum_{m\neq k} p_m \gamma^H \boldsymbol{I}_{k,m}^{(B)}\gamma, && \Rightarrow\ \nabla_{\gamma^*} y_B = \sigma_{\mathrm{RIS}}^2 \widetilde{\boldsymbol{U}}_k \gamma + \sum_{m\neq k} p_m \boldsymbol{I}_{k,m}^{(B)}\gamma,\\
x_E &= p_k\, \gamma^H \boldsymbol{N}_{k,E}\gamma, && \Rightarrow\ \nabla_{\gamma^*} x_E = p_k\, \boldsymbol{N}_{k,E}\gamma,\\
y_E &= \gamma^H \boldsymbol{M}_{k,E}\gamma, && \Rightarrow\ \nabla_{\gamma^*} y_E = \boldsymbol{M}_{k,E}\gamma.
\end{aligned}$$

Affine lower approximations. From (3.3.14) and (3.3.15), with

$$\bar{x}_B = p_k\, \bar{\gamma}^H \boldsymbol{M}_{k,B}\bar{\gamma}, \qquad \bar{y}_E = \bar{\gamma}^H \boldsymbol{M}_{k,E}\bar{\gamma},$$

the affine lower bounds and their gradients are

$$\begin{aligned}
\widetilde{x}_B(\bar{\gamma}) &= \sqrt{p_k}\left(\sqrt{\bar{x}_B} + \frac{\Re\{\bar{\gamma}^H \boldsymbol{M}_{k,B}(\gamma - \bar{\gamma})\}}{\sqrt{\bar{x}_B}}\right), && \nabla_{\gamma^*}\widetilde{x}_B(\bar{\gamma}) = \sqrt{p_k}\frac{\boldsymbol{M}_{k,B}\bar{\gamma}}{2\sqrt{\bar{x}_B}},\\
\widetilde{y}_E(\bar{\gamma}) &= \sqrt{\bar{y}_E} + \frac{\Re\{\bar{\gamma}^H \boldsymbol{M}_{k,E}(\gamma - \bar{\gamma})\}}{\sqrt{\bar{y}_E}}, && \nabla_{\gamma^*}\widetilde{y}_E(\bar{\gamma}) = \frac{\boldsymbol{M}_{k,E}\bar{\gamma}}{2\sqrt{\bar{y}_E}}.
\end{aligned}$$

Gradient of the user-k surrogate. Define the reference scalars

$$\mathsf{A}_{k,B} = \frac{\bar{x}_B}{\bar{y}_B}, \quad \mathsf{B}_{k,B} = \frac{1}{\bar{x}_B + \bar{y}_B}, \quad \mathsf{A}_{k,E} = \frac{\bar{y}_E}{\sigma_E^2}, \quad \mathsf{B}_{k,E} = \frac{1}{\bar{y}_E + \sigma_E^2}, \quad \mathsf{C}_k = \frac{1}{\sigma_E^2 + \bar{x}_E + \bar{y}_E}.$$

Ignoring additive constants (which vanish under differentiation), the gradient of the per-user surrogate $\widetilde{R}_{s,k}^{\mathrm{PCSI}}(\boldsymbol{\gamma})$ from (3.3.16) is

$$\begin{aligned}\nabla_{\boldsymbol{\gamma}^*}\widetilde{R}_{s,k}^{\mathrm{PCSI}}(\boldsymbol{\gamma}) = 2\mathsf{A}_{k,B}\frac{\nabla_{\boldsymbol{\gamma}^*}\widetilde{x}_B}{\sqrt{\bar{x}_B}} - \mathsf{A}_{k,B}\mathsf{B}_{k,B}\big(\nabla_{\boldsymbol{\gamma}^*}x_B + \nabla_{\boldsymbol{\gamma}^*}y_B\big)\\ + 2\mathsf{A}_{k,E}\frac{\nabla_{\boldsymbol{\gamma}^*}\widetilde{y}_E}{\sqrt{\bar{y}_E}} - \mathsf{A}_{k,E}\mathsf{B}_{k,E}\nabla_{\boldsymbol{\gamma}^*}y_E - \mathsf{C}_k\big(\nabla_{\boldsymbol{\gamma}^*}x_E + \nabla_{\boldsymbol{\gamma}^*}y_E\big).\end{aligned} \tag{A.1.93}$$

Substituting the explicit components above gives

$$\begin{aligned}\nabla_{\boldsymbol{\gamma}^*}\widetilde{R}_{s,k}^{\mathrm{PCSI}}(\boldsymbol{\gamma}) = 2\mathsf{A}_{k,B}\frac{\sqrt{p_k}\boldsymbol{M}_{k,B}\bar{\boldsymbol{\gamma}}}{2\sqrt{\bar{x}_B}} - \mathsf{A}_{k,B}\mathsf{B}_{k,B}\Big(p_k\boldsymbol{M}_{k,B}\boldsymbol{\gamma} + \sigma_{\mathrm{RIS}}^2\widetilde{\boldsymbol{U}}_k\boldsymbol{\gamma} + \sum_{m\neq k}p_m\boldsymbol{I}_{k,m}^{(B)}\boldsymbol{\gamma}\Big)\\ + 2\mathsf{A}_{k,E}\frac{\boldsymbol{M}_{k,E}\bar{\boldsymbol{\gamma}}}{2\sqrt{\bar{y}_E}} - \mathsf{A}_{k,E}\mathsf{B}_{k,E}\boldsymbol{M}_{k,E}\boldsymbol{\gamma} - \mathsf{C}_k\Big(p_k\boldsymbol{N}_{k,E}\boldsymbol{\gamma} + \boldsymbol{M}_{k,E}\boldsymbol{\gamma}\Big).\end{aligned}$$

Gradient of the Dinkelbach objective. The concave subproblem (3.3.19) maximizes

$$\Phi_\eta(\boldsymbol{\gamma}) = \sum_{k=1}^{K}\widetilde{R}_{s,k}^{\mathrm{PCSI}}(\boldsymbol{\gamma}) - \eta\big(\operatorname{tr}(\boldsymbol{R}\boldsymbol{\gamma}\boldsymbol{\gamma}^H) + P_{c,eq}^{(a)}\big),$$

subject to constraints (3.3.18b)–(3.3.18c). Its gradient is therefore

$$\nabla_{\boldsymbol{\gamma}^*}\Phi_\eta(\boldsymbol{\gamma}) = \sum_{k=1}^{K}\nabla_{\boldsymbol{\gamma}^*}\widetilde{R}_{s,k}^{\mathrm{PCSI}}(\boldsymbol{\gamma}) - \eta\,\boldsymbol{R}\boldsymbol{\gamma}, \tag{A.1.94}$$

where $\nabla_{\boldsymbol{\gamma}^*}\widetilde{R}_{s,k}^{\mathrm{PCSI}}$ is given in (A.1.93). Since all coefficient matrices are HPSD and the surrogate is concave in $\boldsymbol{\gamma}$, the gradient (A.1.94) can be used in standard first- or second-order methods (e.g., projected gradient or interior-point algorithms). The quadratic constraint (3.3.18b) is convex, and the affine approximation (3.3.18c) ensures feasibility via projection or barrier enforcement in each iteration.

A.2 Implementation Details and Rank-One Penalty Justification

This appendix (i) justifies the rank-one penalty used for the lifted beamforming matrices, (ii) records the exact initialization formulas used in Fig. 4.4.8, and (iii) lists the solver interface used in our code.

A.2.1 Proof that the Rank Penalty Enforces Rank-One

We optimize over lifted transmit covariances $\mathbf{W}_k \succeq \mathbf{0}$ and promote rank-one by adding

$$\rho(\mathbf{W}_k) \triangleq \mathrm{Tr}(\mathbf{W}_k) - \lambda_{\max}(\mathbf{W}_k)$$

to the objective (with a weight). Intuitively, $\mathrm{Tr}(\mathbf{W})$ is the *sum* of all eigenvalues, while $\lambda_{\max}(\mathbf{W})$ is the *largest* one. Their difference therefore measures "energy left in the smaller eigenvalues." If that difference is driven to zero under a fixed trace, all the energy must sit in a single eigenvalue, hence rank-one.

Step 1: Nonnegativity and exact zero only at rank-≤ 1. Let $\mathbf{W} \succeq \mathbf{0}$ have eigenvalues $\lambda_1 \geq \lambda_2 \geq \cdots \geq \lambda_M \geq 0$. Then

$$\rho(\mathbf{W}) = \mathrm{Tr}(\mathbf{W}) - \lambda_{\max}(\mathbf{W}) = \sum_{i=1}^{M} \lambda_i - \lambda_1 = \sum_{i=2}^{M} \lambda_i \geq 0,$$

and $\rho(\mathbf{W}) = 0$ holds iff $\lambda_2 = \cdots = \lambda_M = 0$, i.e., $\mathrm{rank}(\mathbf{W}) \leq 1$.

Step 2: With fixed trace (power closure), minimizing ρ picks rank-one. Assume $\mathrm{Tr}(\mathbf{W}) = P_{\text{data}}$ is fixed by the power budget (directly, or via total power closure). Minimizing $\rho(\mathbf{W}) = \sum_{i=2}^{M} \lambda_i$ subject to $\sum_{i=1}^{M} \lambda_i = P_{\text{data}}$ clearly achieves its minimum when *all* the sum is placed in λ_1 and the rest are zero:

$$(\lambda_1, \lambda_2, \ldots, \lambda_M) = (P_{\text{data}}, 0, \ldots, 0) \quad \Rightarrow \quad \mathrm{rank}(\mathbf{W}) = 1.$$

Hence, among all PSD matrices with the same trace, the minimizers of ρ are exactly the rank-one ones.

What the optimizer "sees." The penalty simply suppresses energy in the tail eigenvalues. When combined with the trace/power constraint, this pushes the solution onto the ray $\mathbf{W} = \lambda\, \mathbf{u}\mathbf{u}^H$ for some unit vector $\mathbf{u}$—precisely rank-one.

Subgradient used in first-order methods. Let $\mathcal{U}(\mathbf{W})$ be the set of unit eigenvectors associated with $\lambda_{\max}(\mathbf{W})$:

$$\mathcal{U}(\mathbf{W}) \triangleq \{\, \mathbf{u} \in \mathbb{C}^M : \mathbf{W}\mathbf{u} = \lambda_{\max}(\mathbf{W})\, \mathbf{u},\ \|\mathbf{u}\| = 1 \,\}.$$

A standard result gives

$$\partial\lambda_{\max}(\mathbf{W}) = \operatorname{conv}\{\, \mathbf{u}\mathbf{u}^H : \mathbf{u} \in \mathcal{U}(\mathbf{W}) \,\}, \quad \Rightarrow \quad \partial\rho(\mathbf{W}) = \mathbf{I} - \partial\lambda_{\max}(\mathbf{W}) \ni \mathbf{I} - \mathbf{u}\mathbf{u}^H.$$

This is the object we plug into KKT/first-order updates when the term $\alpha_k \rho(\mathbf{W}_k)$ is present.

Takeaway. Under a fixed-trace (power) constraint, driving $\rho(\mathbf{W})$ to zero *is equivalent* to enforcing rank-one. This gives a simple, effective substitute for an explicit rank constraint and behaves well in practice.

A.2.2 Derivations of Initialization Strategies

This appendix provides explicit, reproducible formulas for the eight initialization strategies used in Fig. 4.4.8. Each strategy is obtained by combining one choice for (i) metasurface phases, (ii) BS precoder, and (iii) AN covariance. Throughout, $P_{\max}$ denotes the total radiated power budget; the effective user channels $\{\mathbf{h}_k^{\text{eff}}\}_{k=1}^K$ are computed from the fixed channel realizations and the current metasurface phases (when metasurfaces are initialized first).

Notation. Let $\Gamma_t = \operatorname{diag}(\boldsymbol{\gamma}_t)$ and $\Gamma_r = \operatorname{diag}(\boldsymbol{\gamma}_r)$ with $\boldsymbol{\gamma}_t = [\beta_{t,1}, \ldots, \beta_{t,N_t}]^T$, $\boldsymbol{\gamma}_r = [\beta_{r,1}, \ldots, \beta_{r,N_r}]^T$, $|\beta_{t,n}|=|\beta_{r,n}|=1$. Stack user channels in $\mathbf{H} \triangleq [\mathbf{h}_1^{\text{eff}}, \ldots, \mathbf{h}_K^{\text{eff}}] \in \mathbb{C}^{M\times K}$. The data precoder is $\mathbf{W} = [\mathbf{w}_1, \ldots, \mathbf{w}_K] \in \mathbb{C}^{M\times K}$ and the AN covariance is $\mathbf{C}_z \succeq \mathbf{0}$. We let

$$P_{\text{data}} \triangleq \sum_{k=1}^{K} \|\mathbf{w}_k\|^2, \qquad P_{\text{AN}} \triangleq \operatorname{Tr}(\mathbf{C}_z), \qquad P_{\text{data}} + P_{\text{AN}} = P_{\max}.$$

When convenient, we allocate a fraction $\phi \in (0,1)$ to data power and $1-\phi$ to AN:

$$P_{\text{data}} = \phi P_{\max}, \qquad P_{\text{AN}} = (1-\phi) P_{\max}. \tag{A.2.1}$$

A. Metasurface Phase Initializations

A1) Random phases. Draw i.i.d. phases uniformly on the unit circle:

$$\beta_{t,n} = e^{\jmath\theta_{t,n}}, \quad \theta_{t,n} \sim \mathcal{U}[0, 2\pi), \quad n = 1, \ldots, N_t, \tag{A.2.2}$$

$$\beta_{r,n} = e^{\jmath\theta_{r,n}}, \quad \theta_{r,n} \sim \mathcal{U}[0, 2\pi), \quad n = 1, \ldots, N_r. \tag{A.2.3}$$

Set $\Gamma_t = \operatorname{diag}(\boldsymbol{\gamma}_t)$, $\Gamma_r = \operatorname{diag}(\boldsymbol{\gamma}_r)$.

A2) SVD-based phases. Compute leading right-singular vectors of the BS–RHS and RHS–RIS channels:

$$\mathbf{Q}_t = \mathbf{U}_t \mathbf{\Sigma}_t \mathbf{V}_t^H, \quad \mathbf{v}_t \triangleq \mathbf{v}_1(\mathbf{Q}_t) \text{ (first column of } \mathbf{V}_t), \tag{A.2.4}$$

$$\mathbf{Q}_r = \mathbf{U}_r \mathbf{\Sigma}_r \mathbf{V}_r^H, \quad \mathbf{v}_r \triangleq \mathbf{v}_1(\mathbf{Q}_r). \tag{A.2.5}$$

Initialize metasurface phases by phase alignment with the dominant singular directions:

$$\beta_{t,n} = e^{\jmath \angle([\mathbf{v}_t]_n)}, \qquad n = 1, \ldots, N_t, \tag{A.2.6}$$

$$\beta_{r,n} = e^{\jmath \angle([\mathbf{v}_r]_n)}, \qquad n = 1, \ldots, N_r, \tag{A.2.7}$$

and set $\Gamma_t = \mathrm{diag}(\boldsymbol{\gamma}_t)$, $\Gamma_r = \mathrm{diag}(\boldsymbol{\gamma}_r)$. *Remark:* If desired, you may refine SVD-based phases by re-aligning Γ_r with the cascaded steering term $\mathbf{Q}_r \Gamma_t \mathbf{Q}_t$; we keep the simple, reproducible rule above.

B. Linear Precoder Initializations

After fixing (Γ_t, Γ_r), compute effective channels $\{\mathbf{h}_k^{\text{eff}}\}$ and stack $\mathbf{H} = [\mathbf{h}_1^{\text{eff}}, \ldots, \mathbf{h}_K^{\text{eff}}]$.

B1) Maximum-ratio transmission (MRT). Unnormalized MRT beams:

$$\tilde{\mathbf{w}}_k \triangleq \mathbf{h}_k^{\text{eff}}, \qquad k = 1, \ldots, K. \tag{A.2.8}$$

Normalize to meet a target data power $\phi P_{\max}$ (cf. (A.2.1)):

$$\alpha_{\text{MRT}} \triangleq \sqrt{\frac{\phi P_{\max}}{\sum_{k=1}^{K} \|\tilde{\mathbf{w}}_k\|^2}}, \tag{A.2.9}$$

$$\mathbf{w}_k^{(0)} = \alpha_{\text{MRT}}\, \tilde{\mathbf{w}}_k, \qquad k = 1, \ldots, K. \tag{A.2.10}$$

B2) Regularized zero-forcing (RZF). Form the RZF matrix with regularization $\xi > 0$:

$$\tilde{\mathbf{W}} \triangleq \mathbf{H}\Big(\mathbf{H}^H \mathbf{H} + \xi \mathbf{I}_K\Big)^{-1}, \tag{A.2.11}$$

$$\alpha_{\text{RZF}} \triangleq \sqrt{\frac{\phi P_{\max}}{\|\tilde{\mathbf{W}}\|_F^2}}, \qquad \mathbf{W}^{(0)} \triangleq \alpha_{\text{RZF}} \tilde{\mathbf{W}}, \quad \mathbf{w}_k^{(0)} = \mathbf{W}^{(0)} \mathbf{e}_k, \tag{A.2.12}$$

where $\mathbf{e}_k$ is the k-th canonical basis vector. *Choice of ξ:* a robust default is $\xi = \frac{K}{P_{\max}} \sigma^2$ (MMSE-motivated); alternatively set $\xi = \zeta \frac{\mathrm{Tr}(\mathbf{H}^H \mathbf{H})}{K}$ with a small $\zeta \in [10^{-3}, 10^{-1}]$. Either choice yields a well-conditioned $\mathbf{H}^H \mathbf{H} + \xi \mathbf{I}$.

C. Artificial-Noise (AN) Covariance Initializations

C1) Isotropic AN. Allocate power $(1-\phi)P_{\max}$ isotropically in the M-dimensional TX space:

$$\mathbf{C}_z^{(0)} = \rho_{\text{iso}}\,\mathbf{I}_M, \qquad \rho_{\text{iso}} \triangleq \frac{(1-\phi)P_{\max}}{M}. \tag{A.2.13}$$

C2) Null-space AN. Let $\mathbf{W}^{(0)} = [\mathbf{w}_1^{(0)}, \ldots, \mathbf{w}_K^{(0)}]$ and compute a basis of the (left) null-space of $\mathbf{W}^{(0)H}$ via thin SVD:

$$\mathbf{W}^{(0)H} = \mathbf{U}\begin{bmatrix}\mathbf{\Sigma} & \mathbf{0}\end{bmatrix}\begin{bmatrix}\mathbf{V}_1 & \mathbf{V}_\perp\end{bmatrix}^H, \qquad \mathbf{U}_\perp \triangleq \mathbf{V}_\perp \in \mathbb{C}^{M\times(M-K')}, \tag{A.2.14}$$

where $K' = \operatorname{rank}(\mathbf{W}^{(0)}) \le K$ and $\mathbf{U}_\perp$ spans $\operatorname{null}(\mathbf{W}^{(0)H})$. Place AN in that subspace:

$$\mathbf{C}_z^{(0)} = \rho_\perp\,\mathbf{U}_\perp\mathbf{U}_\perp^H, \qquad \rho_\perp \triangleq \frac{(1-\phi)P_{\max}}{M-K'}, \tag{A.2.15}$$

provided $M > K'$. *Edge case:* if $M \le K'$ (no null-space), fall back to (A.2.13).

Note. For numerical stability, the initial AN covariance matrix can be slightly regularized to ensure strict positive definiteness. This is achieved by adding a small diagonal term:

$$\mathbf{C}_z^{(0)} \leftarrow \mathbf{C}_z^{(0)} + \epsilon\,\mathbf{I}_M, \qquad \text{with } \epsilon > 0 \text{ (typically } 10^{-6} \le \epsilon \le 10^{-3}).$$

This adjustment prevents singularities in early iterations and improves the conditioning of matrix operations involving $\mathbf{C}_z$.

D. Power Closure and Edge-Case Handling

The constructions (A.2.10), (A.2.12), (A.2.13), (A.2.15) jointly satisfy the radiated-power constraint:

$$\sum_{k=1}^{K}\|\mathbf{w}_k^{(0)}\|^2 + \operatorname{Tr}(\mathbf{C}_z^{(0)}) = \phi P_{\max} + (1-\phi)P_{\max} = P_{\max}. \tag{A.2.16}$$

If you prefer to avoid the hyperparameter ϕ, you can enforce the total constraint directly by first forming $\tilde{\mathbf{W}}$ (MRT or RZF), scaling it with $\alpha = \sqrt{P_{\max}/(\|\tilde{\mathbf{W}}\|_F^2 + \operatorname{Tr}(\tilde{\mathbf{C}}_z))}$ where $\tilde{\mathbf{C}}_z$ is a pre-choice (e.g., isotropic with ρ=1), and then set $\mathbf{W}^{(0)} = \alpha\tilde{\mathbf{W}}$, $\mathbf{C}_z^{(0)} = \alpha\tilde{\mathbf{C}}_z$.

E. Baseband Power Consumption Model and Parameter Choices

This subsection specifies the baseband (BB) power consumption model and the corresponding parameter values used exclusively for the numerical results reported in Section 4.4. The aim is to document the assumptions underlying the quantitative evaluations without suggesting that the same parameterization is adopted elsewhere in the thesis.

Model rationale. The BB power consumption accounts for the digital signal processing operations required at the transmitter and receiver, including stream processing, RF-chain interfacing, bandwidth-dependent operations, and linear precoder computation. A parametric formulation is adopted when architectural aspects are explicitly compared, so as to capture the scaling of digital complexity with the main system dimensions.

Parametric model. For the numerical investigations in Section 4.4, the BB power consumption is modeled as

$$P_{\mathrm{BB}} = P_{\mathrm{BB}}^{\mathrm{base}} + \alpha_s N_s + \alpha_{\mathrm{RF}}(N_t^{\mathrm{RF}} + N_r^{\mathrm{RF}}) + \alpha_{\mathrm{BW}} \frac{B}{20\,\mathrm{MHz}} + \alpha_{\mathrm{prec}} \mathcal{C}_{\mathrm{prec}}(M, K), \tag{A.2.17}$$

where $P_{\mathrm{BB}}^{\mathrm{base}}$ denotes the static BB power, N_s is the number of data streams, N_t^{RF} and N_r^{RF} are the numbers of transmit and receive RF chains, B is the system bandwidth, and $\mathcal{C}_{\mathrm{prec}}(M, K)$ is a dimensionless measure of the computational cost associated with the chosen linear precoder.

Precoder complexity term. The precoder cost $\mathcal{C}_{\mathrm{prec}}(M, K)$ is modeled through simple scaling laws that reflect the dominant matrix–vector and matrix inversion operations required by standard linear precoders. In particular,

$$\mathcal{C}_{\mathrm{prec}}(M, K) = \begin{cases} MK, & \text{MRT}, \\ MK^2 + K^3, & \text{ZF or RZF}. \end{cases} \tag{A.2.18}$$

The terms in (A.2.18) are dimensionless and capture the leading-order dependence on the number of BS antennas M and the number of served users K. The coefficient α_{prec} in (A.2.17) converts these cost units into watts.

Parameter configuration used in the numerical results. The coefficients adopted in (A.2.17) for the numerical results in Section 4.4 are summarized in Table A.2.1. These values are representative of sub-6 GHz small-cell

TABLE A.2.1: Baseband power model parameters used in Section 4.4.

Parameter	Value	Description
$P_{\mathrm{BB}}^{\mathrm{base}}$	33 dBm ($\approx$ 2.0 W)	Static baseband power offset
α_s	1.0 W / stream	Power per transmitted data stream
α_{RF}	0.3 W / RF chain	Digital interfacing cost per TX or RX RF chain
α_{BW}	0.3 W / 20 MHz	Bandwidth-dependent processing cost
α_{prec}	2×10^{-3} W / cost unit	Precoder computation coefficient

hardware and are used solely for the quantitative comparisons presented therein.

Use in architectural comparisons. The parametric BB model in (A.2.17)–(A.2.18), together with the parameter configuration in Table A.2.1, is employed for the quantitative comparison with fully-digital architectures, i.e., systems not employing RISs or RHSs. This enables implementation complexity, energy efficiency, and hardware cost to be compared on a consistent footing by explicitly accounting for the digital processing burden of fully-digital beamforming. The resulting trade-offs and design implications are discussed in Section 4.4 (references to the corresponding figures will be added later).

Fallback to fixed baseline model. For the remaining numerical studies reported in Section 4.4, namely Figs. 4.4.4, 4.4.6, 4.4.7, and 4.4.8, a simplified BB power model is adopted. In these cases, the BB power consumption is fixed to the baseline value

$$P_{\mathrm{BB}} = P_{\mathrm{BB}}^{\mathrm{base}} = 35 \text{ dBm}, \tag{A.2.19}$$

independently of the system dimensions and signal processing configuration. This choice isolates the impact of the proposed optimization strategies and metasurface configurations, while ensuring consistent comparisons across all considered schemes.

A.2.3 Solver Interface and Numerical Environment (MATLAB/Python + MOSEK)

All convex surrogate subproblems (SDP/SOCP formulations arising in the inner Dinkelbach–SFP loops) were solved using interior-point methods in either *MATLAB* or *Python*. Specifically, CVX (v2.2) with MOSEK or SDPT3

back-ends was used in MATLAB, while `cvxpy` (v1.x) with MOSEK served as the Python counterpart. Both implementations yielded identical numerical results within solver tolerances.

Default barrier and scaling parameters were adopted unless otherwise stated. Feasibility was preserved at each SFP iteration by projecting intermediate solutions onto the convex quadratic or affine constraint sets. Solver tolerances were fixed between $10^{-3} - 10^{-6}$ for primal and dual residuals, providing a reliable balance between numerical accuracy and computational cost. All experiments were conducted on multi-core CPUs with at least 32 GB of RAM.

A.3 Fractional Programming and Dinkelbach-Type Algorithms

This appendix summarizes the fractional programming (FP) framework that forms the mathematical core of all energy- and secrecy-efficiency formulations used in the thesis. It outlines the single-ratio optimization model, explains the Dinkelbach transformation, and discusses how this principle is implemented with alternating optimization (AO) and successive convex approximation (SCA). The presentation follows the rigorous treatment in [95] but is written in a more constructive, algorithmic style for clarity.

A.3.1 Problem setup and assumptions

Let $\mathcal{X} \subset \mathbb{R}^n$ be a nonempty compact convex set. The basic single-ratio fractional program is

$$\max_{\mathbf{x}\in\mathcal{X}} \ \frac{f(\mathbf{x})}{g(\mathbf{x})} \qquad \text{s.t.} \quad g(\mathbf{x}) > 0, \tag{A.3.1}$$

where

- $f(\mathbf{x})$ is a concave objective or a concave *surrogate* of a nonconcave utility (e.g., sum-rate, secrecy rate);
- $g(\mathbf{x})$ is convex and strictly positive (e.g., total consumed power).

This formulation covers all energy- and secrecy-efficiency (EE/SEE) objectives considered in the thesis. Feasibility, continuity, and standard convexity assumptions (e.g., Slater-type conditions) are taken as given.

A.3.2 Dinkelbach transformation and key property

Define the parametric (subtractive) problem

$$\Phi(\eta) \triangleq \max_{\mathbf{x}\in\mathcal{X}} \big[f(\mathbf{x}) - \eta\, g(\mathbf{x})\big], \tag{A.3.2}$$

where η is a real scalar. This transformation converts the fractional form into a family of difference problems that are easier to analyze and solve.

Main principle. If we let $\eta^\star$ denote the optimal ratio value of (A.3.1), then $\Phi(\eta^\star) = 0$. Conversely, if $\Phi(\bar{\eta}) = 0$ for some $\bar{\eta}$, any maximizer of (A.3.2) at $\eta = \bar{\eta}$ also maximizes (A.3.1). In other words, solving the ratio problem is equivalent to finding the zero of the continuous, strictly decreasing function $\Phi(\eta)$.

Intuitive view. For a fixed η, the term $f(\mathbf{x}) - \eta g(\mathbf{x})$ measures how much the "benefit" f exceeds the "cost" ηg. If η is too small, this difference can be positive; if η is too large, it becomes negative. The root $\eta^\star$ is the point where these two forces balance perfectly, yielding the optimal ratio.

A.3.3 Dinkelbach algorithm with exact inner solves

The classical algorithm updates η iteratively while solving (A.3.2) to optimality at each step:

Algorithm — Dinkelbach's method for (A.3.1).

1. Initialize $\eta^{(0)} \in \mathbb{R}$ (e.g., $\eta^{(0)} = 0$) and tolerances $\varepsilon_\Phi, \varepsilon_\eta > 0$.
2. For $t = 0, 1, 2, \ldots$:
   (a) Solve the inner problem $\mathbf{x}^{(t)} = \arg\max_{\mathbf{x}\in\mathcal{X}} [f(\mathbf{x}) - \eta^{(t)} g(\mathbf{x})]$.
   (b) Evaluate the residual $r^{(t)} = f(\mathbf{x}^{(t)}) - \eta^{(t)} g(\mathbf{x}^{(t)})$.
   (c) If $|r^{(t)}| \le \varepsilon_\Phi$, stop and return $(\mathbf{x}^{(t)}, \eta^{(t)})$.
   (d) Update $\eta^{(t+1)} = \dfrac{f(\mathbf{x}^{(t)})}{g(\mathbf{x}^{(t)})}$.
   (e) If $|\eta^{(t+1)} - \eta^{(t)}| \le \varepsilon_\eta$, stop.

Convergence behavior. The sequence $\{\eta^{(t)}\}$ is monotonically nondecreasing and converges to $\eta^\star$. Moreover, $r^{(t)} = \Phi(\eta^{(t)})$ decreases to zero. When f is strictly concave and g convex, the inner solution is unique and $\mathbf{x}^{(t)} \to \mathbf{x}^\star$. See [95, Thm. 2.1–2.3] for proofs.

Interpretation. At each step, the algorithm asks: "for this current guess η, what $\mathbf{x}$ maximizes $f - \eta g$?" Then, it replaces η by the observed ratio at that point. This feedback mechanism automatically steers η toward the true optimum and guarantees monotonic improvement of the ratio.

A.3.4 Inexact inner solves and practical stopping

In practice, the inner problem (A.3.2) may not be solved exactly—especially when handled by AO or SCA subloops. Dinkelbach's method is robust to this, provided the inner error is controlled.

Approximate inner step. Given $\eta^{(t)}$, suppose $\tilde{\mathbf{x}}^{(t)}$ satisfies

$$f(\tilde{\mathbf{x}}^{(t)}) - \eta^{(t)} g(\tilde{\mathbf{x}}^{(t)}) \;\geq\; \Phi(\eta^{(t)}) - \epsilon_t, \qquad \epsilon_t \geq 0.$$

If $\epsilon_t \to 0$ and $\sum_t \epsilon_t < \infty$, the resulting updates $\eta^{(t+1)} = \frac{f(\tilde{\mathbf{x}}^{(t)})}{g(\tilde{\mathbf{x}}^{(t)})}$ still converge to $\eta^\star$ with $r^{(t)} \to 0$ [95, Thm. 2.7].

Residual-based stopping. Instead of checking inner accuracy directly, we monitor the parametric residual $r^{(t)} = f(\mathbf{x}^{(t)}) - \eta^{(t)} g(\mathbf{x}^{(t)})$. Stopping when $|r^{(t)}| \leq \varepsilon_\Phi$ guarantees that the ratio is ε_Φ-optimal.

Warm starts. Each Dinkelbach step reuses the previous solution $\mathbf{x}^{(t-1)}$ as the starting point of the next inner solve. This "warm start" often reduces the number of inner iterations dramatically, especially when the surrogate functions vary smoothly across steps.

A.3.5 Embedding within AO/SCA

At a fixed η, the function $f(\mathbf{x}) - \eta g(\mathbf{x})$ inherits the structural properties of f and g:

- f is concave (or a tight concave lower bound of a nonconcave function built via MM/SCA);
- g is convex or affine in the decision variables.

Therefore, the inner problem remains concave and can be solved efficiently by convex optimization tools or closed-form updates for specific blocks (e.g., MMSE receivers, single-stream RIS updates). The alternating block updates yield monotonic improvements in $f - \eta g$, and coupling this property with

Dinkelbach's monotone outer loop guarantees convergence of the ratio to a stationary point of the original FP [95].

A.3.6 Complexity and implementation overview

Each Dinkelbach step involves one full AO/SCA cycle. The computational load is dominated by matrix inversions of dimension equal to the number of transmit antennas or RIS elements, and by projections onto the global-reflection constraint sets when active. Empirically, fewer than ten Dinkelbach iterations are sufficient once warm-started. Tolerances are set so that the outer residual ε_Φ dominates the inner SCA tolerance, ensuring the accumulated inner inexactness $\sum_t \epsilon_t$ remains finite.

A.3.7 Remarks and extensions

(i) Alternative transforms. For certain designs, the quadratic transform (see [73]) provides an algebraic alternative to Dinkelbach's method; both yield equivalent stationary points when applied within AO/SCA.

(ii) Multiple ratios. This thesis mainly focuses on single-ratio EE/SEE formulations. When multiple ratios are present (e.g., per-user energy efficiencies), one can extend the approach via generalized or nested Dinkelbach iterations [95].

(iii) Constraint handling. Nonconvex or equality constraints are locally convexified through SCA, preserving the concave–convex structure required for the outer Dinkelbach loop to remain valid under inexact convergence.

Takeaway. The Dinkelbach framework provides a robust outer loop for fractional programs: it turns a difficult ratio objective into a sequence of simpler concave subproblems. Its guaranteed monotonicity, tolerance to inexact inner solves, and natural compatibility with AO/SCA make it the cornerstone of the optimization methods developed in this thesis, consistent with the foundational theory in [95].

A.4 Majorization–Minimization and Successive Convex Approximation

This appendix summarizes the *Majorization–Minimization* (MM) / *Successive Convex Approximation* (SCA) tools used to solve the nonconvex inner problems at a fixed Dinkelbach parameter (cf. Appx. A.3). We state the

exact surrogate constructions actually employed and the blockwise update principle. Background and convergence results follow [4], [46], [69], [75].

A.4.1 Setup and MM/SCA prerequisites

Let $\mathcal{X} \subset \mathbb{R}^n$ be nonempty, closed, and convex. Consider

$$\max_{\mathbf{x}\in\mathcal{X}} \; F(\mathbf{x}), \tag{A.4.1}$$

with F continuous on $\mathcal{X}$. At iteration t, given $\mathbf{x}^{(t)}$, MM/SCA builds a *concave lower surrogate* $\tilde{F}(\cdot \,|\, \mathbf{x}^{(t)})$ obeying

(M1) $\tilde{F}(\mathbf{x}^{(t)} \,|\, \mathbf{x}^{(t)}) = F(\mathbf{x}^{(t)})$ (tangency),
(M2) $\tilde{F}(\mathbf{x} \,|\, \mathbf{x}^{(t)}) \le F(\mathbf{x}) \quad \forall\, \mathbf{x} \in \mathcal{X}$ (global lower bound),
(M3) $\tilde{F}(\cdot \,|\, \mathbf{x}^{(t)})$ is concave on $\mathcal{X}$ (tractable subproblem).

The update

$$\mathbf{x}^{(t+1)} \in \arg\max_{\mathbf{x}\in\mathcal{X}} \tilde{F}(\mathbf{x} \,|\, \mathbf{x}^{(t)}) \tag{A.4.2}$$

yields $F(\mathbf{x}^{(t+1)}) \ge \tilde{F}(\mathbf{x}^{(t+1)} \,|\, \mathbf{x}^{(t)}) \ge \tilde{F}(\mathbf{x}^{(t)} \,|\, \mathbf{x}^{(t)}) = F(\mathbf{x}^{(t)})$, hence monotone ascent.

A.4.2 Surrogates used in the thesis (maximization form)

We repeatedly use the following three patterns; they are stated in a way that guarantees a *concave lower* surrogate for maximization.

(A) First-order minorizer of a concave utility. Let $u : \mathbb{R}_+ \to \mathbb{R}$ be concave and differentiable. Then

$$u(z) \;\ge\; u(z^{(t)}) + u'(z^{(t)})(z - z^{(t)}),$$

with equality at $z = z^{(t)}$. We use $u(z) = \log(1+z)$; once a block update exposes a SINR-like scalar z, the right-hand side is an affine (thus concave) lower bound.

(B) DC quadratic form: convex part linearized, concave part kept. For $\mathbf{A} \succeq \mathbf{0}$, $\mathbf{B} \succeq \mathbf{0}$, consider

$$q(\mathbf{x}) \;=\; \underbrace{\mathbf{x}^H\mathbf{A}\mathbf{x}}_{\text{convex}} \;+\; \underbrace{\big(-\,\mathbf{x}^H\mathbf{B}\mathbf{x}\big)}_{\text{concave}}.$$

A global *lower* bound for maximization is obtained by minorizing only the convex term via its first-order affine *under*estimator at $\mathbf{x}^{(t)}$:

$$\mathbf{x}^H\mathbf{A}\mathbf{x} \;\geq\; (\mathbf{x}^{(t)})^H\mathbf{A}\mathbf{x}^{(t)} + 2\,\Re\Big\{(\mathbf{A}\mathbf{x}^{(t)})^H\big(\mathbf{x}-\mathbf{x}^{(t)}\big)\Big\}.$$

Hence

$$q(\mathbf{x}) \;\geq\; (\mathbf{x}^{(t)})^H\mathbf{A}\mathbf{x}^{(t)} + 2\,\Re\Big\{(\mathbf{A}\mathbf{x}^{(t)})^H(\mathbf{x}-\mathbf{x}^{(t)})\Big\} - \mathbf{x}^H\mathbf{B}\mathbf{x},$$

which is concave in $\mathbf{x}$ (affine minus convex). We use (B) from global-reflection power accounting to handle quadratic couplings in metasurface variables.

(C) Log-det DC pattern: linearize one concave term. If $F(\mathbf{Y}) = f_1(\mathbf{Y}) - f_2(\mathbf{Y})$ with f_1, f_2 concave on $\{\mathbf{Y} \succ 0\}$ (e.g., $f_i(\mathbf{Y}) = \log\det\mathbf{Y}_i(\mathbf{Y})$ after an affine mapping), then the tangent of a concave function is a global *upper* bound:

$$f_2(\mathbf{Y}) \;\leq\; f_2(\mathbf{Y}^{(t)}) + \operatorname{tr}\Big(\nabla f_2(\mathbf{Y}^{(t)})(\mathbf{Y}-\mathbf{Y}^{(t)})\Big).$$

Therefore

$$F(\mathbf{Y}) \;=\; f_1(\mathbf{Y}) - f_2(\mathbf{Y}) \;\geq\; f_1(\mathbf{Y}) - \Big[f_2(\mathbf{Y}^{(t)}) + \operatorname{tr}\big(\nabla f_2(\mathbf{Y}^{(t)})(\mathbf{Y}-\mathbf{Y}^{(t)})\big)\Big],$$

which is a concave lower bound because f_1 is concave and the subtracted bracket is affine. Special case: if $f_1(\mathbf{Y}) = \log\det\mathbf{Y}$ (concave), we keep it *exact*; only the other concave term is linearized.

A.4.3 Sequential (blockwise) optimization

Partition $\mathbf{x} = (\mathbf{x}_1, \ldots, \mathbf{x}_B)$ with convex blocks $\mathcal{X}_b$. At iteration t, pick block b_t (cyclically or essentially cyclic [4]), build a concave lower surrogate in that block,

$$\tilde{F}_b(\mathbf{x}_b \,|\, \mathbf{x}^{(t)}) \quad \text{satisfying } \textbf{(M1)–(M3)} \text{ in } \mathbf{x}_b,$$

with $\mathbf{x}_{-b}$ fixed at $\mathbf{x}_{-b}^{(t)}$, and update

$$\mathbf{x}_b^{(t+1)} \in \arg\max_{\mathbf{x}_b \in \mathcal{X}_b} \tilde{F}_b(\mathbf{x}_b \,|\, \mathbf{x}^{(t)}), \qquad \mathbf{x}_{-b}^{(t+1)} = \mathbf{x}_{-b}^{(t)}. \tag{A.4.3}$$

Proposition A.4.1 (Monotone sequential MM over blocks)**.** *Assume for each block b: (i) $\tilde{F}_b(\cdot \,|\, \mathbf{x})$ satisfies **(M1)–(M3)** for all $\mathbf{x} \in \mathcal{X}$; (ii) the subproblem* (A.4.3) *attains a maximizer; and (iii) the level set $\{\mathbf{x} \in \mathcal{X} : F(\mathbf{x}) \geq F(\mathbf{x}^{(0)})\}$ is compact.*

Then $\{F(\mathbf{x}^{(t)})\}$ *is nondecreasing and convergent. Every limit point is* block-stationary *for* (A.4.1)*, i.e.,*

$$\mathbf{x}_b^\infty \in \arg\max_{\mathbf{z}_b \in \mathcal{X}_b} \tilde{F}_b(\mathbf{z}_b \,|\, \mathbf{x}^\infty), \quad \forall b.$$

If, in addition, each block surrogate is strictly concave, block maximizers are unique and any limit point satisfies the first-order necessary conditions of (A.4.1)*.* (See [69, Thm. 1], [4, Thm. 1], and [75].)

Sketch. Updating block b gives

$$F(\mathbf{x}^{(t+1)}) \;\geq\; \tilde{F}_b(\mathbf{x}_b^{(t+1)} \,|\, \mathbf{x}^{(t)}) \;\geq\; \tilde{F}_b(\mathbf{x}_b^{(t)} \,|\, \mathbf{x}^{(t)}) \;=\; F(\mathbf{x}^{(t)}),$$

ensuring monotonicity. Boundedness follows from compact level sets—tangency and continuity transfer block-optimality of surrogates to block-stationarity of F at cluster points.

A.5 Proofs of Propositions and Lemmas

A.5.1 Proof of Lemma 3.1 (Monotone Rearrangement)

Statement. Let $\{z_n\}_{n=1}^N$ be sorted in non-increasing order, i.e. $z_1 \geq z_2 \geq \cdots \geq z_N \geq 0$. Consider any feasible amplitude vector $\boldsymbol{\rho} = [\rho_1, \ldots, \rho_N]$ and let $\boldsymbol{\rho}_o$ be the vector obtained by reordering the entries of $\boldsymbol{\rho}$ in non-increasing order. Then

$$\sum_{n=1}^N \rho_{o,n} z_n \;\geq\; \sum_{n=1}^N \rho_n z_n.$$

Proof. We use an exchange argument. Suppose $\boldsymbol{\rho}$ is identical to $\boldsymbol{\rho}_o$ except that there exists at least one adjacent pair (ρ_i, ρ_{i+1}) such that $\rho_i < \rho_{i+1}$ while $z_i \geq z_{i+1}$. Define $\boldsymbol{\rho}'$ as the vector obtained by swapping these two entries. Then the difference in the weighted sums is

$$\begin{aligned}
\sum_{n=1}^N \rho'_n z_n - \sum_{n=1}^N \rho_n z_n &= \rho'_i z_i + \rho'_{i+1} z_{i+1} - (\rho_i z_i + \rho_{i+1} z_{i+1}) \\
&= \rho_{i+1} z_i + \rho_i z_{i+1} - \rho_i z_i - \rho_{i+1} z_{i+1} \\
&= (\rho_{i+1} - \rho_i)(z_i - z_{i+1}) \;\geq 0, \qquad \text{(A.5.1)}
\end{aligned}$$

since $\rho_{i+1} > \rho_i$ and $z_i \geq z_{i+1}$. Thus the weighted sum does not decrease under such a swap. By iteratively applying adjacent swaps until $\boldsymbol{\rho}$ is ordered

in the same way as $\mathbf{z}$, one obtains $\boldsymbol{\rho}_o$ with

$$\sum_{n=1}^{N} \rho_{o,n} z_n \;\geq\; \sum_{n=1}^{N} \rho_n z_n.$$

This proves the lemma. ■

A.5.2 Proof of Lemma 3.2 (Schur-Convexity on Ordered Sets)

Statement. Over the ordered set $\mathcal{D} = \{\boldsymbol{\rho} : \rho_1 \geq \rho_2 \geq \cdots \geq \rho_N \geq 0\}$, the objective function

$$f(\boldsymbol{\rho}) = \sum_{n=1}^{N} \rho_n z_n,$$

with $z_1 \geq z_2 \geq \cdots \geq z_N \geq 0$, is Schur-convex in $\boldsymbol{\rho}$. Hence, $f(\boldsymbol{\rho})$ is increasing with respect to the majorization order: if $\boldsymbol{\rho}_1$ majorizes $\boldsymbol{\rho}_2$, then $f(\boldsymbol{\rho}_1) \geq f(\boldsymbol{\rho}_2)$.

Proof. We recall that a real-valued function $f : \mathbb{R}^N \to \mathbb{R}$ is Schur-convex if, for all $\boldsymbol{\rho}, \boldsymbol{\rho}'$ such that $\boldsymbol{\rho}$ majorizes $\boldsymbol{\rho}'$, one has $f(\boldsymbol{\rho}) \geq f(\boldsymbol{\rho}')$. A standard sufficient condition (see [61, Thm. A.4]) is that f is symmetric and that for all i, j

$$(\rho_i - \rho_j)\Big(\frac{\partial f}{\partial \rho_i} - \frac{\partial f}{\partial \rho_j}\Big) \;\geq 0. \tag{A.5.2}$$

In our case, $f(\boldsymbol{\rho}) = \sum_{n=1}^{N} \rho_n z_n$. Its partial derivatives are

$$\frac{\partial f}{\partial \rho_i} = z_i.$$

Since $\mathbf{z}$ is sorted in non-increasing order, if $i < j$ then $z_i \geq z_j$. For any $\boldsymbol{\rho} \in \mathcal{D}$, we also have $\rho_i \geq \rho_j$ when $i < j$. Therefore, the product in (A.5.2) is non-negative:

$$(\rho_i - \rho_j)(z_i - z_j) \geq 0.$$

This confirms that f satisfies the Schur-convexity condition over the ordered set $\mathcal{D}$.

Thus, $f(\boldsymbol{\rho})$ is Schur-convex, and the objective function increases as $\boldsymbol{\rho}$ becomes more "spread out" in the majorization sense. ■

A.6 Convergence Analysis of Proposed Algorithms

This appendix provides the convergence justifications for the iterative algorithms introduced in Chapter 2. First, we establish the convergence of the sequential fractional programming (SFP) subroutines used in the RIS and power updates. Then, we address the global alternating maximization scheme that couples all optimization blocks.

A.6.1 Convergence of Sequential Fractional Programming (SFP)

Algorithms 7 and 8 solve nonconvex fractional programs via SFP, which combines Dinkelbach's outer iterations with inner MM/SCA surrogates. Convergence follows from the general SFP framework [60] once three key conditions are verified:

(i) Each surrogate objective is a *global lower bound* of the true objective (valid for all feasible points).

(ii) The surrogate is *tangent* to the actual objective and shares its gradient at the expansion point.

(iii) The surrogate subproblem is *concave or pseudo-concave* over a convex feasible set, ensuring a unique global maximizer.

All three hold in our construction:

- The bounds in (3.3.7)–(3.3.8) and the linearizations in (3.3.14)–(3.3.15) are tight at the current iterate and lower than the actual function elsewhere, satisfying (i).
- By construction, the gradients of the surrogates coincide with those of the original functions at $\bar{\gamma}$ and $\bar{\boldsymbol{p}}$, satisfying (ii).
- The resulting problems (3.3.18) and (3.3.33) are pseudo-concave fractional programs with convex feasible sets that satisfy (iii).

Therefore, each SFP iteration produces a nondecreasing sequence of objective values. By Theorem 1 of [60], this sequence converges to a stationary point of the original fractional program, and the limit point satisfies the Karush–Kuhn–Tucker (KKT) conditions.

A.6.2 Convergence of Alternating Maximization Scheme

Algorithm 9 performs alternating maximization over three blocks: (i) RIS coefficients γ, (ii) transmit powers $\boldsymbol{p}$ (or covariances), and (iii) receiver filters $\boldsymbol{C}$.
Each block update is monotonic:

- The RIS and power blocks employ SFP updates that yield a nondecreasing SEE value by construction (Propositions 3.3.1–3.3.2).
- The LMMSE filter update globally maximizes the numerator of the SEE for fixed $(\gamma, \boldsymbol{p})$, hence cannot decrease the objective.

Consequently, the SEE sequence $\{\mathrm{SEE}^{(t)}\}$ is nondecreasing. Because physical system constraints (finite transmit power, bounded reflection amplitude, and limited bandwidth) impose an upper bound on achievable SEE, the sequence is bounded and therefore convergent.

Finally, by standard results for block-MM and alternating optimization methods (e.g., [4], [8], [69]), any accumulation point of $\{(\boldsymbol{\gamma}^{(t)}, \boldsymbol{p}^{(t)}, \boldsymbol{C}^{(t)})\}$ satisfies the KKT conditions of Problem (3.2.8), completing the convergence proof.

Contributions Made by the Author

[26] R. K. Fotock, A. Zappone, and M. Di Renzo, "Secrecy energy efficiency maximization in RIS-aided wireless networks," *2024 IEEE International Conference on Communications (ICC)*, 2024 (cit. on p. 23).

[27] R. K. Fotock *et al.*, "Secrecy energy efficiency maximization in RIS-aided wireless networks with statistical CSI," *2024 IEEE 25th International Workshop on Signal Processing Advances in Wireless Communications (SPAWC)*, 2024 (cit. on p. 23).

[28] R. K. Fotock, A. Zappone, and M. Di Renzo, "Energy efficiency in ris-aided wireless networks: Active or passive ris?" In *ICC 2023 - IEEE International Conference on Communications*, 2023, pp. 2704–2709. DOI: 10.1109/ICC45041.2023.10279284 (cit. on pp. 21, 80).

[29] R. K. Fotock, A. Zappone, and M. Di Renzo, "Energy efficiency maximization in RIS-aided networks with global reflection constraints," in *ICASSP 2023 - 2023 IEEE International Conference on Acoustics, Speech and Signal Processing (ICASSP)*, 2023, pp. 1–5. DOI: 10.1109/ICASSP49357.2023.10096617 (cit. on p. 21).

[30] R. K. Fotock, A. L. Imoize, A. Zappone, M. Di Renzo, and Y. Zhang, "Energy efficiency maximization of holographic beamforming empowered by nearly-passive rhs," in *2025 IEEE 26th International Workshop on Signal Processing and Artificial Intelligence for Wireless Communications (SPAWC)*, 2025, pp. 1–5. DOI: 10.1109/SPAWC66079.2025.11143314 (cit. on pp. 26, 159, 164).

[31] R. K. Fotock, A. L. Imoize, A. Zappone, and C. D'Elia, "Secrecy energy efficiency maximization in dual-metasurface-aided wireless networks," *EURASIP Journal on Advances in Signal Processing*, vol. 2025, no. 1, p. 24, 2025. DOI: 10.1186/s13634-025-01231-w (cit. on pp. 2, 24, 158).

[32] R. K. Fotock, A. Lucky Imoize, A. Zappone, M. Di Renzo, and R. Garello, "Secrecy energy efficiency maximization in ris-aided networks: Active or nearly-passive ris?" *IEEE Transactions on Information Forensics and Security*, vol. 21, pp. 167–182, 2026. DOI: 10.1109/TIFS.2025.3620227 (cit. on pp. 2, 8, 16, 18, 23, 158).

[33] R. K. Fotock, A. Zappone, A. L. Imoize, and M. D. Renzo, *Energy efficiency maximization of mimo systems through reconfigurable holographic beamforming*, 2026. [Online]. Available: https://arxiv.org/abs/2601.00780 (cit. on pp. 3, 18, 25, 159, 164).

[34] R. K. Fotock, A. Zappone, and M. D. Renzo, "Energy efficiency maximization in ris-assisted networks: Exploring the benefits of global reflection constraints," *Proceedings of the IEEE ISESS Symposium*, 2023 (cit. on pp. 1, 3, 6–8, 16, 17, 22).

[35] R. K. Fotock, A. Zappone, and M. D. Renzo, "Energy efficiency optimization in ris-aided wireless networks: Active versus nearly-passive ris with global reflection constraints," *IEEE Transactions on Communications*, vol. 72, no. 1, pp. 257–272, 2024. DOI: 10.1109/TCOMM.2023.3320700 (cit. on pp. 16, 18, 21, 115).

[79] A. I. Tunalı, R. K. Fotock, A. Zappone, G. Taricco, G. Alfano, and H. A. Çırpan, "Energy efficiency maximization in MIMO links aided by metasurfaces with global reflection constraints," *EURASIP Journal on Applied Signal Processing*, vol. 2025, no. 1, 29, p. 29, Jul. 2025. DOI: 10.1186/s13634-025-01233-8 (cit. on pp. 3, 26, 165).

[80] A. I. Tunalı, R. K. Fotock, *et al.*, "Energy-efficient mimo communication assisted by metasurfaces with global reflection constraints," in *Titolo volume non avvalorato*, IEEE, 2025 (cit. on p. 27).

[93] A. Zappone, M. Di Renzo, and R. K. Fotock, "Surface-based techniques for iot networks: Opportunities and challenges," *IEEE Internet of Things Magazine*, vol. 5, no. 4, pp. 72–77, 2022. DOI: 10.1109/IOTM.001.2200170 (cit. on pp. 26, 165).

Bibliography

[1] G. C. Alexandropoulos and E. Vlachos, "A hardware architecture for reconfigurable intelligent surfaces with minimal active elements for explicit channel estimation," in *ICASSP 2020 - 2020 IEEE International Conference on Acoustics, Speech and Signal Processing (ICASSP)*, 2020, pp. 9175–9179. DOI: 10.1109/ICASSP40776.2020.9053976 (cit. on p. 30).

[2] J. An, C. Xu, D. W. K. Ng, G. C. Alexandropoulos, C. Huang, C. Yuen, and L. Hanzo, "Stacked intelligent metasurfaces for efficient holographic mimo communications in 6g," *IEEE Journal on Selected Areas in Communications*, vol. 41, no. 8, pp. 2380–2396, 2023. DOI: 10.1109/JSAC.2023.3288261 (cit. on p. 164).

[3] J. An, C. Yuen, C. Xu, H. Li, D. W. K. Ng, M. Di Renzo, M. Debbah, and L. Hanzo, "Stacked intelligent metasurface-aided mimo transceiver design," *IEEE Wireless Communications*, vol. 31, no. 4, pp. 123–131, 2024. DOI: 10.1109/MWC.013.2300259 (cit. on p. 164).

[4] A. Beck and L. Tetruashvili, "On the convergence of block coordinate descent type methods," *SIAM Journal on Optimization*, vol. 23, no. 4, pp. 2037–2060, 2013. DOI: 10.1137/120887679. [Online]. Available: https://doi.org/10.1137/120887679 (cit. on pp. 198–200, 203).

[5] A. Ben-Tal and A. Nemirovski, *Lectures on modern convex optimization*. MPS/SIAM series on optimization, 2001 (cit. on p. 54).

[6] A. Ben-Tal and A. Nemirovski, *Lectures on Modern Convex Optimization* (MPS/SIAM Series on Optimization). MPS/SIAM, 2001 (cit. on pp. 91, 139).

[7] D. P. Bertsekas, *Nonlinear Programming*, 2nd. Belmont, Massachusetts: Athena Scientific, 1999 (cit. on p. 54).

[8] D. P. Bertsekas, *Nonlinear Programming*, 2nd. Belmont, MA: Athena Scientific, 1999 (cit. on p. 203).

[9] E. Björnson, J. Hoydis, and L. Sanguinetti, "Massive mimo networks: Spectral, energy, and hardware efficiency," *Foundations and Trends in Signal Processing*, vol. 11, no. 3-4, pp. 154–655, 2017. DOI: 10.1561/2000000093 (cit. on p. 5).

[10] E. Björnson, H. Wymeersch, B. Matthiesen, P. Popovski, L. Sanguinetti, and E. de Carvalho, "Reconfigurable Intelligent Surfaces: A Signal Processing Perspective With Wireless Applications," *IEEE Signal Processing Magazine*, vol. 39, no. 2, pp. 135–158, March 2022. DOI: 10.1109/MSP.2021.3130549 (cit. on pp. 6, 7).

[11] M. Bloch and J. Barros, *Physical-Layer Security: From Information Theory to Security Engineering*. Cambridge University Press, 2011. DOI: 10.1017/CBO9781139043816 (cit. on p. 5).

[12] S. P. Boyd and L. Vandenberghe, *Convex optimization*. Cambridge Univ Press, 2004 (cit. on p. 170).

[13] S. Buzzi, C. D'Andrea, A. Zappone, M. Fresia, Y.-P. Zhang, and S. Feng, "Ris configuration, beamformer design, and power control in single-cell and multi-cell wireless networks," *IEEE Transactions on Cognitive Communications and Networking*, vol. 7, no. 2, pp. 398–411, 2021. DOI: 10.1109/TCCN.2021.3068414 (cit. on p. 91).

[14] S. Buzzi, A. Zappone, C. D'Andrea, M. Fresia, Y.-P. Zhang, and S. Feng, "A survey of energy efficiency in 5g and beyond networks with physical layer security," *IEEE Communications Surveys & Tutorials*, vol. 23, no. 2, pp. 1251–1291, 2021. DOI: 10.1109/COMST.2021.3057252 (cit. on p. 2).

[15] X. Cai, C. Yuen, C. Huang, W. Xu, and L. Wang, "Toward chaotic secure communications: An RIS-enabled M-Ary differential chaos shift keying system with block interleaving," *IEEE Transactions on Communications*, vol. 71, no. 6, pp. 3541–3558, 2023 (cit. on p. 76).

[16] Y. Chen, Y. Wang, Z. Wang, and P. Zhang, "Robust beamforming for active reconfigurable intelligent omni-surface in vehicular communications," *IEEE Journal on Selected Areas in Communications*, vol. 40, no. 10, pp. 3086–3103, 2022 (cit. on pp. 31, 115).

[17] S. P. Chepuri, N. Shlezinger, F. Liu, G. C. Alexandropoulos, S. Buzzi, and Y. C. Eldar, "Integrated sensing and communications with reconfigurable intelligent surfaces: From signal modeling to processing," *IEEE Signal Processing Magazine*, vol. 40, no. 6, pp. 41–62, 2023. DOI: 10.1109/MSP.2023.3279986 (cit. on p. 165).

[18] D. Darsena, F. Verde, I. Iudice, and V. Galdi, "Design of stacked intelligent metasurfaces with reconfigurable amplitude and phase for multiuser downlink beamforming," *IEEE Open Journal of the Communications Society*, vol. 6, pp. 531–550, 2025. DOI: 10.1109/OJCOMS.2025.3526126 (cit. on p. 164).

[19] V. Degli-Esposti, E. M. Vitucci, M. Di Renzo, and S. Tretyakov, "Reradiation and scattering from a reconfigurable intelligent surface: A general macroscopic model," *IEEE Transactions on Antenna and Propagation*, vol. 70, no. 10, pp. 8691–8706, 2022 (cit. on p. 140).

[20] M. Di Renzo, F. Danufane, and S. Tretyakov, "Communication models for reconfigurable intelligent surfaces: From surface electromagnetics to wireless networks optimization," *Proceedings of the IEEE*, vol. 110, no. 9, pp. 1164–1209, 2022 (cit. on pp. 31, 163).

[21] M. Di Renzo, F. H. Danufane, and S. Tretyakov, "Communication models for reconfigurable intelligent surfaces: From surface electromagnetics to wireless networks optimization," *Proceedings of the IEEE*, vol. 110, no. 9, pp. 1164–1209, 2022 (cit. on p. 77).

[22] M. Di Renzo, A. Zappone, M. Debbah, M. Alouini, C. Yuen, J. de Rosny, and S. Tretyakov, "Smart radio environments empowered by reconfigurable intelligent surfaces: How it works, state of research, and road ahead," *IEEE Journal on Selected Areas in Communications*, 2020 (cit. on pp. 2, 7, 16).

[23] M. Di Renzo *et al.*, "Smart radio environments empowered by reconfigurable AI meta-surfaces: An idea whose time has come," *EURASIP Journal on Wireless Communincations and Networking*, vol. 129, 2019 (cit. on pp. 2, 16, 30).

[24] M. Di Renzo, A. Zappone, M. Debbah, M.-S. Alouini, C. Yuen, J. de Rosny, and S. Tretyakov, "Smart radio environments empowered by reconfigurable intelligent surfaces: How it works, state of research, and the road ahead," *IEEE Journal on Selected Areas in Communications*, vol. 38, no. 11, pp. 2450–2525, 2020. DOI: 10.1109/JSAC.2020.3007211 (cit. on p. 30).

[25] C. Feng, H. Lu, Y. Zeng, T. Li, S. Jin, and R. Zhang, "Near-field modelling and performance analysis for extremely large-scale IRS communications," *IEEE Transactions on Wireless Communications*, vol. 23, no. 5, pp. 4976–4989, 2024 (cit. on p. 140).

[36] X. Ge and et al., "Energy efficiency challenges of 5g wireless communication systems," *IEEE Communications Magazine*, vol. 55, no. 5, pp. 184–191, 2017. DOI: 10.1109/MCOM.2017.1600418CM (cit. on pp. 1, 5).

[37] S. Goel and R. Negi, "Guaranteeing secrecy using artificial noise," *IEEE Transactions on Wireless Communications*, vol. 7, no. 6, pp. 2180–2189, 2008. DOI: 10.1109/TWC.2008.060848 (cit. on pp. 116, 119).

[38] G. Gradoni and M. Di Renzo, "End-to-end mutual coupling aware communication model for reconfigurable intelligent surfaces: An electromagnetic-compliant approach based on mutual impedances," *IEEE Wireless Communications Letters*, vol. 10, no. 5, pp. 938–942, 2021. DOI: 10.1109/LWC.2021.3050826 (cit. on p. 163).

[39] W. Hao, J. Li, G. Sun, C. Huang, M. Zeng, O. A. Dobre, and C. Yuen, "Max-min security energy efficiency optimization for RIS-aided cell-free networks," *2023 IEEE International Communications Conference*, 2023 (cit. on p. 115).

[40] T. M. Hoang, C. Xu, A. Vahid, H. D. Tuan, T. Q. Duong, and L. Hanzo, "Secrecy-rate optimization of double RIS-aided space–ground networks," *IEEE Internet of Things Journal*, vol. 10, no. 15, pp. 13 221–13 234, 2023. DOI: 10.1109/JIOT.2023.3262481 (cit. on pp. 76, 115).

[41] C. Huang, A. Zappone, G. C. Alexandropoulos, M. Debbah, and C. Yuen, "Reconfigurable intelligent surfaces for energy efficiency in wireless communication," *IEEE Trans. on Wireless Commun.*, vol. 18, no. 8, pp. 4157–4170, 2019 (cit. on p. 40).

[42] C. Huang *et al.*, "Holographic MIMO surfaces for 6G wireless networks: Opportunities, challenges, and trends," *IEEE Wirless Communications*, vol. 27, no. 5, pp. 118–125, 2020 (cit. on p. 30).

[43] C. Huang, G. C. Alexandropoulos, C. Yuen, and M. Debbah, "Indoor signal focusing with deep learning designed reconfigurable intelligent surfaces," in *2019 IEEE 20th international workshop on signal processing advances in wireless communications (SPAWC)*, IEEE, 2019, pp. 1–5 (cit. on p. 164).

[44] C. Huang, A. Zappone, G. C. Alexandropoulos, M. Debbah, and C. Yuen, "Reconfigurable intelligent surfaces for energy efficiency in wireless communication," *IEEE Transactions on Wireless Communications*, vol. 18, no. 8, pp. 4157–4170, 2019. DOI: 10.1109/TWC.2019.2922609 (cit. on p. 7).

[45] Huawei Technologies, "Green 5G building a sustainable world," *https://www.huawei.com/en/public-policy/green-5g-building-a-sustainable-world*, 2020 (cit. on p. 1).

[46] E. A. Jorswieck and H. Boche, "Majorization and matrix-monotone functions in wireless communications," *Now Publishers: Foundations and Trends in Communications and Information Theory*, vol. 3, no. 6, pp. 553–701, 2006 (cit. on p. 198).

[47] M. H. Khoshafa, T. M. N. Ngatched, M. H. Ahmed, and A. R. Ndjiongue, "Active reconfigurable intelligent surfaces-aided wireless communication system," *IEEE Communications Letters*, vol. 25, no. 11, pp. 3699–3703, 2021 (cit. on p. 30).

[48] X. Li, Y. Zheng, M. Zeng, Y. Liu, and O. A. Dobre, "Enhancing secrecy performance for STAR-RIS NOMA networks," *IEEE Transactions on Vehicular Technology*, vol. 72, no. 2, pp. 2684–2688, 2023. DOI: 10.1109/TVT.2022.3213334 (cit. on pp. 76, 115).

[49] Y. Li, Y. Zou, J. Zhu, B. Ning, L. Zhai, H. Hui, Y. Lou, and C. Qin, "Sum secrecy rate maximization for active RIS-assisted uplink SIMO-NOMA networks," *IEEE Communications Letters*, pp. 1–1, 2023. DOI: 10.1109/LCOMM.2023.3323537 (cit. on pp. 76, 115).

[50] F. Liu, Y. Cui, C. Masouros, J. Xu, T. X. Han, Y. C. Eldar, and S. Buzzi, "Integrated sensing and communications: Toward dual-functional wireless networks for 6g and beyond," *IEEE Journal on Selected Areas in Communications*, vol. 40, no. 6, pp. 1728–1767, 2022. DOI: 10.1109/JSAC.2022.3156632 (cit. on p. 165).

[51] K. Liu, Z. Zhang, L. Dai, S. Xu, and F. Yang, "Active reconfigurable intelligent surface: Fully-connected or sub-connected?" *IEEE Communications Letters*, vol. 26, no. 1, pp. 167 –171, 2022 (cit. on pp. 31, 115).

[52] Y. Liu, Y. Ma, M. Li, Q. Wu, and Q. Shi, "Spectral efficiency maximization for double-faced active reconfigurable intelligent surface," *IEEE Transactions on Signal Processing*, vol. 70, pp. 5397–5412, 2022 (cit. on p. 30).

[53] R. Long, Y. C. Liang, Y. Pei, and E. G. Larsson, "Active reconfigurable intelligent surface-aided wireless communications," *IEEE Transactions Wireless Communications*, vol. 20, no. 8, 4962–4975, Aug. 2021 (cit. on p. 2).

[54] D. López-Pérez, A. D. Domenico, N. Piovesan, G. Xinli, H. Bao, S. Qitao, and M. Debbah, "A survey on 5G radio access network energy efficiency: Massive MIMO, lean carrier design, sleep modes, and machine learning," *IEEE Communications Surveys Tutorials*, pp. 1–1, 2022 (cit. on p. 1).

[55] Y. Lu, "Secrecy energy efficiency in RIS-assisted networks," *IEEE Transactions on Vehicular Technology*, vol. 72, no. 9, pp. 12 419–12 424, 2023. DOI: 10.1109/TVT.2023.3269905 (cit. on p. 115).

[56] W. Lv, J. Bai, Q. Yan, and H.-M. Wang, "Ris-assisted green secure communications: Active RIS or passive RIS?" *IEEE Wireless Communication Letters*, 2022 (cit. on p. 31).

[57] W. Lv, J. Bai, Q. Yan, and H. M. Wang, "RIS-assisted green secure communications: Active RIS or passive RIS?" *IEEE Wireless Communications Letters*, vol. 12, no. 2, 237–241, Feb. 2023 (cit. on p. 76).

[58] Y. Ma, M. Li, Y. Liu, Q. Wu, and Q. Liu, "Active reconfigurable intelligent surface for energy efficiency in MU-MISO systems," *IEEE Transactions on Vehicular Technology*, 2022 (cit. on p. 31).

[59] Y. Ma, M. Li, Y. Liu, Q. Wu, and Q. Liu, "Active reconfigurable intelligent surface for energy efficiency in MU-MISO systems," *IEEE Transactions on Vehicular Technology*, vol. 72, no. 3, 4103–4107, Mar. 2023 (cit. on p. 115).

[60] B. R. Marks and G. P. Wright, "A general inner approximation algorithm for non-convex mathematical programs," *Operations Research*, vol. 26, no. 4, pp. 681–683, 1978 (cit. on pp. 51, 180, 202).

[61] A. W. Marshall and I. Olkin, *Inequalities: theory of majorization and its applications*. Academic Press New York, 1979 (cit. on p. 201).

[62] H. Niu, Z. Lin, K. An, X. Liang, Y. Hu, D. Li, and G. Zheng, "Active RIS-assisted secure transmission for cognitive satellite terrestrial networks," *IEEE Transactions on Vehicular Technology*, 2022 (cit. on p. 30).

[63] H. Niu, J. An, A. Papazafeiropoulos, L. Gan, S. Chatzinotas, and M. Debbah, "Stacked intelligent metasurfaces for integrated sensing and communications," *IEEE Wireless Communications Letters*, vol. 13, no. 10, pp. 2807–2811, 2024. DOI: 10.1109/LWC.2024.3447272 (cit. on p. 164).

[64] Y. Pei, X. Yue, W. Yi, Y. Liu, X. Li, and Z. Ding, "Secrecy outage probability analysis for downlink RIS-NOMA networks with on-off control," *IEEE Transactions on Vehicular Technology*, vol. 72, no. 9, pp. 11 772–11 786, 2023. DOI: 10.1109/TVT.2023.3267531 (cit. on pp. 76, 115).

[65] Q. Peng, Q. Wu, G. Chen, R. Liu, S. Ma, and W. Chen, "Hybrid active-passive IRS assisted energy-efficient wireless communication," *IEEE Communications Letters*, vol. 27, no. 8, pp. 2202–2206, Jul. 2023 (cit. on p. 115).

[66] Q. Peng, G. Chen, Q. Wu, R. Liu, S. Ma, and W. Chen, "Hybrid active-passive irs assisted energy-efficient wireless communication," *ArXiv*, 2023 (cit. on p. 31).

[67] Z. Peng, X. Liu, C. Pan, L. Li, and J. Wang, "Multi-pair D2D communications aided by an active RIS over spatially correlated channels with phase noise," *IEEE Communications Letters*, vol. 11, no. 10, pp. 2090–2094, 2022 (cit. on p. 30).

[68] Z. Peng, R. Weng, Z. Zhang, C. Pan, and J. Wang, "Active reconfigurable intelligent surface for mobile edge computing," *IEEE Wireless Communication Letters*, vol. 11, no. 12, pp. 2482–2486, 2022 (cit. on p. 30).

[69] M. Razaviyayn, M. Hong, and Z.-Q. Luo, "A unified convergence analysis of block successive minimization methods for nonsmooth optimization," *SIAM Journal on Optimization*, vol. 23, no. 2, pp. 1126–1153, 2013. DOI: 10.1137/120891009. [Online]. Available: https://doi.org/10.1137/120891009 (cit. on pp. 198, 200, 203).

[70] W. Saad, M. Bennis, and M. Chen, "A vision of 6g wireless systems: Applications, trends, technologies, and open research problems," *IEEE Network*, vol. 34, no. 3, pp. 134–142, 2020. DOI: 10.1109/MNET.001.1900287 (cit. on p. 1).

[71] R. Schroeder, J. He, and M. Juntti, "Passive RIS vs. hybrid RIS: A comparative study on channel estimation," in *2021 IEEE 93rd Vehicular Technology Conference (VTC2021-Spring)*, 2021, pp. 1–7. DOI: 10.1109/VTC2021-Spring51267.2021.9448802 (cit. on p. 30).

[72] M. W. Shabir, M. Di Renzo, A. Zappone, and M. Debbah, "Electromagnetically consistent optimization algorithms for the global design of ris," *IEEE Wireless Communications Letters*, vol. 14, no. 5, pp. 1286–1290, 2025. DOI: 10.1109/LWC.2025.3529778 (cit. on p. 163).

[73] K. Shen and W. Yu, "Fractional programming for communication systems-part i: Power control and beamforming," *IEEE Transactions on Signal Processing*, vol. 66, no. 10, pp. 2616–2630, 2018 (cit. on pp. 31, 115, 179, 180, 197).

[74] S. Soderi, A. Brighente, S. Xu, and M. Conti, "Multi-RIS aided VLC physical layer security for 6G wireless networks," *IEEE Transactions on Mobile Computing*, vol. in press, 2024 (cit. on p. 115).

[75] Y. Sun, P. Babu, and D. P. Palomar, "Majorization-minimization algorithms in signal processing, communications, and machine learning," *IEEE Transactions on Signal Processing*, vol. 65, no. 3, pp. 794–816, 2017. DOI: 10.1109/TSP.2016.2601299 (cit. on pp. 198, 200).

[76] R. A. Tasci, F. Kilinc, E. Basar, and G. C. Alexandropoulos, "A new RIS architecture with a single power amplifier: Energy efficiency and error performance analysis," *IEEE Access*, vol. 10, pp. 44 804–44 815, 2022. DOI: 10.1109/ACCESS.2022.3167841 (cit. on p. 30).

[77] B. N. Thai, T. N. Tien, K. D. Minh, M. N. Tien, T. T. K. Hue, and N. X. Quyen, "Reconfigurable intelligent surfaces: A hardware-centric review of structures, implementation, evaluation, and integration with uav and machine learning," *IEEE Access*, vol. 13, pp. 96 564–96 588, 2025. DOI: 10.1109/ACCESS.2025.3575583 (cit. on p. 163).

[78] I. Trigui, W. Ajib, and W.-P. Zhu, "Secrecy outage probability and average rate of RIS-aided communications using quantized phases," *IEEE Communications Letters*, vol. 25, no. 6, pp. 1820–1824, 2021. DOI: 10.1109/LCOMM.2021.3057850 (cit. on pp. 76, 115).

[81] Y. Wang, Z. Lin, H. Niu, K. An, Y. Hu, D. Li, G. Zheng, and N. Al-Dhahir, "Secure satellite transmission with active reconfigurable intelligent surface," *IEEE Communications Letters*, vol. 26, no. 12, pp. 3029–3033, 2022 (cit. on pp. 76, 115).

[82] L. Wei, K. Wang, C. Pan, and M. Elkashlan, "Secrecy performance analysis of RIS-aided communication system with randomly flying eavesdroppers," *IEEE Wireless Communications Letters*, vol. 11, no. 10, pp. 2240–2244, 2022. DOI: 10.1109/LWC.2022.3198631 (cit. on p. 76).

[83] Q. Wu and R. Zhang, "Intelligent reflecting surface enhanced wireless network via joint active and passive beamforming," *IEEE Transactions on Wireless Communications*, vol. 18, no. 11, pp. 5394–5409, 2019 (cit. on p. 30).

[84] Q. Wu and R. Zhang, "Towards smart and reconfigurable environment: Intelligent reflecting surface aided wireless network," *IEEE Communications Magazine*, 2019 (cit. on pp. 2, 6, 16, 30, 40).

[85] Q. Wu and R. Zhang, "Intelligent reflecting surface enhanced wireless network: Joint active and passive beamforming design," in *2018 IEEE Global Communications Conference (GLOBECOM)*, 2018, pp. 1–6. DOI: 10.1109/GLOCOM.2018.8647620 (cit. on p. 7).

[86] Q. Wu and R. Zhang, "Beamforming optimization for wireless network aided by intelligent reflecting surface with discrete phase shifts," *IEEE Transactions on Communications*, vol. 68, no. 3, pp. 1838–1851, 2020. DOI: 10.1109/TCOMM.2019.2958916 (cit. on p. 101).

[87] P. Xu, G. Chen, G. Pan, and M. Di Renzo, "Ergodic secrecy rate of RIS-assisted communication systems in the presence of discrete phase shifts and multiple eavesdroppers," *IEEE Wireless Communications Letters*, vol. 10, no. 3, pp. 629–633, 2021. DOI: 10.1109/LWC.2020.3044178 (cit. on pp. 76, 115).

[88] L. Yang, J. Yang, W. Xie, M. O. Hasna, T. Tsiftsis, and M. Di Renzo, "Secrecy performance analysis of RIS-aided wireless communication systems," *IEEE Transactions on Vehicular Technology*, vol. 69, no. 10, pp. 12 296–12 300, 2020. DOI: 10.1109/TVT.2020.3007521 (cit. on pp. 76, 115).

[89] Z. Yigit, E. B. M. Wen, and I. Altunbas, "Hybrid reflection modulation," *IEEE Transactions on Wireless Communications*, 2021 (cit. on p. 30).

[90] C. You and R. Zhang, "Wireless communication aided by intelligent reflecting surface: Active or passive?" *IEEE Wireless Communications Letters*, vol. 10, no. 12, pp. 2659–2663, 2021. DOI: 10.1109/LWC.2021.3111044 (cit. on p. 30).

[91] A. Zappone, M. Di Renzo, and M. Debbah, "Wireless networks design in the era of deep learning: Model-based, AI-based, or both?" *IEEE Trans. on Commun.*, vol. 67, no. 10, pp. 7331–7376, 2019 (cit. on p. 164).

[92] A. Zappone, P. H. Lin, and E. A. Jorswieck, "Energy efficiency of confidential multi-antenna systems with artificial noise and statistical CSI," *IEEE Journal of Selected Topics in Signal Processing*, vol. 10, no. 8, pp. 1462–1477, 2016 (cit. on pp. 2, 114).

[94] A. Zappone, M. Di Renzo, F. Shams, X. Qian, and M. Debbah, "Overhead-aware design of reconfigurable intelligent surfaces in smart radio environments," *IEEE Transactions on Wireless Communications*, vol. 20, no. 1, pp. 126–141, 2021. DOI: 10.1109/TWC.2020.3023578 (cit. on p. 91).

[95] A. Zappone and E. Jorswieck, "Energy efficiency in wireless networks via fractional programming theory," *Foundations and Trends® in Communications and Information Theory*, vol. 11, no. 3-4, pp. 185–396, 2015 (cit. on pp. 49, 51, 54, 99, 123, 180, 194–197).

[96] S. Zargari, A. Hakimi, C. Tellambura, and S. Herath, "Multiuser MISO PS-SWIPT systems: Active or passive RIS?" *IEEE Wireless Communication Letters*, vol. 11, no. 9, pp. 1920–1924, 2022 (cit. on p. 31).

[97] Y. Zhang, Y. Lu, R. Zhang, B. Ai, and D. Niyato, "Deep reinforcement learning for secrecy energy efficiency maximization in RIS-assisted networks," *IEEE Transactions on Vehicular Technology*, vol. 72, no. 9, pp. 12 413–12 418, 2023. DOI: 10.1109/TVT.2023.3269805 (cit. on p. 115).

[98] Z. Zhang, L. Dai, X. Chen, C. Liu, F. Yang, R. Schober, and H. V. Poor, "Active RIS vs. passive RIS: Which will prevail in 6G?" *IEEE Transactions on Communications*, 2022 (cit. on pp. 40, 76, 115).

[99] Z. Zhang *et al.*, "Active RIS vs. passive RIS: Which will prevail in 6G?" *IEEE Transactions on Communications*, vol. 71, no. 3, 1707–1725, Mar. 2023 (cit. on pp. 2, 7).

[100] Z. Zhang, J. H. Qiu, J. W. Zhang, H. D. Li, D. Tang, Q. Cheng, and W. Lin, "Physics-informed machine learning optimization design of reconfigurable intelligent surfaces for iot applications," *IEEE Internet of Things Journal*, pp. 1–1, 2025. DOI: 10.1109/JIOT.2025.3611536 (cit. on p. 164).

[101] M.-M. Zhao, K. Xu, Y. Cai, Y. Niu, and L. Hanzo, "Secrecy rate maximization of RIS-assisted swipt systems: A two-timescale beamforming design approach," *IEEE Transactions on Wireless Communications*, vol. 22, no. 7, pp. 4489–4504, 2023. DOI: 10.1109/TWC.2022.3225969 (cit. on pp. 76, 115).

[102] K. Zhi, C. Pan, H. Ren, K. K. Chai, and M. Elkashlan, "Active RIS versus passive RIS: Which is superior with the same power budget?" *IEEE Communications Letters*, vol. 26, no. 5, pp. 1150–1154, 2022 (cit. on p. 30).

[103] Q. Zhu, M. Li, R. Liu, Y. Liu, and Q. Liu, "Joint beamforming designs for active reconfigurable intelligent surface: A sub-connected array architecture," *IEEE Transactions on Communications*, vol. 70, no. 11, pp. 7628–7643, 2022 (cit. on pp. 31, 115).